Doctoral theses at NTNU, 2022:93

Stephan André Böhme

Tooth Flank Fracture in Spiral Bevel Gears

Multiaxial Fatigue and Material Properties

Doctoral thesis

NTNU
Norwegian University of Science and Technology
Thesis for the Degree of
Philosophiae Doctor
Faculty of Engineering
Department of Mechanical and Industrial
Engineering

NTNU
Norwegian University of
Science and Technology

Stephan André Böhme

Tooth Flank Fracture in Spiral Bevel Gears

Multiaxial Fatigue and Material Properties

Thesis for the Degree of Philosophiae Doctor

Trondheim, April 2022

Norwegian University of Science and Technology
Faculty of Engineering
Department of Mechanical and Industrial Engineering

NTNU
Norwegian University of
Science and Technology

NTNU
Norwegian University of Science and Technology

Thesis for the Degree of Philosophiae Doctor

Faculty of Engineering
Department of Mechanical and Industrial Engineering

ISBN 978-82-326-6184-8 (printed ver.)
ISBN 978-82-326-6399-6 (electronic ver.)
ISSN 1503-8181 (printed ver.)
ISSN 2703-8084 (online ver.)

Doctoral theses at NTNU, 2022:93

Printed by NTNU Grafisk senter

NTNU
Norwegian University of
Science and Technology

TOOTH FLANK FRACTURE IN SPIRAL BEVEL GEARS - MULTIAXIAL FATIGUE AND MATERIAL PROPERTIES

Stephan André Böhme

A thesis submitted for the degree of
Doctor of Philosophy

April 2022

Preface

This Ph.D. thesis is submitted for partial fulfilment of the requirements for the degree of philosophiae doctor at the Norwegian University of Science and Technology (NTNU), Trondheim, Norway. The associated work of this doctoral project was carried out at the Department of Mechanical and Industrial Engineering under the supervision of Prof. Alexei Vinogradov, Dr. Mette Lokna Nedreberg and Dr. Ing. Philippe Mainçon. The project benefited from a fellowship awarded by the Norwegian Research Council and financial support from Kongsberg Maritime AS, ATA Gears Oy, Voith GmbH & Co. KGaA and Schottel GmbH.

Stephan André Böhme
Ålesund, April 2022

Acknowledgements

I gratefully acknowledge that this work is not the achievement of an individual but a group of people. Chief among those are my parents, to whom I hereby express my sincerest gratitude for their unwavering support and guidance. Above all others, my wife played a crucial part in the creation of this academic work, for she has given me purpose and joy and granted me the opportunity to pursue my Ph.D.

I want to thank my mentor and supervisor, Prof. Alexei Vinogradov, for being the foundation of all the academic achievements during my time at the NTNU. Through his mentorship and guidance, we have been able to make contributions to the field of multiaxial fatigue in gears and established a network of researchers and universities throughout Europe. To my co-supervisors, Dr. Mette Lokna Nedreberg and Dr. Ing. Philippe Mainçon, Prof. Filippo Berto, my fellow researchers and colleagues at the NTNU, I would like to express my most profound appreciation and gratitude. Thank you for your counsel and advice, the numerous academic exchanges and your genuine interest in the field. The herein presented results would have not been possible without you.

Of my fellow researchers and colleagues Jan Papuga, Prof. Horst Biermann, PD Dr. Ing. Anja Weidner, Tami Komssi, Alexander Schmiedel, Dr. Steffen Schäfer, Joni Keski-Rahkonen, Gábor Szánti, Dr. Jan Nebel, Leif Aarseth and of my colleagues at the Department of Mechanical and Industrial Engineering Steffen Loen Sunde, Daniele Di Candia, Abedin Gagani, Andrey Krauklis and Szymon Bernat, I would like to thank you all explicitly for your contributions to this thesis.

The gear failure mode Tooth Flank Fracture has been studied by many researchers and institutions over the years with the Forschungsstelle für Zahnräder und Getriebebau (FZG) at the TU München being a key player. Their work has paved the way for the herein presented findings and results. Similarly, I would like to extend my gratitude to all members of the *Improved reliability of thrusters* joint industry project for their support of this project and the many interesting discussions and meetings.

"Knowledge is an unending adventure at the edge of uncertainty"
Frank Herbert in "Children of Dune"

Abstract

Due to the improvements made in the prediction and prevention of surface-initiated gear failure modes like pitting, tooth root breakage, scuffing and micropitting, a transition from surface to subsurface-initiated failures is occurring on spiral bevel gears. The herein presented work continues the efforts of the *Improved reliability of thrusters* joint industry project - a cooperation between thruster suppliers, gear manufacturers, steel suppliers, forging companies and the maritime classification society - and aims at the prediction and prevention of subsurface initiated fatigue or tooth flank fracture in large maritime spiral bevel gears.

In this thesis, the three relevant building blocks for a successful tooth flank fracture prediction, namely a material model for case hardened CrNiMo steel, a numerical stress prediction in the gear tooth's mean cross-section and a, for rolling contact fatigue applicable, multiaxial fatigue criterion are proposed and verified. Tooth flank fracture is not a new failure mode but has been increasing in severity since the beginning of the 21st century. This thesis represents thereby a continuation of the works done by the FZG and Forschungsvereinigung Antriebstechnik (FVA), the International Organization for Standardization (ISO), Det Norske Veritas (DNV) and researchers like MackAldener and Weber, to name a few. It focuses on large maritime bevel gears and extends its applicability to other gear sizes through the derived size and lifetime factors. Numerous uniaxial and shear fatigue tests under alternating and oscillating stresses in the high cycle and very high cycle fatigue regime along with load-controlled bevel gear tests were carried out to derive a material model for case hardened CrNiMo steel and to verify the proposed multiaxial fatigue criterion, the predicted material utilisation and failure origins (i.e. the initiation depths in the studied gear teeth).

While the gear failure mode tooth flank fracture was the focus of this academic work, qualitative evidence is presented for the applicability of the developed methodology to other gear failure modes, namely pitting and tooth root breakage.

Keywords: Tooth flank fracture, multiaxial fatigue, rolling contact fatigue, case hardened steel

Table of Contents

List of Figures

List of Tables

Abbreviations

$B1, 2, 3$	Test gear heat treatment batches 1, 2 and 3
$CrNiMo$	Chromium, Nickel, Molybdenum
$CIRF$	Crack initiation risk factor
DNV	Det Norske Veritas
$EBSD$	Electron backscatter diffraction
EDM	Electric discharge machining
ESR	Electro-slag remelting
FEM	Finite element modelling
FKM	Forschungskuratorium Maschinenbau
FVA	Forschungsvereinigung Antriebstechnik
FZG	Forschungsstelle für Zahnräder und Getriebebau
$G0$	FZG pitting gear set
$G1, 2$	Maritime gear sets 1 and 2
ISO	International Organization for Standardization
$LTCA$	Loaded tooth contact analysis (Becal)
MB	Design point according to ISO10300
MCC	Minimum circumscribing circle
MLM	Maximum Likelihood Method
MRH	Maximum rectangular hull
$NTNU$	Norwegian University of Science and Technology
P	Gear's pitch point
$PAUT$	Phased array ultrasonic scanning
RCF	Rolling contact fatigue
SEM	Scanning electron microscopy
SN	Stress amplitude vs. number of load cycles
TFF	Tooth flank fracture
$TIFF$	Tooth interior fatigue fracture
HCF	High cycle fatigue
$VHCF$	Very high cycle fatigue

Nomenclature

Indices

$1, 2$	Pinion or wheel
a	Amplitude
b	Base
c	Core
eff	Effective
f	Root
i	i'th element
m	Mean
max	Maximum
mod	Modified
n	Normal or perpendicular
ref	Reference
s	Surface
v	Virtual cylindrical gear
AN	Annast
B	Balduzzi
BO	Böhme
CR	Crossland
DNV	Det Norske Veritas
DV	Dang Van
FKM	Forschungskuratorium Maschinenbau
FI	Findley
FO	Fogue
H	Hertz
HE	Hertter
Hs	Hs criterion
ISO	ISO6336-4 technial report
K	Lifetime and size adjusted fatigue strength
LZ	Liu & Zenner
MA	Matake
MB	Design point ISO10300-2

MC	McDiarmid
MU	Murakami
OS	Oster
PCR	Papuga PCR
PN	Papuga PCRN
PI	Papuga PIN
RO	Robert
SI	Sines
T	Timoshenko
WE	Weber

Variables

Latin variables

$\sqrt{area}$	Square root of the projected area of an inclusion	[μm]
b	Tooth width	[mm]
$\widetilde{b}$	Linear function for stress distribution in cross-section	[-]
b_H	Half Hertzian contact width	[mm]
d	Diameter	[mm]
d_{e2}	Outer gear wheel diameter	[mm]
dS	Plain strain condition	[MPa]
d_{va}	Tip diameter of the virtual cylindrical gear	[mm]
f	Fatigue damage parameter	[MPa, MPa^2]
f_{-1}	Uniaxial fatigue strength under alternating load	[MPa]
$f_{-1,up}$	Upper Uniaxial fatigue strength (clean steel)	[MPa]
f_0	Uniaxial fatigue strength under oscillating load	[MPa]
f_{xK}	Conversion factor	[-]
h	Tooth height	[mm]
m_{mn}	Mean normal module	[-]
n	Stress redistribution factor	[-]
$n_{x',y',z'}$	Unit vectors	[1x3]
p_{dyn}	Local surface pressure ISO6336-4	[MPa]
p_H	Hertzian contact pressure	[MPa]
s_{log}	Standard deviation of the log cycles to failure	[-]
s_n	Chordal tooth thickness	[mm]
s'_n	Change in the tooth width	[-]
$s_{n\alpha}$	Perpendicular tooth width underneath studied contact point	[mm]
s_r	Relative standard deviation	[%]
s_{tB-D}	Local tooth width B-D	[mm]
t	Traction vector	[1x3]

t_{-1}	Shear fatigue strength under alternating load	[MPa]
t_0	Shear fatigue strength under oscillating load	[MPa]
x	Coordinate in tooth width or depth direction	[mm]
x_c	Depth of the maximum hardness	[mm]
$x_{HV,max}$	Depth of the maximum hardness	[mm]
y	Coordinate in tooth profile direction	[mm]
z	Coordinate in tooth lengthwise direction	[mm]
z_v	Virtual number of teeth	[mm]
A	Cross-sectional area	[mm^2]
CHD	Case hardening depth	[mm]
D	Material utilisation	[-]
E	Young's Modulus	[-]
F_1	Variable describing the displacement of MB	[N]
F_r	Radial force	[N]
F_t	Tangential force	[N]
HV	Hardness in Vickers	[HV]
HV'_{CHD}	Hardness gradient in CHD	[HV/mm]
I	Inertia of a rectangular cross-section	[mm^4]
$J_{2,a}$	Second invariant of the stress tensor deviator	[MPa^2]
K_A	Application factor	[-]
$K_{F\alpha}$	Transverse load factor for bending stress	[-]
$K_{F\beta}$	Load factor for bending stress	[-]
$K_{F\tau}$	Surface roughness factor	[-]
$K_{H\beta}$	Load factor for contact stress	[-]
$K_{H\beta-be}$	Mounting factor	[-]
K_{NT}	Lifetime factor	[-]
K_v	Dynamic factor	[-]
$K_{1,2}$	Influence factors ISO6336-4	[-]
K_X	Size factor	[-]
M	Mean stress sensitivity	[-]
M_b	Bending moment	[Nm]
N_f	Number of load cycles	[-]
R	Stress ratio	[-]
R	Reliability	[-]
R_m	Ultimate tensile strength	[MPa]
S	Stress matrix	[3x3]
V	Volume	[mm^3]
Y_{BS}	Bevel spiral angle factor	[-]
Y_ε	Contact ratio for bending	[-]
Y_{LS}	Load sharing factor	[-]
Y_{MB}	Tooth form factor in MB	[-]
Z_{MB}	Mid-zone factor	[-]
Z_{AE}	Load factor FVA516	[-]
Z_K	Bevel gear factor	[-]

Greek variables

α	Pressure angle	[°]
α_{Fan}	load application angle at tooth tip	[°]
α_m	Murakami's mean stress sensitivity factor	[-]
α_σ	Geometrical notch factor	[-]
$\beta_{0\mu}$, $\beta_{1\mu}$, β_{0s}, β_{1s}	Maximum Liklihood Method model parameters	[-]
γ	Maximum Liklihood Method fatigue limit	[MPa]
γ_{alpha}	Tooth correction factor	[rad]
κ	Fatigue ratio f_{-1}/t_{-1}	[-]
λ	Standardized normal distribution factor	[-]
μ	Friction coefficient	[-]
μ_{log}	Mean log cycles to failure	[-]
ν	Poisson ratio	[-]
ϕ, θ	Euler angles	[°]
ρ_{eq}	Equivalent radius of curvature	[mm]
σ_a	Stress amplitude during uniaxial fatigue testing	[MPa]
σ_b	Bending stress	[MPa]
σ_{eq}	Equivalent stress	[MPa]
σ_f	True fracture strength	[MPa]
σ_{HB1}	Hertzian contact stress (ISO10300)	[MPa]
σ_{hyd}	Hydrostatic stress	[MPa]
$\sigma_{MB,B1}$	Maximum bending stress in MB	[MPa]
σ_n	Normal stress	[MPa]
σ_{res}	Residual stress	[MPa]
σ'_{res}	Gradient of residual stress	[MPa/mm]
σ_{RS}	Residual stress ISO6336-4	[MPa]
σ_{vM}	Von Mises equivalent stress	[MPa]
σ_y	Bending stress	[MPa]
σ_{y0}	Mean value of the radial stress within the cross-section	[MPa]
σ_{y1}	Maximum radial stress induced by the bending moment within a cross-section (Balduzzi)	[MPa]
$\Delta\sigma_y$	Difference in bending stress between numerical and analytical approach (Balduzzi)	[MPa]
$\sigma_{y,n}$	Transverse normal stress	[MPa]
τ_0	Mean shear stress (Balduzzi)	[MPa]
τ	Shear stress	[MPa]
$\tau_{eff,L}$	Effective or spatial average of the maximum shear stress	[MPa]
$\Delta\tau_{eff,L,RS}$	Quasi-mean shear stress	[MPa]
$\tau_{eff,RS}$	Residual stress equivalent shear stress	[MPa]
τ_{H12}	Main principle shear stress	[MPa]
τ_m	Mean shear stress	[MPa]
τ_{max}	Maximum shear stress	[MPa]

τ_{min}	Minimum shear stress	[MPa]
τ_{xy}	Shear stress	[MPa]
$\tau_{xy,a}$	Orthogonal shear stress amplitude	[MPa]
τ_{zul}	Shear strength (ISO6336-4)	[MPa]
Δ	Material plane	[-]
Ψ	Stress path	[-]

Chapter 1

Introduction

This thesis is closely linked to the maritime industry, azimuthing thrusters, spiral bevel gears and the application-specific dominant failure mode tooth flank fracture (TFF). An introduction to TFF, a failure mode characterisation and a brief historical exposition are given in addition to a summary of all published articles. In this preface, the ISO6336-4 technical report [1] is quoted for its TFF definition.

"Tooth flank fracture is characterised by a primary fatigue crack in the region of the active contact area, initiated below the surface due to shear stresses caused by the flank contact. Tooth flank fracture is most often observed on case carburised gears but failures are also known for nitrided and induction hardened gears."

1.1 Motivations and goals

Typical applications for bevel gears are automotive differentials, main and tail rotors in helicopters and bow or azimuthing thrusters in the maritime industry. Azimuthing thrusters are the preferred propulsion method for platform supply vessels, anchor handlers, ferries, cruise ships and tugboats as they improve manoeuvrability, course stability and dynamic positioning capabilities.

Conventional azimuthing thrusters feature one or two spiral bevel gears between an either vertically or horizontally mounted drive motor and the propeller. Especially the gear set in proximity to the propeller suffers from gear failures, despite a stringent design process that relies on classification standards for marine propulsor like the Det Norske Veritas (DNV) gear rating standard DNVGL-CG-0036 [2]. Figure 1.1a shows the cross-section of an azimuthing thruster with two bevel gear sets mounted between the horizontal input and propeller shafts. The standard material choice is case hardened 18CrNiMo7-6 steel and typical sizes range from 500 to 1500 mm (outer gear wheel diameter d_{e2}), transmitting between 1 to 5 MW of power. In Figure 1.1b, a wheel-initiated TFF after ap-

proximately three years of operation or $3 \cdot 10^8$ load cycles is shown. Figure 1.1c plots a sectioned bevel gear tooth, visualising the typical TFF crack path from the loaded drive flank to the tooth root of the unloaded coast flank.

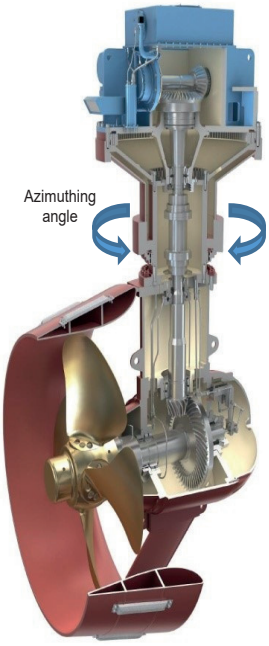

(a) Azimuthing thruster

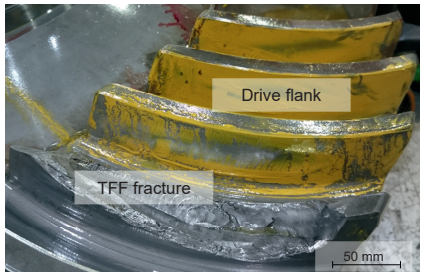

(b) TFF on maritime gear wheel

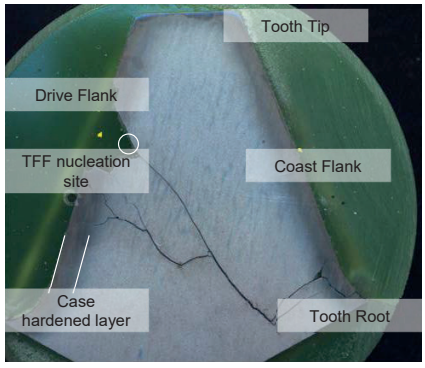

(c) Sectioned TFF gear tooth [3]

Figure 1.1: TFF in maritime bevel gears

Pitting, tooth root breakage, scuffing, micropitting and wear are established and well-defined gear failure modes. They are related to the surface of the loaded tooth flank or the gear's tooth root. As a result of the optimisation of the gear's macro- and microgeometry through advanced simulation tools and 5-axis machining, improvements in regards to the gear's material, the heat treatment process, utilised lubricants and post-processing steps like shot-peening or isotropic superfinishing, a transition from surface to subsurface-initiated failures are occurring on large bevel gears.

While the above-listed failure modes can successfully be avoided through established gear standards [2, 4, 5] and the research and publications by the FZG and FVA [6–9], TFF is becoming increasingly prevalent, ultimately terminating a maritime gear's functionality well before its intended service lifetime of 20 years or more. According to the classification society DNV, approximately 3/4 of all premature gear failures on azimuthing thrusters are caused by TFF. The

unscheduled dry docking of an offshore vessel causes, besides the considerable replacement costs of the broken gear set, a prolonged downtime, leading to additional costs, in the form of off-hire losses. With lead times for large bevel gears being six months or longer, the criticality of TFF is further exacerbated.

1.1.1 Research objectives

Unforeseen TFFs on azimuthing thrusters are a concern to the operation of offshore vessels and among the highest research priorities for the maritime supply industry. This academic work aims at expending the existing knowledge and understanding of the gear failure mode with an explicit focus on large, case hardened, bevel gears. Most gear standards have been developed for relatively small, typically automotive gears and derived from similarly sized test gears ($d_{e2} \approx 170$ mm and mean normal module $m_{mn} of 2$ to 5 mm). The applicability of said standards to spiral bevel gears with wheel diameters > 1 m needs to be questioned, especially when the crack initiation occurs not on the surface but in the case/core interface. One known issue on large gears is the prevalent material anisotropy expressed through the coarse dendritic solidification structure that is only insufficiently broken up during hot forging. With resulting hardness differences in the alloy-rich but carbon-poor and alloy-poor but carbon-rich microstructures over 150 HV, their criticality for the gear's local fatigue behaviour cannot be ignored [10, 11].

Azimuthing thrusters can be subjected to highly dynamic loads during extreme weather conditions, impact events or due to unfavourable inflow conditions to the propeller. The prediction of these conditions and the thruster's response to them have been studied and published for example by the Department of Marine Technology at the Norwegian University of Science and Technology (NTNU). This thesis does not quantify these loads but focuses instead on the development of a methodology that enables the consideration of these conditions.

Material model

Multiaxial fatigue under rolling contact fatigue (RCF) is at the core of the herein studied TFF failure mode. In contrast to through-hardened applications like small and medium-sized bearings, spiral bevel gears are case hardened, resulting in varying material properties throughout the hardened layer. Recent additions to the family of stress-based multiaxial fatigue criteria are the shear stress intensity or integral methods (for example, the shear stress intensity criterion by Liu & Zenner [12]). In the case of the Liu & Zenner criterion, the spatial average of the damage parameter overall material planes is calculated. It considers the shear mean and amplitude stresses (τ_m and τ_a) and the normal mean and amplitude stresses ($\sigma_{n,m}$ and $\sigma_{n,a}$) as functions of the Euler angles ϕ and θ. To weigh these stresses and to calculate the spatial average, four model parameters are required. These model parameters rely in turn on four material constants for their prediction - typically the uniaxial fatigue strength

under alternating load f_{-1}, the uniaxial fatigue strength under oscillating load f_0, the shear fatigue strength under alternating load t_{-1} and the shear fatigue strength under oscillating load t_0. Figure 1.2 visualises the cyclic loading conditions when testing for f_{-1} and f_0 and depicts the effect of compressive and tensile mean stresses on the fatigue strength in the form of a Haigh diagram for 400 HV hard, mild steel according to the FKM guideline [13].

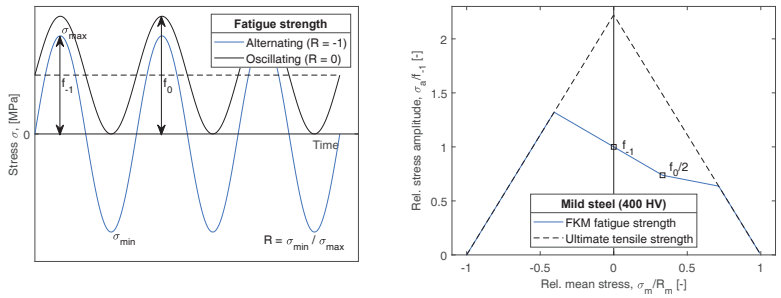

(a) Cyclic loading at varying stress ratios (b) Haigh diagram according to FKM [13]

Figure 1.2: Uniaxial material constants

A material model for case hardened CrNiMo steel needs to be developed that defines these four material constants to enable an accurate fatigue assessment in the TFF critical material depth. Figure 1.3 depicts the case hardened layer of a maritime bevel gear in the vicinity of a TFF-crack, highlighting the hardness profile and changing microstructure. The material properties and residual stresses are a result of the different local material phase compositions, transformation histories and volume expansions. Apparent is also the *channelling* of the carbon in Figure 1.3a in the case/core interface (i.e. 2 to 3 mm), creating parallel *fingers* or areas of high carbon concentration and high hardness and areas of low carbon, but high alloying concentration and low hardness.

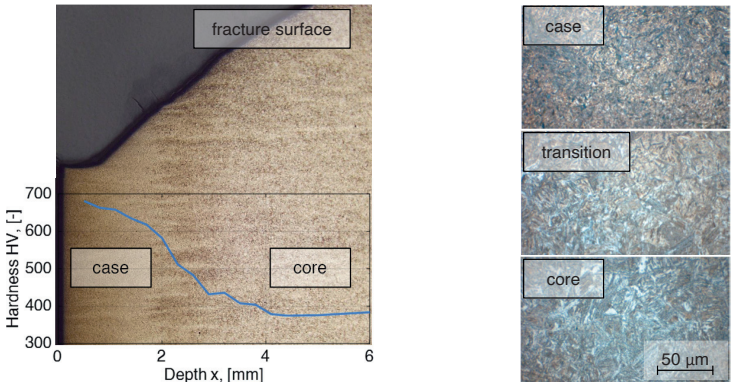

(a) Hardness profile and macrostructure (b) Case, transition and core microstructures

Figure 1.3: Material structure in large, case hardened gears

Stress model

Load-induced and manufacturing-related stresses are superpositioned and locally elevated by inclusions or asperities in the contact during the meshing of pinion and wheel teeth. Existing gear, subsurface stress models [1, 6, 14, 15] are analytical in nature and consider the dynamic Hertzian stresses, the static residual stresses and in some cases, Bernoulli bending and Timoshenko shear stresses, ignoring the effect of the bending moment on the shear stress distribution and the transverse normal stresses in the point of load introduction [16, 17]. A numerical or refined analytical calculation method needs to be developed to improve upon the subsurface stress prediction in gear teeth. Here, a numerical, 2D plane strain, purely elastic model for the stress prediction in the mean cross-section of gear tooth was favoured over 3D contact analysis due to its accuracy and simplicity, enabling in turn higher mesh, load and angular resolutions. A general model definition is visualised in Figure 1.4, depicting the analysed mean-cross section and the definitions of the radius of curvature of pinion and wheel $\rho_{1,2}$, the equivalent radius of curvature ρ_{eq} and the Hertzian surface pressure p_H between the meshing gear teeth for an instantaneous contact position. The predictions of p_H and ρ_{eq} for all contact positions rely on a loaded tooth contact analysis (LTCA) with the FVA software Becal [18]. They can also be derived through analytical equations as outlined in the works by Hombauer and Klein on micropitting and scuffing [7, 8]. LTCA-derived distributions of p_H and ρ_{eq} for the mean cross-section of a pinion tooth are shown in Figure 1.5c. Figure 1.5a demonstrates the stress concentration in the middle or mean cross-section of the studied pinion tooth. The changing equivalent radius of curvature in tooth profile and lengthwise directions is visualised in Figure 1.5b.

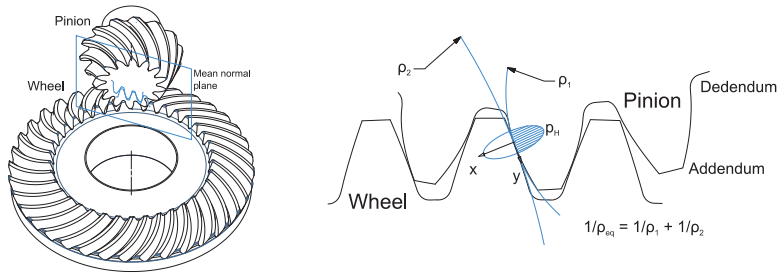

(a) Gear set G1 (b) Mean normal cross-section

Figure 1.4: 2D model definition

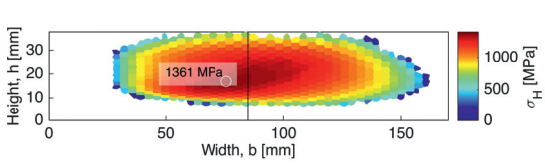

(a) LCTA pressure distribution p_H

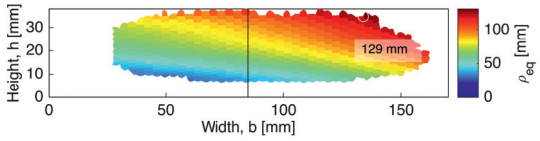

(b) LCTA radius of curvature ρ_{eq}

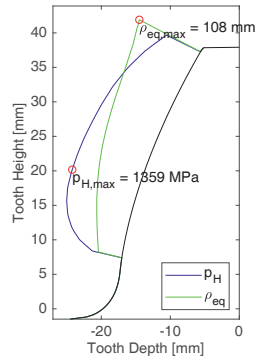

(c) p_H and ρ_{eq} applied to mean cross-section

Figure 1.5: Stress model for a G1 pinion tooth and its mean cross-section (geometry and load according to Papers I and III [10, 19]

Multiaxial fatigue model

The majority of the herein studied stress-based multiaxial fatigue criteria have not been developed for RCF. The Hertzian contact between the meshing gear teeth results in equally large compressive mean normal stresses and normal stress amplitudes in surface near or shallow material layers. These stresses lead to an overestimation of the local fatigue risk underneath the loaded gear flank for most multiaxial criteria. Contrary, the Liu & Zenner shear stress intensity criterion [12] significantly underestimates the local fatigue risk in the same material layer.

A multiaxial fatigue criterion needs to be identified or developed that enables a fatigue prediction under RCF. The criterion's accuracy needs to be verified through benchmarking against other stress-based criteria under conventional

multiaxial fatigue conditions and gear testing of medium-sized spiral bevel gears (i.e. $d_{e2} = 450$ mm). Figure 1.6 displays the predicted material utilisation or material exhaustion D according to Papuga's PIN criterion [20] and the Liu & Zenner shear stress intensity criterion [12] for the mean cross-section of a pinion bevel gear tooth, exemplifying the issue with non-RCF fatigue criteria. The material utilisation is defined as the inverse of the local safety factor or the ratio between the local equivalent stress or spatial average and the material strength.

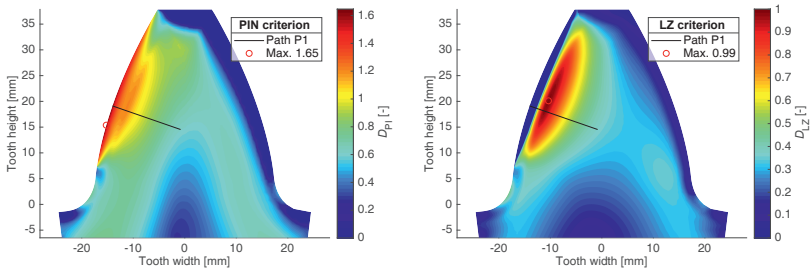

(a) PIN criterion [20] (b) LZ criterion [12]

Figure 1.6: Material utilisation in G1 pinion tooth

Standardised approach

TFF needs to be characterised as a highly complex gear failure mode as it requires numerical calculations, the prediction of local mean and amplitude stresses on multiple material planes, the definition of local constitutive parameters and the application of a, for RCF-suitable, stress-based fatigue criterion. Based on the developed understanding of the failure mode and its governing stresses, a comprehensible or standardisable approach needs to be developed that enables the rudimentary assessment of subsurface fatigue in case hardened gears. The herein developed method follows in the footsteps of the ISO10300 standard [21] and ISO6336-4 technical report [1] and relies entirely on their geometrical definitions and their stress approximations. It is fundamentally aimed at supporting the design phase of a gear, where not all input parameters are defined but rather iterated upon to yield a sufficiently optimised gear design against all failure modes. It foregoes all complex stress calculation in favour of a comprehensible, linear and intuitive subsurface fatigue assessment.

1.2 TFF characterisation

Whereas well-established gear failure modes like pitting, micropitting or scuffing initiate on the load-carrying flank, TFF occurs in a specific material depth,

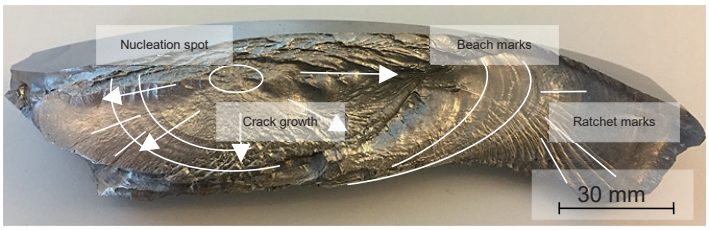

(a) Terminal TFF with fatigue fracture features (i.e. nucleation spot, beach and ratchet marks)

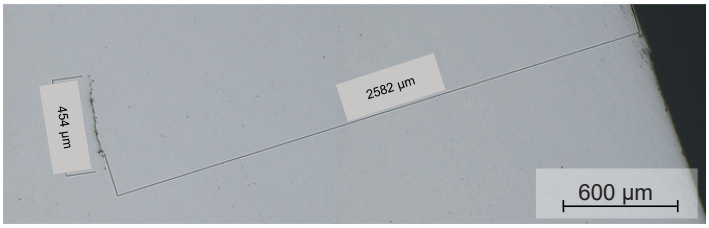

(b) Early, surface-parallel TFF in 2.6 mm depth and 0.5 mm size

Figure 1.7: TFF crack propagation from initially surface-parallel cracks through the entire gear tooth

typically 1 to 2 times the case hardening depth CHD. The failure mode is prevalent in industrial applications that rely on case hardened gears like wind turbines, truck and train transmissions and azimuthing thrusters. Unique to TFF is an initially invisible crack initiation and propagation that leads to a sudden and often catastrophic gear failure. Large metal particles that are released during the tooth fracture will impact other driveline components like bearings and seals. Alternative means than visual inspection are necessary to detect progressing TFFs and prevent tooth fractures.

To avoid catastrophic gear failures, the maritime industry has adopted ultrasonic scanning to identify early-stage TFFs during overhauls and service intervals. Phased array ultrasonic scanning (PAUT) has proven highly accurate in detecting ≤ 0.5 mm cracks several millimetres below the load-carrying flank on large maritime bevel gears. Whereas gearwheel teeth can be scanned efficiently with phased array probes due to the relatively low curvature of the teeth, pinion teeth require non-phased array or monolithic probes. Regardless of which type of probe is employed, accurate crack detection is achieved when scanning the gear's loaded drive flank and not the tooth tip as early-stage TFF cracks are orientated parallel to the flank. Figure 1.7 shows a terminal-stage and an early-stage TFF damage with a 454 μm large, surface parallel, subsurface crack.

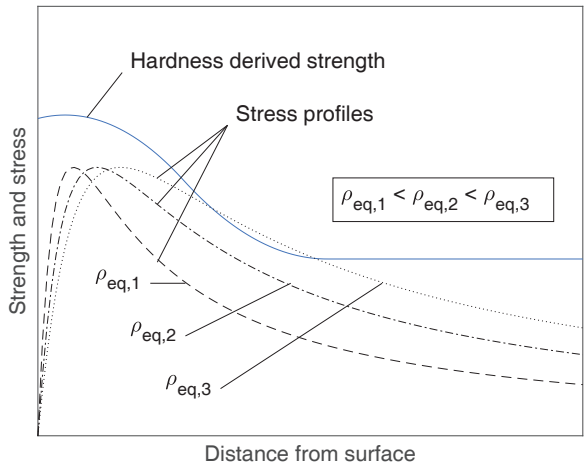

Figure 1.8: Rudimentary TFF model, comparing the local shear strength with the geometry and load-dependent shear stress amplitude [15]

1.2.1 Damage mechanism

With TFF initiating under shear, rudimentary TFF models compare a hardness-derived shear fatigue strength and a geometry and load-derived shear stress amplitude. The shape of the shear stress amplitude is a result of the dynamic Hertzian contact pressure between the meshing gear teeth p_H and the flank's local curvature, expressed in the equivalent radius of curvature ρ_{eq}. Whereas p_H dictates the magnitude of the shear stress profile, the depth of its maximum is a function of ρ_{eq}. As indicated in Figure 1.5, the equivalent radius of curvature ρ_{eq} changes on spiral bevel gears in tooth profile direction and to a lesser degree in tooth lengthwise direction. Assuming equal Hertzian contact stresses, three different shear stress profiles are plotted and compared to an idealised shear strength in Figure 1.8.

As shown for the largest equivalent radius of curvature $\rho_{eq,3}$, crack initiation in the transition zone from hard case to soft core is likely to occur as the local stress exceeds the local fatigue strength. Bevel and hypoid gears - more so than similarly sized cylindrical gears - feature larger curvatures on the tooth flank, requiring deeper case hardening depths to prevent TFFs [22]. Crack initiation and early propagation are parallel to the load-carrying flank in mode II *in-plane shear* or *sliding* and transition into mode I *tension* or *opening* under the acting bending stresses when propagating through the gear tooth. Characteristic TFF features are the formation of primary, secondary and tertiary cracks. The primary crack front will initially grow parallel to the loaded flank and subsequently into the gear tooth in an approximately 45° angle before propagating

to the loaded tooth flank. Once the loaded flank has sufficiently been weakened, secondary and tertiary cracks will form from the primary crack front (see Figure 1.1c). Via PAUT, elliptically shaped 10 mm wide and 0.5 mm high, nearly surface parallel cracks have been documented [11]. They suggest an initial crack growth that is significantly faster in tooth lengthwise than tooth profile direction.

Whereas three shear stress profiles are compared with the local material strength in Figure 1.8, the actual stress state in a bevel gear tooth is significantly more complex. As outlined in the multiaxial fatigue approach by Hertter [6], the stress state in gears is defined through the superposition of the Hertzian contact stresses, frictional shear, localised thermal, bending, transverse shear and the static residual stresses.

1.2.2 Fracture surface

The fracture surface of a TFF damage features clear signs of subsurface initiated fatigue, starting in often a single but occasionally also multiple nucleation spots with or without the presence of an inclusion. Other fatigue features are beach marks in the tooth interior and ratchet marks in the instantaneous fracture area. As shown in Figure 1.7a, the gear tooth is substantially weakened prior to the instantaneous fracture. Typical for TFF is also the formation of a *Fisheye* of considerable size around the crack initiation region. It is the result of micromovements between the fracture surfaces and the smoothening of surface roughnesses. The formation of the *Fisheye* will lead to the removal of the previously mentioned macroscopic fatigue features. Topographic images of a TFF crack origin are provided in Paper I [10]. They reveal two ridges to either side of the identified initiation region, an almost plane crack propagation into the tooth interior and multiple level changes towards the loaded flank.

1.3 Historical context

This section provides a brief historical exposition of the previously published works on TFF, tooth interior fatigue fracture (TIFF), Flankenbruch or subsurface fatigue. Most of the herein listed references are included with their proposed calculation methods in Appendix B.

MackAldener - TIFF

MackAldener published his findings on subsurface fatigue in case hardened idler gears and the optimisation of a gear design regarding noise, quality and costs [23] in 2001. He coined the observed subsurface failures TIFF. The term was later not adopted by the FZG and the ISO as the crack path on MackAldener's idler gears formed a plateau in the middle of the tooth rather than a wedge, typical for single flank loaded cylindrical, bevel or hypoid gears (compare Figures 1.9a and 1.1c).

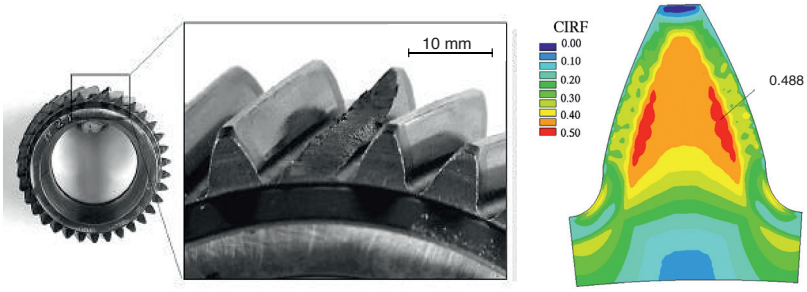

(a) Typical TIFF on truck idler gear

(b) Crack initiation risk factor (CIRF) or material utilisation

Figure 1.9: Visualisation of subsurface fatigue failure and prediction model by MackAldener [23]

MackAldener relied on the Findley criterion [24] to predict a local material utilisation or crack initiation risk factor (CIRF) as the ratio between the Findley criterion's equivalent stress and the fatigue strength in the studied gears. He conducted uniaxial and shear fatigue tests under alternating load of two gear steels prior and post case hardening to estimate the gear's local material properties as a function of the hardness profile. In addition, x-ray and neutron diffraction residual stress measurements were performed to document and consider the compressive residual stresses in the case and tensile residual stresses in the core. For the herein outlined research, a number of the concepts proposed by MackAldener were adapted and expanded upon. Those are the use of conventional fatigue testing to determine the multiaxial fatigue criterion's model parameters and residual stress measurements by means of neutron diffraction. The herein presented results suggest that the implemented Findley criterion is not among the most accurate stress-based criteria and that the by MackAldener utilised calculation of the shear stress amplitude according to Equation 1.1 is not applicable to the non-proportional loading found in gears.

$$\tau_a = \frac{\tau_{max} - \tau_{min}}{2} \tag{1.1}$$

Due to misalignment issues during the uniaxial fatigue testing of the case hardened fatigue specimens, MackAldener approximated a fatigue ratio κ (i.e. the ratio between the uniaxial and shear fatigue strength under alternating loading) of 1 for the hard case. The herein performed literature study and fatigue tests suggest values closer to 1.4 for the hard case.

DNV - Subsurface fatigue

The DNV gear rating standard for maritime cylindrical and bevel gears DNVGL-CG-0036 [2] contains one of the few formalised TFF or subsurface fatigue calcu-

lation methods. It compares the surface-parallel, orthogonal shear stress amplitude below the gear's pitch point to a hardness derived shear fatigue strength. The numerical studies performed in this academic work support the proposed analytical stress amplitude as it accurately captures the critical subsurface stress state. It was therefore adopted for the herein proposed TFF standardised approach (see Chapter 4). The parameters needed for the prediction of the shear stress amplitude $\tau_{xy,a}$ are x, p_H and b_H, the depth underneath the pitch point, the Hertzian contact stress and the half Hertzian contact width.

$$\tau_{xy,a}(x) = 0.25 p_H \cos\left(\frac{\frac{x}{b_H} - 0.5}{\frac{x}{b_H} + 0.5}\,\frac{\pi}{2}\right) \tag{1.2}$$

Rather than approximating a hardness profile from case to core, the standard calls for the calculation of the subsurface fatigue safety factor in the depth of the peaking shear stress amplitude (i.e. $0.5\,b_H$), the CHD (550 HV hardness depth) and the 400 HV hardness depth. Figure 1.10a shows the minimum specified hardness parameters against a minimum required hardness profile as a result of the in Equation 1.2 outlined shear stress profile.

Without the consideration of the compressive residual stress as a result of the case hardening process, the DNV criterion tends to overestimate surface rather than subsurface failures, calling in some cases for an increase in surface hardness HV_S rather than CHD to prevent TFF (see Figure 1.10a). Missing from the gear rating standard is also a size factor and a lifetime factor that reduces the fatigue strength beyond $3 \cdot 10^6$ load cycles. For hard steels, fatigue strength reductions must be expected in the very high cycle fatigue (VHCF) regime.

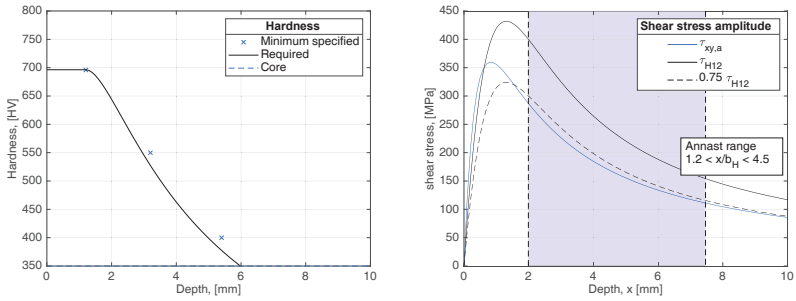

(a) DNV hardness requirement and subsurface fatigue criterion [2]

(b) Stress comparison between orthogonal and main principle shear stresses [2, 14]

Figure 1.10: TFF model comparison

Annast/FZG - Flankenbruch

Annast's research and thesis from 2002 constitute the first TFF or Flankenbruch specific academic work by the FZG in Munich [14]. His thesis includes a detailed damage characterisation of the failure mode on single flank loaded bevel gears, the definition of the TFF-critical heat treatment parameters based on back-to-back gear testing, an application of the shear stress intensity criterion by Oster [25] and the definition of a simplified Flankenbruch or TFF criterion that relies on the main principle shear stress τ_{H12}. The same parameters are used for the prediction of τ_{H12} as for the orthogonal shear stress amplitude $\tau_{xy,a}$.

$$\tau_{H12}(x) = p_H \left(\frac{x}{b_H} - \frac{\left(\frac{x}{b_H}\right)^2}{\sqrt{1 + \left(\frac{x}{b_H}\right)^2}} \right) \tag{1.3}$$

According to Annast, the principal shear stress τ_{H12} and the material hardness $HV(x)$ need to be compared in the transition zone from hard case to soft core. In the specified depth, the residual stresses change from compression to tension and can be ignored for a simplified TFF study. For a subsurface material depth $1.2 \leq x/b_H < 4.5$, Annast observed a nearly constant ratio between Oster's spatial average of the maximum shear stress $\tau_{eff,L}$ and the analytically calculated main principle shear stress τ_{H12} of $\tau_{eff,L}/\tau_{H12} = 0.75$. As Figure 1.10b shows, $0.75\,\tau_{H12}$ is a nearly identical the orthogonal shear stress amplitude $\tau_{xy,a}$ in the by Annast specified material depth.

The DNV and Annast criteria are very comparable in their stress predictions. Differences arise from the different shear strength to hardness ratios (Annast 0.55, DNV 0.625) and the consideration of the safety factor or material utilisation in the half Hertzian contact width of the DNV criterion, yielding a deeper shear stress profile than for the Annast criterion.

Witzig/FZG - TFF

The academic work and thesis by Witzig on TFF [15] from 2012 are at the core of the FVA research project FVA556. The FVA556-I focused on cylindrical gears, expanded upon the shear stress intensity criterion by Oster [25] and proposed an analytical model for the prediction of TFF that was verified through gear testing. The ISO later adopted Witzig's model in the form of the ISO6336-4 technical report [1]. The works by Wickborn and Boiadjiev in the FVA follow-up projects FVA556-II and FVA556-III [26, 27] apply the developed methodology to larger cylindrical gears and bevel or hypoid gears.

Based on extensive gear testing, Witzig was able to quantify the critical load and gear design parameters. Those are the gear loading or surface stress p_H, the gear's curvature ρ_{eq}, the CHD, the residual stresses σ_{res} and the general shape of the hardness profile when transitioning from case to core. As such, the

bending and transverse shear stresses were not considered in the proposed analytical model. The herein presented results suggest an increase of the calculated material utilisation of 11 % when considering the bending stresses.

To predict the material utilisation D_{ISO} below the studied design point, a spatial average of the maximum shear stress $\tau_{eff,L}$ as a result of the surface stress p_H is calculated. To $\tau_{eff,L}$, a quasi-mean shear stress $\Delta\tau_{eff,L,RS}$ is added and a residual stress equivalent shear stress subtracted $\tau_{eff,RS}$. The calculated equivalent stress is subsequently compared with a shear strength τ_{zul}. As such, the Witzig criterion (see Equation 1.4) does not resemble established stress-based multiaxial fatigue criteria and fails to weigh the individual stress components through model parameters or material constants. Quantification of the model's accuracy through conventional multiaxial fatigue tests is not possible as the criterion does not rely on conventional multiaxial fatigue stresses (see Appendix B).

$$D_{ISO}(x) = \frac{\tau_{eff,L}(x) + \Delta\tau_{eff,L,RS}(x) - \tau_{eff,RS}(x)}{\tau_{zul}(x)} + c \tag{1.4}$$

A comparison between the predicted subsurface material utilisations according to the Witzig or ISO criterion and the herein proposed multiaxial fatigue criteria are included in Appendix B and Chapter 4. The documented close match between these criteria in the TFF-critical material depth verifies the herein developed advanced and simplified subsurface fatigue criteria. Especially in the hard case, the Witzig criterion seems to underestimate the local material utilisation. Critically, Witzig implements Lang's hardness model [28], which is not applicable for large maritime gears as it underestimates the hardness gradient from case to core. Also, the correctness of the adjustment factor K_2 are discussed in this thesis.

Weber

Weber did not propose a new fatigue criterion in his 2015 research on TFF in case hardened, cylindrical gears [29]. Instead, he developed an improved analytical stress model by interpreting a gear tooth as a wedge-shaped beam. The apparent transverse normal stress profile under a Hertzian line contact was estimated through numerical beam calculations and interpolated for the studied gear teeth.

To document and model the compressive and tensile residual stresses, Weber employed the contour method by Prime [30] and adapted the residual stress model by Lang [28] to his findings. The principle of the contour method is visualised in Figure 1.11a. It requires the sectioning of a gear tooth with wire electrical discharge machining (EDM), the measurement of the contour of the relaxed tooth section and the numerical calculation of the necessary stresses to move the deformed section into its pre-relaxed plane state. Weber was thereby able to obtain a residual stress map for an entire gear tooth compared to only point measurements by means of hole drilling, neutron diffraction or x-ray (see Figure 1.11b). Whereas the contour method yields reliable results for tensile

stresses in the tooth interior, Weber relied on conventional measurement techniques for the hard case and the compressive residual stresses. The herein proposed residual stress model is comparable to Weber's measurements and model suggestions but improves upon the transition from compressive to tensile residual stresses and the symmetric constraint in the gear tooth's neutral axis.

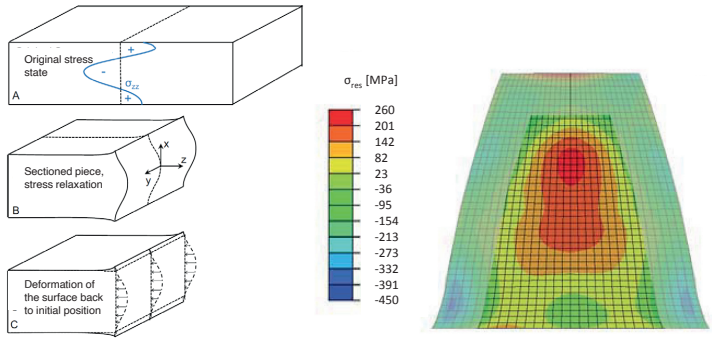

(a) Contour method principle (b) Residual stress map

Figure 1.11: Residual stress map as a result of contour method measurements [29]

Beyond the analytical stress model and residual stress predictions, Weber carried out VHCF testing at $R = 0.05$ up to $1 \cdot 10^{10}$ load cycles for 18CrNiMo7-6 steel at various carbon saturations (0.18, 0.35, 0.55 and 0.64 wt. %). His results show only a minimal strength increase between the 0.35 and 0.64 wt.% steel variants, which he attributes to the increasing mean stress sensitivity. Also, the spread and Basquin parameters for the 0.35, 0.55 and 0.64 steels were very comparable.

In his studies, Weber reports a crack initiation during VHCF testing from predominantly aluminium oxides. For the development of a material model as a function of the steel's hardness and inclusions size, Weber implemented Murakami's $\sqrt{area}$ model [31]. He proved the general applicability of the $\sqrt{area}$ model in capturing the documented fatigue properties but modifies Murakami's mean stress sensitivity by implementing the equations suggested by the Forschungskuratorium Maschinenbau (FKM) [13]. According to his measurements, the mean stress sensitivity presented by Murakami fails to comply with the documented results. Equation 1.5 outlines Weber's material model. The uniaxial fatigue strength under alternating and oscillating load f_{-1} and f_0 are derived from the Vicker's hardness HV, the square root of the projected area of an inclusion $\sqrt{area}$, the stress ratio R, Murakami's mean stress sensitivity factor α_m, the FKM's mean stress sensitivity M and the ultimate tensile strength R_m. The indices MU and WE refer to Murakami and the modification by Weber through the implementation of the FKM guideline.

$$
\begin{aligned}
f_{-1,MU} &= 1.56\,\frac{HV+120}{\sqrt{area}^{1/6}} \\
f_{0,MU} &= f_{-1,MU}\left(\frac{1-R}{2}\right)^{\alpha_m} \qquad \text{with} \quad \alpha_m = 0.226 + HV\cdot 10^{-4} \\
f_{0,WE} &= \frac{2f_{-1,MU}}{1+M} \qquad\qquad \text{with} \quad M = 3.5\cdot 10^{-4} R_m - 0.1 \\
&\qquad\qquad\qquad\qquad\quad \text{and} \quad R_m = 3.3HV
\end{aligned}
\tag{1.5}
$$

While the combination of Murakami and FKM notably improved the correlation between tested and modelled fatigue strength, $f_{-1,MU}$ significantly underestimates the fatigue strength of the 390 HV soft 18CrNiMo7-6 steel (0.18 wt.% carbon). The fatigue test results in Paper II [32] agree with Weber's observation and suggest therefore a transition from Murakami's upper to lower fatigue limit in the range of 300 to 550 HV or 0.18 to 0.35 wt.% carbon.

1.4 Thesis outline

As highlighted in Chapter 1.1, an accurate multiaxial fatigue assessment of case hardened bevel gears requires three elements:

- A material model that covers up to four material constants as a function of the local hardness
- A numerical stress model that considers all relevant subsurface stresses and calculates the normal and shear stress components on each material plane
- A multiaxial fatigue criterion that enables the prediction of the subsurface and ideally surface fatigue under RCF

The term material utilisation refers to the ratio between the criterion-specific equivalent stress and a material constant, typically the uniaxial fatigue strength under alternating loading f_{-1}.

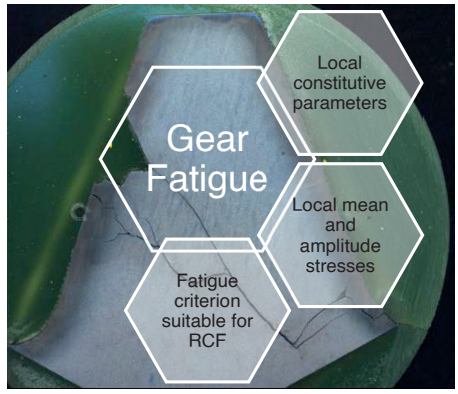

Figure 1.12: Gear fatigue - model definition

The layout of this academic work follows the same logic, whereby after a general introduction to TFF in Chapter 1, a material model for carburised CrNiMo steel is presented in Chapter 2 and the numerical stress model and the multiaxial fatigue criterion are outlined in Chapter 3. The presented TFF methodology is paired in Chapter 4 with a standardised TFF approach, foregoing the need for complex numerical calculations. Appendices A, B and C contain all published articles, a list of the studied stress-based multiaxial fatigue criteria and their application to the mean cross-section of a gear tooth under RCF and the derivation of the size factor proposed in this thesis. The following table gives a summary of each chapter's content.

Chapter 1	Outlines the context of the academic work and the generated scientific publications. A brief historical overview of TFF-related research is given, along with an industrial context of TFF for the maritime industry.
Chapter 2	Presents the material model for carburised CrNiMo steel. Special attention is given to the fatigue ratio κ and the mean stress sensitivity M.
Chapter 3	Outlines the numerical calculation model. In the later part of the chapter, the material and stress model are combined with the developed integral multiaxial fatigue criteria for the prediction of fatigue in case hardened gears.
Chapter 4	Presents and verifies a simplified TFF criterion intended for the analytical assessment of subsurface fatigue in gears.
Chapter 5	Summarises the findings of this academic work and presents the concluding remarks.
Appendix A	Contains the scientific articles published in the context of this Ph.D. project.

Appendix B	Lists and compares several stress-based multiaxial fatigue criteria and gear-specific fatigue criteria to the herein proposed and outlined BO and Hs criteria.
Appendix C	Outlines the calculation model used to predict the size factor according to the weakest link theory.

1.5 List of contributions

Several scientific papers have been published related to subsurface fatigue in gears that encompass a general damage characterisation, a material model for carburised CrNiMo steel, a numerical model for the stress prediction in the mean cross-section of a bevel gear tooth, an advanced, integral multiaxial fatigue criterion alongside a rationalised TFF criterion and the findings from bevel gear back-to-back testing. They are included in Appendix A and summarised here.

1.5.1 Paper I

The first publication was written in cooperation with the Institute of Advanced Technologies of the Togliatti State University in Russia and supported by DNV's metallurgical laboratory in Høvik, Oslo [10]. The authors are Stephan André Böhme and Alexei Vinogradov of the NTNU and Professor Dmitry Merson of the Togliatti State University.

Three marine bevel gear failures of the same design but distinctly different case hardening layer thicknesses were analysed and classified as TFF or subsurface fatigue failures. The case hardening layer thicknesses were measured to 3.0, 2.5 and 2.1 mm with TFFs initiating in 5.5, 4 and 2.5 to 3.8 mm on the respective gear sets. A strong correlation between the produced case hardening depth and the TFF initiation depth is suggested. Based on the metallographic analysis and hardness measurements, the inhomogeneous microstructure with its microsegregations in longitudinal and transverse tooth direction were documented and quantified.

On one of the studied gear sets, a multitude of early-stage TFF cracks were detected through ultrasonic scanning. After sectioning the affected gear teeth and polishing the transverse cross-sections, 0.5 mm large, surface-parallel cracks were identified. Derived from the Dang Van multiaxial fatigue criterion, a TFF model is presented that utilises the surface-parallel orthogonal shear stresses amplitude as defined in DNVGL-CG-0036 [2] in combination with the residual stress profile according to Lang [28]. The proposed model is compared with the DNV subsurface fatigue criterion and shown to improve upon the predicted TFF crack initiation depth.

On subsurface initiated failures in marine bevel gears
Böhme, S. A. and Merson, D. and Vinogradov, A.
Engineering Failure Analysis, Volume 110, 2020, 104415
https://doi.org/10.1016/j.engfailanal.2020.104415

1.5.2 Paper II

Marine bevel gears are typically case hardened to increase their load-carrying capacity. As a result, the carbon content and material properties vary throughout the case hardened layer, requiring a material model as a function of the local material hardness. Paper II outlines a material model for carburised CrNiMo steel based on the extensive high cycle and very high cycle fatigue testing of hourglass-shaped fatigue specimen [32]. The paper was written in cooperation with the Institute of Materials Engineering at the TU Bergakademie in Freiberg, Germany and supported by Sonats, Europe Technologies in France and PWT - Prüf- und Werkstofftechnik in Germany. Its authors are Stephan André Böhme and Alexei Vinogradov from the NTNU and Horst Biermann, Anja Weidner, Alexander Schmiedel and Sebastian Henkel from the TU Freiberg.

Stress-based, multiaxial fatigue criteria require up to four material constants (typically the uniaxial fatigue strength under alternating and oscillating load f_{-1}, f_0 and the shear fatigue strength under alternating and oscillating load t_{-1}, t_0) for the calibration of their model parameters and the correct weighing of the different stress components (i.e. the shear mean and shear amplitude stress $\tau_m(\theta,\phi)$, $\tau_a(\theta,\phi)$ and normal mean and normal amplitude stress $\sigma_{n,m}(\theta,\phi)$, $\sigma_{n,a}(\theta,\phi)$). Whereas t_0 was estimated according to Equation 1.6 (Liu & Zenner in [12]), the steels 18CrNiMo7-6, 34CrNiMo6 and 18NiCrMo14-6 were tested for their f_{-1}, f_0 and t_{-1} fatigue properties.

$$t_0 = \frac{4t_{-1}}{\frac{2f_{-1}}{f_0} + 1} \tag{1.6}$$

The derived results were paired against literature findings to derive a material model for carburised CrNiMo steel with the following characteristics.

- A transition in uniaxial fatigue strength f_{-1} from Murakami's upper to lower limit in the range from 300 to 550 HV [31]
- A fatigue ratio κ (ratio between f_{-1} and t_{-1}) as a linear function of the local hardness
- A mean stress sensitivity based on the FKM guideline [13] and the ratio between the theoretical upper fatigue limit and the obtained uniaxial fatigue strength under alternating loading f_{-1}

When modelling the uniaxial fatigue strength according to Murakami's lower limit, the square root of the projected area of an inclusion $\sqrt{area}$ needs to be quantified. Its average value for all tested steels was estimated to be 80 μm and based on extensive fractographic studies of the VHCF specimen, revealing either crack initiation from MgO-Al_2O_3 spinels or large austenite grains.

Especially the mean stress sensitivity is deemed critical for a correct fatigue prediction under RCF. The herein proposed correlation follows the FKM's linear trend for mild and soft steels but deviates significantly for hard steels. The

mean stress sensitivity model is inspired by Bell & Benham [33], who propose a reduced mean stress sensitivity for notched compared to an unnotched specimen of the same material. All steels tested in Paper II [32] featured comparable inclusion size distributions but inferior fatigue properties and lower mean stress sensitivity for the 500 HV hard 34CrNiMo6 steel. As the uniaxial fatigue strength f_{-1} is affected by the presence of inclusions in hard steels, so is the mean stress sensitivity.

Fatigue of carburised CrNiMo steel: Testing and modelling concept
Böhme, S. A. and Vinogradov, A. and Biermann, H. and Weidner, A. and Schmiedel, A. and Henkel, S.
Fatigue & Fracture of Engineering Materials & Structures, Volume 44, Pages 788-804, 2020
`https://doi.org/10.1111/ffe.13394`

1.5.3 Paper III

A 2D plane strain numerical model for the stress prediction in case hardened spiral bevel gears is presented along with a novel, stress-based, integral multiaxial fatigue criterion, developed explicitly for the fatigue prediction under RCF [19]. The publication was supported by the Czech Technical University in Prague and authored by Stephan André Böhme, Alexei Vinogradov and Filippo Berto from the NTNU and Jan Papuga from the Czech Technical University.

The proposed BO criterion is shown to be capable of predicting subsurface fatigue in large marine bevel gears and pitting and tooth root breakage in small spiral bevel, test gears [9]. Its accuracy is further verified through a statistical comparison based on conventional multiaxial fatigue test results under compressive or tensile, static, normal stresses and alternating shear stresses [34–37]. Compared to other stress-based multiaxial fatigue criteria, the documented accuracy is on par with highly accurate Liu & Zenner [12], Crossland [38] and PIN [20] criteria, outperforming the Dang Van [39], Sines [40] and Hertter criteria [6]. A common weakness for stress-based multiaxial fatigue criteria is the under- or overestimation of the material utilisation in the outer material layer under Hertzian stresses. The BO criterion overcomes that weakness and enables the prediction of surface and subsurface fatigue in gears.

An improved version of the Hertter criterion and an alternate version of the BO criterion were furthermore presented. Both BO criteria differ in their consideration of the mean shear stress $\tau_m(\theta, \phi)$, which alters the predicted material utilisation in the surface-near material layer. Depending on which mean stress sensitivity model is chosen, either version can yield correct results.

A novel predictive model for multiaxial fatigue in carburised bevel gears
Böhme, S. A. and Vinogradov, A. and Papuga, J. and Berto, F.
Fatigue & Fracture of Engineering Materials & Structures, Volume 44, Pages 2033-2053, 2021
https://doi.org/10.1111/ffe.13475

1.5.4 Paper IV

This publication pairs the previously published material, stress and fatigue models with the results from load-controlled bevel gear testing [41]. It was written in cooperation with ATA Gears Oy, Kongsberg Maritime Finland Oy and supported by the Tampere University in Finland. Its authors are Stephan André Böhme and Alexei Vinogradov of the NTNU, Gabor Szanti and Tami Komssi of ATA Gears, Joni Keski-Rahkonen of Kongsberg Maritime and José Garcia Santaella of the Tampere University.

Ten spiral bevel gear sets were tested in a back-to-back test rig under specific loads and hardening layer thicknesses, yielding an improved lifetime factor derived according to the Maximum Likelihood Method (MLM) [42]. Six TFFs occurred on the test gears, of which five initiated on wheel teeth and one on a pinion tooth. In addition, a single pinion-initiated pitting damage was documented. Through the study and implementation of the hardening layer differences between the tested pinions and wheels and the consideration of the geometrical differences between all gears, accurate stress and failure prediction were possible that correctly predict the majority of wheel-initiated TFF failures and the single pinion-initiated pitting failure.

Using scanning electron microscopy, fractographic analyses were carried out on the single pinion-initiated TFF failure and two wheel-initiated TFFs. Whereas the wheel teeth featured *Fisheyes* of considerable size and a by and large smoothened fracture surface, a 1.4 mm long MgO-Al_2O_3 spinel was found in the crack initiation site on the pinion tooth.

Tooth flank fracture - An applied fatigue study of case hardened bevel gears
Böhme, S. A. and Gabor, S. and Keski-Rahkonen, J. and Komssi, T. and Santaella, J. G. and Vinogradov, A.
Engineering Failure Analysis, Volume 132, 2022, 105911
https://doi.org/10.1016/j.engfailanal.2021.105911

Chapter 2

Material model

The material macro- and microstructure in maritime bevel gears are inherently inhomogeneous. The steels anisotropy stems from:

- The carbon profile introduced during the case hardening process
- The segregation structure created during the solidification of the steel melt

Figure 2.1 plots a typical heat treatment cycle for gear steels post hot forging and during the gas carburising cycle. All steels tested in the context of this project were heat treated to the same specification and extracted from 430 x 430 x 900 mm^3 forged blanks, resulting in a large gear equivalent macro- and microstructure.

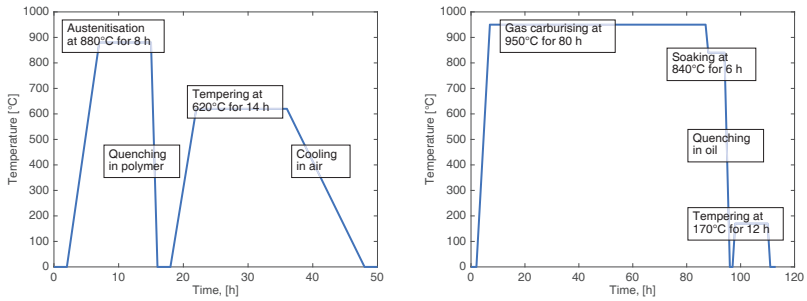

(a) Post forging heat treatment

(b) Gas carburising

Figure 2.1: Heat treatment cycle for large maritime bevel gears

2.1 Case hardening

Case hardening is applied to gears to increase the surface hardness and thereby wear resistance and load-carrying capacity. During carburising and quench-

ing of the commonly used 18CrNiMo7-6 steel, compressive residual stresses are introduced in the carburised layer, further adding to the gear's load-carrying capacity. Unique to large gears is a gas carburising at multiple carbon potentials (boost phase at 0.9 to 1.3 % and secondary phase at 0.6 to 0.8 %) to economically achieve the intended CHD and to ensure the targeted surface hardness HV_s. Inadvertently, this leads to a steeper hardness gradient from case to core and a reduced load-carrying capacity in the case/core interface [19, 41]. Due to the gear's size and targeted CHD, long diffusion times can lead to grain growth if not compensated through microalloying additions (Nb, Ti, Al and N). Carburising is followed up by quenching and tempering to achieve a hard, primarily martensitic microstructure that retains a level of ductility. Besides tempered martensite, retained austenite and carbides are present in the case and bainite and potentially ferrite in the core. For maritime gears made of 18CrNiMo7-6 steel and a core hardness HV_c requirement of $\geq$ 350 HV, rapid cooling rates are necessary to achieve a primarily martensitic microstructure.

During gas carburising, the gears are exposed to temperatures between 920 to 950 °C to ensure a fast carbon diffusion into the face centred cubic austenite. In the subsequent quenching stage, a diffusionless transformation from austenite to the metastable, body centred tetragonal martensite takes place, trapping the diffused carbon as interstitial impurities. Depending on the alloying composition of the material, the severity of the quenching media (water > oil > air > furnace) and the size and shape of the workpiece (surface to volume ratio) carbides, martensite, bainite, pearlite and ferrite form. For the surface of case hardened gears, a carbon content of 0.7 wt.% is typical, featuring between 5 to 25 % retained austenite due to the relatively low martensitic start and sub-zero finish temperatures (cryotreatment to achieve lower austenite concentration). Quenching is followed up by a tempering stage at temperatures from 150 to 200 °C to improve the steel's ductility and toughness whilst maintaining most of the steel's hardness and strength. During tempering, carbon segregation takes place in the martensite, forming very fine particles of transition carbide.

To model the hardness profile across varying gear sizes, the hardness model by Thomas is recommended [43]. It describes the hardness profile as two-second order polynomials up to and beyond the case hardening depth CHD and is uniquely suited to consider case hardening at single or multiple carbon potentials and the auto-tempering response of large gears through its parameter $x_{HV,max}$ [19, 41]. Rather than describing the depth of the hardness peak, $x_{HV,max}$ is redefined to capture the hardness gradient in the transition point (i.e. CHD). Equation 2.1 outlines the hardness model by Thomas and adds a hardness limit of HV_s to avoid excessively large hardness peaks for large $x_{HV,max}$ values. The model requires the definition of the surface hardness HV_s, the core hardness HV_c and the CHD.

$$
\begin{aligned}
HV(HV > HV_s) &= \quad HV_s \quad \text{hardness limit} \\
HV(x > x_c) &= \quad HV_c \quad \text{core hardness} \\
HV(x \leq CHD) &= \quad a_a x^2 + b_a x + c_a \\
HV(x_c \geq x > CHD) &= \quad a_b x^2 + b_b x + c_b
\end{aligned}
$$

$$
\begin{aligned}
a_a &= \frac{550 - HV_s}{CHD^2 - 2x_{HV,max} CHD} & a_b &= \frac{HV_{dC}}{2\,(CHD - x_c)} \\
b_a &= -2\,a_a x_{HV,max} & b_b &= -2\,a_b x_c \\
c_a &= HV_s & c_b &= 550 - a_b CHD^2 - b_b CHD
\end{aligned}
$$

$$
\begin{aligned}
HV'_{CHD} &= \quad 2\,a_a CHD + b_b \\
a_1 &= \quad -HV'_{CHD} \\
b_1 &= \quad 2\,CHD\,HV'_{CHD} + 2\,(HV_c - 550) \\
c_1 &= \quad -CHD^2\,HV'_{CHD} - 2\,CHD\,(HV_c - 550) \\
x_c &= \quad \frac{-b_1 + (b_1^2 - 4a_1c_1)^{0.5}}{2a_1}
\end{aligned}
\tag{2.1}
$$

The measured hardness curves of the test gear B3-2 are plotted in Figure 2.2 [41]. For the two blue, half-tooth height curves, the parameter $x_{HV,max}$ was set to -0.8 on the pinion and 0.48 mm on the wheel to capture the measured differences adequately. With the modelled residual stresses being a function of the measured hardness, the differences in subsurface load-carrying capacity between B3-2 pinion and wheel teeth are further amplified.

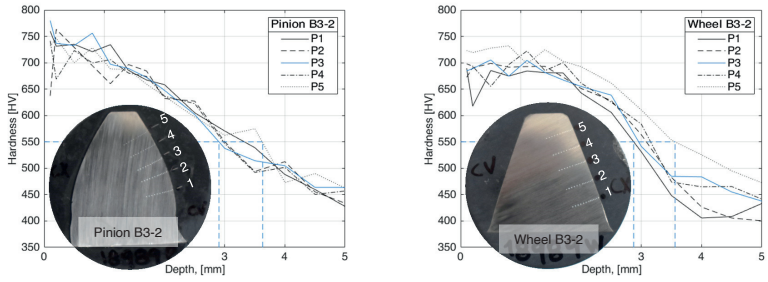

(a) B3-2 pinion tooth (b) B3-2 wheel tooth

Figure 2.2: HV10 hardness measurements in tooth profile direction

Austenite

Retained austenite in the hard case increases the ductility and reduces the local hardness. A low concentration of austenite is desirable as it helps to arrest cracks and transforms under load to untempered martensite, further increasing local compressive residual stresses. The fractographic analyses performed on

uniaxial fatigue specimens tested in the context of this project suggest that large austenite grains could potentially have a detrimental effect on subsurface initiated fatigue [32]. The second most prevalent failure mode on the tested 34CrNiMo6 steel was failures not from non-metallic inclusions but the steel's matrix. Electron backscatter diffraction (EBSD) identified islands of austenite in the otherwise martensitic microstructure (see Figure 2.3 and Paper II [32]). The matrix failures potentially initiated either from large, soft austenite grains or the low solute regions of the banded microstructure. Through microhardness measurements, hardness differences of 175 HV0.1 are documented in the banded microsegregation structure of the tested 34CrNiMo6 specimens compared to 50 HV0.1 on the 18CrNiMo7-6 specimens that were free of matrix failures.

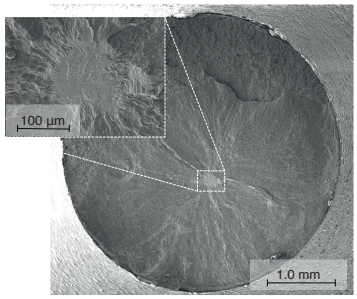

(a) Matrix failure

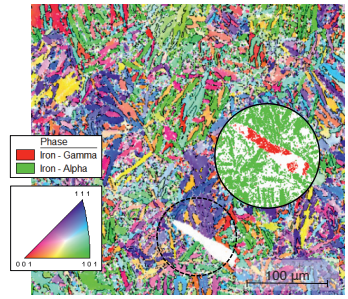

(b) EBSD microstructure with mostly alpha and islands of gamma iron

Figure 2.3: VHCF failure from austenite islands in 34CrNiMo6 steel [32]

Residual stresses

An attribute of the martensitic transformation are the residual stresses. The martensitic start temperature is a function of the steel's carbon content and is highest in the core and lowest in the carbon-rich case. The onset of the martensitic transformation will therefore occur in the case/core interface and continue into the tooth before transforming the case. Due to the volume expansion during the diffusionless transformation, compressive residual stresses are generated in the case and tensile residual stresses in the core. Conventional residual stress measurement techniques like the hole drilling method can adequately be used to document the surface near compressive stresses, but not the tensile stresses in the core. X-ray and neutron diffraction methods have successfully been applied to measure compressive and tensile residual stresses up to an 8 mm depth [44, 45]. Another promising technique to quantify the tensile residual stresses is the contour method through the sectioning of gear teeth and the study of the local deformation as a result of the stress relaxation [29, 30].

Based on the contour method and neutron diffraction measurements [29, 44, 45], an iteration of the residual stress model by Lang [28] was developed and implemented in Paper III [19]. It models the residual stresses as a function of

the local hardness $HV(x)$, the core hardness HV_c, the case hardening depth CHD and the perpendicular tooth width underneath the studied contact point $s_{n\alpha}$. All parameters above are local parameters and change in tooth profile and lengthwise direction. The perpendicular tooth width $s_{n\alpha}$ is calculated based on the local chordal tooth thickness s_n and the local pressure angle α. Up to the CHD, the modelled compressive stresses are identical to Lang's prediction [28]. The conversion from compression to tension beyond the CHD is modelled as a fourth-order polynomial with constraints as outlined in Equation 2.2. The polynomial's coefficients a, c and e are determined based on the continuous and tangential constraints in the CHD and the stress equilibrium condition along the path $s_{n\alpha}$.

$$\begin{aligned}
\sigma_{res}(x) &= -5/4\,(HV(x) - HV_c) && \text{for} \quad HV(x) - HV_c \leq 300 \\
\sigma_{res}(x) &= 2/7\,(HV(x) - HV_c) - 460 && \text{for} \quad HV(x) - HV_c > 300 \\
\sigma_{res}(x) &= a(x - s_{n\alpha})^4 + c(x - s_{n\alpha})^2 + e && \text{for} \quad x \geq CHD \\
\text{with} \quad s_{n\alpha} &= \frac{s_n}{2\cos(\alpha)} \quad \text{and} \quad \int_0^{s_{n\alpha}} \sigma_{res}(x)dx = 0
\end{aligned} \tag{2.2}$$

Whereas the polynomial's coefficients a and b can be calculated according to Equation 2.3, c needs to be set iteratively until the stress equilibrium along $s_{n\alpha}$ is reached. The parameters $\sigma_{res,CHD}$ and $\sigma'_{res,CHD}$ refer to the residual stress and the gradient of the residual stress in the CHD. They can either be derived directly from Lang's residual stress model or from its derivative.

$$\begin{aligned}
a &= \frac{-\sigma_{res,CHD} + \frac{\sigma'_{res,CHD}}{2}(CHD - s_{n\alpha}) + c}{(CHD - s_{n\alpha})^4} \\
b &= \frac{\sigma'_{res,CHD} - 4a(x_c - s_{n\alpha})^3}{2(CHD - s_{n\alpha})}
\end{aligned} \tag{2.3}$$

Figure 2.4 plots neutron diffraction measurements obtained on the convex flank of multiple gearwheel teeth 15 mm off the tooth tip and in a centred lengthwise position. The modelled transverse residual stresses according to Equation 2.2 are plotted for the same tooth position in Figure 2.4a and for the entire tooth cross-section in Figure 2.4b highlighting the location of the neutron diffraction measurements. Following the contour method measurements by Weber [29], the proposed fourth-order polynomial predicts a transition of the tensile residual stress peak from the case/core interface to the middle of the tooth in the tooth tip.

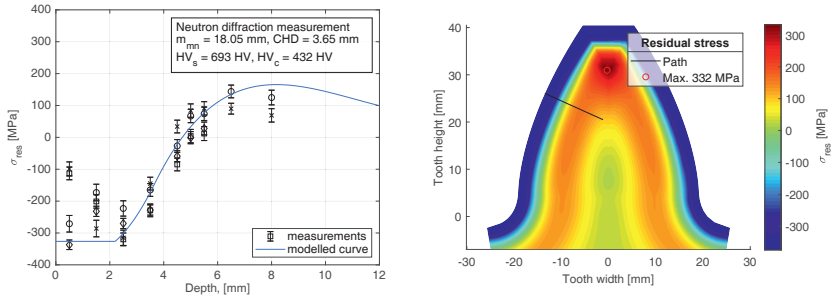

(a) ND measurements

(b) Modelled residual stresses

Figure 2.4: Residual stress measurements and modelling for maritime bevel gear [19, 44, 45]

Compressive residual stresses in gear teeth can further be promoted by shot peening, essentially increasing the gear's load-carrying capacity further. Shot peening of maritime gears is not common practice and has historically only been applied to the gear's tooth root, where its positive effect on the acting tensile bending stresses is well understood and documented. Led by research conducted by NASA in the 1980s and 1990s [46, 47], shot peening has successfully been applied to the gear's load-carrying flank, increasing the time to failure or pitting safety significantly. Similar to the research conducted in this academic work, compressive residual stresses are proven to be beneficial not just for dynamic tensile stresses in the gear's tooth root but also dynamic shear stresses underneath the gear flank. As shown in the latter part of this chapter, a hardness increase does not necessarily imply a significant material strength increase as the material becomes increasingly sensitive to crack-initiating heterogeneities. The larger positive effect on the gear's load-carrying capacity stems from the via case hardening and/or shot peening introduced compressive residual stresses.

2.2 Segregation structure

The second source of anisotropy in case hardened gears has its origin in the casting and forging process and is especially prevalent in large maritime bevel gears. During the solidification of the steel melt, a segregation structure forms due to a permanent, non-uniform distribution of minority atoms in the solid phase. The concentration differences and local supercooling lead to the formation and growth of dendrites. Substitutional atoms like manganese, chromium and molybdenum have a far lower diffusivity than carbon (diffusivity ratio $C/Cr = 10000$), resulting in high and low solute regions, which in turn attract and bind carbon. For the core of the gear tooth, the hardenability of high solute regions leads to the formation of martensite, whereas the low solute regions form bainite. In the case/core interface, the hardness trend is reversed.

The high solute regions will hinder the diffusion of carbon during the gas carburising phase, leading to lower local hardnesses than in the low solute regions. If the orientation of the banded microstructure is perpendicular to the gear flank, *channelling* can occur, leading to large local hardness differences. In the hard case, the carbon saturation is very high and uniform, leading to an even hardness distribution. The term *banded microstructure* describes the formation of parallel stringers in the flow direction during hot forging. Especially on large gears, polished and etched cross-sections sometimes show casted or dendritic microstructure without adequate through-working of the steel. Figure 2.5a plots a gear tooth with an *as cast* or *dendritic* microstructure in Figure 2.5b and an early-stage TFF crack in a high solute, low-carbon area in the case/core interface. The local hardness varied from 635 to 444 HV1 in the carbon-rich and poor regions. The identified subsurface cracks were seemingly contained within a single stringer.

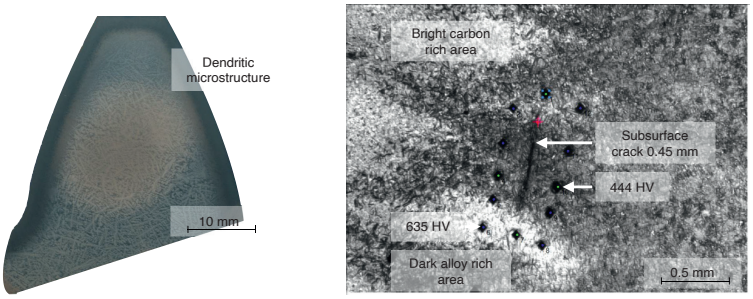

(a) Dendritic microstructure pinion (b) Hardness around subsurface crack [11]

Figure 2.5: Segregation structure in large marine bevel gears

How to adequately deal with the steel's anisotropy due to its segregation structure requires further research. The orientation of the banded microstructure seems far more critical than the degree of through working (i.e. the forging ratio) as the Joint Industry Project (JIP) - phase 2 results show for the 2D vs 3D forged 18CrNiMo7-6 steel variants [32, 48]. 2D and 3D forging refer to a single stretching or a multitude of stretching and upsetting cycles during the hot forging process. None of the subsequent heat treatment steps shown in Figure 2.1 are able to redistribute the substitutional alloying elements, leading to microsegregations with higher chromium and carbon concentrations. This could potentially be another advantage to electro-slag-remelted (ESR) steels, as they form a 45° orientated solidification structure to the casting or melting direction, featuring identical fatigue properties in transverse and longitudinal direction [48].

Especially on long pinion shafts, where a majority of the hot forging will be done to reduce the cross-section of the casting down to the approximate outer pinion diameter, an anisotropy is created through the elongation of non-metallic

inclusions. Whereas the yield and tensile strength will not be significantly affected, the elongation, fracture toughness and fatigue properties longitudinal and transverse to the stretching direction will vary significantly [49].

To capture the lower end of fatigue properties in the steels tested in the context of this research, all specimens were extracted in transverse direction after forging the initial casting from 770 x 770 mm^2 to 430 x 430 mm^2 cross-sections.

2.3 Fatigue testing

The steels 18CrNiMo7-6, 18NiCrMo14-6 and 34CrNiMo6 were tested regarding their static strength, impact work, microhardness, grain size and fatigue properties in the high cycle fatigue (HCF) and very high cycle fatigue (VHCF) regimes. Testing was carried out under uniaxial loading at stress ratios $R = -1$ and $R = 0$ (also $R = -7$ for 34CrNiMo6) and under torsion at $R = -1$. For the 18CrNiMo7-6 steel, 2D and 3D forged variants with forging reduction ratios of 3.2 and 12.8 were studied. The 18NiCrMo14-6 steel was 3D forged at a reduction ratio of 7.1 and the 34CrNiMo6 steel 2D forged at 3.2, achieved through either a single stretching process or a combination of stretching and upsetting operations. The specimens were machined out of 25 x 25 x 280 mm^3 steel bars, extracted in a depth of 50 mm from 430 x 430 x 900 mm^3 large forgings. To accurately simulate the material structure and fatigue properties found in the core and the case of large maritime bevel gears, all steels underwent gear-typical forging and the same heat treatment protocols (see Figure 2.1). The static and dynamic properties of these three steels or four steel variants are listed in Paper II [32]. Paper II also specifies the specimen dimensions, testing machines and conditions used during the material investigation.

The HCF and VHCF specimens were ultrasonic shot-peened to promote subsurface failures and to avoid initiation from the surface due to roughness effects, slip localisation or non-metallic inclusions on or in the vicinity of the surface [31]. To evaluate the fatigue test results under torsion, the Liu & Zenner multiaxial fatigue criterion was applied to consider the introduced compressive residual stresses in the derivation of the shear fatigue strength under alternating loading t_{-1} [12]. Ultrasonic shot peening was favoured over conventional shot peening, nitriding or carburising. It achieves a very uniform residual stress profile, a smooth surface finish and does not alter the introduced microstructure. Figure 2.6 shows the designed treatment chamber and fixture that rotates the VHCF specimens alongside a dimensional sketch for the tested VHCF specimens. The cross-section and thereby the highly loaded volume between the HCF and VHCF were kept constant. As per the results in Paper II [32], the shot peening treatment can be deemed a success as all failures during VHCF testing were initiated from the bulk of the material and only minor degradation of the residual stress was observed during testing.

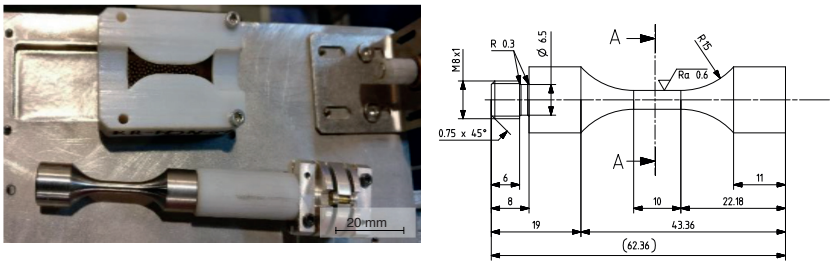

(a) Ultrasonic shot peening treatment chamber (b) Dimensional sketch of VHCF specimen

Figure 2.6: VHCF specimen preparation and dimensions

The fatigue test results were analysed with the pearl string method to determine the Basquin parameters in the HCF and VHCF regime, the staircase method to derive the fatigue strength at $2 \cdot 10^6$ load cycles ($5 \cdot 10^6$ for t_{-1}) and the maximum likelihood method to combine all test results for a specific steel and stress ratio to a single continuous curve [42, 50]. All VHCF fracture surfaces were investigated through scanning electron microscopy to determine the size and type of potential non-metallic inclusions.

Beyond the steels included in Paper II [32], an ESR variant of the 18CrNiMo7-6 standard gear steel was tested under alternating uniaxial load in the VHCF regime. The steel's static and dynamic results are listed here and compared to the 2D forged variant of the 18CrNiMo7-6 steel included in Paper II [32]. The ESR process cleans the steel of large non-metallic inclusions through either a chemical reaction with the slag or physical removal when floating to the top of the molten pool. Any remaining inclusions are very small and evenly distributed. The in JIP - phase 2 [48] documented fatigue properties and solidification structure were equal for specimens, extracted transverse or longitudinal to the forging direction. They showed a banded microstructure in a 45 ° angle to the casting direction. All other tested steels in [48] showed 15 to 20 % higher fatigue strength in longitudinal than transverse direction.

The VHCF specimens were machined out of remaining HCF specimens of the *Improved reliability of thrusters* joint industry project to the dimensions specified in Figure 2.6b and ultrasonic shot-peened according to the same recipe as the 18CrNiMo7-6 2D specimens [32]. The 18CrNiMo7-6 ESR steel was 3D forged to a reduction ratio of 7.8 from an initially 750 mm round bar. Its chemical composition is compared to the 18CrNiMo7-6 2D steel in Table 2.1.

Table 2.1: Chemical composition 18CrNiMo7-6 2D [32] and 18CrNiMo7-6 ESR 3D [48]

	Composition. (wt.%)											
Materials	C	Mn	P	S	Si	Ni	Cr	Mo	Cu	V	Al	N
2D	0.17	0.63	0.008	0.006	0.29	1.52	1.65	0.31	0.16	0.006	0.024	0.011
ESR 3D	0.19	0.66	0.005	0.001	0.27	1.55	1.65	0.32	0.12	0.016	0.026	0.012

The ESR steel shows lower concentrations of phosphor and sulphur, ensuring a high ductility. The elevated concentration of vanadium should improve hardenability. Tables 2.2 and 2.3 list the steels' obtained static and dynamic properties and compare it with the 2D forged reference. All properties were derived from specimens extracted transverse to the forging direction. VHCF testing was carried out on an ultrasonic BOKU fatigue testing machine, operating at 19.5 kHz with 10^9 load cycles defined as the run-out limit and 25 MPa as the step size.

Table 2.2: Static strength, impact work and microhardness 18CrNiMo7-6 2D [32] and 18CrNiMo7-6 ESR 3D [48]

	Tensile tests ISO6892-1				Impact work	Hardness
	R_{p02}	R_m	A	Z	ISO148-1	
Materials	(MPa)	(MPa)	%	%	(J)	(HV0.1)
2D	773	1115	19.5	58.6	56 ± 8.9	341 ± 14
ESR 3D	749	1071	18.1	57.7	69 ± 12.6	366 ± 5.5

The static properties of both steels are very comparable, with the ESR variant showing a slightly better impact work and a higher and more uniform hardness distribution. Figure 2.7 plots the VHCF results under alternating uniaxial load and combines the results to a fatigue curve according to the maximum likelihood method (MLM) outlined in Equation 2.4 [42]. The parameters μ_{log}, s_{log} and γ describe the mean log cycles to failure, the standard deviation of the log cycles to failure and the material's fatigue limit. The model parameters $\beta_{0\mu}$, $\beta_{1\mu}$, β_{0s}, β_{1s} along with γ are iterated to maximise the sample likelihood parameter. The stress amplitude for each fatigue specimen is considered through σ_a. The fatigue strength (here uniaxial under alternating load f_{-1}) is expressed as a function of the number of load cycles N_f.

$$\begin{aligned} \mu_{log}(\sigma_a) &= \beta_{0\mu} + \beta_{1\mu} \ln \sigma_a - \gamma \qquad \text{for} \quad \sigma_a > \gamma \\ s_{log}(\sigma_a) &= \exp(\beta_{0s} + \beta_{1s} \ln \sigma_a) \qquad \text{for} \quad \sigma_a > \gamma \\ f_{-1}(N_f) &= \exp(\frac{\ln N_f - \beta_{0\mu}}{\beta_{1\mu}}) + \gamma \end{aligned} \tag{2.4}$$

Table 2.3: Uniaxial VHCF, maximum likelihood method results at $R = -1$ for 18CrNiMo7-6 2D [32] and 18CrNiMo7-6 ESR 3D [48]

	Maximum likelihood method				
Materials	$\beta_{0\mu}$	$\beta_{1\mu}$	β_{0s}	β_{1s}	γ (MPa)
2D	40.5	-5.6	40.1	-6.4	422
ESR 3D	35.0	-4.3	38	-6.1	453

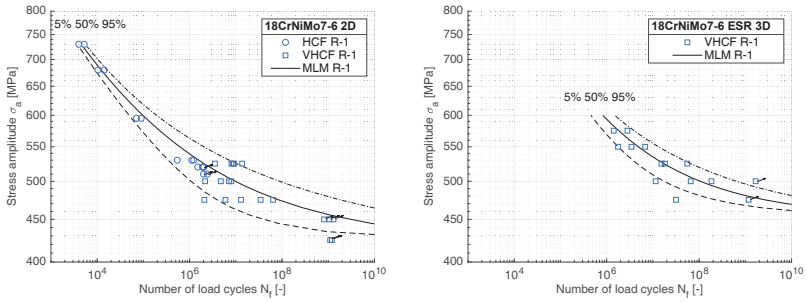

(a) 18CrNiMo7-6 2D (b) 18CrNiMo7-6 ESR 3D

Figure 2.7: SN curves for 18CrNiMo7-6 2D and 18CrNiMo7-6 ESR 3D under alternating uniaxial loading

Across the range from $1 \cdot 10^6$ to $1 \cdot 10^9$ load cycles, the ESR variant shows a between 12 to 6 % higher uniaxial fatigue strength. For large gears suffering from subsurface initiated fatigue, the ESR process could significantly improve reliability due to its small and evenly distributed inclusions and its unique segregation structure.

2.4 Model development

Based on the fatigue measurements reported in Paper II [32] and the documented results by other researchers on soft, mild and hard steels, a material model for case hardened CrNiMo steels was developed. It is briefly summarised here. To allow an accurate multiaxial fatigue assessment of a case hardened gear tooth, four material constants need to be defined:

- The uniaxial fatigue strength under alternating load f_{-1}
- The uniaxial fatigue strength under oscillating load f_0
- The shear fatigue strength under alternating load t_{-1}
- The shear fatigue strength under oscillating load t_0

The shear fatigue strength under oscillating load t_0 is approximated through the correlation proposed by Liu & Zenner [12] and repeated in Equation 2.5.

$$\frac{4t_{-1}}{t_0} - \frac{2f_{-1}}{f_0} = 1 \tag{2.5}$$

2.4.1 Uniaxial, alternating load

The material model for case hardened CrNiMo steel relies for the prediction of the uniaxial fatigue strength under alternating load f_{-1} on Murakami's $\sqrt{area}$ model. It proposes a transition from Murakami's upper to lower fatigue limit within the range of 300 to 550 HV [31].

The fractographic analysis of the VHCF fracture surfaces yielded almost identical distributions of mostly MgO-Al_2O_3 spinels across all tested steels. The average obtained inclusion size or $\sqrt{area}$ parameter was 80 μm [32]. The derived stress amplitude vs the number of cycles (SN) curves show inferior fatigue strength for the 498 HV hard 34CrNiMo6 steel beyond $1 \cdot 10^5$ load cycles compared to the softer 18CrNiMo7-6 2D, 18CrNiMo7-6 3D and 18NiCrMo14-6 steels. Defining f_{-1} as the fatigue strength at $2 \cdot 10^6$ load cycles, Equation 2.6 outlines the first parameter of the proposed material model. The cyclic behaviour of f_{-1} is covered through a lifetime factor K_{NT}, originally based on the HCF and VHCF uniaxial test results in Paper II [32] and finally on the obtained TFFs during gear testing in Paper IV [41].

$$\begin{aligned} f_{-1}(HV) &= 1.6\,HV && \text{for} \quad HV < 300 \\ f_{-1}(HV) &= \frac{1.56(HV+120)}{(\sqrt{area})^{1/6}} && \text{for} \quad HV > 550 \\ f_{-1}(HV) &\approx 505\,\text{MPa} && \text{else} \end{aligned} \tag{2.6}$$

The reported results and the proposed model are in accordance with the findings by Garwood and Nishijima [51, 52], whereby for soft and mild steels, an approximately linear correlation between the hardness and fatigue strength exists. Hard steels defy that trend and are much more susceptible to internal defects. Other microstructural heterogeneities that were especially prevalent on the hard 34CrNiMo6 steel were the banded microstructure, the large local hardness differences and the austenite islands documented through EBSD.

Figure 2.8 plots the uniaxial fatigue strength under alternating load at $2 \cdot 10^6$ load cycles for the tested 18CrNiMo7-6 2D, 18CrNiMo7-6 3D, 18NiCrMo14-6 3D, 34CrNiMo6 2D and 18CrNiMo7-6 ESR 3D steels. The fatigue strength for the 18CrNiMo7-6 ESR 3D steel was not estimated based on staircase testing but according to Equation 2.4 and the constants listed in Table 2.3. Also plotted are the upper and lower fatigue limits suggested by Murakami [31] and the Velten and Winderlich [53, 54]. Velten and Winderlich are included in this comparison as they studied the fatigue strength of hardened surface layers.

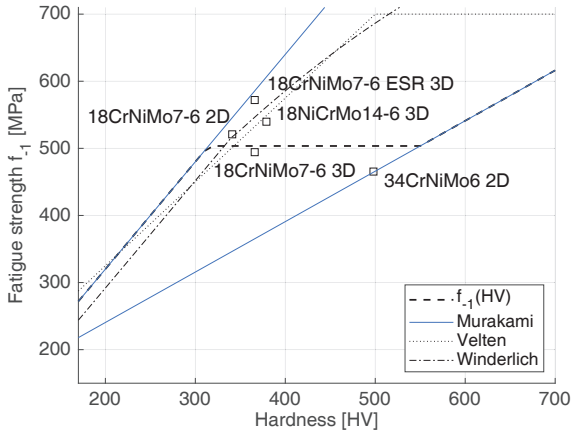

Figure 2.8: Reported uniaxial fatigue strength under alternating load compared to Murakami, Velten and Winderlich models [31, 53, 54]

All reported fatigue limits fall between the upper and lower limit set by Murakami. Here, the lower limit does not rely on the maximum but average inclusions size as not the lowest, but average fatigue results are considered (staircase testing). The 498 HV hard steel deviates significantly from the other tested steels and an increase in hardness did not yield an increase in fatigue strength. Whereas the mild steels are close to Murakami's upper limit and in good accordance with the models by Velten and Winderlich, the 34CrNiMo6 steel achieves the lowest recorded fatigue strength at $2 \cdot 10^6$ load cycles. Based on the plotted results, a transition in fatigue strength between Murakami's upper and lower limit occurs between 300 to 550 HV. The results for the 34CrNiMo6 steel illustrate the issue that arises in the case/core interface of large gears, where the steel's local anisotropy lowers the local load-carrying capacity.

Other observable trends based on the presented fatigue results are:

- 3D in comparison to 2D forging did not increase the fatigue strength
- The ESR treatment increased the fatigue strength by approximately 16% compared to the equally hard and similarly forged 18CrNiMo7-6 3D variant
- In the HCF regime, the higher nickel concentration in the 18NiCrMo14-6 steel resulted in a higher hardness and elevated fatigue properties

2.4.2 Uniaxial, oscillating load

The second model parameter is the uniaxial fatigue strength under oscillating load f_0. Its prediction relies on an iteration of the FKM guideline [13] and

considers the achieved fatigue strength under alternating load f_{-1} to alter the FKM's mean stress sensitivity M. Established definitions of M like the FKM guideline or Murakami's $\sqrt{area}$ model agree rather well for soft steels but deviate significantly for mild and hard steels [13, 31].

Figure 2.9 shows the profound effect of M on the allowable stress amplitude in a Haigh diagram under constant mean stresses and a dynamic stress amplitude. The shape of the plotted curves relies on the BO2 criterion (see Chapter 3 or Paper III [19]) and the material model outlined in Paper II [32]. Only the mean stress sensitivity M was varied according to the FKM guideline and Murakami's $\sqrt{area}$ model. Plotted are two diagrams, one for a 200 HV soft steel and one for a 600 HV hard steel. The y and x-axes show the relative stress amplitude (σ_a/f_{-1}) and the relative mean stress (σ_m/σ_f) with σ_f expressing the true fracture strength. Even though the gear tooth critical shear stress amplitude is not considered in this comparison, the profound effect of the mean stress sensitivity on the allowable stress amplitude and the uncertainty related to its definition for hard steels are adequately visualised.

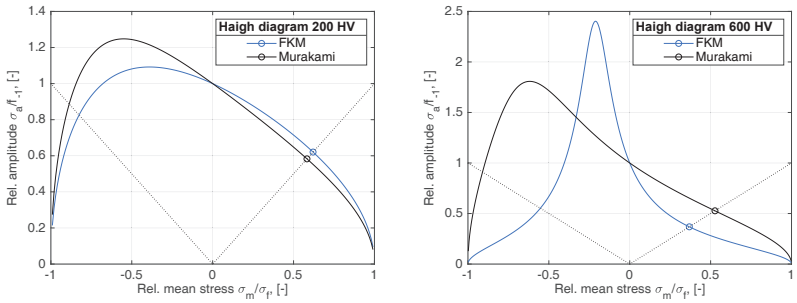

(a) Soft steel 200 HV (b) Hard steel 600 HV

Figure 2.9: Effect of mean stress sensitivity on allowable stress amplitude, Haigh diagram according BO2 criterion, FKM, Murakami [13, 19, 31]

A detailed discussion of the correlation between the FKM guideline, Murakami's $\sqrt{area}$ model, the obtained fatigue test results and additional literature sources is included in Paper II [32]. In summary, the FKM model adequately predicts M for soft and mild steels but deviates significantly from the analysed literature sources and herein acquired results for steels beyond 400 HV. Murakami appropriately predicts the obtained results for the 498 HV hard 34CrNiMo6 steel but underestimates the mean stress sensitivity of the three tested mild steels. By testing a 105 HV soft S10C steel and a 740 HV hard maraging steel, Murakami observed a weak correlation between the mean stress sensitivity and the steel's hardness. By not testing mild or medium strength steels, Murakami did not observe the in Paper II documented correlation.

The herein proposed mean stress sensitivity model attempts to bridge the

gap between the FKM guideline and Murakami's $\sqrt{area}$ model by considering the achieved uniaxial fatigue strength under alternating load f_{-1} in the prediction of the mean stress sensitivity M. It is based on the observations by Bell & Benham regarding the mean stress sensitivity of notched specimen [33] and the analogy regarding the observable effect of non-metallic inclusions on the fatigue strength of hard steels. A notch factor α_σ as the ratio between Murakami's upper fatigue limit and the achieved uniaxial fatigue strength under alternating loading f_{-1} is defined to reduce the FKM's mean stress sensitivity M once the two deviate from one another. As shown in the previous chapter, soft and mild steels show an almost linear trend between the steel's hardness or ultimate tensile strength R_m and the uniaxial fatigue strength under alternating load f_{-1}. The notch factor α_σ will be close to 1 for those steels, leaving the FKM's prediction of M unchanged. Hard steels that are affected in their fatigue properties by large non-metallic inclusions will have a significantly lower mean stress sensitivity and larger uniaxial fatigue strength under oscillating loading f_0.

Equation 2.7 lists the mean stress sensitivities for the FKM [13], Murakami [31], Goodman [55], Morrow [56] and Böhme [32] and compares them with the obtained fatigue results in Table 2.4 and Figure 2.10.

$$
\begin{aligned}
f_0 &= \frac{2f_{-1}}{1+M} \\
\text{FKM}: \quad M &= 3.5 \cdot 10^{-4} R_m - 0.1 \quad \text{with} \quad R_m = 3.18HV + \frac{HV^2}{5000} \\
\text{Murakami}: \quad M &= 2^{\alpha_m} - 1 \quad \text{with} \quad \alpha_m = 0.226 + HV \cdot 10^{-4} \\
\text{Goodman}: \quad M &= \frac{f_{-1}}{R_m} \\
\text{Morrow}: \quad M &= \frac{f_{-1}}{\sigma_f} \quad \text{with} \quad \sigma_f = R_m + 345MPa \\
\text{Böhme}: \quad M &= \frac{M_{FKM}}{\alpha_\sigma} \quad \text{with} \quad \alpha_\sigma = \frac{f_{-1,up}}{f_{-1}} \quad \text{and} \quad f_{-1,up} \approx 0.5R_m
\end{aligned}
\tag{2.7}
$$

Another way to present the proposed mean stress sensitivity model is the definition of the FKM guideline based on the uniaxial fatigue strength f_{-1} rather than the ultimate tensile strength R_m.

$$
\text{Böhme}: \quad M \approx 7.0 \cdot 10^{-4} f_{-1} - 0.1 \tag{2.8}
$$

Table 2.4: Mean stress sensitivities according to fatigue data, FKM guideline, Murakami, Goodman, Morrow and Böhme [13, 31, 32, 55, 56]

Materials	**Tests**	*FKM*	*Mura*	*Good*	*Morr*	*BO*
18CrNiMo7-6 2D	**0.37**	0.29	0.20	0.47	0.36	0.28
18CrNiMo7-6 3D	**0.30**	0.31	0.20	0.42	0.32	0.29
18NiCrMo14-6 3D	**0.34**	0.33	0.20	0.44	0.34	0.29
34CrNiMo6 2D	**0.12**	0.48	0.21	0.28	0.23	0.23

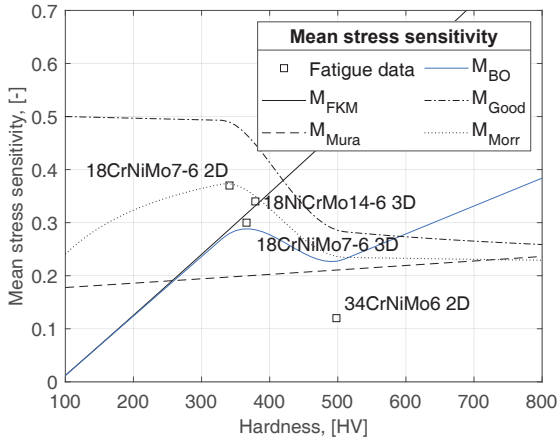

Figure 2.10: Mean stress sensitivity comparison between fatigue data, FKM guideline, Murakami, Goodman, Morrow and Böhme based on f_{-1} as defined in Paper II [32]

As highlighted in Table 2.4 and Figure 2.10, the Goodman model shows a reduction in mean stress sensitivity when transitioning from mild to hard steels for the in Chapter 2.4.1 outlined definition of f_{-1}. Whereas R_m increases nearly linearly with the local hardness, f_{-1} shifts from Murakami's upper to lower limit in the range from 300 to 550 HV, resulting in the noticeable drop in mean stress sensitivity according to Goodman [55]. The predicted values for M below 400 HV do not reflect the mostly ductile behaviour of soft steels and are deemed inappropriate. Improving upon Goodman's model is the modification by Morrow [56], which relies on the ratio between f_{-1} and the steel's true fracture strength σ_f. Here, σ_f is predicted according to Dowling [57]. For soft steels, the relative difference between R_m and σ_f is large, resulting in lower values for M. For hard steels, said difference diminishes, resulting in nearly equal predictions for both models. The projected negative trend for M for hard steels, according to Goodman and Morrow, is in contrast to all other analysed models.

Up to a hardness of 500 HV, the mean stress sensitivity predicted by Morrow seems to describe the behaviour of CrNiMo steels adequately. Beyond 500 HV, it wrongly predicts a negative gradient for M. Up to 500 HV, the consideration of f_{-1} in the prediction of M significantly improves the model accuracy as it considers the effect of internal defects on the fatigue strength and mean stress sensitivity. The suggested modification of the FKM model through f_{-1} in the form of a notch factor α_σ reduces M for hard steels that are severely affected by impurities. It achieves a suitable accuracy for the herein analysed steels and the materials studied in the cited literature sources in Paper II [32].

2.4.3 Shear, alternating load

The third model parameter is the shear fatigue strength under alternating load t_{-1}. Other than f_{-1}, only HCF tests were carried under torsion, with the fatigue limit being determined by staircase testing up to $5 \cdot 10^6$ rather than $2 \cdot 10^6$ load cycles. Identical hourglass-shaped, ultrasonic-treated HCF specimens were tested under shear, resulting in a complex multiaxial stress state in the outer shot-peened layer. The Liu & Zenner shear stress intensity criterion [12] was used to combine the alternating shear stresses with the static, compressive, normal stresses to predict t_{-1}. During testing, failures and run-outs occurred at 375 MPa (alternating shear stress). Due to the up to 700 MPa large compressive stresses in longitudinal and transverse directions, the true fatigue strength according to the Liu & Zenner criterion was closer to 345 MPa. When considering the specimens' geometrical notch factor α_σ, the stress redistribution factor n, surface roughness factor $K_{F\tau}$ (according to FKM guideline [13]) and a size factor K_X based on the weakest link theory [58], the true shear fatigue strength for the tested 18CrNiMo7-6 3D and 34CrNiMo6 steels was calculated to 319 and 329 MPa respectively. Owning to the stress gradient in the HCF specimens during shear testing, a significantly smaller volume than during uniaxial testing was subjected to large, cyclic stresses. For example, for the 18CrNiMo7-6 3D forged HCF specimens, a 13 times smaller volume was highly loaded during shear than uniaxial testing.

The fatigue ratios κ as the ratio between f_{-1} and t_{-1} for the two tested steels were measured to 1.55 and 1.41. Based on the obtained results and the literature findings [35, 59–79], a fatigue ratio as a function of the steel's hardness is suggested for case hardened CrNiMo steels (see Equation 2.9).

$$\kappa(HV) = -5 \cdot 10^{-4} HV + \sqrt{3} \quad \text{with} \quad t_{-1} = \frac{f_{-1}}{\kappa} \tag{2.9}$$

Figure 2.11 plots the obtained fatigue ratios against literature findings on various steels [35, 59–79] and visualises the linear approximation of κ.

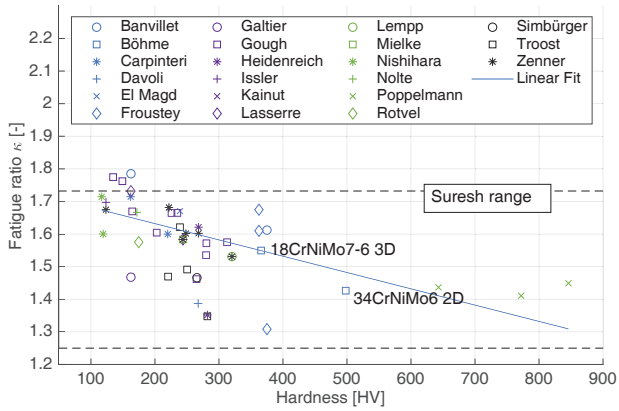

Figure 2.11: Fatigue ratio κ for carburised CrNiMo steels [32]

2.4.4 Gear testing

A set of 10 medium-sized spiral bevel gears was tested on a back-to-back endurance test rig, resulting in six TFF damages, of which five occurred on the tested gear wheels and one on a pinion tooth (see Paper IV [41] for the gear geometry and tested $CHDs$ and loads). The combination of the outlined material model, stress model and the multiaxial fatigue criterion described in Chapter 3 was used to analyse the predicted subsurface material utilisations in pinion and wheel teeth to derive a TFF-specific lifetime factor.

As three different hardening layer thicknesses were tested (batches B1, B2 and B3), a surface or shear stress-based lifetime factor was not appropriate, also when considering the test gear's gear ratio of 9/33 and the larger number of load cycles but fewer TFFs on the tested pinions. Relying instead on the predicted material utilisations and the documented hardening layer differences between pinion and wheel teeth, a lifetime factor K_{NT} was proposed in magnitude and shape comparable to the established tooth root and pitting lifetime factors of the ISO10300 [21, 80].

Similar to the presented uniaxial fatigue curves, K_{NT} relies for its prediction on the MLM [42], resulting in a continuous rather than a multi-staged SN curve. Considering failures and run-outs of the tested pinion and wheel teeth, an appropriate sample size was available even though only ten gear sets were tested. The derived TFF-specific lifetime factor is given in Equation 2.10. It is compared to the predicted material utilisations in Figure 2.12a and the tooth root and pitting lifetime factors Y_{NT} and Z_{NT} in Figure 2.12b. K_{NT} changes as a function of the number of load cycles N_f and is conservatively capped at 1.6.

$$K_{NT}(N_f) = \exp\frac{\ln N_f - 10.42}{-2.73} + 0.89 \quad \text{with} \quad K_{NT} \leq 1.6 \tag{2.10}$$

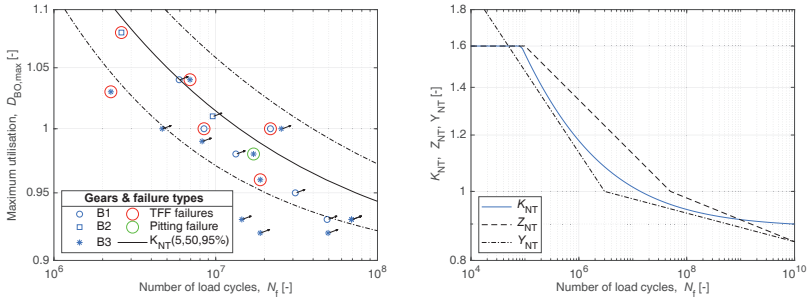

(a) Failures, run-outs and K_{NT} (b) Lifetime factors K_{NT}, Z_{NT} and Y_{NT}

Figure 2.12: Gear test results and ISO comparison [21, 41, 80]

Another factor that needs to be considered to predict the local fatigue strength is the size factor K_X. The same weakest link theory that was applied to the prediction of t_{-1} was used to predict K_X through the comparison of the highly stressed volumes in the studied HCF specimens and several maritime and test gears [58]. The detailed steps for the calculation of the size factor are listed in Appendix C. Here, only the simplified version that relies on the mean normal module m_{mn} is repeated in Equation 2.11.

$$K_X(m_{mn}) = 1.05 - 0.01 m_{mn} \quad \text{with} \quad 0.87 \leq K_X \leq 1 \tag{2.11}$$

As is typical for gear standards [2, 4], not the mean but 1 % fatigue strength is utilised for the safety factor calculation. Based on the analysis of the VHCF uniaxial fatigue results of the 34CrNiMo6 steel through the pearl string method [50], a relative standard deviation of 4 % is estimated. Said standard deviation leads to a conversion factor f_{xK} of 0.91. When designing a new gear, f_{xK} should be considered to yield ISO-comparable failure probabilities, but not during a failure investigation or a gear test programme.

Multiaxial fatigue criteria, like the Liu & Zenner shear stress intensity criterion, compare an equivalent stress amplitude $\sigma_{eq,LZ}$ to the uniaxial fatigue strength under alternating load f_{-1} when calculating the material utilisation D_{LZ}. To consider the above outlined lifetime, size and conversion factors, they are multiplied with f_{-1} as per Equation 2.12.

$$\begin{aligned} D_{LZ} &= \frac{\sigma_{eq,LZ}}{f_{-1,K}} \\ f_{-1,K} &= f_{-1} \cdot f_{xK} K_X K_{NT} \end{aligned} \tag{2.12}$$

Chapter 3

Numerical stress prediction

This chapter recaptures the numerical stress model and multiaxial fatigue criteria introduced in Paper III [19] and verified through gear testing in Paper IV [41]. Focus is given to the validation of the developed 2D plane strain numerical stress model. It is initially compared to established analytical models that rely on the Euler-Bernoulli and Timoshenko beam theory and subsequently more advanced analytical models that consider the tooth shape in the prediction of the transverse shear stress and the transverse normal stress in the point of load introduction. Two contracted gear tooth studies are cited to substantiate the chosen 2D approach over complex 3D tooth and stress models. They are used to highlight the complexity of 3D tooth contact analysis and compare the 2D vs 3D subsurface stress state for a static and a dynamic gear tooth engagement.

The impact of the mean normal stress $\sigma_{n,m}$ on local material utilisation throughout a gear tooth is outlined in the latter part of the chapter. The comparison between different multiaxial fatigue criteria and their implementation of $\sigma_{n,m}$ is used to describe the development process of the BO criteria. The uncertainty in estimating the mean stress sensitivity M is used to demonstrate the validity of the BO1 and BO2 criteria.

In a study of the shear and normal stresses as a function of the Euler angles ϕ and θ, the Dang Van, Liu & Zenner and BO1 criteria are compared in regards to their fatigue damage parameters and the material planes in which crack initiation is likely to occur. For a more detailed outline of the developed 2D plane strain numerical approach, the reader is referred to Paper III [19].

3.1 Rolling Contact Fatigue

The stress state, load history and failure mechanism that define RCF in bearings or rail-wheel contacts and subsurface fatigue or TFF in gears are comparable. Similarities and differences are highlighted in this chapter to give a general introduction to subsurface fatigue in gears and the governing stresses.

It is common to differentiate between two types of RCF damages in bearings, gears or rail-wheel contacts. For applications with smooth surfaces, good lubrication and low surface friction, RCF will occur in the form of subsurface-initiated spallings in the maximum shear stress depth (see Figure 3.1 for gear and bearing examples). In the case of rough surfaces or oil contamination, a surface-initiated crack will form on stress raisers due to localised plastic deformation. After a short surface-parallel crack propagation, the crack branches or turns towards the surface, creating a small pit [81]. Also, coalescing or large pits are referred to as spalling.

(a) Maritime pinion gear

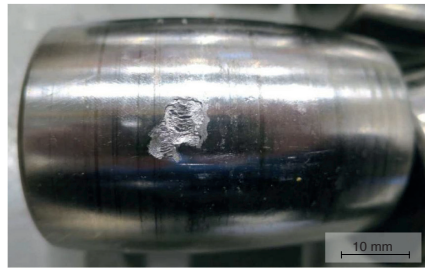

(c) Roller bearing

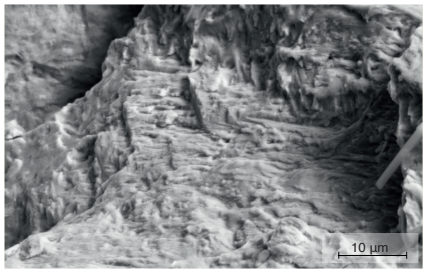

(b) SEM image spalling ground

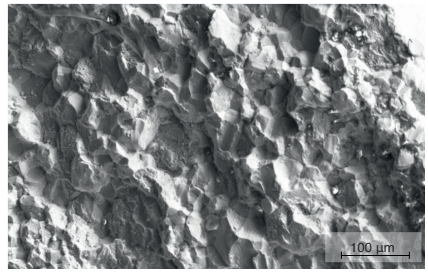

(d) SEM image spalling edge

Figure 3.1: RCF or spalling on maritime gear and large roller bearing, SEM images with fatigue striations in the spalling ground and intergranular brittle fracture from prior austenite grain boundaries close to the gear's surface [82]

Recent gear improvements regarding the optimisation of the gear's macro- and microgeometry (i.e. the stress distribution in the contact), material and lubricant improvements and gear post-processing steps like shot-peening or isotropic superfinishing have led to a transition from surface-initiated failures like pitting or scuffing to subsurface failures like TFF. Especially large maritime bevel gears that suffer from subsurface material inhomogeneities are critically affected by subsurface fatigue (see Chapter 2).

The stress state in RCF and TFF is governed by Hertzian contact theory and is complex, multiaxial and non-proportional. Whereas the maximum shear stress depth is critical in smooth, well-lubricated and through-hardened bearings, a failure initiation is likely to occur in the transition zone between the hard case and the soft core of case hardened gears. For roller bearings and conventional cylindrical gears, a Hertzian line contact adequately captures the surface stress distribution (see Figure 3.2b for the equivalent cylinder/plane or line contact model). The governing parameters are the half Hertzian contact width b_H and maximum Hertzian pressure p_H. Spiral bevel gears are more complex in their stress distribution, leading to changing Hertzian parameters along an instantaneous contact line and the path of contact (i.e. the motion of the contact line along the tooth surface during meshing). Figure 3.2a shows a how single contact line is defined as a multitude of cylinder/plane models as a result of the changing curvature along the tooth flank. 3D, numerical contact simulations or an LTCA with the FVA program Becal can be performed to capture the stress distribution between meshing pinion and wheel teeth. The LTCA relies on the lengthwise and heightwise discretisation of gear tooth in line contact segments [18].

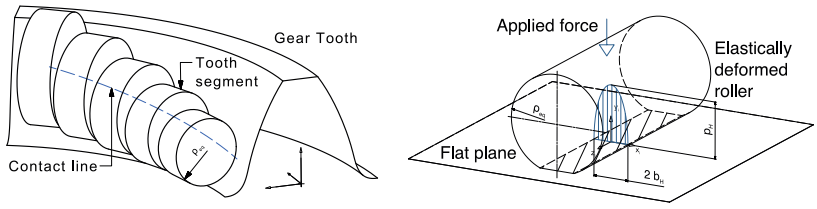

(a) LTCA, tooth segmentation (b) Line contact model

Figure 3.2: Spiral bevel gear tooth load discretisation

The subsurface stresses in case hardened gears of this position- or time-dependent stress field are comprised of Hertzian, transverse shear, out-of-phase bending, frictional shear and static, compressive and tensile residual stresses. For pitting or RCF, the modification of the Hertzian contact stress distribution through elastohydrodynamic and surface roughness effects needs to be considered. They critically affect the shallow, surface-near stress field but can be neglected for the study of TFF.

3.2 Stress model

The 2D plane strain approach utilised for the subsurface stress prediction in the mean cross-section of either pinion or wheel, spiral bevel gear tooth is presented in detail in Paper III [19]. Here, further context is given to established analytical

models, advanced analytical calculations, the chosen 2D numerical approach and full 3D contact analysis.

3.2.1 Analytical and numerical comparison

Established analytical, subsurface stress predictions in cylindrical gears rely on the 2D plane strain assumption, the Hertzian stress prediction based on the cylinder/plane model, a constant friction coefficient in the contact, the Euler-Bernoulli beam theory for the prediction of a linear bending stress distribution and the Timoshenko beam theory for the prediction of transverse shear stress [1, 6, 15]. The static residual stresses as a result of the case hardening process are modelled as a function of the hardness profile [28] and added to the dynamic stresses of either analytical or numerical calculations. They are outlined in Chapter 2 and Equation 2.1 and therefore excluded from this comparison. Equations 3.1, 3.2 and 3.3 detail the analytical prediction of Hertzian and frictional stresses for a cylinder/plane line contact and the 2D plane strain assumption. The coordinate system is situated in the middle of the Hertzian stress distribution. The x-axis is orientated perpendicular to the surface and the y-axis tangential to the point of contact. A constant friction coefficient μ across the Hertzian contact width b_H is implemented.

$$\begin{aligned}
\sigma_{x,H}(x,y) &= \frac{-2}{\pi}\int_{-b_H}^{b_H} p_H\sqrt{1-\left(\frac{t}{b_H}\right)^2}\,\frac{x^3}{\left(x^2+(y-t)^2\right)^2}dt \\
\sigma_{y,H}(x,y) &= \frac{-2}{\pi}\int_{-b_H}^{b_H} p_H\sqrt{1-\left(\frac{t}{b_H}\right)^2}\,\frac{x(y-t)^2}{\left(x_l^2+(y-t)^2\right)^2}dt \\
\tau_{xy,H}(x,y) &= \frac{-2}{\pi}\int_{-b_H}^{b_H} p_H\sqrt{1-\left(\frac{t}{b_H}\right)^2}\,\frac{x^2(y-t)}{\left(x^2+(y-t)^2\right)^2}dt
\end{aligned} \tag{3.1}$$

$$\begin{aligned}
\sigma_{x,\mu}(x,y) &= \frac{-2}{\pi}\int_{-b_H}^{b_H} p_H\sqrt{1-\left(\frac{t}{b_H}\right)^2}\,\mu\frac{x^2(y-t)}{\left(x^2+(y-t)^2\right)^2}dt \\
\sigma_{y,\mu}(x,y) &= \frac{-2}{\pi}\int_{-b_H}^{b_H} p_H\sqrt{1-\left(\frac{t}{b_H}\right)^2}\,\mu\frac{(y-t)^3}{\left(x^2+(y-t)^2\right)^2}dt \\
\tau_{xy,\mu}(x,y) &= \frac{-2}{\pi}\int_{-b_H}^{b_H} p_H\sqrt{1-\left(\frac{t}{b_H}\right)^2}\,\mu\frac{x(y-t)^2}{\left(x^2+(y-t)^2\right)^2}dt
\end{aligned} \tag{3.2}$$

$$\sigma_z(x,y) = \nu\left(\sigma_x(x,y)+\sigma_y(x,y)\right) \tag{3.3}$$

The simplification of the gear tooth as a cantilever beam for the analytical stress prediction is common practice (reference ISO10300-3 tooth root breakage [80]). For TFF, the Euler-Bernoulli bending and Timoshenko shear stresses are

added to the Hertzian contact stresses. The parameters in Equation 3.4 denote a shear force F_t, a radial force F_r, the moment of inertia of a rectangular cross-section I, the cross-sectional area A, the height of the beam h and its width b. If a gear tooth is modelled, b needs to be replaced with the height-dependent tooth width $s_n(y)$. Whereas the coordinate system for the calculation of the Hertzian stress distribution was placed in the middle of the line contact (i.e. representing a local coordinate system), the coordinate system in Equation 3.4 is situated in the root of the beam and its neutral axis (i.e. representing the global coordinate system). Here, x refers to the perpendicular distance to the neutral axis and y to the distance to the point of load introduction. Shear and radial forces are predicted according to the gear flank's local pressure angle α.

$$\begin{aligned} \text{Euler}: \ \sigma_y(x,y) &= \frac{F_r}{A(y)} + \frac{M_b(y)x}{I(y)} \quad \text{with} \quad M_b(y) = F_t \cdot y \\ \text{Timoshenko}: \ \tau_{xy,T}(x,y) &= \frac{F_t}{2I(y)} \left(\frac{b(y)^2}{4} - x^2 \right) \quad \text{with} \quad I(y) = \frac{hb(y)^3}{12} \end{aligned} \tag{3.4}$$

Figure 3.3 plots the calculated numerical and analytical von Mises equivalent stress σ_{vM} for a cantilever beam loaded at 2000 MPa at a half Hertzian contact width of 2 mm, assuming linear elastic material behaviour and the 2D plane strain stress state. Even though the Hertzian stress dominates the plotted von Mises equivalent stress, a superposition of bending and shear stresses is apparent. The analytical stresses were modelled according to Equations 3.1, 3.3 and 3.4.

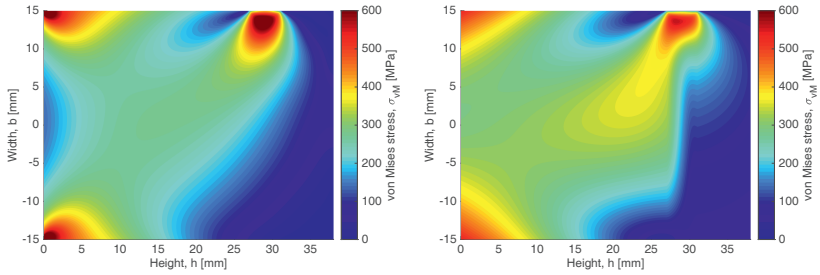

(a) Numerical (b) Analytical

Figure 3.3: Cantilever beam under Hertzian stress - Model comparison

While the plotted beam is an oversimplification of the involute mean cross-section of a gear tooth, the stress difference between both models is evident. Significant differences are found in the root of the beam and underneath the Hertzian contact. To better visualise the model deviations, Figure 3.4a plots the bending stress difference between the numerical and analytical model $\Delta\sigma_y =$

$\sigma_{y,num} - \sigma_{y,ana}$. In the literature, the missing stress in the outlined analytical model is referred to as the transverse normal stress $\sigma_{y,n}$ and occurs in the point of load introduction and the constrained or fixed face of the beam. The transverse normal stress is a result of the prevented arcing of the beam's cross-section. Figure 3.4b plots the stress profile underneath the Hertzian contact (Plane 2) and the beam's root (Plane 1) for the numerical model and compares them to the analytical transverse normal stress according to Hofmann [17].

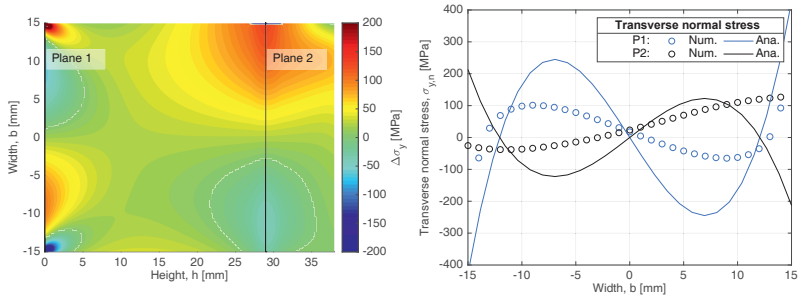

(a) Numerical - Analytical (b) Comparison to Hofmann [17]

Figure 3.4: Cantilever beam under Hertzian stress - Visualisation of the transverse normal stress

Hofmann's transverse normal stress matches the observed general trend in Planes 1 and 2 but deviates significantly from the numerical results, especially in the vicinity to the Hertzian line contact. A difference that can readily be attributed to the assumed symmetric arcing of the beam's cross-section due to an assumed load introduction in the beam's neutral axis in Hofmann's model. Due to the distance between Planes 1 and 2, an almost symmetric transverse stress profile is apparent in Plane 1. Böhme in [16] proposes a more accurate transverse normal stress profile underneath a Hertzian stress distribution in a beam or gear tooth as a function of the applied tangential force and beam's height or tooth's width (see Equation 3.5). The appreciation and depreciation of the proposed transverse normal stress should be modelled according to Hofmann [17].

$$\sigma_{y,n}(x) = \frac{6}{5}\frac{F_t}{bh}\left(4\left(\frac{x}{b}\right)^3 - 5\left(\frac{x}{b}\right)^2 + 1\right) \tag{3.5}$$

So far, only the numerical and analytical stress differences for a straight cantilever beam under Hertzian line contact have been discussed. The inaccuracies of the analytical model are amplified when studying a gear tooth or non-prismatic beam. Balduzzi et al. and Beltempo et al. show in [83, 84] that Timoshenko's shear stress model no longer applies to non-prismatic beams, where the shear stress distribution depends not only on the vertical or shear

force but also on the horizontal or radial force and the bending moment. For symmetric gear teeth, an adapted version of Balduzzi's shear stress distribution is given in Equation 3.6. The terms σ_{y0}, σ_{y1} and τ_{y0} are referred to as the mean value of the radial stress within the cross-section, the maximum radial stress induced by the bending moment within a cross-section and the mean shear stress. The distribution of the stresses in the cross-section is described through the linear function $\widetilde{b}(x,y)$. Relevant is also the change in the tooth width s_n' in the tooth profile direction, which can be adequately modelled through the local pressure angle $\alpha(y)$. Similarly, improvements for the shear stress distribution in gear teeth are suggested by Weber, who relies on the approximation of the gear tooth as a wedge [29].

$$\begin{aligned}
\text{Balduzzi}: \ \tau_{xy,B} &= -\frac{s_n'(y)}{2}\left(\sigma_{y0}(y)\widetilde{b}(x,y) + \sigma_{y1}(y)\left(-\frac{1}{2}+\frac{3}{2}\widetilde{b}(x,y)^2\right)\right) \\
&\quad + \frac{3}{2}\tau_0(y)(1-\widetilde{b}(x,y)^2) \\
\sigma_{y1}(y) &= \frac{6yF_t}{bs_n(y)^2} \quad \sigma_{y0}(y) = \frac{F_r}{A(y)} \quad \tau_{y0}(y) = \frac{F_t}{A(y)} \\
\widetilde{b}(x,y) &= -\frac{x}{s_n(y)} \quad \text{with} \quad |\widetilde{b}(x,y)| \leq 1
\end{aligned} \tag{3.6}$$

Figure 3.5 plots the numerical shear stress τ_{xy} for the mean pinion cross-section of the studied G1 gear set (see Papers I & III [10, 19]) and compares the shear stress distributions along three planes in 6, 12.5 and 19 mm distance to the origo to Timoshenko's and Balduzzi's shear stress models.

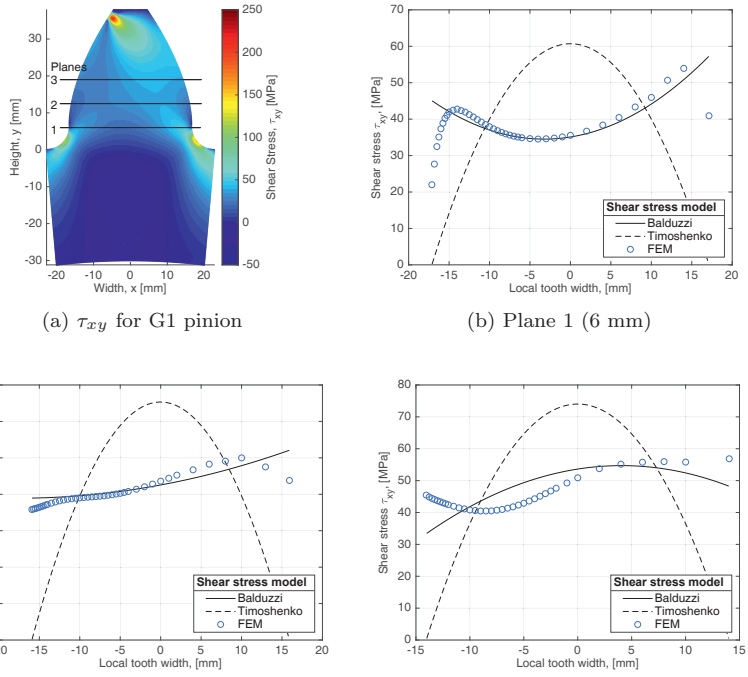

(a) τ_{xy} for G1 pinion

(b) Plane 1 (6 mm)

(c) Plane 2 (12.5 mm)

(d) Plane 3 (19 mm)

Figure 3.5: Shear stress distribution for mean pinion cross-section of G1 gear set according to numerical, Timoshenko and Balduzzi models [83]

For the studied material planes, the shear stress model by Balduzzi guarantees a superior analytical stress prediction compared to the parabolic distribution predicted by Timoshenko. The herein plotted shear stresses were not derived from the suggested local pressure angle $\alpha(y)$ but a constant pressure angle across the entire tooth height. The modelled shear stress profile is thereby more akin to that of a trapezoid or wedge than an involute gear tooth.

Several equations have been presented to improve the analytical stress prediction in a beam and subsequently involute gear tooth under Hertzian stresses. The inaccuracies of the Euler and Timoshenko stress predictions are partially overcome with the models by Hofmann and Balduzzi [17, 83]. As shown by Weber in [85], even a highly complex, analytical wedge model deviates between 5 to 20 % from a numerical stress prediction. Weber calculates a relative stress difference between the analytically and numerically predicted maximum von Mises equivalent stress during the meshing of pinion and wheel teeth. Regarding the computational complexity of the presented analytical model, there is no perceivable advantage to the, in the context of this academic work developed, numerical MATLAB code. Especially the integrals listed in Equations 3.1 and

3.2 are computationally expensive.

Due to the computational complexity, inaccuracy and missing consideration of the geometrical notch in the tooth root of the analytical model, a numerical stress prediction was favoured.

3.2.2 3D and 2D numerical comparison

This chapter relies on the results of two contracted gear tooth studies [86, 87] to discuss the differences between 3D and 2D numerical models. Two numerical approaches are commonly discussed and compared in the literature when assessing the surface and subsurface stresses in a spiral bevel gear tooth:

- A full 3D contact analysis of typically three pinion and wheel teeth over several contact positions, simulating the complete over-rolling of a single gear tooth
- A 2D analysis of the gear's mean cross-section under the plane strain assumption with surface loads based on an LTCA or analytical equations [7, 8]

While a 2D analysis can be performed without an LTCA (for conventional microgeometries, the simplification of the octoid tooth shape as an involute and a load prediction based on analytical equations [7, 8]), the 3D approach requires an LTCA, even if the contact stresses are calculated by numerical means. The modelling of a spiral bevel gear tooth with its specific macro- and microgeometry is no trivial task and relies typically on the machining simulation of pinion and wheel. With the tool parameters specified, the FVA program Becal [18] (here referred to as LTCA) models the gear geometry based on a machining simulation, segments each gear tooth, runs a load-free simulation to assess the distances between the meshing pinion and wheel surface nodes and predicts the contact and tooth root stresses in a loaded tooth contact analysis in a fraction of the time a full 3D FEM simulation would require. The tooth segments are joined through an iterated stiffness matrix that ensures the correct load distribution between all segments. For a 3D gear study, point clouds are exported from Becal to model the gear teeth as a set of splines and surfaces. In the contracted gear study by DNV [86], a large maritime bevel gear was analysed with various 3D models and the 2D plane strain approach. The mesh layout of the full 3D and 2D analyses are plotted in Figure 3.6.

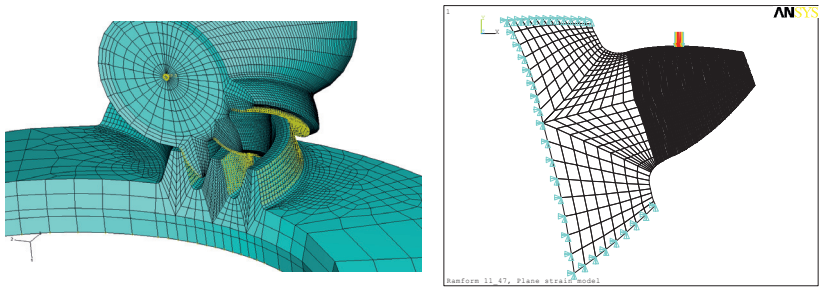

(a) 3D FE model (b) 2D FE model

Figure 3.6: 3D and 2D model comparison in DNV study [86]]

Due to the gear's overlap ratio, three tooth pairs need to be modelled for the 3D contact analysis. The DNV study relied on Becal or the LTCA to predict the gear's geometry through the machining simulation. The different mesh resolutions visualised in Figures 3.6a and 3.6b are a result of the computational complexity of the 3D contact analysis. Compared to the 2D plane strain model, which requires mere seconds, the referenced 3D contact analysis took 60 hours for the visualised coarse 1 mm mesh resolution and a limited ten contact positions. Any advantages that the full contact analysis might yield due to a more accurate stress distribution and load representation are diluted by the occurring inaccuracy due to the coarse mesh resolution and the limited number of load steps. Average values for the half Hertzian contact width b_H for the analysed gear and loading condition were 1.5 to 2 mm. Given the contact width and mesh resolution, the parabolic Hertzian stress distribution was introduced over 2 to 4 end nodes in the tooth profile direction. In a study performed by Böhme in 2012 [16], a minimum number of 8 end nodes is suggested to yield an accurate subsurface stress profile.

Other effects considered in an LTCA-derived stress distribution and the herein implemented 2D plane strain analysis are the displacement of the gear's contact pattern and changes in the stress distribution due to the load-induced elastic deformation of the driveline and gear environment. A 3D contact analysis would require the modelling of additional parts of the gear's environment to capture those effects, further adding to the computational complexity. Due to the coarse element size, inaccurate subsurface stress prediction and extreme computational complexity, the validity of the 2D plane strain approach was not tested against the full 3D contact analysis in the DNV study [86], but a 3D half-tooth model with and without an inclined contact line (see Figure 3.7). The inclined model resembles the orientation of an actual contact line, whereas the straight model resembles the 2D plane strain approach.

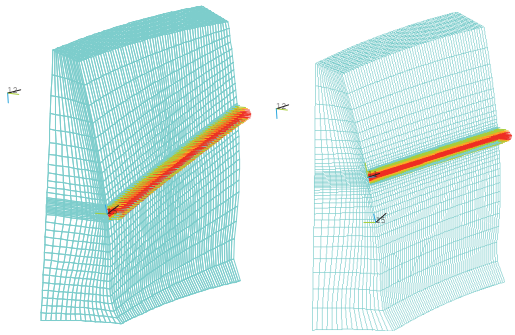

(a) Inclined line contact (b) Straight line contact

Figure 3.7: Half tooth model under line load with $p_H = 1350$ MPa and $b_H = 2$ mm [86]

Figure 3.8 plots the subsurface stress profiles σ_x, σ_y and σ_z tangential, perpendicular and longitudinal to the tooth surface (see Figure 3.6b for the orientation of the specific coordinate system) for the 3D contact model, the half-tooth straight and inclined models and the 2D plane strain stress approach. The coarse mesh resolution of the 3D contact analysis is visualised in Figure 3.8 through the element nodes in 1 mm spacings and their stresses.

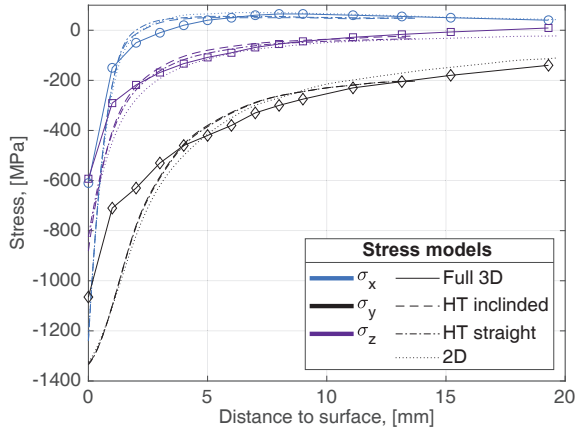

Figure 3.8: Subsurface stress σ_x, σ_y and σ_z for full 3D, half tooth inclined and straight and 2D plane strain model [86]

All solutions converge below a 5 mm depth, indicating that the simple 2D plane strain model is sufficient in capturing the complex subsurface stress state

in the TFF-relevant material depth. Whereas the two half-tooth models and the 2D plane strain model agree very well, the 3D solution diverges significantly in the shallow material depth due to the coarse mesh resolution and load introduction over a limited number of nodes. All models predict tensile σ_x stresses below a 3 mm depth, representative of the aforementioned transverse normal stresses (see Equation 3.5). In order to assess the applicability of the plane strain stress assumption in the 2D model, a plane strain condition or stress $dS = \sigma_z - \nu(\sigma_x + \sigma_y)$ was defined and studied [86]. Figure 3.9a plots dS for all four models and compares furthermore the maximum shear stress in Figure 3.9b.

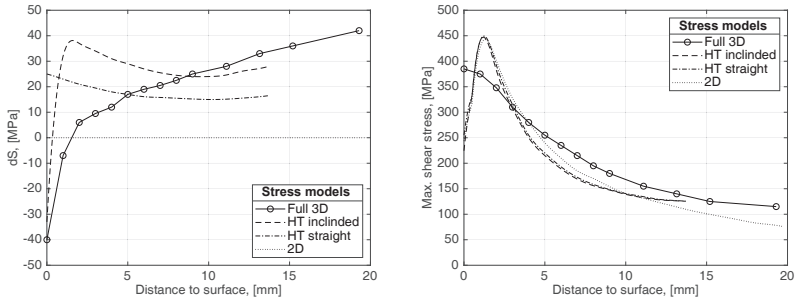

(a) Validity of plane strain assumption (b) Max shear stress comparison

Figure 3.9: Stress model comparison [86]

While there is a noticeable difference between the 2D plane strain assumption and the other stress models, it is overall small compared to the other acting stresses. The maximum shear stress plot indicates that the plane strain assumption leads to higher shear stresses than the half-tooth models in the TFF critical material depth of 3 to 7 mm. Between those three models, the stress differences are minor. The 3D contact model fails to capture the maximum shear stress peak underneath the surface but predicts elevated stress levels 4 mm below the loaded surface. The stress difference between the full 3D and 2D models are attributed to mesh and load inconsistencies and not inaccuracies in the 2D approach.

The second contracted stress study [87] similarly compared the subsurface stresses in a 3D gear tooth model and a 2D plane strain model. A single pinion tooth was studied and loaded according to the LTCA's predicted stress distribution across 25 sequential contact lines to avoid a numerical contact analysis. This approach ensured that the same surface stresses were present in the 3D and 2D models. As a result, not just the stress differences for a single contact position were studied, but the stress history for subsurface nodes in 2, 4, 6 and 8 mm depths along a surface perpendicular path. Figure 3.10a visualised the application of the LTCA's contact lines and stress distributions to the 3D

tooth model. Figure 3.10b plots the shear stress history $\tau_{xy,a}$ for the 25 contact positions in 2, 4, 6 and 8 mm depths along a surface perpendicular path.

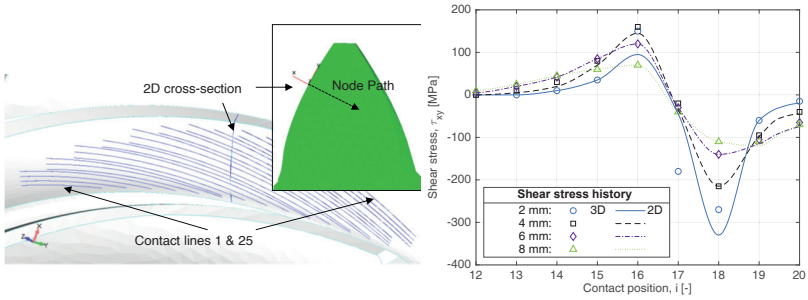

(a) 3D model and contact lines

(b) Shear stress history

Figure 3.10: 3D and 2D stress comparison focusing on shear stress τ_{xy} [87]

The shear stress comparison demonstrates the accuracy of the 2D plane strain assumption for the subsurface stress prediction in large bevel gears. The only appreciable difference occurred in the surface vicinity, where the short distance between the loaded surface nodes and analysed subsurface nodes resulted in numerical inaccuracies. In the presented study, the same stresses and geometries were analysed in the 3D and 2D models. Both models relied on the LTCA for the surface stress distribution and the geometry of the analysed gear tooth or cross-section. The 2D cross-section was extracted from the 3D tooth geometry and not simulated as an involute tooth.

Sufficient evidence for the accuracy of a 2D plane strain, numerical stress analysis to capture the subsurface stresses for meshing spiral bevel gears has been presented in this chapter. The quoted studies suggest that the 2D analysis can be regarded as conservative as higher stress amplitudes were predicted [86, 87]. As highlighted in Paper III [19], the lengthwise crowning applied to bevel gear teeth ensures a stress concentration in the middle of the gear tooth. Evidence of the stress concentration in the centre of the tooth for gear set G1 is provided in Figure 1.5 in Chapter 1.

3.3 Multiaxial fatigue

With the stress history in the mean cross-section of a spiral bevel gear tooth defined, the local material utilisation D can be predicted based on the material model outlined in Chapter 2. The motion of the Hertzian contact along the tooth flank yields a non-proportional stress field with changing principal stress directions and ratios. For gears, bearings, shafts or other mechanical components with failures in the high to very high cycle fatigue regime, stress-based

multiaxial fatigue criteria suitably predict the risk for material fatigue. Rather than relying on the components of the stress tensor S, the mean and amplitude, normal and shear stresses on each material plane need to be predicted.

3.3.1 Normal and shear stresses

The calculation of $\sigma_{n,m}$, $\sigma_{n,a}$, τ_m and τ_a are outlined in Paper III [19] and briefly repeated here. The traction vector t describes the stress on a given material plane Δ. The plane itself is perpendicular to the unit vector $n_{x'}$, which is defined through the spherical angles θ and ϕ. Through the use of $n_{x'}$, $n_{y'}$ and $n_{z'}$, t can be decomposed into the time-dependent shear stresses $\tau_{x'y'}$ and $\tau_{x'z'}$ and the normal stress σ_n (see Equations 3.7, 3.8 and 3.9).

$$n_{x'} = \begin{pmatrix} \sin\phi\cos\theta \\ \sin\phi\sin\theta \\ \cos\phi \end{pmatrix} \quad n_{y'} = \begin{pmatrix} -\sin\theta \\ \cos\theta \\ 0 \end{pmatrix} \quad n_{z'} = \begin{pmatrix} -\cos\phi\cos\theta \\ -\cos\phi\sin\theta \\ \sin\phi \end{pmatrix} \tag{3.7}$$

$$t = S \cdot n_{x'} \quad \text{with} \quad S = \begin{bmatrix} \sigma_{xx} & \tau_{xy} & 0 \\ \tau_{xy} & \sigma_{yy} & 0 \\ 0 & 0 & \sigma_{zz} \end{bmatrix} \tag{3.8}$$

$$\begin{aligned} t &= \tau + \sigma_n \cdot n_{x'} = \tau_{x'y'} \cdot n_{y'} + \tau_{x'z'} \cdot n_{z'} + \sigma_n \cdot n_{x'} \\ \tau_{x'y'} &= t \cdot n_{y'} \quad \text{and} \quad \tau_{x'z'} = t \cdot n_{z'} \quad \text{and} \quad \sigma_n = t \cdot n_{x'} \end{aligned} \tag{3.9}$$

The prediction of the mean and amplitude of the normal stress σ_n is possible by conventional means. Paper III [19] references the minimum circumscribing circle (MCC) [39, 88] and maximum rectangular hull (MRH) [89] methods as two candidates to derive the mean and amplitude of the shear stress τ_m and τ_a from the shear stress path Ψ. Equations 3.10 and 3.11 define both methods, which are illustrated in Figure 3.11. Whereas the MCC tries to minimise the size of the circumscribing circle around all incidences of Ψ, capturing the τ_m in its centre and τ_a in its radius, the MRH tries to find the largest rectangle through its rotation over the angle α. For the MRH, τ_a appears as half of the length of the square's diagonal with τ_m in its centre. The MRH was developed to improve the prediction of the shear stress amplitude for non-proportional loading. The variables in Equation 3.11 $a_{1,2}$, α and $\tau_{1,2}$ refer to the width and length of the rectangle, its rotational angle and the shear stress instances.

$$\begin{aligned} \tau_{m,MCC} &= \min_{\tau*} \left(\max_t |\tau(t) - \tau*| \right) \\ \tau_{a,MCC} &= \max_t |\tau(t) - \tau_{m,MCC}| \end{aligned} \tag{3.10}$$

$$\begin{aligned} a_{k=1,2} &= \frac{1}{2} \left(\max_t \left(\tau_k(\alpha, t) - \min_t(\tau_k(\alpha, t)) \right) \right) \\ \tau_{a,MRH} &= \max_\alpha \sqrt{a_1^2(\alpha) + a_2^2(\alpha)} \end{aligned} \tag{3.11}$$

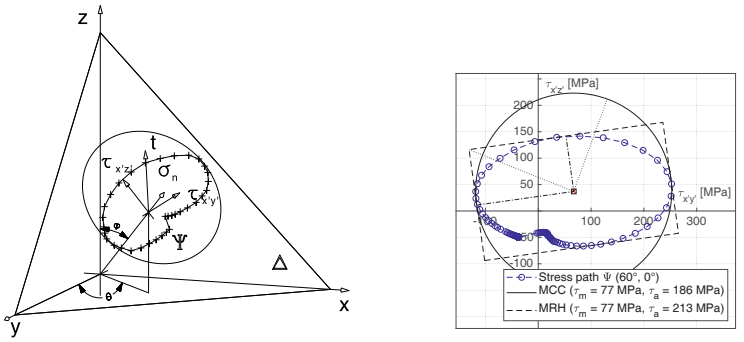

(a) Material plane, traction vector and its components

(b) Shear stress path analysis

Figure 3.11: MCC and MRH comparison for subsurface node 2.6 mm below the loaded surface of G1 pinion tooth [19]

As highlighted by Papuga et al. [90], critical plane criteria benefit from the prediction of the shear stress amplitude via the MRH, whereas integral or shear stress intensity criteria yield better results when using the MCC. When coding both models in MATLAB, the MRH allows for a higher degree of vectorisation, ensuring a far quicker computation and higher material plane resolution. This and the fact that critical plane and integral criteria were compared in this academic study meant that the MRH was favoured for the shear stress estimation.

3.3.2 Fatigue criteria

A number of stress-based, critical plane and integral multiaxial fatigue criteria and gear specific fatigue criteria were applied to the calculated subsurface stresses and the developed material model. The studied criteria were the Sines [40], Crossland [38], Dang Van [39], Findley [24], McDiarmid [91], Matake [92], Robert [93], Fogue [93], Liu & Zenner [12], Papuga PCR [94], PCRN [95, 96], PIN [20], Annast [14], DNV [2], Hertter [6], Hertter modified [19], Oster [25] and ISO6336-4 or FVA556 I,III [1, 15, 27]. Their respective model definitions, model parameters and predicted material utilisations for a G1 pinion tooth are listed the Appendix B. The definition of the in Paper III [19] proposed BO1 and BO2 criteria are discussed in reference to the Fogue and Liu & Zenner criteria here. They are outlined in Equations 3.12 and 3.13.

$$
\begin{aligned}
D_{FO} &= \frac{\sqrt{\frac{1}{4\pi}\int_0^{2\pi}\int_0^{\pi}\left(a_{FO}\tau_a + b_{FO}\sigma_{n,a} + d_{FO}\sigma_{n,m}\right)^2 \sin(\phi)\, d\phi d\theta}}{f_{-1}} \\
b_{FO} &= f_{-1}\sqrt{\frac{15 - 3\sqrt{25 - 8(\kappa^2-3)^2}}{2}} \\
a_{FO} &= f_{-1}\sqrt{\frac{12\kappa^2 - 21 + b_{FO}^2}{2}} \\
d_{FO} &= f_{-1}\,\frac{-(3b_{FO}+2a_{FO}) + \sqrt{(3b_{FO}+2a_{FO})^2 + 45\left(4\left(\frac{f_{-1}}{f_0}\right)^2 - 1\right)}}{3}
\end{aligned}
\tag{3.12}
$$

$$
\begin{aligned}
D_{LZ} &= \frac{\sqrt{\frac{15}{8\pi}\int_0^{2\pi}\int_0^{\pi}\left(a_{LZ}\tau_a^2\left(1 + c_{LZ}\tau_m^2\right) + b_{LZ}\sigma_{n,a}^2\left(1 + d_{LZ}\sigma_{n,m}\right)\right)\sin(\phi)\, d\phi d\theta}}{f_{-1}} \\
a_{LZ} &= \frac{1}{5}\left(3\kappa^2 - 4\right) \qquad b_{LZ} = \frac{1}{5}\left(6 - 2\kappa^2\right) \\
c_{LZ} &= \frac{28}{3a_{LZ}t_0^2}\left(\left(\frac{f_{-1}}{t_0}\right)^2 - \frac{\kappa^2}{4}\right) \\
d_{LZ} &= \frac{28}{15b_{LZ}f_0^3}\left(\left(\frac{2f_{-1}}{f_0}\right)^2 - \frac{a_{LZ}c_{LZ}f_0^2}{21} - 1\right)
\end{aligned}
\tag{3.13}
$$

The performance of both criteria is plotted in Figure 3.12 for the G1 maritime gear set studied in Papers I and III [10, 19] and the test gear B1-2 from Paper IV [41]. Both gears failed from TFF. The maximum predicted contact stresses were 1359 MPa for the maritime gear and 1934 MPa for the test gear.

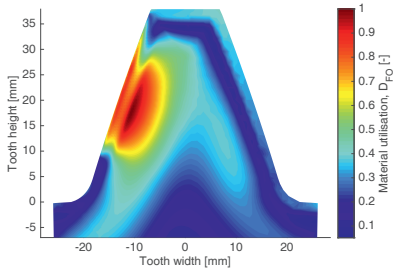

(a) G1 Fogue

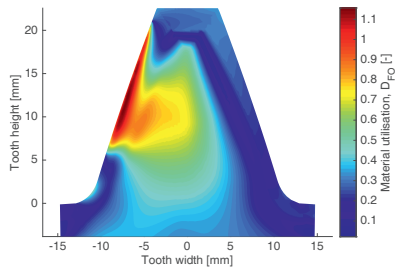

(b) B1-2 Fogue

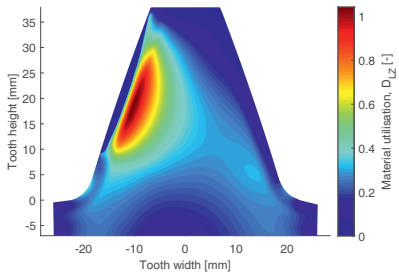

(c) G1 Liu & Zenner

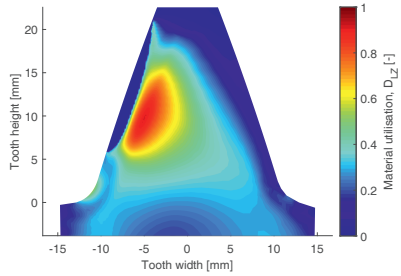

(d) B1-2 Liu & Zenner

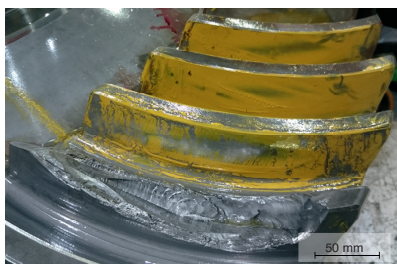

(e) G1 with TFF

(f) B1-2 with TFF

Figure 3.12: Material utilisation and failure pictures for gears G1 and B1-2 according to the Fogue and Liu & Zenner criteria [12, 93]

The Liu & Zenner criterion fails to predict a material utilisation for the outer material layer of gear sets G1 and B1-2 due to the consideration of the mean normal stress $\sigma_{n,m}$ in the form of $\sigma_{n,a}^2\,(1+\sigma_{n,m})$. The width of the layer is influenced by the magnitude of the contact stress and the implemented mean stress sensitivity M. The larger p_H or M, the wider the fatigue-free layer becomes. The Fogue criterion predicts an adequate material utilisation for G1

but estimates a surface rather than subsurface failure for B1-2. Critically, a material utilisation is predicted throughout the studied gear teeth, even for extreme contact stresses. This behaviour can be attributed to the squaring of the material plane stresses in the form of $(a_{FO}\tau_a + b_{FO}\sigma_{n,a} + d_{FO}\sigma_{n,m})^2$. Even for large, compressive mean normal stresses, the Fogue criterion will not result in negative expressions under the square root of Equation 3.12.

A majority of the stress-based multiaxial fatigue criteria studied in the context of this academic work overestimate surface failures for the gears tested in Paper IV [41]. The Liu & Zenner criterion is the only criterion that consistently underestimates surface failures due to the overestimation of $\sigma_{n,m}$ on the local material utilisation. To predict adequate surface utilisation levels even under extreme surface pressures, a modification to the Liu & Zenner's mean normal stress expression that relies on the stress' quadrature in the form of $(1 + \sigma_{n,m})^2$ is suggested. Equation 3.14 outlines the prediction of the BO criterion's equivalent stress $\sigma_{eq,BO}$ without the mean shear stress τ_m. Two different versions of the BO criterion are outlined in Paper III [19], which differ only in their consideration of τ_m.

$$\sigma_{eq,BO} = \sqrt{\frac{15}{8\pi}\int_0^{2\pi}\int_0^{\pi}\left(\left(a_{BO}\tau_a^2 + b_{BO}\sigma_{n,a}^2\right)\left(1 + c_{BO}\sigma_{n,m}\right)^2\right)\sin(\phi)\,d\phi d\theta} \tag{3.14}$$

Whereas the BO1 criterion uses the expression $\tau_a\tau_m$, the BO2 criterion relies on τ_m^2 for the consideration of the mean shear stress. Equations 3.15 and 3.16 outline both versions of the BO integral criterion along with the definition of their model parameters from the material constants f_{-1}, f_0, t_{-1} and t_0 or σ_f. The true fracture strength σ_f is estimated according to Dowling [57]. The model parameters a_{BO} and b_{BO} are identical to those of the Liu & Zenner shear stress intensity criterion. The BO1, BO2 and Liu & Zenner criteria predict the same material utilisation for mean stress-free stress states.

$$\begin{aligned}
D_{BO1} &= \frac{\sqrt{\frac{15}{8\pi}\int_0^{2\pi}\int_0^{\pi}\left(\left(a_{BO}\tau_a^2 + b_{BO}\sigma_{n,a}^2\right)\left(1 + c_{BO1}\sigma_{n,m}\right)^2 + d_{BO1}\tau_a\tau_m\right)\sin(\phi)\,d\phi d\theta}}{f_{-1}} \\
a_{BO} &= \frac{1}{5}\left(3\kappa^2 - 4\right) \quad b_{BO} = \frac{1}{5}\left(6 - 2\kappa^2\right) \\
c_{BO1} &= -\frac{3f_0(11 - 2\kappa^2)}{70C} + \sqrt{\left(\frac{3f_0(11 - 2\kappa^2)}{70C}\right)^2 + \frac{1}{C}\left(\left(\frac{2f_{-1}}{f_0}\right)^2 - 1 - \frac{\kappa^2}{3}\left(\left(\frac{2t_{-1}}{t_0}\right)^2 - 1\right)\right)} \\
d_{BO1} &= \frac{\kappa^2}{3}\left(\left(\frac{2t_{-1}}{t_0}\right)^2 - 1 - \frac{c_{BO1}^2 t_0^2}{35\kappa^2}(8 - \kappa^2)\right) \quad \text{with} \quad C = \frac{f_0^2}{84}(17 - 4\kappa^2) - \frac{t_0^2}{105}(8 - \kappa^2)
\end{aligned} \tag{3.15}$$

$$
\begin{aligned}
D_{BO2} &= \frac{\sqrt{\frac{15}{8\pi}\int_0^{2\pi}\int_0^{\pi}\left(\left(a_{BO}\tau_a^2 + b_{BO}\sigma_{n,a}^2\right)\left(1 + c_{BO2}\sigma_{n,m}\right)^2 + d_{BO2}\tau_m^2\right)\sin(\phi)\,d\phi d\theta}}{f_{-1}} \\
c_{BO2} &= -\frac{18}{5f_0}\left(\frac{11-2\kappa^2}{17-4\kappa^2}\right) + \sqrt{\left(\frac{18}{5f_0}\left(\frac{11-2\kappa^2}{17-4\kappa^2}\right)\right)^2 + \frac{84}{f_0^2(17-4\kappa^2)}\left(\left(\frac{2f_{-1}}{f_0}\right)^2 - d_{BO2} - 1\right)} \\
d_{BO2} &= \left(\frac{f_{-1}}{\sigma_f}\right)^2 \quad \text{with} \quad \sigma_f = R_m + 345MPa
\end{aligned}
\tag{3.16}
$$

A benchmarking test between the Dang Van [39], Sines [40], Crossland [38], Liu & Zenner [12], Papuga PIN [20], Hertter [6] and the proposed BO criteria was performed in Paper III [19]. The comparison focused on soft and mild steels under conventional multiaxial fatigue loading. Tested were the aforementioned criteria under static, compressive or tensile normal stresses and alternating shear stresses. The studied stress state is thereby similar to the gear stresses found in the TFF-critical material depth. Both versions of the BO criterion were on par with the highly accurate Papuga PIN [20] and Liu & Zenner [12] criteria. The BO2 criterion achieved an appreciable lower standard deviation than the BO1 criterion. The performance of both criteria is plotted in Figures 3.13 and 3.14 for the G1 and B1-2 gear sets at two different definitions of the mean stress sensitivity M. The figures on the left rely on the herein outlined moderate mean stress sensitivity $M = 7.0 \cdot 10^{-4} f_{-1} - 0.1$ and the figures on the right on an assumed lower mean stress sensitivity $M = 5.0 \cdot 10^{-4} f_{-1} - 0.1$ akin to Murakami's mean stress effect [31].

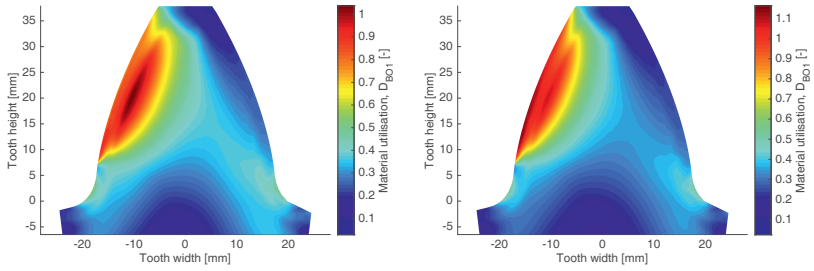

(a) BO1($M = 7.0 \cdot 10^{-4} f_{-1} - 0.1$)

(b) BO1($M = 5.0 \cdot 10^{-4} f_{-1} - 0.1$)

(c) BO2($M = 7.0 \cdot 10^{-4} f_{-1} - 0.1$)

(d) BO2($M = 5.0 \cdot 10^{-4} f_{-1} - 0.1$)

Figure 3.13: Material utilisations in G1 pinion tooth according to BO1 and BO2 criteria for moderate and low mean stress sensitivity

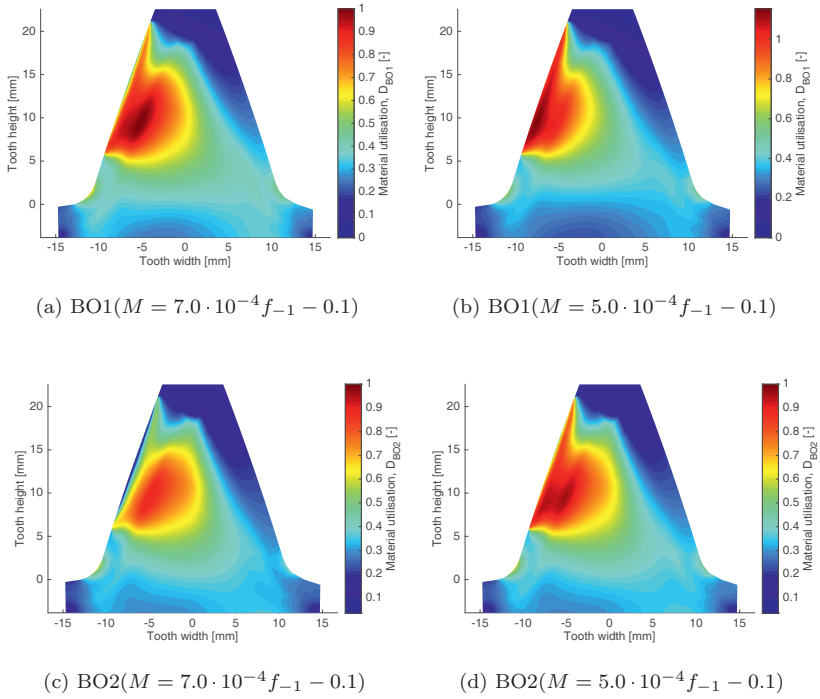

(a) BO1($M = 7.0 \cdot 10^{-4} f_{-1} - 0.1$)

(b) BO1($M = 5.0 \cdot 10^{-4} f_{-1} - 0.1$)

(c) BO2($M = 7.0 \cdot 10^{-4} f_{-1} - 0.1$)

(d) BO2($M = 5.0 \cdot 10^{-4} f_{-1} - 0.1$)

Figure 3.14: Material utilisations in B1-2 wheel tooth according to BO1 and BO2 criteria for moderate and low mean stress sensitivity

Figures 3.13 and 3.14 demonstrate the profound impact of the mean stress sensitivity on the predicted material utilisation under moderate surface stresses and elevated or test rig loading conditions. Chapter 2 outlines the variation of M for hard steels with established material models like Goodman, FKM Guideline, Murakami and Morrow [13, 31, 55, 56]. The two analysed cases in Figures 3.13 and 3.14 represent a medium and medium to low mean stress sensitivity and fall between the mentioned models. Which of the two criteria should ultimately be used for TFF or RCF strongly depends on the approximated mean stress sensitivity M. For the herein implemented moderate mean stress sensitivity, the BO1 criterion proved superior.

3.3.3 Uniaxial loading

To give further context to the developed multiaxial fatigue criteria, their behaviour under pure uniaxial loading at various mean stresses σ_m is demonstrated here. Both criteria can be simplified to yield exact expressions for the allowable uniaxial stress amplitude σ_a under constant mean stresses σ_m without the need

for a stress integration.

$$
\begin{aligned}
C_{1,2} &= 1 + \frac{6(11-2\kappa^2)}{35} c_{BO1,2}\sigma_m + \frac{17-4\kappa^2}{21}(c_{BO1,2}\sigma_m)^2 \\
\sigma_{a,BO1}(\sigma_m) &= -\frac{d_{BO1}\sigma_m}{2C_1} + \sqrt{\left(\frac{d_{BO1}\sigma_m}{2C_1}\right)^2 + \frac{f_{-1}^2}{C_1}} \\
\sigma_{a,BO2}(\sigma_m) &= \sqrt{\frac{f_{-1}^2 - d_{BO2}\sigma_m^2}{C_2}}
\end{aligned}
\tag{3.17}
$$

The model parameters c_{BO} and d_{BO} used in Equation 3.17 are determined according to the obtained fatigue constants f_{-1}, f_0 and t_{-1}, the true fracture strength σ_f and the approximated shear fatigue strength under oscillating load t_0 for the 34CrNiMo6 steel tested in Paper II [32]. The strength parameters are listed in Tables 3.1. The resulting Haigh diagrams are plotted for the uniaxial versions of the BO1 and BO2 criteria in Figure 3.15.

Table 3.1: Fatigue constants and static strength for 34CrNiMo6 2D [32]

Material	f_{-1} (MPa)	f_0 (MPa)	t_{-1} (MPa)	t_0 (MPa)	f_{-7} (MPa)	R_m (MPa)	σ_f (MPa)
34CrNiMo6	465±2	830±6	329	621	554±6	1646±18	2006

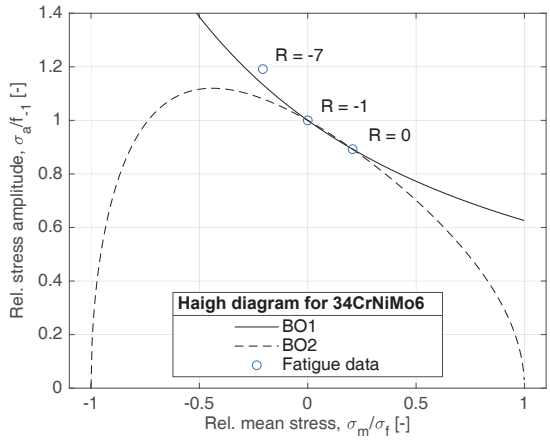

Figure 3.15: Comparison between the predicted Haigh diagrams according to BO1 and BO2 criteria and the obtained fatigue results (Paper II [32])

Whereas the BO1 criterion predicts an asymptotic trend akin to the mean

stress effect proposed by Murakami [31], the allowable stress amplitude estimated by the BO2 criterion appears like an idealised Haigh diagram. Intuitively, a reduction in σ_a should occur for very large, compressive or tensile mean stresses. Compared to the reported results for the 34CrNiMo6 steel at $R = -7, -1$ and 0, the BO1 criterion achieves a closer match. Additional fatigue testing at large, compressive or tensile mean stresses is necessary to validate either criterion.

The performed fatigue tests in Paper II [32] did not include testing of the shear fatigue strength under oscillating load t_0. The material constant was instead approximated through the equation proposed by Liu & Zenner [12].

$$\frac{4t_{-1}}{t_0} - \frac{2f_{-1}}{f_0} = 1 \tag{3.18}$$

Similar to Equation 3.17, both criteria can be modified to yield the allowable shear stress amplitude τ_a for a constant shear mean stress τ_m under pure shear. The correlation for the BO2 criterion is given in Equation 3.19.

$$\tau_a(\tau_m) = \sqrt{\frac{f_1^2 - 3d_{BO2}\tau_m^2}{\kappa^2 + \frac{4}{35}c_{BO2}^2\tau_m^2(8-\kappa^2)}} \tag{3.19}$$

An expression for t_0 can readily be derived from Equation 3.19 for $\tau_a = \tau_m = t_0/2$, yielding a shear fatigue strength of 631.5 MPa compared to 621 MPa according Equation 3.18. Further studies are necessary to compare the respective accuracies of Equations 3.18 and 3.19 in predicting t_0.

3.3.4 Critical plane study

This section compares the fatigue damage parameters $f(\phi, \theta)$ of the Dang Van [39], Liu & Zenner [12] and BO1 multiaxial fatigue criteria. Studied are two nodes 0.48 and 2.87 mm below the loaded flank of the aforementioned G1 pinion tooth. The comparison is intended to yield a clear understanding of the criteria-specific, critical material planes in which crack initiation is likely to occur.

To clarify the analysed load distribution, geometry and nodal positions for this study, Figure 3.16 plots the Hertzian stress p_H and equivalent radius of curvature ρ_{eq} in the gear's mean cross-section and the resulting maximum von Mises equivalent stress over all contact positions. Node 1's position in the pinion dedendum and a shallow depth of 0.48 mm places it in the pitting-prone part of the gear tooth, whereas node 2's position further up the tooth and in a depth of 2.87 mm represents the TFF-prone material layer of the gear tooth.

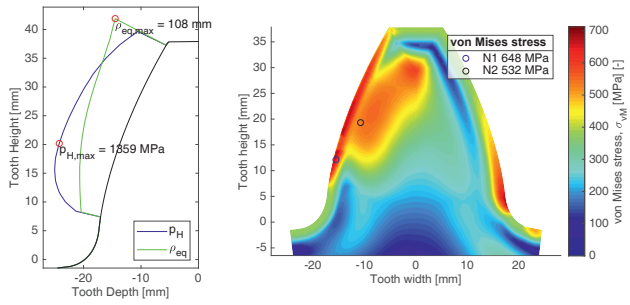

(a) Gear loading (b) von Mises equivalent stress σ_{vM}

Figure 3.16: Specification of load, geometry and nodal positions for critical plane study on G1 pinion tooth

Figures 3.17 and 3.18 plot the normal and shear stress amplitudes and mean stresses for nodes 1 and 2 as functions of ϕ and θ. Highlighted are their respective maxima and the material planes or normal vectors $n_{x'}$ in which they occur. For example the maximum normal stress amplitude $\sigma_{n,a}$ for node 1 of 570.3 MPa occurs for $n_{x'}(\phi = 90°, \theta = 146°)$.

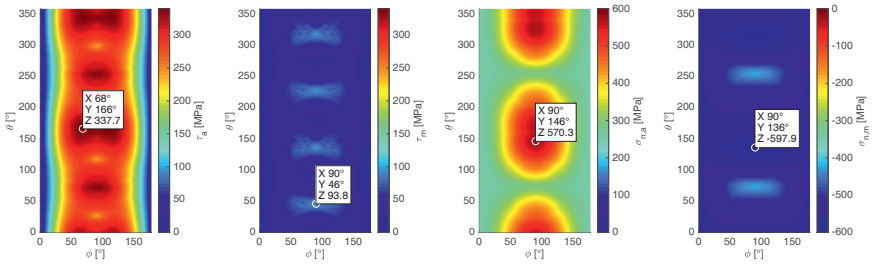

(a) $\tau_a(\phi, \theta)$ (b) $\tau_m(\phi, \theta)$ (c) $\sigma_{n,a}(\phi, \theta)$ (d) $\sigma_{n,m}(\phi, \theta)$

Figure 3.17: Node 1: Stress components for all material planes

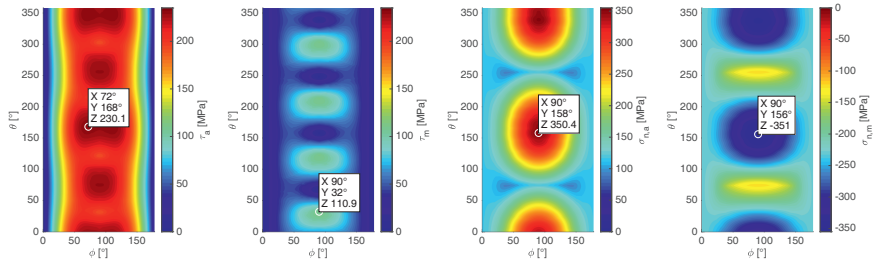

(a) $\tau_a(\phi, \theta)$ (b) $\tau_m(\phi, \theta)$ (c) $\sigma_{n,a}(\phi, \theta)$ (d) $\sigma_{n,m}(\phi, \theta)$

Figure 3.18: Node 2: Stress components for all material planes

The symmetry of the stress fields is immediately apparent. For the studied 2D plane strain state, essentially, only a quarter of the range of possible material planes need to be analysed. Considering the computationally expensive prediction of τ_a, this simplifies the stress analysis dramatically. In the developed MATLAB code, the *flip array* function was subsequently utilised to populate the not assessed material planes.

For nodes 1 and 2, the pressure angles α of the nearest surface nodes are 13.5 and 21.5° respectively. The surface-perpendicular normal vectors are thereby $n'_{x1}(90°, 166.5°)$ and $n'_{x2}(90°, 158.5°)$. Focusing on node 2, the maximum shear stress amplitude τ_a of 230.1 MPa is predicted for $n'_x(72°, 168°)$ in an almost surface parallel material plane ($\Delta\phi = 18°$ and $\Delta\theta = 9.5°$). A TFF crack initiation underneath the loaded flank in approximately surface parallel material planes as been discussed throughout this academic work. Observations of the orientation of early-stage TFF failures are given in Chapters 1 and 4 and Figures 1.7b and 4.1. The shear stress difference between $\tau_a(90°, 158.5°)$ and $\tau_a(72°, 168°)$ in node 2 is less than 2 %.

For critical plane criteria like the Dang Van criterion [39], the fatigue damage parameter is maximised and compared against the fatigue strength. The angles in which $f(\phi, \theta)$ reaches its maximum define the material plane in which crack initiation is likely to occur. Equation 3.20 defines the fatigue damage parameter $f_{DV}(\phi, \theta)$.

$$\begin{aligned} f_{DV}(\phi, \theta) &= a_{DV}\tau_a(\phi, \theta) + b_{DV}\sigma_{hyd,max} \\ a_{DV} &= \frac{f_{-1}}{t_{-1}} \quad b_{DV} = 3 - 3/2\,\frac{f_{-1}}{t_{-1}} \end{aligned} \tag{3.20}$$

The Liu & Zenner and BO1 shear stress intensity or integral criteria do not calculate a plane specific damage parameter. Therefore, the integration over all material planes is replaced with the summation of all plane instances, with each instance defining a local fatigue damage parameter $f(\phi_i, \theta_j)$. The Liu & Zenner fatigue damage parameter is outlined in Equation 3.21 and the

BO1 parameter in Equation 3.22. The unit and magnitude of these damage parameters is different to that of the Dang Van criterion.

$$\sigma_{eq,LZ} = \sqrt{\frac{15}{8\pi} \sum_{i=1}^{m} \sum_{j=1}^{n} \Delta\phi \, \Delta\theta \, f_{LZ}(\phi_i, \theta_j) \, \sin(\phi_i)} \tag{3.21}$$
$$f_{LZ}(\phi_i, \theta_j) = a_{LZ}\tau_a^2 \left(1 + c_{LZ}\tau_m\right)^2 + b_{LZ}\sigma_{n,a}^2 \left(1 + d_{LZ}\sigma_{n,m}\right)$$

$$\sigma_{eq,BO1} = \sqrt{\frac{15}{8\pi} \sum_{i=1}^{m} \sum_{j=1}^{n} \Delta\phi \, \Delta\theta \, f_{BO1}(\phi_i, \theta_j) \, \sin(\phi_i)} \tag{3.22}$$
$$f_{BO1}(\phi_i, \theta_j) = \left(a_{BO}\tau_a^2 + b_{BO}\sigma_{n,a}^2\right) \left(1 + c_{BO1}\sigma_{n,m}\right)^2 + d_{BO1}\tau_a\tau_m$$

As the maximum hydrostatic stress $\sigma_{hyd,max}$ is independent of the Euler angles ϕ and θ, the orientation of $f_{DV,max}$ depends solely on τ_a. Crack initiation is thereby predicted for $n'_{x1}(68°, 166°)$ and $n'_{x2}(72°, 168°)$ according to the Dang Van criterion. Figures 3.19 and 3.20 plot the fatigue damage parameters for the Dang Van, Liu & Zenner and BO1 criteria for nodes 1 and 2.

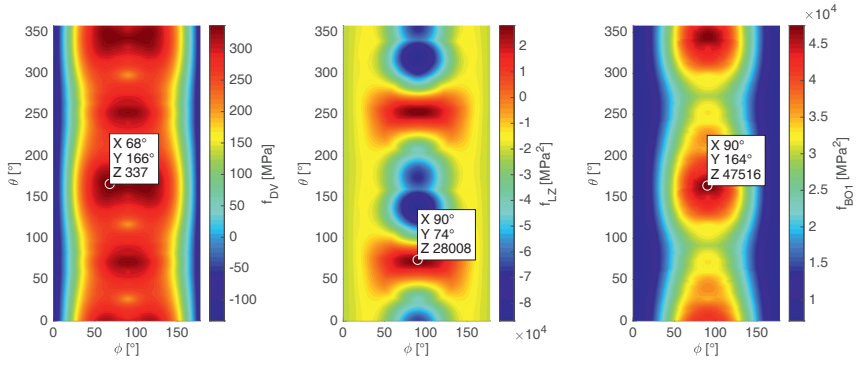

(a) Dang Van (b) Liu & Zenner (c) BO1

Figure 3.19: Node 1: Fatigue damage parameters

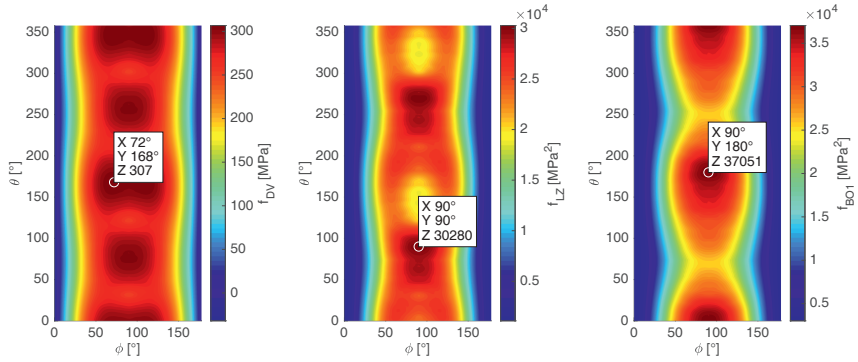

(a) Dang Van (b) Liu & Zenner (c) BO1

Figure 3.20: Node 2: Fatigue damage parameters

Whereas the Dang Van and BO1 criteria predict similar plane orientations to be critical for both nodes, the Liu & Zenner criterion predicts a normal vector perpendicular to that of the BO1 criterion. For both nodes, the Liu & Zenner criterion fails to predict meaningful damage parameters for planes with large normal stress amplitudes $\sigma_{n,a}$ in the presence of large compressive mean stresses $\sigma_{n,m}$. The fatigue damage parameter f_{LZ} effectively visualises the shortcomings of the Liu & Zenner criterion under RCF or Hertzian stresses. For node 1, negative values for f_{LZ} are predicted in the presence of large $\sigma_{n,a}$ and $\sigma_{n,m}$ stresses.

Comparing the Dang Van and BO1 criteria, similar values for θ are calculated for both nodes and both criteria. The consideration of $\sigma_{n,a}$ and $\sigma_{n,m}$ in the BO1 criterion move the predicted maximum fatigue damage parameter into the $\phi = 90°$ plane. Relying on the results published in Paper III [19], the BO1 criterion and its predicted material plane orientations are favoured for three reasons.

- Maritime bevel gears on azimuthing thrusters are only loaded at moderate loads for most of their service life. In a measurement campaign spanning eight vessels over a 2 to 5-year interval, gear loads equivalent to 60 to 80 % of the nominal design load were measured (based on the ISO6336-5 standard's equivalent load [97]). According to the study of gear set G1 in Paper III, the Dang Van criterion predicts a 34% lower material utilisation than the BO1 criterion, making a crack initiation under the measured, modest loads unlikely.

- The performed benchmarking tests in Paper III of both criteria under alternating shear stresses and static normal stresses underline the accuracy of the BO1 criterion, yielding a lower standard deviation and an average failure index closer to 0 than the Dang Van criterion.

- A large number of crack-like indications have been identified and documented through PAUT during service intervals on G1 and G2 gears. The depth of the BO1's maximum material utilisation aligns well with the measured depth of these indications. Paper III plots the Weibull distributions of the documented crack-like indications and compares them to the BO1's material utilisation in a surface-perpendicular path that intersects the maximum utilisation.

Due to its comprehensibility and widespread use for RCF, the Dang Van criterion is investigated further in Chapter 4 for its applicability to a standardised TFF approach.

Chapter 4

Standardised approach

This section revisits the in Paper I [10] presented simplified subsurface fatigue criterion and implements an improved stress model alongside the findings from Papers II, III and IV [19, 32, 41]. The abbreviation Hs is chosen for the criterion in reference to the ISO10300's pitting safety factor [21] as the same contact point is studied and due to the subsurface nature of the failure mode. Targeted is an analytical and standardisable assessment of the gear failure mode tooth flank fracture for a given gear design and loading condition. All numerical calculations and the computationally expensive prediction of the shear stress amplitude are foregone in favour of a purely analytical prediction.

This section presents and compares the predicted stresses, strengths and material utilisation of the Hs criterion to the BO1 criterion's numerical results for the mean cross-section of gear set G1 studied in Papers I and III [10, 19]. The fatigue analyses of gear sets G0, G2 and B2-1 are included in Chapter 4.4.1. The Hs criterion can similarly be applied to all contact points between meshing pinion and wheel teeth but requires ideally a numerical calculation of the local maximum hydrostatic stress $\sigma_{hyd,max}$. The Hs criterion is an interpretation of the Dang Van, critical plane, multiaxial fatigue criterion and simplifies the calculation of the equivalent stress (the numerator in Equation 4.1).

$$\begin{aligned} D_{DV} &= \frac{\max\limits_{\theta,\phi}\left(a_{DV}(\tau_a(\theta,\phi)) + b_{DV}\sigma_{hyd,max}\right)}{f_{-1}} \\ a_{DV} &= \frac{f_{-1}}{t_{-1}} \qquad b_{DV} = 3 - 3/2\frac{f_{-1}}{t_{-1}} \end{aligned} \tag{4.1}$$

The Dang Van criterion [39] is a favoured multiaxial fatigue criterion for the study and fatigue analysis of RCF or Hertzian contacts [98–100]. It assumes local plasticity in the mesoscale, even if the material is only loaded elastically in the macroscale. The version of the Dang Van criterion studied in this academic work relies on the MRH derived shear stress amplitude and maximum hydrostatic stress per load cycle. As shown by Papuga [96], this interpretation

of the Dang Van criterion yields a superior result accuracy when studying non-proportional loading like the Hertzian contact in gears.
The Dang Van criterion calculates an equivalent stress from the maximum of the shear stress amplitude over all material planes (Euler angles θ and ϕ) and the maximum of the hydrostatic stress and compares said stress to the uniaxial fatigue strength under alternating load f_{-1}. Its model parameters a_{DV} and b_{DV} are derived from material constants, typically f_{-1} and t_{-1}, the uniaxial and shear fatigue strength under alternating load.

4.1 Maximum shear stress amplitude

During 5-year service intervals, marine bevel gears are inspected by means of PAUT. If subsurface cracks are detected, the gears are scrapped. Failure investigations of these gears suggest that early-stage TFF cracks are orientated parallel to the load-carrying flank in a depth of 1 to 2 times the case hardening depth CHD [10, 11]. Figure 4.1 exemplifies two early-stage, surface-parallel TFF cracks (9° and 14° to the flank) in a depth of 2.6 and 3.3 mm, respectively 0.45 and 0.65 mm in size. Both images belong to the same G1 gear wheel that featured subsurface crack-like indications on 25 wheel teeth [11]. Visible are furthermore the indentations from the HV1 and HV10 hardness measurements.

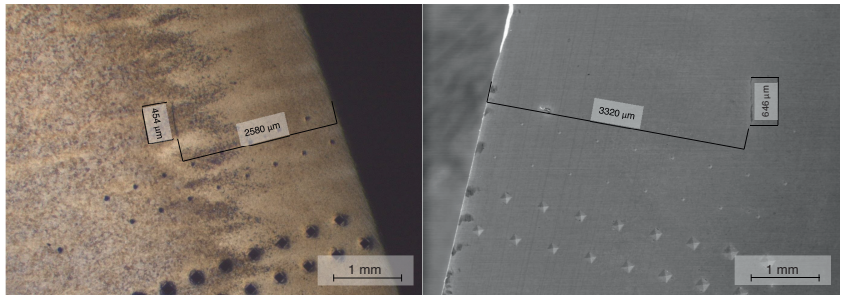

(a) TFF 2.6 mm deep and 0.45 mm large (b) TFF 3.3 mm deep and 0.65 mm large (SEM image)

Figure 4.1: Early-stage TFF cracks on G1 wheel teeth [11]

This finding advocates that the iteration over all material planes to identify the maximum shear stress amplitude could be forgone, favouring the exclusive study of surface parallel material planes. The hypothesis is supported by the comparison of the maximum of the MRH derived shear stress amplitude over all material planes with the orthogonal shear stress amplitude for surface parallel planes. For the in Papers I and III [10, 19] studied gear set G1, the relative difference between both shear stress amplitudes is less than 3% in the relevant material depth of 2 to 7 mm. More significant differences occur towards the load-carrying flank, where the orthogonal shear stress amplitude fails to capture the

frictional stresses between the meshing gear teeth.

The in Paper I [10] adopted equation for the calculation of the orthogonal shear stress amplitude $\tau_{xy,a}$ remains unchanged (see Equation 4.2 according to [2]). It relies on the ISO10300-2's [21] Hertzian contact pressure σ_{HB1} and the half Hertzian contact width b_H for its calculation. The parameter x describes the depth underneath the tooth flank perpendicular to the studied contact point MB, ρ_{eq} the radius of relative curvature vertical to the contact line of the virtual cylindrical gear, ν the Poisson ratio and E the Young's modulus. The ISO's mid-zone factor Z_{MB} and bevel gear factor Z_K [4, 21] need to be considered to adapt the contact pressure from the pitch point P to the design point MB and to study the true Hertzian contact stress in the engagement.

$$\tau_{xy,a}(x) = 0.25 \frac{\sigma_{HB1}}{Z_K} \cos\left(\frac{\frac{x}{b_H} - 0.5}{\frac{x}{b_H} + 0.5} \frac{\pi}{2} \right) \tag{4.2}$$

$$b_H = 4 \frac{\sigma_{HB1}\, \rho_{eq}}{Z_K\, Z_{MB}^2} \frac{1-\nu^2}{E}$$

Figure 4.2a plots the MRH-derived maximum shear stress amplitude for the mean cross-section of a G1 pinion tooth and compares it in Figure 4.2b along path P1 to the orthogonal shear stress amplitude according to Equation 4.2. P1 defines a surface perpendicular path starting in MB. The observable match between the computational expensive MRH-derived shear stress amplitude and the simple orthogonal shear stress amplitude forms the foundation for the Hs criterion. For the calculation of $\tau_{xy,a}$, the ISO's mounting factor $K_{H\beta-be}$ and thereby the face load factor for contact stress $K_{H\beta}$ were adjusted to yield the same surface stresses in MB between both approaches.

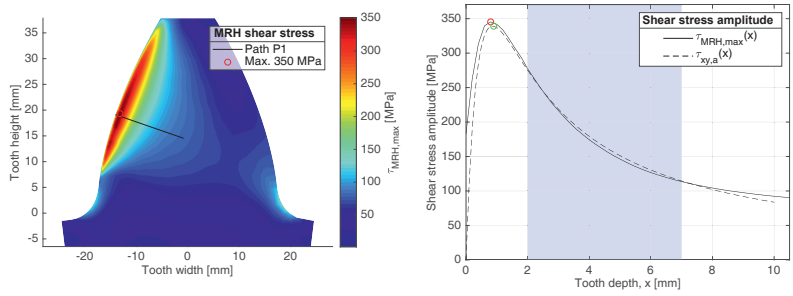

(a) Mean cross-section of G1 pinion tooth (b) Path P1

Figure 4.2: MRH derived maximum shear stress amplitude compared to orthogonal shear stress amplitude

The observable surface-near stress differences occur due to the omission of the frictional surface stresses in the analytical approach. For a subsurface fatigue study and gear typical friction coefficients, frictional stresses can be omitted.

4.2 Maximum hydrostatic stress

The second stress component needed for the calculation of the Dang Van equivalent stress is the maximum hydrostatic stress $\sigma_{hyd,max}$. Subsurface stresses in gears are dictated by the Hertzian contact between the meshing gear teeth. Assuming a 2D plane strain stress state and a line contact between the contacting teeth, the resulting compressive subsurface stresses can readily be approximated from Hertzian theory (see Equation 3.1 in Chapter 3). These compressive Hertzian stresses are inconsequential to the maximum hydrostatic stress. Critical are instead the static residual stress and the out-of-phase bending stress.

The approximation of the maximum hydrostatic stress profile as a result of the static residual stresses is outlined in Paper I [10]. It relies on the residual stress model by Lang [28] and the hardness approximation by Thomas [43]. Contrary to the advanced subsurface fatigue calculation in Paper III [19], only the compressive residual stresses are considered in the Hs criterion. The iterative estimation of the tensile residual stresses in the tooth core is foregone. With TFF damages typically initiating in the case or case/core interface, neglecting the tensile residual stresses in the core is deemed appropriate for a standardised approach. For gears with core hardnesses over 400 HV, Lang's residual stress model yields diminishing compressive residual stresses in the carburised case, leading to an overestimation of surface- rather than subsurface-initiated fatigue for high surface stresses. In those cases, the hardness and residual stress profiles should be modelled with an assumed 400 HV core hardness. The maximum hydrostatic stress as a result of the static residual stresses along path P1 or any surface perpendicular path can readily be approximated to $2/3\,\sigma_{res}$. Tangential and longitudinal residual stresses in a case hardened gear tooth are assumed to be equal and normal residual stresses to be zero. The parameters $HV(x)$ and HV_c in Equation 4.3 specify the local hardness along path P1 and the tooth's core hardness.

$$\begin{aligned} \sigma_{res}(x) &= -5/4\,(HV(x) - HV_c) \qquad \text{for} \quad HV(x) - HV_c \leq 300 \\ \sigma_{res}(x) &= 2/7\,(HV(x) - HV_c) - 460 \quad \text{else} \\ \max_t(\sigma_{hyd}(x,t)) &= \text{tr}\begin{pmatrix} 0 & 0 & 0 \\ 0 & \sigma_{res}(x) & 0 \\ 0 & 0 & \sigma_{res}(x) \end{pmatrix} = 2/3\,\sigma_{res}(x) \end{aligned} \tag{4.3}$$

Figure 4.3a plots the stress difference between the maximum hydrostatic stress $\Delta\sigma_{hyd,max}$ for gear set G1 considering (i) the superposition of all static and dynamic stress components based on an accurate numerical simulation and (ii) the maximum hydrostatic stress as a function of the residual stress as per

Equation 4.3. Tensile residual stresses are disregarded in both cases. The stress difference along path P1 is plotted in Figure 4.3b.

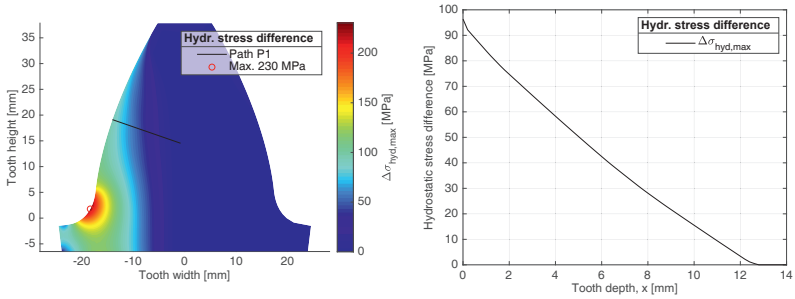

(a) Mean cross-section of G1 pinion tooth (b) Path P1

Figure 4.3: Hydrostatic stress difference between numerical and analytical calculation

A nearly linear stress difference along path P1 is observable, indicative of the missing bending stress component in Equation 4.3. For the path P1, only the last contact position in tooth profile direction is responsible for the plotted stress difference, allowing for the simplified hydrostatic and bending stress calculation according to the ISO10300-3 [80]. The ISO's tooth root breakage model relies on the beam theory for short, elastically deformed beams and simplifies the acting bending, normal and shear stresses to a study of the bending stress as a result of the tangential force and resulting bending moment. Even though Figure 4.3a demonstrates the influence of the compressive normal stress on the bending stress distribution (i.e. the bending or hydrostatic stress does not transition in the neutral axis from tension to compression), the ISO's simplified bending stress model is adapted. A numerical calculation of the maximum hydrostatic stress is recommended if the Hs criterion is applied to the TFF study of an entire gear tooth. Equation 4.4 outlines the simplified bending stress model to calculate the maximum hydrostatic stress below the design point MB. Negative bending stresses are ignored as the maximum hydrostatic stress for the tooth interior shall be ≥ 0 MPa. The stress in tooth-lengthwise direction σ_z relies on the plane strain assumption.

$$\begin{aligned}\max_t(\sigma_{hyd}(x,t)) &= 2/3\,\sigma_{res}(x) + \operatorname{tr}\begin{pmatrix}0 & 0 & 0\\ 0 & \sigma_b(x) & 0\\ 0 & 0 & \nu\sigma_b(x)\end{pmatrix} \\ &= 2/3\,\sigma_{res}(x) + \frac{1+\nu}{3}\sigma_b(x) \quad \text{with} \quad \sigma_b(x) \geq 0\end{aligned} \tag{4.4}$$

To allow for a simplified calculation of the bending stress distribution, not the bending stress along the surface-perpendicular path P1 but a horizontal path

is proposed. This allows for the calculation of the bending stress from a constant rather than height-dependent tooth width. The rotation of the stress matrix from the global to the local, contact-specific coordinate system does not affect the hydrostatic stress as it remains constant under coordinate transformation. For the simplified model, the local pressure angle in the design point α_{MB} and its effect on the depth of the acting bending stresses is similarly disregarded.

The first step in the calculation of the bending stress σ_b is the prediction of the position of MB along the line of action in the transverse tooth section. Keeping with the definition of the ISO's mid-zone factor Z_{MB} [21], the diameter of the design point d_{vMB} is defined in reference to the base diameter of the virtual cylindrical gear d_{vb}, the tip diameter of the virtual cylindrical gear d_{va} and the number of teeth of the virtual cylindrical gear z_v. Equation 4.5 and the following expressions are defined for the pinion but apply equally to the wheel by replacing the index 1 with 2. The variable F_1 is defined according to the ISO10300-2 and moves the design point along the line of action. Similarly, all herein utilised gear geometries, angles and factors that are not outlined in the following equations, rely on the ISO10300 for their prediction.

$$d_{vMB1} = \sqrt{\left(\sqrt{\left(\frac{d_{va1}}{d_{vba1}}\right)^2 - 1} - F_1 \frac{\pi}{z_{v1}}\right)^2 + 1}\, d_{vb1} \tag{4.5}$$

For the calculation of tooth width in the design point s_{nMB}, the transverse diameter d_{vMB} needs to be translated into its normal cross-section equivalent d_{vMBn}. For that purpose, the ISO's root diameter of the virtual gear d_{vf} [4], the mean dedendum h_{fm} and the reference diameter of the virtual cylindrical gear in the normal cross-section d_{vn} are used.

$$\begin{aligned} h_{MB1} &= 0.5\,(d_{vMB1} - d_{vf1}) \\ d_{vMBn1} &= d_{vn1} + 2\,(h_{MB1} - h_{fm1}) \end{aligned} \tag{4.6}$$

With d_{vMBn} established, the local pressure angle α_{MB}, its involute $inv(\alpha_{MB})$ and subsequently the local tooth width s_{MBn} can be approximated from the assumed involute tooth profile. The parameter α_n specifies the generated pressure angle and s_{mn} the tooth width in the pitch point P.

$$\begin{aligned} \alpha_{MB1} &= \arccos\left(\frac{d_{vbn1}}{d_{vMBn1}}\right) \\ inv(\alpha_{MB1}) &= \tan(\alpha_{MB1}) - \alpha_{MB1} \\ s_{MBn1} &= d_{vMBn1}\left(\frac{s_{mn1}}{d_{vn1}} + inv(\alpha_n) - inv(\alpha_{MB1})\right) \end{aligned} \tag{4.7}$$

The bending moment arm h_{MBa} utilises the intersection between the surface-perpendicular force vector in the tooth tip and the gear tooth's neutral axis in

the diameter d_{Fan}. The diameter prediction relies on the auxiliary angle for the tooth form and tooth correction factor γ_a, the load application angle at the tooth tip of the virtual cylindrical gear α_{Fan} and the tip diameter of the virtual cylindrical gear in the normal section d_{van}.

$$\begin{aligned} d_{Fan1} &= d_{van1}\left(\cos(\gamma_{a1}) - \sin(\gamma_{a1})\tan(\alpha_{Fan1})\right) \\ h_{MBa1} &= 0.5\left(d_{Fan1} - d_{vMBn1}\right) \end{aligned} \tag{4.8}$$

Following the ISO10300-3 [80], the tooth form factor in the design point Y_{MB} can be calculated along with the maximum bending stress $\sigma_{MB,B1}$. The required tooth geometries and load factors are the mean module m_{mn}, the load application angle at the tooth tip of the virtual cylindrical gear α_{Fan}, the generated pressure angle α_n, the nominal tangential force of the virtual cylindrical gear F_{vmt}, the face width of the virtual cylindrical gear b_v, the contact ratio factor for bending Y_ε, the bevel spiral angle factor Y_{BS}, the load sharing factor Y_{LS}, the application factor K_A, the dynamic factor K_v, the face load factor for bending stress $K_{F\beta}$ and the transverse load factor for bending stress $K_{F\alpha}$ (consult ISO10300 for their calculation).

$$\begin{aligned} Y_{MB1} &= \frac{6\dfrac{h_{MBa1}}{m_{mn}}\cos(\alpha_{Fan1})}{\left(\dfrac{s_{MBn1}}{m_{mn}}\right)^2\cos(\alpha_n)} \\ \sigma_{MB0,B1} &= \frac{F_{vmt}}{b_v m_{mn}}\, Y_{MB1} Y_\varepsilon Y_{BS} Y_{LS} \\ \sigma_{MB,B1} &= \sigma_{MB0,B1}\, K_A K_v K_{F\beta} K_{F\alpha} \end{aligned} \tag{4.9}$$

To calculate the bending stress distribution along the studied path P1, the following correlation is applied.

$$\sigma_b(x) = \sigma_{MB,B1}\left(1 - \frac{2x}{s_{MBn1}}\right) \tag{4.10}$$

With both the residual and bending stresses defined, the maximum hydrostatic stress along path P1 can suitably be approximated. Figure 4.4a plots the numerically calculated maximum hydrostatic stresses for the mean cross-section of G1 and compares it in Figure 4.4b to the analytically calculated maximum hydrostatic stress along with P1.

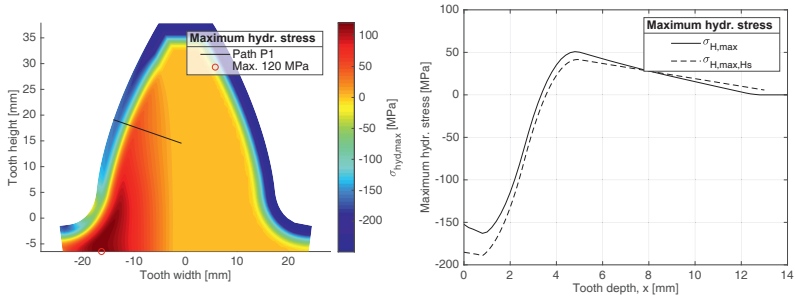

(a) Mean cross-section of G1 pinion tooth (b) Path P1

Figure 4.4: Maximum hydrostatic stress according to numerical and analytical model

The analytical maximum hydrostatic stress along P1 matches the numerical prediction accurately. For most of the carburised case, the analytical model slightly underestimates the bending stresses, resulting in lower maximum hydrostatic stresses than for the numerical model. As highlighted previously, the face load factor $K_{H\beta}$ was adjusted to yield the same contact stress in MB between the numerical and analytical model and thereby the same subsurface shear stress profile. The resulting bending stress prediction in MB and the tooth root according to the ISO10300-3 is significantly lower than predicted according to the LTCA [18]. The LTCA predicts a maximum tooth root stress of 452 MPa compared to the ISO's 340 MPa. This 30 % difference is similarly observable in the hydrostatic stress plot in Figure 4.4b. This suggests that the predicted hydrostatic stress differences are not due to the inaccuracy of the proposed analytical model but due to the magnitude of the predicted normal force in the tooth tip between the LTCA and ISO10300-3.

The presented consideration of the bending stress in the gear tooth fatigue analysis might also give insight into the failure mode pitting and its predominantly occurrence in the pinion dedendum. As per the ISO10300 and FVA411 [9, 21], the negative sliding between meshing gear teeth (ISO10300 Annex A, slip factor Z_S) is stated as the reason for the higher pitting likelihood below the pinion's pitch line. Alternatively, the presence of the progressively increasing bending stress towards the pinion's tooth root can be seen as an explanation. The equivalent radius of curvature increases from the pinion's tooth root to the tooth tip, resulting in elevated contact stresses in the pinion's dedendum. (see FVA516 [7] load factor Z_{AE}). The higher contact stress equates to a higher shear stress amplitude in combination with a larger maximum hydrostatic stress due to the bending stresses. In the matching wheel addendum, the lack of bending results in a lower material utilisation, despite the same acting shear stress amplitude in the same shallow material depth.
Chapter 4.5 details the resulting material utilisations for pinion and wheel teeth

of gear sets G1 and G0 according to the Hs criterion based on a numerically derived maximum hydrostatic stress in the gears' mean cross-section. The predicted pitting failure locations and probabilities align accurately with reported failures [9, 101].

4.3 Material model

The material model for the Hs criterion relies on the performed fatigue tests and derived material constants in Paper II [32], the developed influence factors in Papers III and IV [19, 41] and the alignment of the predicted material utilisations between the BO1 and Hs criteria.

4.3.1 Hardness and residual stress

To predict the local material properties, a hardness profile as a result of the case hardening process needs to be defined. The input parameters surface hardness HV_s, core hardness HV_c and case hardening depth CHD need to be specified. As shown in Papers I, III and IV [10, 19, 41], especially the hardness gradient in the transition zone from case to core is critical for an accurate subsurface fatigue prediction. Uniquely suited to capture the differences between small and large gears is the hardness model by Thomas [43]. It describes the hardness profile as two-second order polynomials connected in the case hardening depth CHD (i.e. the depth in which the hardness reaches 550 HV). The parameter $x_{HV,max}$ that describes the depth of the hardness peak in Thomas's model is redefined to capture the gradient in the transition point between both polynomials. The larger $x_{HV,max}$, the steeper the transition from case to core and the faster the hardness and compressive residual stresses depreciate.

Equation 2.1 in Chapter 2.1 defines the hardness model by Thomas [43] and Equation 4.3 the residual stress model by Lang [28]. The Hs criterion aligns itself with the ISO6336-4 technical report for the TFF prediction in cylindrical gears [1] by relying on the same residual stress and hardness model. The ISO6336-4 lists also Lang's hardness model, which is not favoured for the Hs criterion as it fails to intersect the specified CHD and features a low hardness gradient only applicable to small gears.

4.3.2 Local fatigue strength

Equation 4.11 outlines the translation of the predicted hardness profile into the local fatigue constants. Whereas four material parameters are outlined and defined in Paper II [32], only the uniaxial and shear fatigue strength under alternating load (f_{-1} and t_{-1}) need to be specified for Hs criterion. The model parameters a_{Hs} and b_{Hs} are identical to those of the Dang Van criterion. The performed benchmarking test in Paper III [19] compared two definitions of the Dang Van model parameters, yielding the highest result accuracy when relying on f_{-1} and t_{-1}.

While the definition of the fatigue ratio κ ($\kappa = f_{-1}/t_{-1}$) is implemented as outlined in Paper II [32], the definition of f_{-1} is altered. A constant ratio of 0.8 between the local hardness HV and f_{-1} is chosen to align the predicted material utilisations of the BO1 and Hs criteria. Equation 4.11 defines the local fatigue constants and the size and lifetime factors K_X and K_{NT} according to Papers III and IV [19, 41].

$$\begin{aligned} f_{-1}(x) &= 0.8\,HV(x) \\ t_{-1}(x) &= \frac{f_{-1}(x)}{\kappa(x)} \quad \text{with} \quad \kappa(x) = -5 \cdot 10^{-4} HV(x) + \sqrt{3} \\ f_{-1,K}(x) &= f_{-1}(x)\, K_X K_{NT} f_{xK} \\ K_X &= 1.05 - 0.01\, m_{mn} \quad \text{with} \quad 0.87 \leq K_X \leq 1 \\ K_{NT} &= \exp \frac{\ln(N_f) - 10.42}{-2.73} + 0.89 \quad \text{with} \quad K_{NT} \leq 1.6 \end{aligned} \tag{4.11}$$

The size factor K_X is based on the comparison of the highly stressed volume in the tested uniaxial fatigue specimen and various gear sizes (sized m_{mn} 2 to 25 mm) and the obtained standard deviation of 4 % during uniaxial fatigue testing. By converting K_X to rely on the mean normal module m_{mn}, the effect of the applied load and the number of teeth is disregarded. The suggested correlation achieves a very close match for the studied gears, is simple in its application and identical to the size factor used in the ISO10300-3 for the prediction of the tooth root strength [80]. The derivation of K_X according to the weakest link theory is outlined in Appendix C.

The lifetime factor K_{NT} is based on the gear test results outlined in Paper IV [41] and relies on the number of load cycles on either pinion or wheel N_f for its prediction. K_{NT} lies between the ISO's pitting and tooth root breakage lifetime factors and outlines a continuous degradation of the material strength in the very high cycle fatigue regime (i.e. $N_f \geq 10^7$ load cycles). Depending on what failure probability is studied, a conversion factor f_{xK} based on the obtained standard deviation of 4 % can be defined. For a 1 % fatigue strength, f_{xK} can be set to 0.91. Unless specifically stated, all calculations in this section omit the conversion factor and utilise thereby the average fatigue strength.

As shown in Paper II [32], a constant fatigue ratio of $\kappa = \sqrt{3}$ as assumed in the FKM guideline [13] and the von Mises criterion. It is only applicable for highly ductile steels and decreases considerably as a function of the steel's hardness. The fatigue ratio $\kappa(HV)$ thereby captures the transition from a ductile material behaviour in the soft core of the gear tooth to a more brittle behaviour in the hard case. For the Dang Van and Hs criteria, this translates to a large, positive effect of the compressive residual stresses in the case and a diminished, negative effect of potential tensile residual stresses in the core (model parameter b_{Hs}). Similarly, the ductile core is more susceptible to the acting shear stress amplitude than the case (model parameter a_{Hs}). Both model parameters for

the Hs criterion are given in Equations 4.1 and 4.12 and illustrated in Figure 4.5b along path P1.

Figure 4.5a plots local fatigue strength $f_{-1,K,BO}$ as defined in Paper III [19] for the mean pinion cross-section of G1 and compares it in Figure 4.5b with the local fatigue strength $f_{-1,K,Hs}$ according to Equation 4.11 along path P1. Especially for the core, the implemented material model underestimates the local fatigue strength when compared with the measurement results in Paper II [32]. In order to achieve the same subsurface utilisation levels with the BO1 and Hs criteria, $f_{-1,K,Hs}$ had to be adapted.

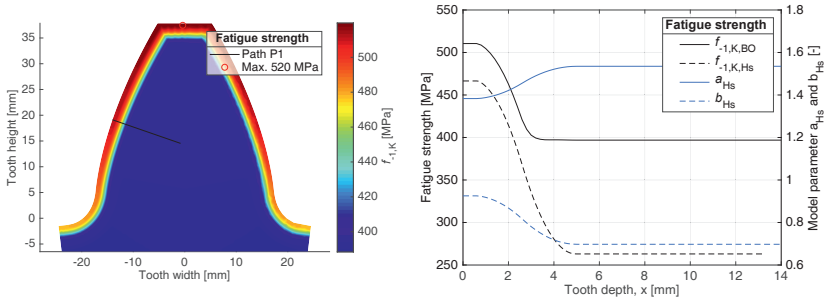

(a) Mean cross-section of G1 pinion tooth (b) Path P1

Figure 4.5: Local fatigue strength $f_{-1,K}$ according to BO1 and Hs criteria in addition to model parameters a_{Hs} and b_{Hs}

4.4 Material utilisation

For the specific purpose of assessing the risk of TFF in spiral bevel gears along a surface perpendicular path P1 below the gear's design point MB, the Dang Van criterion can be rationalised to yield the following expression defining the Hs criterion.

$$D_{Hs}(x) = \frac{a_{Hs}(x)\tau_{xy,a}(x) + b_{Hs}\left(\frac{2}{3}\sigma_{res}(x) + \frac{1+\nu}{3}\sigma_b(x)\right)}{f_{-1,K}(x)} \quad \text{with} \quad \sigma_b(x) \geq 0$$
$$a_{Hs}(x) = \kappa(x) \quad b_{Hs}(x) = 3 - 3/2\,\kappa(x) \tag{4.12}$$

To assess the accuracy of the proposed stress, material and fatigue models, the Hs criterion's material utilisation is compared with the BO1 [19], the Dang Van [39, 96], the Hertter [6] and the ISO6336-4 [1] or FVA556 I&III [15, 27] criteria. Whereas the Hs criterion follows the material model outlined in Equation 4.11, the BO1 and Dang Van material constants are set according to Papers II, III and IV [19, 32, 41], the Hertter's parameters are set according

to his material model [6] and the ISO's or FVA's according to their respective sources [1, 15, 27]. Figure 4.6a plots the BO1's material utilisations for the mean cross-section of a G1 pinion tooth and compares the predicted utilisations in Figure 4.6b along path P1 according to the BO, Dang Van and Hs criteria.

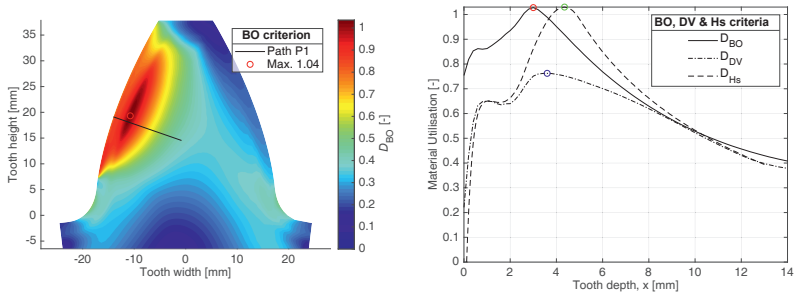

(a) Mean cross-section of G1 pinion tooth (b) Path P1

Figure 4.6: Material utilisation according to BO1, Dang Van and Hs criteria

The BO1 criterion is chosen as a reference for the other criteria as it has been calibrated against the back-to-back bevel gear test results in Paper IV [41]. The predicted utilisation peak of 1.03 in a depth of 3.0 mm aligns well with the documented failure frequency on G1 and the detected crack depth (Weibull distribution from PAUT reports [19]). Since the material utilisation is calculated against the average fatigue strength ($f_{xK} = 1$), it suggests a considerable failure probability even at moderate loads.

As outlined in Paper III [19], the Dang Van criterion predicts a significantly lower, maximum material utilisation of 0.76 in a depth of 3.6 mm. The Hs criterion relies on the same stresses and model parameters when predicting the local material utilisation. To lift the predicted utilisation of the Hs criterion to the level of the BO1 criterion, the utilised uniaxial fatigue strength f_{-1} had to be lowered. Essentially, for the Hs criterion, Murakami's lower fatigue limit was assumed across the entire hardness range, rather than considering the transition from Murakami's upper to lower fatigue limit in the range of 350 to 550 HV [31, 32]. Whilst the modification ensures equal utilisations for the BO1 and Hs criteria (1.03 for both cases), the depth of the utilisation peak is moved towards greater depths (from 3.0 to 4.3 mm). The displacement of the utilisation peak is partly due to the altered material model and the Dang Van criterion's considered stresses. When studying TFF with the Hs criterion, crack initiation should be expected in a shallower than predicted material depth.

4.4.1 Case study

The Hs criterion's accuracy is quantified by studying the subsurface material utilisation in the maritime bevel gears G1 and G2, the FZG's test gear G0

and the tested bevel gear B2-1. Their respective geometries, hardening layer thicknesses and applied loads are specified in Papers III and IV [19, 41]. The material utilisation is studied along path P1 for the Hs, Hertter and ISO6336-4 criteria and the gear's mean cross-section according to the Hertter and ISO criteria. For each gear set, pictures of the dominant gear failure mode are shown.

The criteria specific material utilisations for gear set G1 are given in Figure 4.7, for G2 in 4.8, for G0 in 4.9 and for B2-1 in 4.10. For all gears, the surface stresses in MB according to the ISO10300 standard [4] were adjusted through the face load factor $K_{H\beta}$ to match the LTCA'a surface stress in the same point.

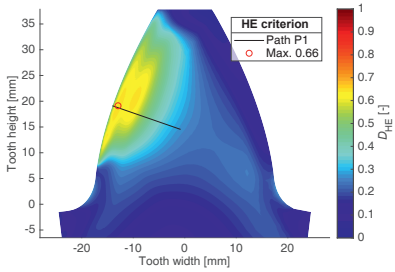

(a) Hertter criterion[6]

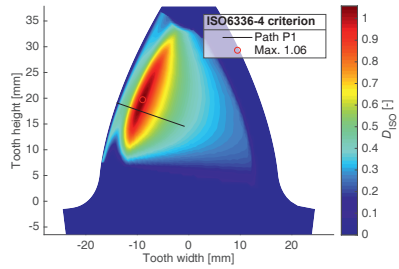

(b) ISO6336-4 criterion[1]

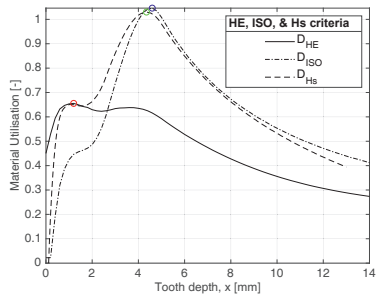

(c) Comparison along path P1

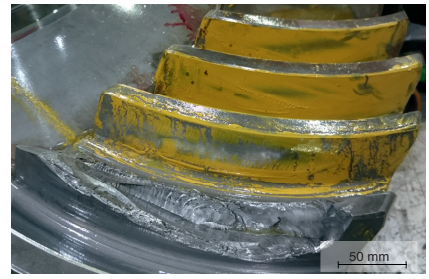

(d) Wheel initiated TFF on G1

Figure 4.7: Material utilisation comparison, G1 pinion

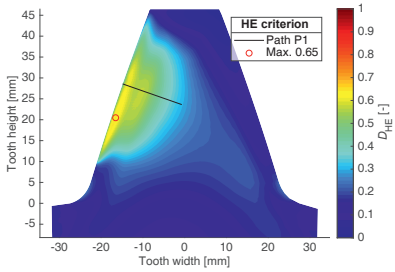

(a) Hertter criterion[6]

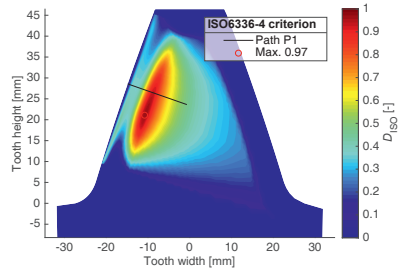

(b) ISO6336-4 criterion[1]

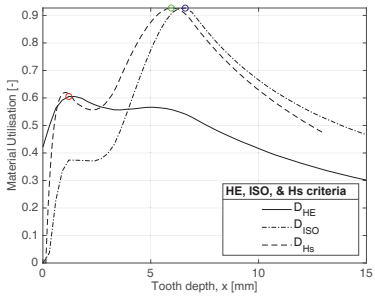

(c) Comparison along path P1

(d) Wheel initiated TFF on G2

Figure 4.8: Material utilisation comparison, G2 wheel

For the two maritime gear sets G1 and G2, comparable utilisation levels are predicted according to the Hs and ISO criteria in the TFF-critical material depths and the Hs and Hertter criterion in the pitting-critical outer material layer. While the ISO criterion focuses on TFF or subsurface initiated fatigue, Hertter studied the gear failure modes pitting and tooth root breakage. The results of this qualitative comparison suggest that the Hs criterion is potentially able to differentiate between and predict surface and subsurface fatigue in bevel and potentially cylindrical gears. Figures 4.7b and 4.8b show that the maximum subsurface material utilisation does not occur along path P1 but a different tooth height. For gears with a conventional microgeometry, the error is less than 3 % and can therefore be accepted. The calculated maximum subsurface material utilisations of 1.03 and 0.92 accurately reflect differences in failure occurrences on gear sets G1 and G2.

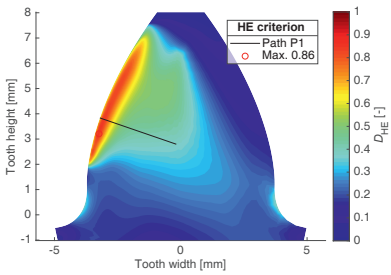

(a) Hertter criterion[6]

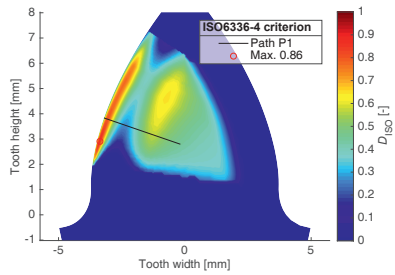

(b) ISO6336-4 criterion[1]

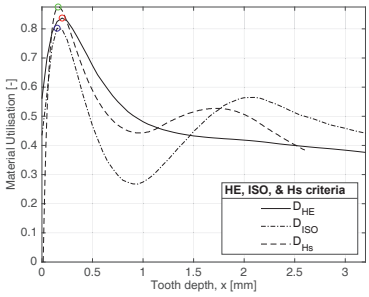

(c) Comparison along path P1

(d) Pinion initiated pitting on G0

Figure 4.9: Material utilisation comparison, G0 pinion (FZG-G0 gear set [9]

Elevated surface material utilisations are predicted for the FZG pitting test gear G0 for all three criteria. The Hs criterion predicts the highest material utilisation in a shallow 0.2 mm material depth of the three studied criteria. The elevated material utilisation in comparison to the ISO6336-4 is attributed to the considered bending stress in the prediction of the maximum hydrostatic stress $\sigma_{hyd,max}$. Only moderate subsurface utilisation levels are predicted for gear set G0, expressing an overall low TFF likelihood.

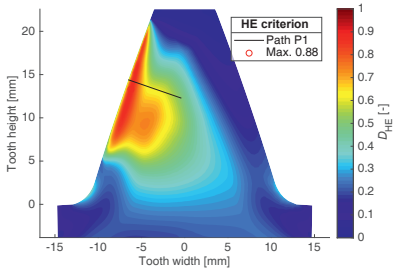

(a) Hertter criterion[6]

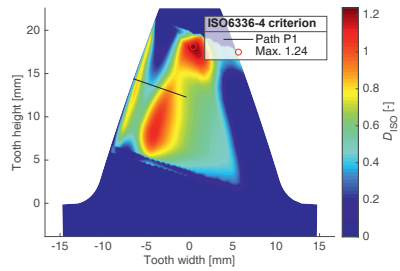

(b) ISO6336-4 criterion[1]

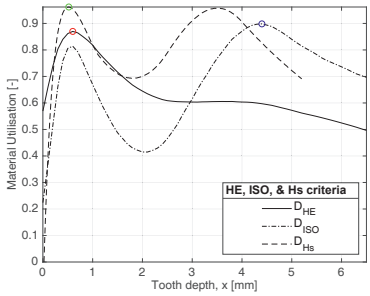

(c) Comparison along path P1

(d) Wheel initiated TFF on B2-1

Figure 4.10: Material utilisation comparison, B2-1 wheel [41]

The highest subsurface material utilisation along path P1 for test gear B2-1 is predicted according to the Hs criterion, aligning itself well with the observed wheel-initiated TFF after $2.62 \cdot 10^6$ load cycles. The Hertter and ISO criteria clearly show that the stresses below MB and thereby along the surface perpendicular path P1 do not yield the highest subsurface material utilisation. A considerable error is made when relying on the study of the material utilisation along path P1 alone. For test gears under high loads and gears with strongly modified microgeometries, focusing on Path P1 might lead to erroneous results.

All four gear sets suggest that an analysis of a surface perpendicular path starting in the half tooth height might be a better choice than the design point MB. More gear sets need to be studied to verify this observation.

The predicted material utilisation according to the ISO6336-4 is plotted in Figure 4.10b. A utilisation peak is predicted in the centre of the tooth tip. Since no tensile residual stresses are considered in the ISO, another explanation for the observed maximum utilisation must exist. The ISO calculates an equivalent shear stress τ_{eff} through the consideration of the dynamic or load related, effective shear stress $\tau_{eff,L}$, the quasi mean shear stress $\Delta\tau_{eff,L,RS}$ and the residual stress equivalent shear stress $\tau_{eff,RS}$ as per Equation 4.13.

$$\tau_{eff}(x) = \tau_{eff,L}(x) - \Delta\tau_{eff,L,RS}(x) - \tau_{eff,RS}(x) \tag{4.13}$$

In the 5 mm material depth in the tooth tip, the hardness profile has transitioned from the case to the core and the residual stresses from compression to zero (see Lang [28] or Equation 4.3 for reference). The residual stress equivalent shear stress $\tau_{eff,RS}$ has therefore no influence on the predicted material utilisation. The surface stress and equivalent radius of curvature in the closest surface node are $p_H = 1680$ MPa and $\rho_{eq} = 10.44$ mm. The resulting load-related shear stress $\tau_{eff,L}$ peaks in a depth of 0.18 mm and has dropped to 37.1 MPa in the studied 5 mm material depth. Compared to the local hardness of 414 HV and the shear fatigue strength τ_{zul}, the applied load is small compared to the local fatigue strength. The local utilisation peak in the B2-1 tooth tip can be traced back to the quasi mean stress $\Delta\tau_{eff,L,RS}$. Equation 4.14 outlines the calculation of $\Delta\tau_{eff,L,RS}$ and the adjustment factor K_2. The parameters in the equation are the influence factor K_1, the residual stress σ_{RS}, the material depth x, the local radius of curvature ρ_{eq}, the case hardening depth CHD, the maximum residual stress $\sigma_{RS,max}$ (maximum of the absolute of the residual stress) and the local surface pressure p_{dyn}.

$$\begin{aligned}
\Delta\tau_{eff,L,RS}(x) &= K_1(x)\frac{|\sigma_{RS}(x)|}{100}\,32\tanh\left(9x^{1.1}\right) - K_2(x) \\
K_2(x) &= \left(-\tanh\left(0.1\left(\rho_{eq}-10\right)\right)+1\right)\cdot \\
&\quad \left(\frac{CHD^2}{16}\,x\left(\frac{\sigma_{RS,max}}{10}\tanh\left(\frac{-2\left(\frac{p_{dyn}}{100}-200\right)}{100}\right)+\frac{\sigma_{RS,max}}{10}\right)\right)
\end{aligned} \tag{4.14}$$

For all studied gear sets in the context of this academic research K_2 is very small, typically below 10 MPa. For gear set B2-1, the material depth and contact position, K_2 has grown to 139.8 MPa. Figure 4.11a plots the expression $f(\rho_{eq}) = -\tanh\left(0.1\left(\rho_{eq}-10\right)\right)+1$ and the ISO's material utilisation for the meshing pinion tooth.

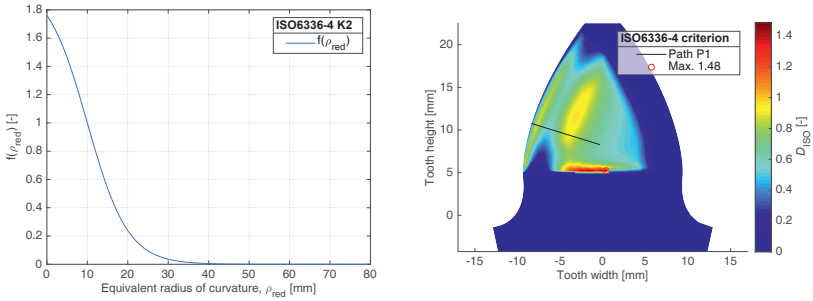

(a) $f(\rho_{eq})$ (b) D_{ISO} for B2-1 pinion

Figure 4.11: Detailed study of adjustment factor K_2 [1]

The term $f(\rho_{eq})$ increases for radii $\leq$ 20 mm and reaches for the studied equivalent radius of curvature of 10.44 mm a value close to 1. No explanation to the observable trend of K_2 as a function of the equivalent radius of curvature is provided in the ISO6336-4 or the FVA556-I upon which the ISO is based [1, 15]. Since K_2 usually assumes small values, its omission from the local material utilisation is suggested at least if utilisation levels are calculated for $\rho_{eq} \leq 20$ mm.

4.5 Discussion

The predictions made by the proposed Hs criterion are in line with the accurate BO1 criterion and the ISO6336-4 technical report [1]. Both Hs and ISO deviate in the predicted depth of the maximum utilisation from the BO1 criterion and the performed PAUT scans [19]. This is attributed to the stress and material model differences. To allow for an analytical TFF prediction, the offset in the predicted initiation depth is deemed acceptable.

The Hs criterion improves upon the ISO6336-4 by relying on the well-established Dang Van multiaxial fatigue criterion and a comprehensible prediction of the relevant stress components. Also, the weighting of the different stress components as a function of the material ductility or Dang Van's model parameters is demonstrated. These stresses are the surface-parallel orthogonal shear stress amplitude according to the DNV's gear rating standard [2, 10], the static residual stress in accordance to Lang [28] and a modified ISO10300-3 [80] bending stress modelled. An 11 % higher material utilisation is predicted along a surface-perpendicular path P1 below MB when considering the out-of-phase bending stresses. The consideration of the bending stress in the prediction of the surface fatigue failure mode pitting can be regarded as an alternative explanation to the ISO10300's slip factor Z_S [21].

The proposed material model considers, like the ISO6336-4, a size factor that depends on the mean normal module m_{mn} rather than the local tooth width

s_{tB-D} and, unlike the ISO, a lifetime factor that implies a material degradation also in the VHCF regime. By including a conversion factor, specific failure probabilities can be calculated to suit either a TFF failure analysis or a gear design process. Critical for TFF is furthermore the accurate representation of the gear size-specific hardness profile. The hardness peak depth factor x_{HVmax} in the Thomas hardness model [43] was redefined to capture the hardness transition from case to core as a function of the gear's size.

The Hs criterion can readily be adapted if a TFF prediction for a gear's mean cross-section or entire tooth flank is targeted. Suggested is the numerical calculation of the maximum hydrostatic stress and the analytical calculation of the orthogonal shear stress amplitude according to Equation 4.2. By foregoing the shear stress amplitude calculation through the MCC or MRH method, an accurate TFF prediction is possible for an entire gear tooth in a fraction of the time that the BO or Dang Van criteria would require. Figure 4.12 plots the material utilisations according to the Hs criterion for the mean pinion and wheel cross-sections of gear set G1.

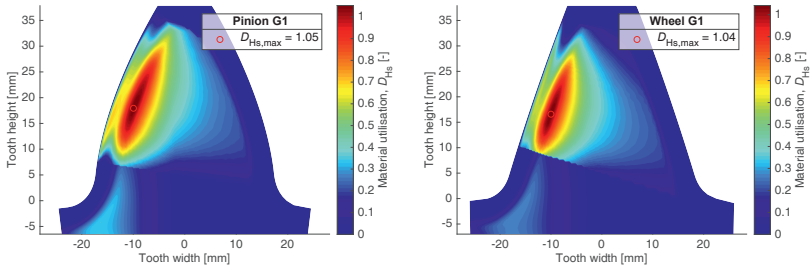

(a) Mean cross-section of G1 pinion tooth (b) Mean cross-section of G1 wheel tooth

Figure 4.12: Material utilisation according to modified Hs criterion

Comparable subsurface but different surface material utilisation are predicted for pinion and wheel. The combination of large, surface-near shear and considerable bending stresses in the pinion dedendum increase the local pitting risk over the wheel's addendum. On pinion and wheel, the maximum surface utilisations are 0.72 and 0.61 in a depth of 0.6 and 0.8 mm and a tooth height of 15.1 and 19.2 mm, respectively. Whereas the pinion's dedendum is identified as the pitting prone area, pitting would occur first in the wheel's half tooth height. The simulations align themselves with in-service observations on the gear set G1 and the reported results in the FVA project FVA749-I [101], whereby a single wheel survived testing against multiple pinion sets with the eventual pitting failure initiating in the wheel's half tooth height, not the wheel dedendum as anticipated by the slip factor Z_S.

Further evidence of the Hs criterion's capability to predict surface fatigue

is given in Figure 4.13 for the pitting-specific gear set FZG-G0 [9]. Figure 4.13a and 4.13b plot material utilisation for G0 with the geometry, loads and hardnesses specified in [9, 19] according to the BO and Hs criteria.

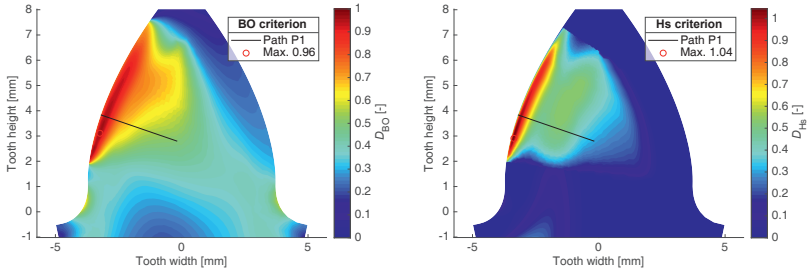

(a) BO1 criterion (b) Hs criterion

Figure 4.13: BO1 and Hs criteria for mean cross-section of FZG-G0 pinion tooth

Both criteria predict a pitting probability in pinion dedendum. The herein presented results give merit to the consideration of the bending stress in both the study of the gear failure modes subsurface fatigue or TFF and pitting.

4.6 Gear geometry

Using the Hs criterion, the impact of varying gear macrogeometries on TFF can be studied. The geometry on the maritime gear set G1 is alternated to study the relative changes in Hertzian contact pressure σ_{HB1}, equivalent radius of curvature ρ_{eq} and subsurface material utilisation D_{Hs}. The heat treatment parameters CHD, HV_s, HV_c and $x_{HV,max}$ are kept constant. Table 4.1 lists the original macrogeometry of gear set G1 and its load and heat treatment parameters. The input parameters to the calculation of D_{Hs} are derived from the ISO10300 standard [4, 21, 80].

Table 4.1: Macrogeometry, load and heat treatment parameters for gear set G1

Description	Unit	Pinion	Wheel
Pressure angle, α	°	20	
Number of teeth, z	-	14	37
Outer pitch diameter, d_e	mm	348.1	920.1
Tooth width, b	mm	170	
Mean spiral angle, β_m	°	35	
Profile shift, x_{hm}	-	0.33	-0.33
Addendum/Dedendum factor, k_{hap}/k_{hfp}	-	1/1.25	
Case hardening depth, CHD	mm	2.6	
Surface/core hardness, HV_s/HV_c	HV	697/393	
Hardness peak, $x_{HV,max}$	mm	0.0	0.4
Power, P	kW	2200	
RPM, n	1/min	556	210.4
Cycles to failure, N_f	-	$3 \cdot 10^8$	$1.14 \cdot 10^8$

The parameters d_e and b are also kept constant in order to ensure that the iterated gear design fits in the same design envelope (i.e. the gear housing). In general, d_e and b should be maximised to reduce the risk for TFF on a given gear design. Studied are instead the parameters β_m, x_{hm}, z_1 and the addendum factors k_{hap}. Each parameter is varied individually, keeping all other design parameters constant. For z_1, the initial gear ratio $u = 37/14$ is fixed, resulting in an uneven number of wheel teeth z_2 when changing z_1. This is done to isolate the effect of z_1 on D_{Hs} and to avoid changes in u affected D_{Hs}. For k_{hap}, the dedendum factor k_{hfp} is modified alongside and calculated according to $k_{hfp} = 1.25\, k_{hap}$.

In reference to Equation 4.2, the positive effect of a reduction in σ_{HB1} and ρ_{eq} on D_{Hs} is apparent. A quadratic correlation between σ_{HB1} and D_{Hs} can be found, as σ_{HB1} appears in the expression for the orthogonal shear stress amplitude $\tau_{xy,a}$ and the half Hertzian contact width b_H. As ρ_{eq} only appears in b_H, a linear correlation exist between ρ_{eq} and D_{Hs}. How D_{Hs} response to changes in σ_{HB1} and ρ_{eq} is relevant as increases in β_m and x_{hm} reduce σ_{HB1} but increase ρ_{eq}. Optimising a gear design to avoid TFF compared to pitting is thereby more difficult as σ_{HB1} and ρ_{eq} need to be considered in tandem.

Figure 4.14 visualises the effect of changes in β_m, x_{hm}, z_1 and k_{hap} on σ_{HB1}, $\rho_{eq,MB}$ and D_{Hs}. Here, $\rho_{eq,MB}$ refers to the radius of curvature in the ISO10300's design point MB and is calculated through $\rho_{eq,MB} = \rho_{eq}/Z^2_{MB}$. Figure 4.14 also highlights on the described quadratic and linear correlations between σ_{HB1}, $\rho_{eq,MB}$ and D_{Hs}.

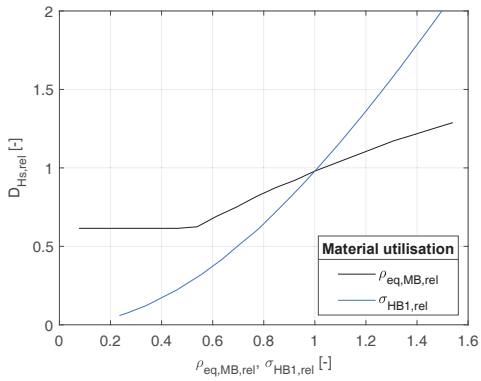

(a) Maritime pinion gear

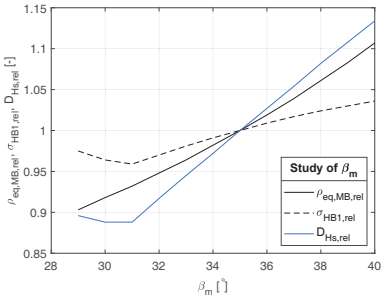

(b) β_m

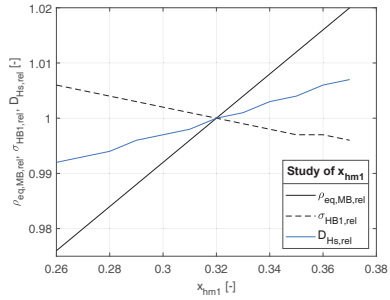

(d) x_{hm1}

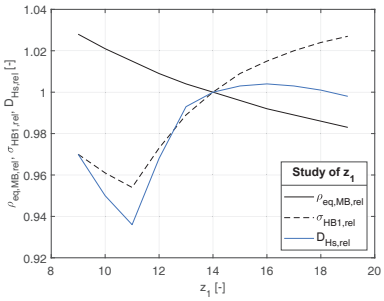

(c) z_1

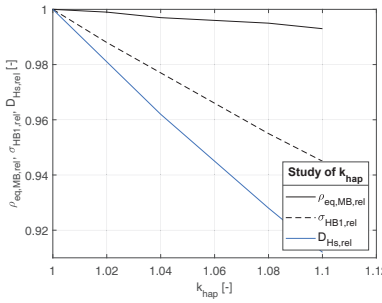

(e) k_{hap}

Figure 4.14: Macrogeometry study according to Hs criterion

This iteration suggests that a reduction in TFF on the studied spiral bevel gear can be achieved for a modest spiral angle $\beta_m = 31°$, a reduction in profile shift x_{hm}, 11 rather than 14 teeth on the pinion and an increase in addendum

factor to $k_{hap} = 1.1$. The combination of β_m and z_1 shows that the lowest material utilisation ($D_{Hs} = 0.74$) is achieved for larger number of teeth $z_1 = 17$ and a low spiral angle $\beta_m = 29°$. For the above proposed $z_1 = 11$, the ideal spiral angle is $\beta_m = 35°$, resulting in $D_{Hs} = 0.85$. Both variants considered $k_{hap} = 1.1$. Table 4.2 lists the final TFF-optimised gear design.

Table 4.2: Optimised macrogeometry, load and heat treatment parameters for gear set G1

Description	Unit	Pinion	Wheel
Pressure angle, α	°	20	
Number of teeth, z	-	17	45
Outer pitch diameter, d_e	mm	347.59	920.1
Tooth width, b	mm	170	
Mean spiral angle, β_m	°	29	
Profile shift, x_{hm}	-	0.32	-0.32
Addendum/Dedendum factor, k_{hap}/k_{hfp}	-	1.1/1.375	
Case hardening depth, CHD	mm	2.6	
Surface/core hardness, HV_s/HV_c	HV	697/393	
Hardness peak, $x_{HV,max}$	mm	0.0	0.4
Power, P	kW	2200	
RPM, n	1/min	556	210
Cycles to failure, N_f	-	$3 \cdot 10^8$	$1.13 \cdot 10^8$

Figure 4.15 depicts the predicted subsurface material utilisation for a surface-perpendicular path underneath the design point MB. Visualised are the material utilisations of pinion and wheel for the original and optimised gear designs.

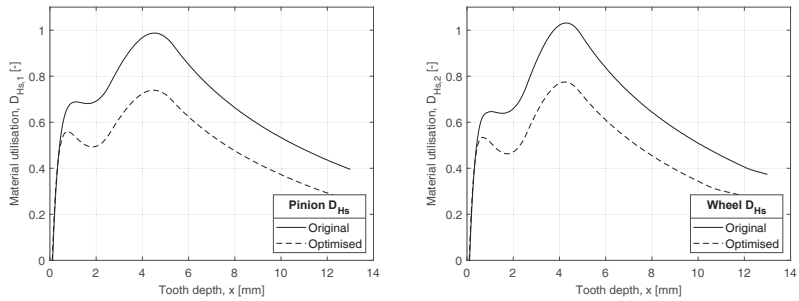

(a) G1 pinion (b) G1 wheel

Figure 4.15: Original and TFF-optimised G1 gear set

In order to verify the predictions made by the Hs criterion and the ISO10300, the study is repeated with LTCA and Becal [18] derived stresses. The calculated

material utilisations in the gear's mean cross-sections are plotted according to the BO and Hs criteria in Figure 4.16. As outlined previously, the Hs criterion relies here on the numerical calculation of the hydrostatic stress σ_{hyd}.

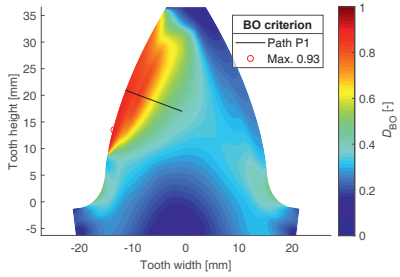

(a) G1 pinion BO

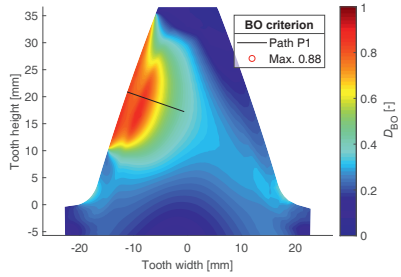

(d) G1 wheel BO

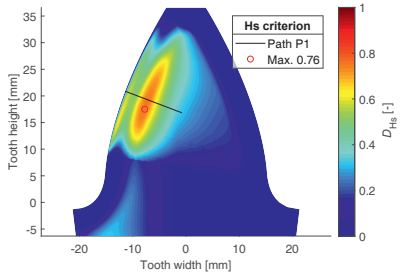

(b) G1 pinion Hs

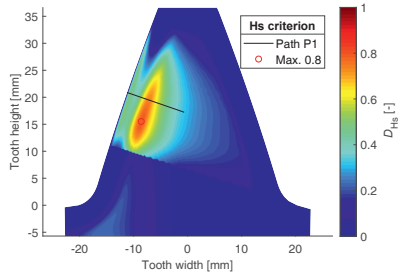

(e) G1 wheel Hs

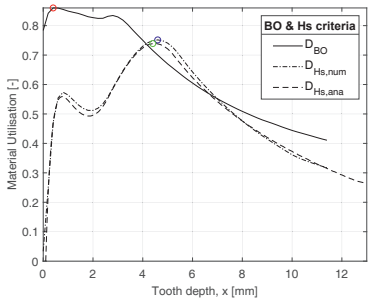

(c) Comparison BO, Hs

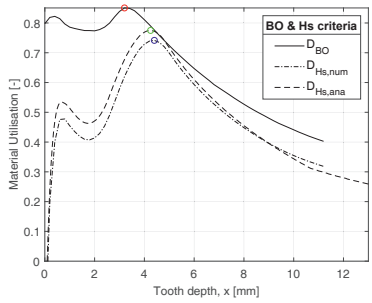

(f) Comparison BO, Hs

Figure 4.16: TFF-optimised G1 gear set

The comparison between the original material utilisations (see Figures 4.6 and 4.12) and the optimised geometry demonstrates the profound impact of the

macrogeometry on TFF. In summary, an increase in number of teeth, a reduction in spiral bevel angle and an increase in addendum factor seem to reduce the Hertzian pressure between the meshing gear teeth and the equivalent radius of curvature, resulting in a TFF-optimised and more balanced gear design.

Chapter 5

Conclusion

Critical for the safe and failure-free operation of azimuthing thrusters on platform supply vessels, anchor handlers, ferries, cruise ships and tugboats is the prediction and prevention of all gear failure modes on the employed spiral bevel gears. Whereas surface-initiated failures are well understood and mostly avoided by considering gear standards or classification guidelines, subsurface-initiated fatigue constitutes the dominant failure mode on large, maritime bevel gears on azimuthing thrusters. The gear failure mode has been coined *tooth flank fracture* and *subsurface fatigue*. Quantitative and qualitative research into the material properties of carburised CrNiMo steel, the subsurface stresses in spiral bevel gears and their combination in the form of novel multiaxial fatigue criteria have been conducted to improve the prediction and enable the prevention of tooth flank fracture.

5.1 Material model

Spiral bevel gears are typically hot forged and case hardened to increase their load-carrying capacity. In the context of TFF on large gears, this process results in anisotropic material properties due to the introduced carbon profile during gas carburising and the persistent segregation structure created during the solidification of the steel melt. While the carbon-rich gear flank achieves a homogeneous hardness and material properties, the gear tooth's core and even more so the interface between the hard case and soft core are dominated by gear-size-dependent microstructural heterogeneities. Documented heterogeneities are the dendritic or banded microstructure and its effect on the carbon penetration during carburising (i.e. channelling), the size and orientation of non-metallic inclusions and retained soft austenite grains. Localised hardness differences of 200 HV were documented with nested TFF cracks in the alloy-rich but carbon-poor parts of the banded microstructure.

Extensive fatigue tests of four gear steels and one high-carbon CrNiMo steel were carried out under uniaxial loading and shear with alternating and oscil-

lating stresses in the high cycle and very high cycle fatigue regime to develop a fatigue model for carburised CrNiMo steel. The multiaxial and non-proportional stress history in gear teeth requires the consideration of as many as four material constants for an accurate fatigue assessment.

Material constants

The four studied material constants were the uniaxial fatigue strength under alternating load f_{-1}, the uniaxial fatigue strength under oscillating load f_0, the shear fatigue strength under alternating load t_{-1} and the shear fatigue strength under oscillating load t_0. Specimens were extracted from large forgings that underwent gear-like production processes (i.e. hot forging, austentisation and gas carburising whilst being protected against carbon penetration) to simulate the macro- and microstructure found in the soft core and hard case of large, case hardened, spiral bevel gears. All specimens were ultrasonic shot-peened, applying compressive residual stresses in a 0.15 mm wide outer material layer to specifically study the bulk material properties.

The results obtained for f_{-1} underline the detrimental effect of non-metallic inclusion on the fatigue strength and load-carrying capacity of large gears. The electro-slag refined variant of the 18CrNiMo7-6 base steel showed superior fatigue properties throughout the high and very high cycle fatigue regime. Of the tested steels, especially the 498 HV hard 34CrNiMo6 steel was severely affected by the documented MgO-Al_2O_3 inclusions. The obtained fatigue properties beyond $1 \cdot 10^5$ load cycles were inferior to the 150 HV softer gear steels. The results suggest a transition in f_{-1} between 350 and 500 HV from an upper fatigue limit that is nearly independent of the documented non-metallic inclusions to a lower fatigue limit that is dominated by the presence of these inclusions. Comparable inclusion distributions were established for all steels, leading to an average $\sqrt{area}$ parameter of 80 μm and the definition of the lower fatigue limit through Murakami's $\sqrt{area}$ model. The also studied effect of a higher forging ratio on f_{-1} did not show the expected improvement.

Existing models for the prediction of the mean stress sensitivity M diverge significantly for large hardnesses. Two prominent examples are the FKM guideline and Murakami's $\sqrt{area}$ model. Neither capture the documented f_0 results adequately. The FKM guideline significantly overestimated M for the tested hard steel but accurately predicted the results for the tested gear steels. Contrarily, Murakami's model matches the hard steel's results but underestimated M and overestimated f_0 for the other steels. As Hertzian contact between meshing gear teeth is defined by large, compressive, mean normal stresses and large normal and shear stress amplitudes, the correct definition of the mean stress sensitivity is paramount for an accurate fatigue prediction under rolling contact fatigue. A mean stress sensitivity model is proposed that bridges the gap between Murakami and the FKM by considering the effect of non-metallic inclusions on M. According to herein obtained results and related research by Bell & Benham, notches or non-metallic inclusions decrease f_{-1} and M for hard

steels, resulting in larger values for f_0 than otherwise predicted. The proposed correlation is repeated here and compared to the FKM guideline.

$$\begin{aligned} \text{FKM}: \ & M = 3.5 \cdot 10^{-4} R_m - 0.1 \\ \text{Böhme}: \ & M \approx 7.0 \cdot 10^{-4} f_{-1} - 0.1 \end{aligned} \tag{5.1}$$

The comparison between the reported fatigue test results and the mean stress sensitivity models by Morrow and Goodman suggests that the consideration of f_{-1} in the prediction of M is better suited to approximate f_0 for hard steels than correlations that rely solely on the hardness or ultimate tensile strength.

The mild 18CrNiMo6 steel and the hard 34CrNiMo6 were tested under alternating shear and showed comparable values for t_{-1} at $5 \cdot 10^6$ load cycles despite the previously described differences in f_{-1}. Based on the obtained results and supporting literature findings, a linear function for $\kappa = f_{-1}/t_{-1}$ was proposed that captures the transition from a more ductile material behaviour in the soft tooth core to a more brittle material behaviour in the hard case. The fourth material constant t_0 was not tested for but predicted according to Liu & Zenner's correlation.

Influence factors

Large maritime bevel gears in azimuthing thrusters accumulate over $3 \cdot 10^8$ load cycles within the first five years of service. The degradation of the fatigue strength of hard steels in the very high cycle regime is discussed in the literature and captured through multistage fatigue life diagrams. Based on the performed gear endurance test, a TFF-specific, lifetime factor K_{NT} was derived from the maximum likelihood method. K_{NT} is positioned between the ISO's pitting and tooth root breakage lifetime factors and portrays a continuous strength decrease in the high and very high cycle regime. The obtained standard deviation was used to propose a conversion factor to express specific material strengths and failure probabilities.

A statistical size factor K_X was proposed based on the weakest link theory and the study of the highly stressed volumes in bevel gears of various sizes. Due to the computational complexity of a volume-based size factor, a rationalised, mean normal module dependent version was proposed. Its trend and magnitude are comparable to the ISO10300-2 tooth root breakage size factor. Whilst K_X adequately captures the statistical size effect, it does not cover the technological size effect. This thesis promotes the implementation of Thomas's hardness model to predict the hardness profile in gear teeth. Conversely, the parameter x_{HVmax} is not used to capture the depth of the maximum hardness peak but to describe the hardness gradient in the case hardening depth (i.e. the depth in which the local hardness reaches 550 HV). Large gears and especially wheels suffer from a steep hardness gradient in the case/core interface, weakening the, for TFF critical, material depth. Contributing factors are the auto-tempering

response during quenching, prolonged cooling times, the gas carburising in multiple stages and the dendritic or banded microstructure. Based on extensive hardness measurements on failed maritime gear sets and supporting measurements from the gear supplier industry, the following ratio is suggested between 400 HV and 550 HV depths.

$$\frac{T400}{T550} = 1.9 - \frac{m_{mn} - 5}{65} \quad \text{with} \quad \frac{T400}{T550} \leq 1.9 \tag{5.2}$$

With an increase in gear size or mean normal module m_{mn}, the accelerated transition from the hard case to the soft core weakens the TFF critical, subsurface material layers. To avoid TFF on large gears, a larger relative case hardening depth is required to cover the increasing equivalent radius of curvature and the statistical and technological size effects.

5.2 Stress and fatigue prediction

The subsurface stresses in spiral bevel gears are a superposition of Hertzian stresses, transverse shear and transverse normal stresses, out-of-phase bending stresses, frictional shear stresses, and static, residual stresses. This highly complex, multiaxial and non-proportional stress state lends itself to a numerical rather than analytical stress study. With surface stresses between meshing gear teeth readily available from the FVA program Becal, a 2D plane strain analysis of the mean cross-section of a gear tooth was favoured to ensure a fine mesh and material plane resolution during the multiaxial fatigue analysis.

2D plane strain

A MATLAB script was developed that imports the Becal stress profile, models the mean cross-section of the studied gear tooth as an involute profile with a trochoidal tooth root shape, meshes it according to the chosen element type, size and resolution, runs a finite element subsurface stress prediction under the 2D plane strain assumption, calculates the shear and normal stresses in each node and material plane for the chosen nodal and angular resolution and combines the predicted material constants according to the modelled hardness profile with the estimated stresses in the form of stress-based, multiaxial fatigue criteria. Despite the very fine element resolution, load increments and angular resolution, computational times of 350 sec were achieved, allowing for the efficient and iterative study of material or heat treatment parameters and multiaxial fatigue criteria.

Multiaxial fatigue criteria

A selection of stress-based critical plane, integral and second stress invariant derived multiaxial fatigue criteria were studied under the proposed material model and predicted subsurface stress state. Their results were compared to

TFF-specific calculation models. A significant scatter is observed for the studied multiaxial criteria, especially in the surface near material layer. Two novel, rolling contact fatigue specific, integral, multiaxial fatigue criteria were developed. The BO1 and BO2 criteria performed well in the conducted benchmarking test and were on par with the highly accurate Liu & Zenner and Papuga PIN criteria. Contrary to these two criteria, they enable a fatigue prediction throughout the gear's entire cross-section. The tests conducted in this thesis support the applicability of the BO1 criterion to the study of TFF, pitting and tooth root breakage.

5.3 Standardised approach

Targeting a rationalised or standardisable TFF approach akin to the ISO6336-4 technical report, an iteration of the Dang Van criterion is presented that limits itself to the study of the subsurface stresses and material strength underneath the ISO's design point for pitting damages. The index or alphabetical letter assigned to pitting in the ISO standards is *H*. As the same design point was studied in the proposed approach, the criterion is adequately coined *Hs*. The *s* expresses the subsurface nature of the studied failure mode. Through ultrasonic scanning of in-service, maritime gear sets, sectioning of damaged gear teeth and the microscopic study of early-stage TFFs, crack initiation in nearly surface-parallel material layers was proven. For stress-based, critical plane, multiaxial fatigue criteria, this observation removes the iterative identification of the critical plane. The comparison between the DNV-based orthogonal shear stress amplitude (i.e. orthogonal to the gear tooth's surface) and the maximum rectangular hull derived shear stress amplitude show an exceptional correlation, further adding to the rationalisation of the Dang Van criterion. A set of analytical equations is presented for the prediction of the maximum hydrostatic stress along the surface-perpendicular path. It relies on the estimation of the compressive residual and maximum bending stresses. For the bending stress prediction, dimensions and definitions are taken from the ISO10300-3 standard for tooth root breakage. By using the same influence factors and an adjusted material model, a close correlation between the advanced BO1 criterion and rationalised Dang Van or Hs criterion was achieved without the need for complex numerical computation. The Hs criterion agrees very well with the TFF model outlined in the ISO6336-4 technical report but introduces a lifetime factor and proposes a well-founded and understandable multiaxial fatigue approach based on damage observations and rationalised stress analysis.

5.4 Concluding remarks

TFF is a highly complex gear failure mode as the material properties change in the relevant tooth depth and due to the multiaxial and non-proportional stress state. Based on quantitative and qualitative research into the material proper-

ties of carburised CrNiMo steel, the subsurface stresses in spiral bevel gears and their combination in the form of novel multiaxial fatigue criteria, a methodology is presented that achieves the outlined objective. The evidence provided in this thesis suggests furthermore that other gear fatigue failure modes like pitting and tooth root breakage could also be studied with the same methodology, opening up new possibilities for the optimisation of gear designs and heat treatment parameters in one rather than multiple, individual calculations. The utilised 2D plane strain approach and the assumptions made in this thesis promote the application of the developed methodology to cylindrical gears.

Bibliography

[1] ISO. *ISO/TS 6336-4:2019 - Calculation of load capacity of spur and helical gears - Part 4: Calculation of tooth flank fracture load capacity*. Switzerland: ISO copyright office, 2019.

[2] DNV GL. *DNVGL-CG-0036: Calculation of gear rating for marine transmissions*. Oslo, 2015.

[3] G. M. Bakken. *Fracture Mechanics - Tooth interior fatigue fracture*. Report. Det Norske Veritas AS, 2012.

[4] ISO. *ISO 10300-1:2014 - Calculation of load capacity of bevel gears*. Switzerland: ISO copyright office, 2014.

[5] DIN. *DIN3991-2: Tragfähigkeitsberechnung von Kegelrädern ohne Achsversetzung - Berechnung der Grübchentragfähigkeit*. Berlin: Deutsches Institut für Normung e.V., 1988.

[6] T. Hertter. "Rechnerischer Festigkeitsnachweis der Ermudungstragfahigkeit verguteter und einsatzgeharteter Stirnrader". Thesis. 2003.

[7] M. Hombauer. *Bestimmung der Graufleckentragfähigkeit von Kegelrad- und Hypoidverzahnungen*. Vol. Heft 1055. Forschungsvorhaben Nr. 516. Forschungsvereiningung Antriebstechnik e.V., 2013.

[8] M. Klein. *Bestimmung der Fresstragfähigkeit von Kegelrad- und Hypoidverzahnungen*. Vol. Heft 1071. Forschungsvorhaben Nr. 519. Forschungsvereinigung Antriebstechnik e.V., 2013.

[9] C. Wirth. *Entwicklung eines Berechnungsberfahrens zur Grübchen- und Zahnfußtragfähigkeit von Hypoidrädern*. Vol. Heft 887. Forschungsvorhaben Nr. 411. Forschungsvereinigung Antriebstechnik e.V., 2009.

[10] S. A. Böhme, D. Merson, and A. Vinogradov. "On subsurface initiated failures in marine bevel gears". In: *Engineering Failure Analysis* 110 (2020), p. 104415. ISSN: 13506307. DOI: 10.1016/j.engfailanal.2020.104415.

[11] M. Søfferud. *2021-3014: Examination and testing of gearwheel*. Report. Det Norske Veritas, 2021.

[12] H. Zenner, A. Simbürger, and J. Liu. "On the fatigue limit of ductile metals under complex multiaxial loading". In: *Int. J. Fatigue* 22 (2000), pp. 137–145.

[13] FKM (Forschungskuratorium Maschinenbau). *Analytical Strength Assessment of Components*. Vol. 6th Edition. Frankfurt: VDMA, 2012.

[14] R. Annast. *Flankentragfähigkeit und Laufverhalten von hart-feinbearbeiteten Kegelrädern, Schadensform Flankenbruch*. Vol. Heft 690. Forschungsvorhaben Nr. 240 II. Forschungsvereinigung Antriebstechnik e.V., 2002.

[15] J. Witzig. *Entwicklung eines erweiterten Berechnungsverfahrens zur Ermittlung optimaler Zahnflankentragfähigkeit bis in den Bereich grosser Werkstofftiefe*. Vol. Heft 1000. Forschungsvorhaben Nr. 556 I. Forschungsvereinigung Antriebstechnik e.V., 2012.

[16] S. A. Böhme. "Flankenbruch - Spannungstiefenverlauf in maritimen Kegelradstufen unter Berücksichtigung der Last- und Eigenspannungen". Thesis. 2012.

[17] T. J. Hofmann. "Beitrag zur verfeinerten Balkentheorie". Thesis. 1992.

[18] V. Baumann et al. "Programm zur Berechnung der Zahnflanken – und Zahnfußbeanspruchung an Kegelrad – und Hypoidgetrieben". In: Heft 548 (1998).

[19] S. A. Böhme et al. "A novel predictive model for multiaxial fatigue in carburized bevel gears". In: *Fatigue & Fracture of Engineering Materials & Structures* (2021). ISSN: 8756-758X 1460-2695. DOI: 10.1111/ffe.13475.

[20] J. Papuga, L. Suchý, and M. Růžička. "Mean shear stress effect built into the multiaxial fatigue strength estimation method of an integral type". In: *MATEC Web of Conferences* 300 (2019), p. 16010. ISSN: 2261-236X. DOI: 10.1051/matecconf/201930016010.

[21] ISO. *ISO 10300-2:2014 - Calculation of load capacity of bevel gears - Part 2: Calculation of load capacity of bevel gears*. Switzerland: ISO copyright office, 2014.

[22] C. Wirth. *Normgerechte Wahl zur Einsatzhärtetiefe der Kegelräder*. Vol. Heft 918. Forschungsvorhaben Nr. 509. Forschungsvereinigung Antriebstechnik e.V., 2009.

[23] M. MackAldener. "Tooth Interior Fatigue Fracture & Robustness of Gears". Thesis. 2001.

[24] W. N. Findley. "Fatigue of Metals Under Combinations of Stresses". In: *Transactions of ASME* 79 (1957).

[25] P. Oster. "Beanspruchung der Zahnflanken unter Bedingungen der Elastohydrodynamik". Thesis. 1982.

[26] C. Wickborn. *Entwicklung eines erweiterten Berechnungsverfahrens zur Ermittlung optimaler Zahnflankentragfahigkeit bis in den Bereich großer Werkstofftiefen - Erganzungsversuche zur Verifizierung an großeren Zahnradern*. Forschungsvorhaben Nr. 556 II. München: Forschungsvereinigung Antriebstechnik, 2013.

[27] I. Boiadjiev. “Normfähiger Berechnungsansatz zum Flankenbruch bei Kegelrad- und Hypoidgetrieben”. In: *Forschungsvorhaben Nr. 556 III.* München: Forschungsvereinigung Antriebstechnik, 2014.

[28] O.R. Lang. “Berechnung und Auslegung induktiv randschichtgehärteter Bauteile”. In: *Kloos, K. H. (Hrsg.); Grosch, J. (Hrsg.): Induktives Randschichthärten. Berichtsband, Tagung 23. bis 25. März 1988, München: Arbeitsgemeinschaft Wärmebehandlung und Werkstofftechnik (AWT)* (1989), pp. 332–348.

[29] R. Weber. “Auslegungskonzept gegen Volumenversagen in einsatzgehärteten Stirnradern”. Thesis. 2015.

[30] M. Prime. “Cross-sectional mapping of residual stresses by measuring the surface contour after a cut”. In: *Journal of Engineering Materials and Technology* 123 (2001), pp. 162–168.

[31] Y. Murakami. *Metal Fatigue: Effects of Small Defects and Non-metallic Inclusions*. Cambridge: Academic Press, 2019. ISBN: 9780128138762. DOI: https://doi.org/10.1016/C2016-0-05272-5.

[32] S. A. Böhme et al. “Fatigue of carburised CrNiMo steel: Testing and modelling concept”. In: *Fatigue & Fracture of Engineering Materials & Structures* 44.3 (2020), pp. 788–804. ISSN: 8756-758X 1460-2695. DOI: 10.1111/ffe.13394.

[33] W.J. Bell and P.P. Benham. “The effect of mean stress on fatigue strength of plain and notched stainless steel sheets in the range of 10 to 106 cycles.” In: *Symposium on Fatigue Tests of Aircraft Structures: Low-Cycle, Full-Scale, and Helicopters* (1962), pp. 25–46.

[34] F. Baier. “Zeit- und Dauerfestigkeit bei überlagerter statischer und schwingender Zug-Druck- und Torsionbeanspruchung”. Thesis. 1970.

[35] A. Simbürger. “Festigkeitsverhalten zäher Werkstoffe bei einer mehrachsigen phasenverschobenen Schwingbeanspruchung mit körperfesten und veränderlichen Hauptspannungsrichtungen”. Thesis. 1975.

[36] H.-P. Lüpfert and H.-J. Spies. “Fatigue strength of heat-treatable steel under static multiaxial compression stresses”. In: *Advanced Engineering Materials* 6.7 (2004), pp. 544–550.

[37] J. Papuga and F. Fojtík. “Multiaxial fatigue strength of common structural steel and the response of some estimation methods”. In: *International Journal of Fatigue* 104 (2017), pp. 27–42. DOI: 10.1016/j.ijfatigue.2017.07.001.

[38] B. Crossland. “Effect of large hydrostatic pressure on the torsional fatigue strength of an alloy steel.” In: *Proceedings of International Conference on Fatigue of Metals, London* Institution of Mechanical Engineers (1956), pp. 138–149.

[39] K. Dang Van. “Sur la résistance à la fatigue des métaux”. In: *Sciences et Technique de l’Armement* 3eme fascicule (1973), pp. 647–722.

[40] G. Sines. *Behavior of metals under complex static and alternating stresses*. New York: McGraw Hill, 1959, pp. 145–469.

[41] S. A. Böhme et al. "Tooth flank fracture – An applied fatigue study of case hardened bevel gears". In: *Engineering Failure Analysis* 132 (2022), p. 105911. ISSN: 13506307. DOI: 10.1016/j.engfailanal.2021.105911.

[42] F. Pascual and W. Meeker. "Analysis of fatigue data with run-outs based on a model with non constant standard deviation and a fatigue limit parameter". In: *Journal of Testing and Evaluation* 25 (1997), pp. 292–301.

[43] J. Thomas. "Flankentragfähigkeit und Laufverhalten von hart-feinbearbeiteten Kegelrädern". Thesis. 1998.

[44] R. L. Peng and B Trostell. *Neutron Diffraction Measurement of Residual Stress in Two Carburised Gear Teeth*. Report. Studsvik Neutron Research Laboratory, 2003.

[45] R. L. Peng and A. Seaton. *Neutron Diffraction Measurements of Residual Stress in Two Carburised Gear Teeth*. Report. Studsvik Neutron Research Laboratory, 2012.

[46] NASA. "Effect of Shot Peening on Surface Fatigue Life of Carburized and Hardened AISI 9310 Spur Gears". In: *NASA Technical Paper* 2047 (1982).

[47] NASA. "Improvement in Surface Fatigue Life of Hardened Gears by High-Intensity Shot Peening". In: *NASA Technical Memorandum* 105678 (1992).

[48] G. M. Bakken. *Improved reliability of thrusters - Joint Industry Project: Report 2015-1332 Phase 2 - Material Testing*. Report. Det Norske Veritas Germanischer Lloyd AS, 2016.

[49] E. Pessard et al. "Microstructural heterogeneities and fatigue anisotropy of forged steels". In: *Materials Science and Engineering: A* 529.Supplement C (2011), pp. 289–299. ISSN: 0921-5093. DOI: https://doi.org/10.1016/j.msea.2011.09.031. URL: http://www.sciencedirect.com/science/article/pii/S0921509311009919.

[50] DIN. *DIN 50100:2016 - Schwingfestigkeitsversuche - Durchführung und Auswertung von zyklischen Versuchen mit konstanter Lastamplitude für metallische Werkstoffproben und Bauteile*. Berlin: Deutsches Institut für Normung e.V., 2016.

[51] M. F. Garwood, H. H. Zurburg, and M. A. Erickson. "Correlation of laboratory tests and service performance, interpretation of tests and correlation with service". In: *ASM* (1951), pp. 1–77.

[52] S. Nishijima. "Statistical Analysis of Fatigue Test Data". In: *J. Soc. Mater. Sci. Japan* 29 (1980), pp. 24–29.

[53] E. Velten. “Entwicklung eines Schwingfestigkeitskonzeptes zur Berechnung der Dauerfestigkeit thermochemisch randschichtverfestigter bauteilahnlicher Proben”. Thesis. 1984.

[54] B. Winderlich. “Das Konzept der lokalen Dauerfestigkeit und seine Anwendung auf martensitische Randschichten, insbesondere Läserhärtungsschichten”. In: *Mat.-wiss. u. Werkstofftech.* 21 (1990), pp. 378–389.

[55] J. O. Smith. “The effect of range of stress on the fatigue strength of metals”. In: *University of Illinois Engineering Experiment Station* Bulletin series No. 334 (1942).

[56] J. A. Graham, SAE Iron, and Steel Technical Committee. *Fatigue design handbook*. Fatigue design handbook. New York: Society of Automotive Engineers, 1968.

[57] N.E. Dowling, C.A. Calhoun, and A. Arcari. “Mean stress effects in stress-life fatigue and the Walker equation”. In: *Fatigue & Fracture of Engineering Materials & Structures* 32 (2009), pp. 163–179. DOI: https://doi.org/10.1111/j.1460-2695.2008.01322.x.

[58] R. Rabb. *Todennäköisyysteoriaan pohjautuva väsymisanalyysi*. Norderstedt: Books on Demand, 2013. DOI: 9789522862105.

[59] A. Banvillet, T. Palin-Luc, and S. Lasserre. “A volumetric energy based high cycle multiaxial fatigue citerion”. In: *International Journal of Fatigue* 25.8 (2003), pp. 755–769.

[60] A. Carpinteri and A. Spagnoli. “Multiaxial high-cycle fatigue criterion for hard metals”. In: *International Journal of Fatigue* 23.2 (1985), pp. 135–145.

[61] P. Davoli et al. “Independence of the torsional fatigue limit upon a mean shear stress”. In: *International Journal of Fatigue* 25 (2003), pp. 471–480.

[62] E. El Magd and S. Mielke. “Dauerfestigkeit bei überlagerter zweiachsiger statischer Beanspruchung”. In: *Konstruktion* 29.Heft 7 (1977), pp. 253–257.

[63] C. Froustey and S. Lasserre. *Fatigue des aciers sous sollicitations combinees - Application a l’acier 30NCD16*. Report. ENSAM, 1988.

[64] A. Galtier. “Contribution a l’etude de l’endommagement des aciers sous sollicitations uni ou multiaxiales”. Thesis. 1993.

[65] H. J. Gough and H. V. Pollard. “The strength of metals under combined alternating stresses”. In: *Proceedings of Institute of Mechanical Engineering 131* (1935), pp. 1–103.

[66] H. J. Gough. “Engineering Steels Under Combined Cyclic and Static Stresses”. In: *Journal of Applied Mechanics* 17.2 (1950), pp. 113–125. DOI: https://doi.org/10.1243%2FPIME_PROC_1949_160_040_02.

[67] H. J. Gough, H. V. Pollard, and W. J. Clenshaw. *Some Experiments on the Resistance of Metals to Fatigue under Combined Stresses*. Report. 1951.

[68] R. Heidenreich and H. Zenner. *Festigkeitshypothese - Berechnung der Dauerfestigkeit für beliebige Beanspruchungskombinationen*. Report. 1976.

[69] L. Issler. "Festigkeitsverhalten metallischer Werkstoffe bei mehrachsiger phasenverschobener Beanspruchung mit verschiedenen Spannungszeitverlaufen." Thesis. 1973.

[70] C. Kaniut. "Zur Betriebsfestigkeit metallischer Werkstoffe bei mehrachsiger Beanspruchung". Thesis. 1983.

[71] S. Lasserre and C. Froustey. "Multiaxial fatigue of steel - testing out of phase and in blocks: validity and applicability of some criteria". In: *International journal of fatigue* 14.2 (1992), pp. 113–120.

[72] W. Lempp. "Festigkeitsverhalten von Stählen bei mehrachsiger Dauerschwingbeanspruchung durch Normalspannungen mit überlagerten phasengleichen und phasenverschobenen Schubspannungen". Thesis. 1977.

[73] S. Mielke. "Festigkeitsverhalten metallischer Werkstoffe unter zweiachsiger schwingender Beanspruchung mit verschiedenen Spannungszeitverlaufen". Thesis. 1980.

[74] T. Nishihara and M. Kawamoto. "The strength of metals under combined alternating bending and torsion with phase difference". In: *Mem. College Engng.* Kyoto Imperial University 11 (1945), pp. 85–112.

[75] F. Nolte. "Dauerfestigkeitsuntersuchungen an Stahlwellen bei umlaufender Biege- und überlagerter statischer Verdrehbeanspruchung". Thesis. 1973.

[76] C. M. Poeppelmann. "Axial and Torsion Fatigue of High Hardness Steels". Thesis. 2011.

[77] F. Rotvel. "Biaxial fatigue tests with zero mean stresses using tubular specimens". In: *International Journal of Mechanical Sciences* 12.7 (1970), pp. 597–613.

[78] A. Troost, O. Akin, and F. Klubberg. "Dauerfestigkeitsverhalten metallischer Werkstoffe bei zweiachsiger Beanspruchung durch drei phasenverschoben schwingende Lastspannungen". In: *Konstruktion* 39 (1987), pp. 479–488.

[79] H. Zenner, Heidenreich, and I. R. Richter. "Dauerschwingfestigkeit bei nichtsynchroner mehrachsiger Beanspruchung". In: *Materialwissenschaft und Werkstofftechnik* 16.3 (1985), pp. 101–112.

[80] ISO. *ISO 10300-3:2014 - Calculation of load capacity of bevel gears - Part 3: Calculation of tooth root strength*. Switzerland: ISO copyright office, 2014.

[81] AGMA. *Appearance of Gear Teeth - Terminology of Wear and Failure*. ANSI/AGMA 1010-E95. Virginia: American Gear Manufacturers Association, 2007.

[82] A. Moore. “6472067-A: Investigation report - Gear and pinion neck bearing failure”. In: *Kongsberg and Eurofins* (2020).

[83] G. Balduzzi et al. “Non-prismatic beams: A simple and effective Timoshenko-like model”. In: *International Journal of Solids and Structures* 90 (2016), pp. 236–250. ISSN: 0020-7683. DOI: https://doi.org/10.1016/j.ijsolstr.2016.02.017.

[84] A. Beltempo et al. “Analytical derivation of a general 2D non-prismatic beam model based on the Hellinger–Reissner principle”. In: *Engineering Structures* 101 (2015), pp. 88–98. ISSN: 0141-0296. DOI: https://doi.org/10.1016/j.engstruct.2015.06.020.

[85] R. Weber et al. “Load stresses and residual stresses in the tooth interior A2 - Velex, Philippe”. In: *International Gear Conference 2014: 26th–28th August 2014, Lyon* (2014), pp. 804–813. ISSN: 978-1-78242-194-8. DOI: https://doi.org/10.1533/9781782421955.804. URL: https://www.sciencedirect.com/science/article/pii/B9781782421948500859.

[86] T.I. Arvidsen. *Technical Report: Klingelnberg Bevel Gear, stress prediction report*. Report. DNV for Rolls-Royce Marine, 2005.

[87] K. Varis et al. *Examination of the Crack Initiation and Propagation in a Spiral Bevel Gear*. Report. Stressfield for Rolls-Royce Marine, 2014.

[88] A. Bernasconi and I.V. Papadopoulos. “Efficiency of algorithms for shear stress amplitude calculation in critical plane class fatigue criteria”. In: *Computational Materials Science* 34 (2005), pp. 355–368.

[89] J.A. Araújo et al. “On the characterization of the critical plane with a simple and fast alternative measure of the shear stress amplitude in multiaxial fatigue”. In: *International Journal of Fatigue* 33.8 (2011), pp. 1092–1100. ISSN: 0142-1123. DOI: https://doi.org/10.1016/j.ijfatigue.2011.01.002.

[90] J. Papuga, E. Cízová, and A. Karolczuk. “Validating the Methods to Process the Stress Path in Multiaxial High-Cycle Fatigue Criteria”. In: *materials* 14.206 (2021).

[91] D. L. McDiarmid. “A general criterion for high cycle multiaxial fatigue failure”. In: *Fatigue Fract. Engng. Mater. Struct.* 14.4 (1991), pp. 429–453.

[92] T. Matake. “An Explanation on Fatigue Limit under Combined Stress”. In: *Bulletin of JSME* 20.141 (1977), pp. 257–263.

[93] J. L. Kenmeugne, J. L. Vidal-Salle E. Robert, and R. J. Bahuaud. “On a new multiaxial fatigue criterion based on a selective integration approach”. In: *Fatigue ’96, Proc. of the Sixth Int. Fatigue Congress* II (1996), pp. 1013–1018.

[94] J. Papuga. “Mapping of Fatigue Damages – Program Shell of FE-Calculation”. Thesis. 2005. DOI: http://www.pragtic.com/.

[95] J. Papuga. “Improvements of two criteria for multiaxial fatigue limit evaluation”. In: *Bull. Appl. Mech.* 5 (2010), pp. 80–86.

[96] J. Papuga. “A survey on evaluating the fatigue limit under multiaxial loading”. In: *International Journal of Fatigue* 33 (2011), pp. 153–165.

[97] ISO. *ISO 6336-5:2016 - Calculation of load capacity of spur and helical gears - Part 5: Strength and quality of materials*. Switzerland: ISO copyright office, 2016.

[98] M. Cerullo. “Application of Dang Van criterion to rolling contact fatigue in wind turbine roller bearings under elastohydrodynamic lubrication conditions”. In: *Proceedings of the Institution of Mechanical Engineers, Part C: Journal of Mechanical Engineering Science* 228.12 (2014), pp. 2079–2089. DOI: 10.1177/0954406213516946.

[99] H. Desimone, A. Bernasconi, and S. Beretta. “On the application of Dang Van criterion to rolling contact fatigue”. In: *Wear* 260.4-5 (2006), pp. 567–572. ISSN: 00431648. DOI: 10.1016/j.wear.2005.03.007.

[100] P. S. van Lieshout, J. H. den Besten, and M. L. Kaminski. “Validation of the corrected Dang Van multiaxial fatigue criterion applied to turret bearings of FPSO offloading buoys”. In: *Ships and Offshore Structures* 12.4 (2016), pp. 521–529. ISSN: 1744-5302 1754-212X. DOI: 10.1080/17445302.2016.1182461.

[101] T. Reimann. *Untersuchungen zur erweiterten Quantifizierung der Tellerradgrübchentragfähigkeit bei Kegelrad- und Hypoidverzahnungen*. Forschungsvorhaben Nr. 748 I. Forschungsvereinigung Antriebstechnik e.V., 2020.

[102] B. Kenmeugne et al. “More accurate taking into account of the large compressive mean stresses in fatigue criteria by a threshold approach”. In: *International Journal of Advanced Engineering Sciences and Technologies* 7.1 (2011), pp. 122–132.

[103] I.V. Papadopoulos et al. “A comparative study of multiaxial high-cycle fatigue criteria for metals”. In: *Int Jnl of Fatigue* 19 (1997), pp. 219–235.

[104] F. Fojtík et al. “Validation of Multiaxial Fatigue Strength Criteria on Specimens from Structural Steel in the High-Cycle Fatigue Region”. In: *Materials* 14.116 (2021). DOI: https://doi.org/10.3390/ma14010116.

[105] C. Wirth, B.-R. Höhn, and C. Braykoff. “New Methods for the Calculation of the Load Capacity of Bevel and Hypoid Gears”. In: *AGMA Technical Paper* 12FTM15 (2012).

Appendix A

Publications

A.1 Paper I

Abstract In this study, the microstructure of three large bevel gears with evident tooth flank fractures is investigated to define the effect of material inhomogeneities on the probability of subsurface initiated fatigue in case hardened structural steels. The observed micro-segregation structure in the core and case/core interface of the gear teeth features a bainitic and martensitic matrix with large variations in the local hardness. Applying an orthogonal shear stress based subsurface fatigue model, alongside a hardness map obtained through multiple hardness profile measurements, an improved method to predict tooth flank fracture is proposed.

Engineering Failure Analysis 110 (2020) 104415

Contents lists available at ScienceDirect

Engineering Failure Analysis

journal homepage: www.elsevier.com/locate/engfailanal

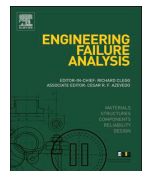

On subsurface initiated failures in marine bevel gears

Stephan André Böhme[a,*], Dmitry Merson[b], Alexei Vinogradov[a]

[a] Norwegian University of Science and Technology (NTNU), Department of Mechanical and Industrial Engineering, Trondheim 7491, Norway
[b] Togliatti State University, Institute of Advanced Technologies, Togliatti 445020, Russia

A B S T R A C T

In this study, the microstructure of three large bevel gears with evident tooth flank fractures is investigated to define the effect of material inhomogeneities on the probability of subsurface initiated fatigue in case hardened structural steels. The observed micro-segregation structure in the core and case/core interface of the gear teeth features a bainitic and martensitic matrix with large variations in the local hardness. Applying an orthogonal shear stress based subsurface fatigue model, alongside a hardness map obtained through multiple hardness profile measurements, an improved method to predict tooth flank fracture is proposed.

1. Introduction and motivation

Subsurface fatigue in cylindrical and bevel gears is a fatigue phenomenon, where cracks initiate in the transition zone between the hardened case and soft core [1–5]. For bevel gears, the failure mode is commonly referred to as subsurface fatigue [6], flank breakage [2] or tooth flank fracture (TFF) [1,7] and remains the most dominant failure mode for large bevel gears used in marine applications such as azimuthing thrusters, despite existing standards [6], technical reports [7] and ongoing research [1–3,5]. Typically, a TFF damage initiates and propagates parallel to the surface of the tooth under the acting shear stresses in mode II and alters its trajectory after a critical crack size has been reached, propagating in mode I under the acting bending stresses, resulting in large sections of the tooth breaking off.

To increase the load carrying capacity, marine bevel gears are case-carburized to an optimal case hardening depth (CHD), balancing the tooth flank's and root's safety factors [6]. TFF damages commonly initiate in a depth of 1 to 2 times the CHD. Whereas fine-grained martensite dominates the hard case of the gear, a coarser-grained martensitic and bainitic matrix represents the transition zone from case to core, and the positive surface near-compressive residual stresses are diminished or replaced by tensile residual stresses. Especially for large bevel gears, the microstructure, which has evolved in the course of the casting, forging and heat treatment process, becomes increasingly important as micro-segregations and elongated inclusions significantly influence the fatigue behaviour of the steel [8,9].

Aiming at developing potential mitigating solutions for subsurface failures, three failed marine bevel gear sets, used in the same thruster type but different installations, are studied to characterise the critical material microstructure in large bevel gears. Subsurface fatigue calculations according to a modified version of the classification rules set forth by DNV GL [6] are carried out for the gear's cross-section and compared to the measured hardness profiles, to investigate their applicability in capturing the documented damages. Whereas the stress state inside gear teeth is multiaxial and non-proportional, the studied criteria rely solemnly on a comparison between acting orthogonal shear stress, static residual stress and the local hardness or strength.

2. Background

Azimuthing thrusters are the preferred propulsion method for ships such as platform supply vessels, ferries, anchor handlers,

* Corresponding author.
E-mail address: stephan.a.bohme@ntnu.com (S.A. Böhme).

https://doi.org/10.1016/j.engfailanal.2020.104415
Received 9 October 2019; Received in revised form 23 January 2020; Accepted 27 January 2020
Available online 28 January 2020
1350-6307/

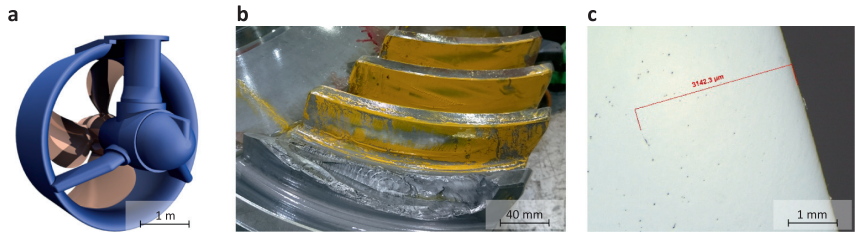

Fig. 1. Azimuthing thruster (a) inboard and underwater unit, (b) G1 gear failure and no load contact pattern, (c) G3 gear failure after cutting and polishing.

cruise, tug, drill and supply ships as they increase manoeuvrability, course stability and dynamic positioning capabilities. To transfer torque from an either horizontally or vertically mounted inboard motor one or two bevel gear stages are utilized. In the case of the studied gear sets, the engines were mounted horizontally, requiring two bevel gear stages with the failures occurring exclusively on the underwater gear set, closest to the propeller.

All gear sets are of the same design and 18CrNiMo7-6 high grade or ME quality steel [10,11], a common steel for highly strained carburized machine parts, such as gears and shafts. A typical azimuthing thruster, alongside gear failures one and three (G1, G3) are shown in Fig. 1. The subsurface failures on G3 were detected prior to their propagation to the surface of the gear teeth by means of ultrasonic scanning using a portable phased array detector. 9 of the 14 teeth on G3 showed crack-like indications, with some teeth revealing multiple defects along the tooth width. Whereas all defects were scanned to be approximately 5 mm in length, their length- and heightwise positions as much as initiation depth varied across the tooth flank and are illustrated in Figs. 6 and 7. The depicted crack extends 0.5 mm in heightwise direction and was found 3.1 mm below the load carrying flank.

Gear sets main geometry and load parameters are listed in Table 1. The subsurface stress state inside a bevel gear tooth resembles a rolling contact fatigue (RCF) situation found in bearings or railways, where cyclic loading causes microcracks to develop at material inhomogeneities. Whereas the stress state in bearings and railways is to a large extent governed by the Hertzian contact theory, out of phase bending, shear and residual stresses further complicate the loading of gears. By nature, the stress state is complex and multiaxial, with changing principal stress directions during a loading cycle [1,3,12,13]. Similar to RCF found in bearings, the orthogonal shear stresses as a result of the Hertzian contact play a critical role and depend on the contact stress σ_H and equivalent radius of curvature ρ_{eq}. Both parameters are a result of the gear's macro- and microgeometry, the applied load, as much as the gear's deflections.

3. Experimental procedure

The macro- and microscopic analysis of the fracture surfaces and sectioned gear teeth were carried out to study the crack initiation and propagation through the gear teeth and to quantify the failure mode, subsurface material properties and potential inhomogeneities as documented in [8,9]. After the initial macroscopic study of the fracture surfaces G1 and G2, both teeth were cut 5 mm to either side of the crack initiation, and longitudinal and transverse cross-sections were prepared. Out of the remaining centrepieces of G1 and G2, plane specimen were created, enabling a scanning electron microscopy (SEM) study of the early stages of the subsurface crack evolution. The subsurface defects in G3 were detected through ultrasonic scanning during a service procedure followed by sectioning and grinding the gear teeth in the transverse direction.

To identify the crack origin location and to determine the failure mode and crack propagation mechanism, the fracture surfaces of failures G1 and G2 were analysed using a Hirox RH-2000 digital microscope prior to sectioning the teeth. A secondary, more detailed analysis of the crack origin location was conducted, using a FEI Helios scanning electron microscope and a Hitachi SU6600 FESEM microscope. Both SEMs were equipped with an energy-dispersive X-ray scanner (EDS) to investigate the chemical composition of relevant material depth. In order to classify the gear damages, the fracture path and location on all gear teeth were compared to defining characteristics of TFF damages as outlined in [1,5,13]. Due to the small size of the subsurface defect detected on G3, normal

Table 1
Gear and load parameters.

Description	Unit	Pinion	Wheel
Pressure angle, α	deg	20	
Number of teeth, z		14	37
Outer pitch diameter, d_e	mm	348.1	920.1
Tooth width	mm	170	
Mean spiral angle, β_m	deg	35	
Case hardening depth, CHD	mm	2.6	
Power	kW	2500	
RPM	1/min	660	249.7

sections through teeth 6 and 9 were prepared to enable a study of cross-sections of the defects using optical microscopy, SEM and EDS.

The analysis of the microstructure of the specimen was carried by means of laser microscopy (Olympus LEXT OLS4000 laser microscope) at magnifications 50, 100, 250, 650 and 1300 times. In order to describe the transition from the carburized layer to the interior of the tooth, images were taken on the surface, in a 5 mm depth and in the core. The macroscopic images of longitudinal and transverse cross-sections shown in Fig. 3 were taken with a Zeiss Stemi-2000C stereoscopic microscope after mechanically polishing the specimen to a mirror-like finish on a Struers polishing machine and etching in a 4% alcoholic solution of HNO_3. To quantify the observed microstructural differences and produced contra the specified CHD, Vickers hardness measurements were performed in accordance to the ISO6507 standard [14] on a hardness tester with loads of 1 and 10 kgf. In order to document the variation of the hardness profile from root to tip, HV10 hardness measurement were carried out on G1 and G2 near the crack and towards the tip of the transverse cross-section and on G3 close to the tooth root, the approximate pitch height and the tip of the tooth (see Fig. 4a and Table 2 for exact locations). Additional HV10 core hardness measurements were taken on all teeth. 20 low-force Vickers hardness measurements in the approximate CHD region and core of gear teeth 6 and 9 of G3 were carried out to quantify the effect of an increasingly bainitic microstructure on the hardness distribution.

Evaluation of non-metallic inclusions was carried out on an Axiovert 40MAT inverted microscope, equipped with image recognition metallographic software Thixomet Pro^{TM}. The size and number of inclusions were characterized according to the ASTM E45 standard [15], method A for inclusion type D (globular type), differentiating between thick and fine series. Analysed were the transverse and longitudinal cross-sections of G1 and G2 and the transverse cross-section of G3. It was the intention to quantify the effect of hot forging on the shape, size and orientation of the inclusions and thereby describe the anisotropy of the mechanical and fatigue properties of the steel [8,9]. Additionally, the prior austenite grain size was evaluated through optical microscopy in accordance to the ISO643 standard [16] on the Nital-etched G3 surfaces.

4. Subsurface fatigue

Assuming purely elastic material behaviour, the subsurface stresses in gears present themselves as a superposition of load induced and manufacturing related stresses, which are locally elevated by inclusions or asperities in the contact. Similarly to bearings, a rolling contact evolves between the teeth of pinion and wheel, where surface stresses are suitably described through the Hertzian contact model and frictional shear stresses. As the evolving contact line moves across the tooth flank, the orientation of the subsurface principle stress tensor changes, resulting in a rotating multiaxial stress state.

Despite 20 years of research [1–3,5] and emerging standards [6,7], subsurface fatigue remains the most critical failure mode for marine bevel gears, with significant financial implications in case of vessel downtime due to unforeseen failures. To tackle this industry-wide problem, a cooperation between thruster suppliers, gear, steel and forging companies alongside the classification society DNV GL was initiated in 2012. In the first phase of the joint industry project (JIP), an anonymous database of gear failures was provided by and shared between all partners, revealing that of the 86 studied gear failures, 51 were classified as or likely subsurface fatigue failures. Hardening layer measurements, carried out for 70 gear sets show that 61% of all cases had a thinner than specified CHD, as a result of either excessive material removal during hard machining or faulty heat treatment.

Historically, the specification of the CHD for bevel gears is based on suggestions for cylindrical gears and given as a ratio to the normal module m_{nm}, usually 0.1 to 0.4 depending on if the root of flank is optimized [11]. Later publications on the mater [17] show that the equivalent radius of curvature in the midpoint is a superior measure when designing the flank's CHD for bevel gears. Applying [17] to the JIP database, only 22% of all specified hardening layer thicknesses are deemed appropriate. Clearly, the large discrepancy between specified and measured CHD and possibly a non-conservative specification to begin with, can be seen as a partial explanation to the high number of subsurface fatigue failures in the industry, alongside the micro-segregation structure, found in large bevel gears (see chapter 5.2).

A gear standard for subsurface fatigue should be conservative and account for manufacturing and load uncertainties, yielding acceptably low failure probabilities. Torque measurements on failure prone platform supply vessels prove that gears are commonly loaded below the design limits used in the classification process for the gears with the occasional high loads in extreme weather conditions. High subsurface fatigue failure frequencies, alongside mostly moderate loads during operation prove that the current version of the DNV GL [6] standard is non-conservative. Simply requiring a higher safety factor is not feasible, as the standard commonly leads to an increased surface hardness, rather than deeper CHD, as the criterion predicts failures in the depth of the largest shear stresses rather than the transition between case and core (see Table 5 in Section 5.5). Keeping the applicability of the calculation model high, modifications to the existing standard are proposed, improving the correlation between acting and modelled stresses and expected material strength, whilst keeping with the linear, standard-like calculation approach.

The DNV GL method [6] for subsurface fatigue, similarly to Lundberg and Palmgren's model for bearings [18], is based on a comparison of the local orthogonal shear stress amplitude and shear strength. Compared are the local orthogonal shear stress as a function of the rolling contact between pinion and wheel, assuming a homogenous and isotropic material, linear elastic material behaviour, and an otherwise stress-free material. Early stage subsurface fatigue failures show that cracks initiate parallel to the surface (see Fig. 1c), limiting the analysis of the load induced stresses in the DNV GL method to a set of surface parallel planes. The methods disregards the transverse shear, friction and bending stresses and solemnly considering the subsurface stresses as a result of the Hertzian contact.

For a plane parallel to the surface the DNV GL and Findley criterion [3] are essentially identical as the Findley criterion's maximum normal stresses on the critical plane are assumed to be zero. During a tooth engagement, the maximum normal stress on a

plane parallel to the surface equals the normal residual stress, which is commonly assumed to be zero for carburized parts [3,19]. Without the effect of compressive residual stresses in the hard case of a gear tooth, the DNV GL method predicts a crack initiation in the depth of the maximum orthogonal shear stress, rather than the transition between hard case and soft core. For bevel gears, this leads to increasing surface hardness requirements rather than increasing CHD to avoid subsurface fatigue failures. In an attempt to correctly predict the fatigue initiation depth and improve the design process for marine bevel gears an alternative method, based on the Dang Van multiaxial fatigue criterion is proposed.

Adhering to the above stated assumptions, that only planes parallel to the surface are considered, the orthogonal shear stress amplitude $\tau_{a,DNV}$ is adopted from the original DNV GL method. The formulation makes use of the correlation between maximum Hertzian σ_{HR} and maximum orthogonal shear stress amplitude of 0.25 and the maximum depth of the shear stress in 0.5 times the half Hertzian contact width b_H. In alignment with the DNV GL method [6], a safety factor S_{Hss} is introduced to the stress and half Hertzian contact width.

$$\tau_{a,DNV}(x) = 0.25\ S_{Hss}\ \sigma_{HR}\ \cos\left(\frac{\frac{x}{b_H} - 0.5}{\frac{x}{b_H} + 0.5} \cdot 90^{\circ}\right) \tag{1}$$

Neutron diffraction [3,20,21], X-ray diffraction and contour method [5] residual stress measurements on gears prove the effectiveness of the carburizing and quenching cycle in introducing compressive residual stresses in the hard case. Fulfilling the equilibrium condition, tensile residual stresses are present in the interior of the tooth and increase towards the narrower tooth tip [5,13,20,21]. For the surface and hard case of the tooth, the model by Lang [19] is often times applied, whereas a 3rd order polynomial seems best suited to describe the transition from case to core and the level of tensile residual stresses [5]. The consideration of tensile residual stresses for subsurface fatigue calculations is critical, but requires iterative calculations to achieve equilibrium conditions for each subsurface element and cross section. In order to ensure a linear, standard-like calculation of the modified DNV GL method, tensile residual stresses are disregarded from the subsurface stress calculation, but partially considered through an elevated half Hertzian contact width (factor 1.1 in Eq.(2)). The model aligns itself thereby with the FVA and ISO [1,7]. To ensure comparability between gear rating calculations and more accurate local methods such as Becal, the mid-zone factor Z_{MB} is introduced to the gear rating calculation. It increases the equivalent radius of curvature ρ_{eq} by shifting the studied contact from the pitch to the midpoint of the contact line. The half Hertzian contact width b_H is calculated as:

$$b_H = 1.1\ S_{Hss}\left(4\ \sigma_{HR}\frac{\rho_{eq}}{Z_{MB}^2}\cdot\frac{(1-\nu^2)}{E}\right) \tag{2}$$

where ν is the Poisson ration and E is the Young's modulus of the material. The mid-zone factor Z_{MB} according to ISO10300 [22] can be simplified to always predict the midpoint rather than single point of contact [17] using the transverse pressure angle α_{et}, virtual base diameter d_{vb}, tip diameter d_{va}, number of teeth z_v and transverse contact ratio $\varepsilon_{v\alpha}$:

$$Z_M = \frac{\tan\alpha_{et}}{\sqrt{\left[\sqrt{\left(\frac{d_{va1}}{d_{vb1}}\right)^2 - 1} - \varepsilon_{v\alpha}\frac{\pi}{z_{v1}}\right]\cdot\left[\sqrt{\left(\frac{d_{va2}}{d_{vb2}}\right)^2 - 1} - \varepsilon_{v\alpha}\frac{\pi}{z_{v2}}\right]}} \tag{3}$$

Besides the orthogonal shear stresses, the compressive residual stresses σ_{res} in the hard case need to be estimated [12,19] as

$$\sigma_{res}(x) = -1.25\ (HV(x) - HV_c),\ \ for\ HV(x) - HV_c \le 300 \tag{4}$$

$$\sigma_{res}(x) = 0.2857\ (HV(x) - HV_c) - 460,\ \ else$$

where HV_c represents the core and $HV(x)$ the local hardness of the gear tooth. The linear correlation between the material hardness HV and the shear fatigue strength t_{-1} of 0.625 for the original DNV GL model is modified to 0.571 or 4/7 to account for the high failure probability using the current design approach and to take the documented macro- and micro-hardness differences in large bevel gears into account (see Sections 5.2 and 5.3):

$$t_{-1}(x) = 0.571\ HV(x) \tag{5}$$

Ideally, the influencing factors accounting for the very high cycle fatigue behaviour of the material and a size factor, considering the hardenability of large gears and any statistical size effects should be applied here. They are part of ongoing investigations and will be covered in later publications. Also material strength effects, related to the production or refinement of the steel should be considered here, for example electro-slag remelting.

The variant of the Dang Van criterion found in [23] considers the shear stress amplitude on every material plane alongside the maximum hydrostatic stress max($\sigma_{Hyd}(x,t)$) per volume element during a load cycle or tooth engagement. Since the Hertzian stresses are compressive and large in comparison to the static residual stresses, the maximum hydrostatic stress can be simplified to the trace of the residual stress matrix or 2/3 of the tangential or radial residual stress $\sigma_{res}(x)$, as they are measured to be approximately equal. Assuming that all subsurface fatigue failures initiate parallel to the surface, the above-proposed approach to predict the local orthogonal shear stress amplitude $\tau_{a,DNV}(x)$ is applicable. When deriving the local material utilization $D(x)$, two model constants α and $\beta(x)$ define the influence of the maximum hydrostatic stress on the equivalent stress $f(x)$ and the material strength that the stress is compared to. Assuming ductile material behaviour, represented through a fatigue ratio κ of $3^{0.5}$ between the alternating uniaxial and

shear fatigue strength, along with a model set-up comparing the equivalent stress to the local shear fatigue strength $t_{-1}(x)$, the Dang Van criterion calculates the following:

$$\alpha = 3/\kappa - 3/2 = \sqrt{3} - 3/2$$
$$\beta(x) = t_{-1}(x)$$
$$f(x) = \tau_{a,DNV}(x) + \alpha \max(\sigma_{Hyd}(x,t)) = \tau_{a,DNV}(x) + 2/3\ \alpha\ \sigma_{res}(x) \approx \tau_{a,DNV}(x) + 0.155\ \sigma_{res}(x) \quad (6)$$
$$D(x) = f(x)/\beta(x) = f(x)/t_{-1}(x)$$

5. Results & discussion

Based on the product documentation and material certificates, all gear sets fulfil the requirements set forth by [10,11] for ME or high-grade quality gear steel and specific drawing requirements in regards to the chemical composition, forging reduction ratios, material cleanliness, achieved surface hardness and CHD on the material coupons. Whereas G1 and G2 showed failures on individual wheel teeth, the subsurface cracks on G3 initiated on 9 out of 14 pinion teeth. The location of the failures of G1 and G2 coincides with the highly stressed section of the tooth, both in the heightwise and lengthwise directions, but is abnormally position towards the toe on G3.

5.1. Fracture surface

The G1 fracture surface given in Fig. 2a shows clear signs of subsurface initiated failure from a single nucleation spot, alongside signs of a fatigue crack propagation into the interior of the tooth and towards the tooth root of the opposite flank, forming an approximately 50° angle to the load-carrying convex tooth flank. Macroscopic fatigue features such as beach marks are clearly visible in the interior of the tooth, indicating the progression of the crack caused by load changes during operation. Ratchet marks towards the extreme ends of the crack surface in the toe and heel region combined with a small instantaneous fracture area; underline the high ductility of the material.

The topographic image of the initiation site (Fig. 2b) features two ridges, meeting in the approximate location where the crack initiated. Whereas the fracture surface shows an even crack propagation into the core of the tooth, level changes are visible towards the surface of the tooth. The SEM analysis of the crack initiation side did not reveal fatigue striations or an inclusion, but rather a large degree of plastic deformation caused by the relative motion between the two crack surfaces. The same is true for fracture surface on G2, where an even larger degree of plastic deformation removed also macroscopic fracture features.

5.2. Microstructure

Low magnification images of the polished and etched transverse and longitudinal cross-sections of G1 and G2 show a coarse and inhomogeneous, dendritic microstructure throughout both cross-sections, but no apparent directionality (see Fig. 3). Segregations appear as a result of the solidification process of the steel after casting, where regions that convert to the solid-state first, have different chemical compositions than the material nucleating at later stages. The subsequent carburization and quenching stages lead to different cooling responses from the austenitizing temperature, resulting in a higher carbon concentration in the alloy-rich areas with corresponding hardness differences. As per the material certificates of the gear sets, both wheels were ring-forged to a reduction ratio greater than four. The polished and Nital-etched transverse cross-section of G3 features a favourable segregation structure as the dendrites appear to be broken up. The forging process for the pinion gear was stretching-upsetting-stretching with a similarly large reduction ratio as for the wheels.

Throughout all gear sets, the fine martensitic microstructure with a fraction of retained austenite was observed in the carbon-rich surface layer, coupled with the coarse tempered martensitic structure combined with bainite in the core. The study of the microstructure surrounding the subsurface crack of G3 after etching the cross-section with the Nital solution, revealed a white etching area (WEA) indicating alterations in the microstructure from local plastic deformation. The branching, occurring towards the end of the crack (Fig. 5b), is indicative of the transition from the stage B to C for RCF subsurface damages progression, where alternating tensile-compressive stresses and not shear stresses are driving the crack propagation.

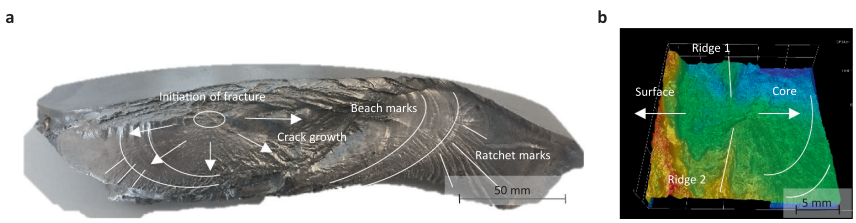

Fig. 2. Fractured tooth and failure initiation site of G1 with (a) macroscopic (b) microscopic features.

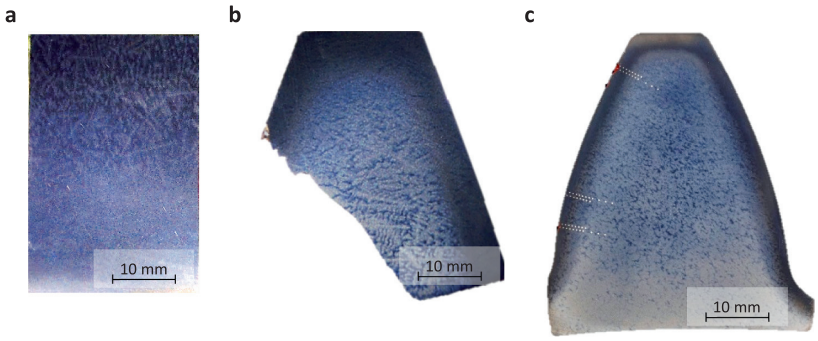

Fig. 3. Cross sections etched with Nital of G1 (a) longitudinal, (b) transverse and (c) G3 transverse.

5.3. Hardness

Three hardness profiles in tooth height direction were obtained for teeth 6 and 9 of G3 and two profiles on G1 and G2 (see Table 2). The hardness requirements are a minimal CHD of 2.6 mm, a surface hardness of 690 HV and a core hardness of 350 HV. Rather than featuring similar hardnesses across the three gear sets, a large process variation is apparent for the case-carburizing process, where especially the CHD varies significantly. The results furthermore underline the findings of Tobie [24] that for large gears, the difference in CHD from the tooth tip to the tooth root has to be expected. Tobie documents the 10–15% reduction in CHD from flank to root for cylindrical gears, whereas the trend for bevel gears seems to be even larger and is in the order of 20% for the studied gears. Towards the often unmachined tip, an in average 16% higher CHD than in the middle of the tooth was found.

Four low-force Vickers hardness measurements were carried out on tooth 6 and 9 in the martensitic case and martensitic and bainitic core of G3 (see Table 3). Despite the lack of a coarse dendritic microstructure, significant low-force hardness differences remain in G3 with an increasing trend towards the core. Assuming that subsurface fatigue failures can also initiate from large bainite grains, micro- rather than macro-hardnesses should be used for a subsurface fatigue estimation.

For the discretization of the hardness measurements, the model by Thomas [25] was used and is visualized for the three measured hardness profiles on the tooth 9 of G3 in Fig. 4a. Other commonly used hardness models [3,19] were also tested, but are not recommended for large bevel gears as both methods fail to predict hardness profiles crossing the specified CHD, and, in the case of [19], overestimates the hardness in the transition zone from hard case to soft core.

Even though for the production of large bevel gears 18CrNiMo7-6 steel variants are purposefully chosen with favourable alloying compositions to ensure exceptional hardenability, the microstructure in the core and case/core interface presents itself as a combination of bainite and martensite. The resulting low force and macro hardness differences will contribute to a weakening of the subsurface layers and thereby an increased risk for TFF. For the presented subsurface fatigue model, those differences should be considered through a size factor and not as a modified fatigue strength. More HV1 hardness measurements on differently sized gear sets are necessary to derive such a size factor quantitatively. Continuing with the discretized HV10 profiles, a hardness map for a G3 pinion cross section is visualised in Fig. 4.

The shown hardness map for G3 displays the described hardness change across the tooth height with a significantly thinner case depth in the root contra the midpoint and tip of the flank. As a result of faster quenching times towards to the tooth tip, also the core hardness increases.

5.4. Inclusions and grain size

The dominant inclusion type was identified as the manganese sulphide (MnS) alongside traces of the aluminium oxide (Al_2O_3). Volume fraction measurements show an exponential distribution towards smaller inclusion sizes with approximately 60% of all inclusions being smaller than 2.7 µm. In the longitudinal cross-sections of G1 and G2, no elongated inclusions were detected. Listed

Table 2
Hardness measurements in varying positions.

ISO6507 – HV10	Unit	G1		G2		G3 – Tooth 6		
		Crack	Tip	Crack	Tip	Root	Pitch	Tip
Tip distance	mm	10	4	15	6	30	22.5	6
CHD	mm	3	3.7	2.5	2.6	1.5	2.1	2.4
HV_S	HV10	430	640	690	705	697	700	705
HV_C	HV10	388	390	380	368	329	352	367

Table 3
Low force hardness measurement on tooth 6 and 9 of G3.

ISO6507 – HV1	Unit	Tooth 6		Tooth 9	
		CHD	Core	CHD	Core
Mean	HV	538	340	571	328
Standard deviation	HV	21	33	19	27

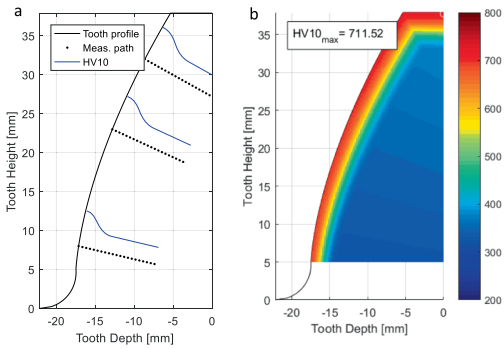

Fig. 4. G3 HV10 hardness as (a) measurement path and (b) local hardness map.

inclusion distributions shown in Table 4 are within the requirements for MQ quality gear steels outlined in ISO6336-5 but outside of the ME requirement for the fine series [11].

Additional EDS mapping of the subsurface crack on G3 did not reveal an inclusion along the crack path (see Fig. 5).

As described above, the plane specimens were produced of the initiation regions of G1 and G2 and studied under a Hirox RH-2000 optical microscope and FEI Helios NanoLab SEM microscope. The SE microscope was equipped with an EDS scanner to study the chemical composition in relevant region. No inclusions or traces of inclusions were found on in the initiation site on either G1 and G2, possibly due to excessive plastic deformation of the crack surfaces during the crack propagation or because the crack initiated in the matrix from a large bainite grain or from a void. Typical globular MnS inclusions were identified along the crack front on G1.

Prior austenite grain size was evaluated through optical microscopy in accordance to the ISO643 standard [16] on the Nital etched surfaces of G3. Grain size index on G3, tooth 6 and 9 was measured to G = 8–8.5 with an average prior austenite grain size of 12–22 μm.

5.5. Model results

The in Section 4 outlined subsurface fatigue model can be applied to gear rating standards such as the ISO10300 [22] or DNV GL-CG-0036 [6] and more accurate local calculation methods such as Becal. Table 5 lists the relevant parameters for a DNV GL-CG-0036 based calculation of the three studied gear sets. Since all gears have the same geometry and rating, the load parameters are comparable and only the strength of the material, defined through the measured hardness profiles varies. Shown are also the results for the conventional DNV GL subsurface fatigue standard, underlining the motivation for the proposed changes, as for G1 and G2, the crack initiation is predicted near the maximum orthogonal shear stresses rather the transition from case to core.

The table also lists the depth of the ultrasonic measured crack indications for G3 and initiation depth on the fracture surfaces of G1 and G2, proving a good correlation between the measurements and predictions of the revised model. Fig. 6 documents the material utilization for a G3 pinion cross-section based on the local calculation approach and measured hardness map, its maximum of 1.02 in 3.8 mm, along with the position and depth of all measured indications. The lengthwise position of the analysed cross-section and subsurface indications is given in Fig. 7.

Table 4
Inclusion classification in transverse and longitudinal direction.

ASTM E45 - A	G1		G2		G3
Inclusion type D (globular)	Trans.	Long.	Trans.	Long.	Trans.
Fine	1.5	1.5	1.5	1.5	2.0
Thick	0.5	0.5	0.5	0.5	

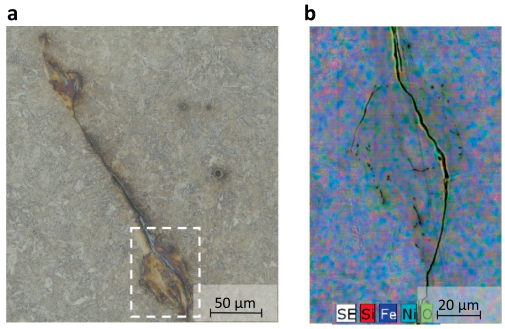

Fig. 5. Optical microscopy of crack on G3 after etching with Nital (a) and (b) the SEM EDS map corresponding to the fragment of the crack shown by a dashed rectangle in (a).

Table 5
Material utilizations for G1, G2 and G3 according to DNV GL and revised model.

		G1	G2	G3
Equivalent radius of curvature, ρ_{eq}	mm	64.9		
Surface pressure, σ_{HR}	MPa	1443		
Case hardening depth, CHD	mm	3.0	2.5	2.1
Surface hardness, HV_S	HV	(6 9 0)	690	700
Core hardness, HV_c	HV	388	380	352
Maximum DNV GL utilization and depth, D_{DNV}	–/mm	0.87/1.3	0.88/1.4	0.95/3.5
Maximum utilization an depth, D	–/mm	0.84/4.8	0.90/4.2	0.99/3.9
Measured failure depth	mm	5.5	4	2.5–3.8

As most G3 indications were found in a toe-orientated position, the contact pattern as a product of all relevant deflections under load was offset using a 0.6 mm axial pinion displacement. The resulting contact pattern and stress distribution correspond well with the position of the observed subsurface indications. As the pattern shifts towards the toe, the heightwise stress profile as shown in Fig. 6 shifts towards the root of the flank. Regardless, not the pitch point but midpoint is critical for the predicted subsurface material utilization, proving the applicability of the mid-zone factor Z_M for gear rating standards such as DNV GL-CG-0036 [6].

For G1 and G2, the maximum material utilizations are 0.84 and 0.90 for the gear rating standard and 0.85 and 0.93 for the local calculation method and visualized for the mean wheel cross section in Fig. 8. Also shown are the measured crack initiation points, maximum predicted utilizations and crack path for both gears sets.

A good correlation between the model and failure locations is proven for all three studied failures. Keeping with the safety factor requirement outlined in DNV GL-CG-0036 [6], a maximum material utilization of 0.833 or minimum safety factor S_{Hss} of 1.2 is required, deeming all three gear sets as critical in regards to subsurface fatigue. The extremely large material utilization of 1.02 on G1 corresponds well with the number of reported subsurface indications. As failures tend to initialize half way up the tooth, moderate tensile residual stresses can be expected in the critical subsurface material layers, which are adequately represented by the elevated

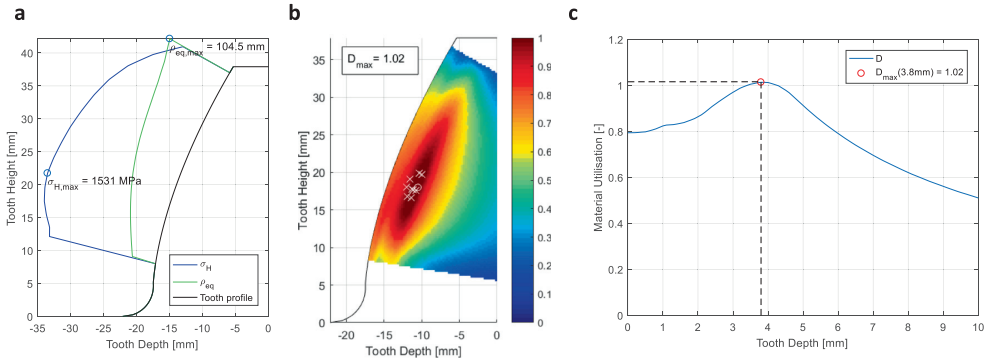

Fig. 6. Loading and material utilization as (a) Becal contact stress and equivalent radius of curvature, (b) DNV material utilization map (crosses for position and depth of UT indications) and (c) path through maximum.

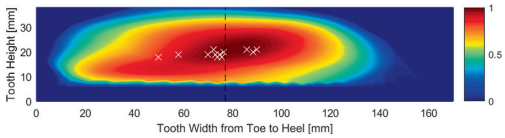

Fig. 7. G3 material utilization for pinion flank (crosses for position of the UT indications; dotted line representing the analysed cross section in Fig. 6).

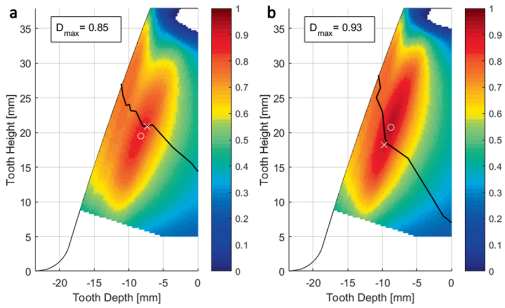

Fig. 8. Material utilization, fracture path and fracture point for (a) mean gearwheel cross section of G1 and (b) mean gearwheel cross section of G2.

half Hertzian contact width b_H (see equation (2)) and thereby the depth of the acting shear stresses.

A comparison between the necessary CHD based on the outlined method in [17] and the presented subsurface fatigue model, aligns well, as both suggest a CHD of 3.1 mm to avoid subsurface fatigue on the studied gear design. A linear correlation between hardness and shear strength is at best applicable for hardness values below 400 HV [26] and a fatigue ratio κ of $3^{0.5}$ only valid for highly ductile materials and not the hard case of the gear tooth. Extensive fatigue testing to derive the very high cycle fatigue behaviour, strength and hardness correlation and fatigue ratio, alongside a comparison to more advanced multiaxial fatigue models, considering all stress components is intended for later publications.

6. Conclusion

The presented gear damages can all be classified as tooth flank fractures with apparent crack initiations in the transition zone from hard case to soft core and subsequent crack growth towards the root of the unloaded flank, breaking off large sections of the gear tooth. A strong correlation was found between the depth of the cracks and the manufactured case hardening depth, which varied significantly from gear set to gear set and along the tooth profile. In case of the studied pinion, a shallow hardening layer of 2.1 mm resulted in multiple failures approximate 3 mm below the surface, whereas the studied wheels had a 2.5 to 3 mm case depth and failures in 4 to 5.5 mm. Typically, the failures initiate in a half tooth height, heel orientated position, where the combination of high loads and large curvatures results in particularly deep subsurface stresses. Only the pinion showed an abnormally toe orientated fracture, possibly indicative of excessive material removal during the final machining in this area or a misplaced contact pattern during operation. The early stage tooth flank fracture on the pinion teeth showed a crack initiation and early propagation parallel to the gear flank, indicating a mode II and shear stress initiated failure. The orientation and the shape of the fracture surfaces of the two terminal stage wheel failures support a transition from mode II to I under acting bending stresses.

Besides the apparent effect of the hardening layer thickness on subsurface fatigue, the variation of the hardness at a given depth was proven to be critical. On large gears, an inhomogeneous material microstructure with clear micro-segregations in longitudinal and transverse direction has to be expected with consequences on the micro-hardness of the material and thereby the likelihood of subsurface initiated fatigue cracks. As none of the studied gear sets shows a crack initiation from inclusions, an initiation from large, softer bainite grains seems plausible. Low-force hardness measurements prove suitable to describe these local differences of an increasingly bainitic matrix from case to core.

While surely not the only definition of the Dang Van fatigue criterion, the proposed method enables a simple consideration of the compressive residual stresses in the case, achieving a significantly better correlation between predicted and observed initiation depth of subsurface failures.

Declaration of Competing Interest

The authors declared that there is no conflict of interest.

Acknowledgement

The authors would like to thank the staff of the Institute of Advanced Technologies of the Togliatti State University, who supported the research into the microstructure of the presented gear failures along with the materials technology and failure group of DNV GL for their contributions and input. Gratitude is also extended to the JIP partners for supporting this investigation.

References

[1] I. Boiadjiev, J. Witzig, T. Tobie, K. Stahl, Tooth flank fracture – basic principles and calculation model for a subsurface initiated fatigue failure mode of case hardened gears A2 – Velex, Philippe, International Gear Conference 2014: 26th–28th August 2014, Chandos Publishing, LyonOxford, 2014, pp. 670–680.
[2] M. Klein, J. Seabra, B.R. Höhn, K. Michaelis, R. Annast, Theoretical and experimental investigations about flank breakage in bevel gears, Ind. Lubr. Tribol. 63 (1) (2011) 5–10.
[3] M. MackAldener, Tooth Interior Fatigue Fracture & Robustness of Gears, PhD, Department of Machine Design, KTH – Stockholm, Stockholm, 2001.
[4] Y. Song, S. Sasaki, A study on the subsurface strength of marine bevel gears, *International Symposium on*, Marine Engineering (2011).
[5] R. Weber, Auslegungskonzept gegen Volumenversagen in einsatzgehärteten Stirnradern, PhD, Institut für Werkstofftechnik, Universität Kassel, 2015.
[6] DNVGL-CG-0036: Calculation of gear rating for marine transmissions, 2015.
[7] ISO/TS 6336-4:2019 – Calculation of load capacity of spur and helical gears – Part 4: Calculation of tooth flank fracture load capacity, 2019.
[8] R.K.A. Mathesiusova, The difference in quality of 18CrNiMo7-6 Steel and its influences at deformation after carburizing, presented at the Metal 2012, Brno, Czech Republic, 2012.
[9] E. Pessard, F. Morel, C. Verdu, L. Flacelière, G. Baudry, Microstructural heterogeneities and fatigue anisotropy of forged steels, Mater. Sci. Eng. A 529 (2011) 289–299.
[10] DNV: General Requirements for Materials – Pt.2 Ch.1, 2011.
[11] ISO 6336-5:2016 – Calculation of load capacity of spur and helical gears – Part 5: Strength and quality of materials, 2016.
[12] T. Hertter, Rechnerischer Festigkeitsnachweis der Ermüdungstragfähigkeit vergüteter und einsatzgehärteter Stirnräder, Doktor-Ingenieur, Fakultät für Maschinenwesen, Technische Universität München, München, 2003.
[13] J. Witzig, Entwicklung eines erweiterten Berechnungsverfahrens zur Ermittlung optimaler Zahnflankentragfähigkeit bis in den Bereich grosser Werkstofftiefe, in Forschungsvorhaben Nr. 556 I, 2012.
[14] ISO 6507-1:2018 – Metallic materials – Vickers hardness test – Part 1: Test method, 2018.
[15] ASTM E45:18a – Standard Test Methods for Determining the Inclusion Content of Steel, 2018.
[16] ISO 643:2012 – Steels – Micrographic determination fo the apparant grain size, 2012.
[17] C. Wirth, Normgerechte Wahl zur Einsatzhärtetiefe der Kegelräder, in Forschungsvorhaben Nr. 509, Forschungsstelle für Zahnräder und Getriebebau2009, vol. FVA 509.
[18] G.P.A. Lundberg, Dynamic capacity of roller bearings, Acta Polytechnica Mech. Eng. Ser. 96 4 (2) (1952).
[19] O.R. Lang, Berechnung und Auslegung induktiv randschichtgehärteter Bauteile, Kloos, K. H. (Hrsg.); Grosch, J. (Hrsg.): Induktives Randschichthärten. Berichtsband, Tagung 23. bis 25. März 1988, München: Arbeitsgemeinschaft Wärmebehandlung und Werkstofftechnik (AWT), 1989, pp. 332–348.
[20] R.L. Peng, B. T., Neutron Diffraction Measurement of Residual Stress in Two Carburised Gear Teeth, Nyköping, 2003.
[21] R.L.S.A. Peng, Neutron Diffraction Measurements of Residual Stress in Two Carburised Gear Teeth, Studsvik Neutron Research Laboratory, 2012.
[22] ISO 10300-1:2014 – Calculation of load capacity of bevel gears, 2014.
[23] J. Papuga, A survey on evaluating the fatigue limit under multiaxial loading, Int. J. Fatigue 33 (2011) 153–165.
[24] T. Tobie, Härtetiefen-Großzahnräder, in Forschungsvorhaben Nr. 271, Forschungsstelle für Zahnräder und Getriebebau, 2001.
[25] J. Thomas, Flankentragfähigkeit und Laufverhalten von hart-feinbearbeiteten Kegelrädern, PhD, TU München, Munich, 1998.
[26] Y. Murakami, Metal Fatigue: Effects of Small Defects and Nonmetallic Inclusions, Academic Press, 2019.

A.2 Paper II

Abstract In this study, a testing and modelling concept is presented, aimed at estimating the local fatigue properties of carburised CrNiMo steel, covering the fatigue limit under axial and torsional loading at various mean stresses. Aimed at predicting the bulk material properties, all specimens were ultrasonic shotpeened prior to testing. Fractographic analyses were conducted on all specimens using scanning electron microscopy to define the type, size and chemical composition of crack initiation-related discontinuities. An iteration of the FKM guideline is presented, relying on the external notch concept to explain the effect of large internal notches on the mean stress sensitivity.

Received: 3 August 2020 | Revised: 19 October 2020 | Accepted: 14 November 2020

DOI: 10.1111/ffe.13394

ORIGINAL CONTRIBUTION

FFEMS Fatigue & Fracture of Engineering Materials & Structures WILEY

Fatigue of carburised CrNiMo steel: Testing and modelling concept

Stephan André Böhme[1] | **Alexei Vinogradov**[1] | **Horst Biermann**[2] | **Anja Weidner**[2] | **Alexander Schmiedel**[2] | **Sebastian Henkel**[2]

[1]Department of Mechanical and Industrial Engineering, Norwegian University of Science and Technology (NTNU), Trondheim, 7491, Norway

[2]Institute of Materials Engineering, Technische Universität Bergakademie Freiberg, Gustav-Zeuner-Straße 5, Freiberg, D-09599, Germany

Correspondence
Stephan André Böhme, Norwegian University of Science and Technology (NTNU), Department of Mechanical and Industrial Engineering, Trondheim 7491, Norway.
Email: stephan.a.bohme@ntnu.no

Funding information
Norges Forskningsråd, Grant/Award Number: 270828; German Research Foundation (DFG), Grant/Award Number: 169148856; Sonats, Europe Technologies

Abstract

In this study, a testing and modelling concept is presented, aimed at estimating the local fatigue properties of carburised CrNiMo steel, covering the fatigue limit under axial and torsional loading at various mean stresses. Aimed at predicting the bulk material properties, all specimens were ultrasonic shot-peened prior to testing. Fractographic analyses were conducted on all specimens using scanning electron microscopy to define the type, size and chemical composition of crack initiation-related discontinuities. An iteration of the FKM guideline is presented, relying on the external notch concept to explain the effect of large internal notches on the mean stress sensitivity.

KEYWORDS

case hardening, materials testing, multiaxial fatigue, subsurface crack initiation, very high-cycle fatigue

1 | INTRODUCTION

This work is part of a wider research project, aimed at predicting and preventing subsurface initiated fatigue failures on large marine bevel gears and continues the efforts of the 'Improved reliability of thrusters' joint industry project—a cooperation between thruster suppliers, gear manufacturers, steel suppliers, forging companies and the classification society. The characteristics of subsurface fatigue, flank breakage (FB),[1] tooth flank fracture (TFF)[2,3] or tooth interior fatigue fracture (TIFF)[4] are a crack initiation in the transition zone between the hardened case and the soft core and a subsequent fracture of the entire gear tooth. Whereas cracks start under acting shear stress in mode II, oftentimes parallel to the load-carrying flank,[5] the acting bending stresses drive the crack in mode I through the tooth, resulting in large sections breaking off. Although the failure mechanisms are comparable, the differently shaped fracture surfaces as a result of the load trajectory warrant the differentiation into plateau shaped TIFF damages on idler gears and wedge shaped TFF or FB damages on single flank loaded cylindrical or bevel gears. Even though this work focuses on carburised bevel gears, the derived material model and testing approach should be applicable to other materials and applications.

Typical main propulsion equipment on ferries, anchor handlers, platform supply and drill ships are azimuthing thruster, featuring either one or two bevel gear stages, connecting an electric motor with a 360° steerable propeller. Whereas other gear damages like scuffing, pitting or micropitting are occasionally observed, subsurface fatigue presents the most critical failure mode in regards to its failure frequency and the

implications for the vessel. Continued operation of the propulsion equipment is oftentimes not possible, requiring immediate dry-docking and thruster service to prevent failures of other driveline components. Thus, avoiding subsurface fatigue failures on case carburised bevel gears is an important topic and the focus of ongoing research.

Aimed at improving the reliability of marine propulsion equipment, extensive material tests of the commonly used steel 18CrNiMo7-6, 34CrNiMo6—a steel featuring a comparable alloying composition and a higher carbon content and steel 18NiCrMo14-6—a bearing steel with an increased Nickel content and thereby toughness were conducted. Assessing the effect of different forging reduction ratios on the cyclic behaviour of the base steel, 2D (stretching) and 3D (stretching-upsetting-stretching) forged variants were studied. All specimens were extracted from $430 \times 430 \times 900$ mm^3 castings that underwent gear-like production cycles composed of forging, quenching, annealing, carburising and tempering to ensure the applicability of the obtained fatigue results to large bevel gears. Under push–pull fatigue testing, failures tend to initiate from the surface (i.e., at surface roughness, slip localisation or nonmetallic inclusions on or in the vicinity to the surface), especially in the high cycle and less so in the very high cycle regime ($N_f > 10^7$). As the study focuses on subsurface fatigue and the derivation of the governing material parameters for subsequent multiaxial fatigue calculations, an ultrasonic shot-peening process was applied to all specimens, decreasing the likelihood of surface effects dictating the cyclic behaviour of the tested materials. Ultrasonic shot peening was favoured over conventional shot-peening, nitriding or carburising to achieve a uniform residual stress profile, relatively smooth surface finish and to preserve the designed microstructure.

Historically, assessing the risk of crack initiation in the subsurface layer of gears is done with stress-based critical plane or integral multiaxial fatigue models such as Findley,[6] Dang Van,[7] Oster,[8] Hertter[9] and Liu and Zenner.[10] Testing of small gear sets (Ø < 200 mm) and a material model derived from engineering best practices are commonly applied to verify the model predictions. Comparing Murakami's √area model[11,12] and the FKM guideline[13] in regards to the estimated uniaxial fatigue strength and mean stress sensitivity for hard steels reveals a significant uncertainty when predicting the local, cyclic behaviour of case hardened steel. Therefore, in order to accurately determine the change in cyclic behaviour of the base steel with an increasing carbon content throughout the hardened layer, the paper focuses on high cycle fatigue (HCF) and very high cycle fatigue (VHCF) testing of steels 18CrNiMo7-6 and 34CrNiMo6 under uniaxial push–pull loading at different mean stresses or stress ratios (R) and torsional loading. Other researchers[14,15] have verified an increase in toughness, core hardness and overall load carrying capacity for gears made from alloys with an increased Nickel content, warranting the inclusion of steel 18NiCrMo14-6 in this study. As an inhomogeneous or dendritic microstructure has to be expected for large bevel gears, the fatigue properties of steel 18CrNiMo7-6, exposed to a single stage, hot forging operation ('stretching' referred to as 2D forging, from 770×770 mm^2 to 430×430 mm^2 cross-section) and a three stage process ('stretching-upsetting-stretching' referred to as 3D forging, from 770×770 mm^2 to 430×430 mm^2 to 610×610 mm^2 to 430×430 mm^2) were analysed. The mechanical properties and fatigue behaviour were determined by means of tensile and impact testing, microhardness measurements, optical and electron backscatter diffraction (EBSD) grain size measurements and HCF and VHCF testing. The HCF testing was equally done at $R = -1$, $R = 0.05$ and $R = -7$ (only on 34CrNiMo6). Approximating the change in the fatigue ratio $\kappa = f_{-1}/t_{-1}$ throughout the hardened layer was made possible through torsion tests. All VHCF fracture surfaces were investigated by means of scanning electron microscopy (SEM) alongside energy dispersive X-ray analysis (EDS), revealing the size, location, type and chemical composition of the crack initiation point. The fatigue properties were evaluated according to DIN50100,[16] the maximum likelihood method (MLM)[17] and Murakami's '√area' model.[11,12]

2 | MATERIAL AND EXPERIMENTAL SETUP

Recreating the material properties found in large bevel gears transmitting up to 3.5 MW or 60 kN m, specimens were cut from $430 \times 430 \times 900$ mm^3 forgings (cross-section prior to forging 770×770 mm^2) after austenitisation (880°C for 8 h), quenching in polymer, tempering (620°C for 14 h followed by air cooling), gas carburising (950°C for 80 h), soaking (840°C for 6 h), quenching in oil and tempering (170°C for 12 h). To avoid carbon penetration during the carburising cycle, a protective coating (Conduron G55HK) was applied to the surface of the forgings, using the inherent carbon content of the steels to determine the mechanical and cyclic properties, whilst subjecting the material to a similar grain growth found in gears with a case hardening depth of 4 mm. The size of the forgings was chosen to reproduce a—for large gears typical—coarse dendritic microstructure and martensitic/bainitic matrix due to microsegregations,[5] insufficient through-section working

during forging and prolonged cooling times during quenching. As all specimens were extracted in the transverse direction, the effect of elongated inclusions on the cyclic behaviour was equally modelled.[18] Table 1 lists the chemical compositions of the tested steels taken from the production documents, alongside the applied forging reduction ratios. As per ISO 6336-5,[19] a minimum hot working area reduction ratio of 3:1 is required for ingot cast, case hardened, wrought gear steels. As shown in,[5,20] a coarse dendritic microstructure can usually not be avoided for large gears, warranting the consideration of the 3D forged variant of steel 18CrNiMo7-6. The 18CrNiMo7-6 2D and 3D forgings were produced from the same melt.

The static strength and impact work of all materials were obtained from four specimens, in 0, 3, 6 and 9 o'clock positions in each forging. The acquired mean values and standard deviations, alongside the microhardness measurements ($HV_{0.1}$) obtained from 10 indents on fractured VHCF specimens and grain size measurements based on EBSD and optical line-intercept measurements, are listed in Table 2. Apparent are the differences in grain size for both methods due to the identification of twin boundaries and low-angle grain boundaries in the EBSD method.

Because subsurface fatigue failures on marine bevel gears are typically reported after 3–5 years of service, equivalent to 0.5 to $1{\cdot}10^8$ load cycles, the steels cyclic behaviour in the HCF and VHCF regime need to be investigated. Uniaxial push–pull fatigue testing was performed on (i) a MTS Model 809 axial/torsion servo-hydraulic testing machine, (ii) a servo-hydraulic Schenk Hydropuls PSA 100 and (iii) two ultrasonic BOKU fatigue testing machines. Torsional fatigue testing was carried out on a 600 N m MTS hydraulic torsion machine. A total of 135 HCF and 68 VHCF specimens were tested to failure. The test frequencies, run-out limits and step size were for (i) the HCF uniaxial and torsional tests 10 and 4 Hz using the pearl string method to determine the Basquin parameters, (ii) the long life fatigue (LLF) uniaxial and torsion tests, 30 Hz up to $2{\cdot}10^6$ cycles at 10 MPa and 4 Hz up $5{\cdot}10^6$ cycles at 20 MPa using the staircase method to evaluate the mean fatigue limit and standard deviation and (iii) the VHCF uniaxial ultrasonic tests 19.5 kHz up to 10^9 cycles at 25 MPa, determining a second set of Basquin parameters. Estimating the mean stress sensitivity was done for the HCF and LLF regime under axial loading at stress ratios $R = 0.05$ (all materials) and $R = -7$ (only 34CrNiMo6 2D). Converting the fatigue results for the three distinct parts of the stress amplitude versus number of cycles to failure (SN) diagram into a single curve was done with the maximum likelihood method (MLM) considering run-outs, a nonconstant standard deviation and a fatigue limit parameter.[17]

All tests were carried out at ambient, laboratory conditions with additional air-spot cooling and an infrared thermo-camera (VarioCAM HR Head 780) installed for the ultrasonic testing. Avoiding excessive heat development during testing ($\Delta T < 10$ K) due to intrinsic material damping, a pulse/pause ratio of 500/1000 ms was set for all ultrasonic tests, resulting in an effective testing frequency of 6.5 kHz.

3 | SURFACE INTEGRITY OF THE FATIGUE SPECIMEN

Two prominent models, when estimating the fatigue properties of a given steel as a function of its hardness *HV* or ultimate tensile strength R_m, are the FKM guideline[13] and √area model by Murakami.[12] A combination of both approaches forms the basis for the herein proposed material model for carburised CrNiMo steel. The FKM guideline[13] relies in its prediction of the fatigue strength for steels under alternating axial and shear stresses, on the following linear relations, where R_m expresses the ultimate tensile strength and κ the fatigue ratio.

$$f_{-1} = 0.45 R_m \text{ and } t_{-1} = \frac{f_{-1}}{\kappa} \text{ with } \kappa = \frac{1}{0.577} \approx \sqrt{3}. \quad (1)$$

TABLE 1 Chemical composition of all tested steels and forging reduction ratio

Materials	Forging reduction	Composition (wt.%)											
		C	Mn	P	S	Si	Ni	Cr	Mo	Cu	V	Al	O
18CrNiMo7-6 2D	3.2	0.17	0.63	0.008	0.006	0.29	1.52	1.65	0.31	0.16	0.006	0.024	0.0007
18CrNiMo7-6 3D	12.8	0.17	0.63	0.008	0.006	0.29	1.52	1.65	0.31	0.16	0.006	0.024	0.0007
18NiCrMo14-6 3D	7.1	0.17	0.48	0.006	0.004	0.29	3.35	1.42	0.19	0.14	0.013	0.023	0.0009
34CrNiMo6 2D	3.2	0.35	0.6	0.005	0.006	0.22	1.5	1.6	0.26	0.07	0.01	0.028	0.0006

TABLE 2 Average static strength, impact work, microhardness and grain size of all tested steels

Materials	Tensile tests (ISO 6892-1)				Impact work (ISO 148-1)	Hardness	Grain size	
	R_{p02} (MPa)	R_m (MPa)	A (%)	Z (%)	(J)	($HV_{0.1}$)	EBSD (µm)	ISO 50601 (µm)
18CrNiMo7-6 2D	773 ± 3	1115 ± 7	19.5 ± 0.9	58.6 ± 2.0	56.0 ± 8.9	341 ± 14	11.4 ± 7.1	
18CrNiMo7-6 3D	866 ± 9	1183 ± 13	16.5 ± 1.3	56 ± 3.1	57.7 ± 9.5	366 ± 7		19.0 ± 2.7
18NiCrMo14-6 3D	875 ± 5	1230 ± 2	14.5 ± 0.6	61 ± 1.9	107.7 ± 6.8	379 ± 22	5.1 ± 3.0	17.6 ± 2.6
34CrNiMo6 2D	1099 ± 4	1646 ± 18	6.8 ± 0.5	28.6 ± 0.9	19.7 ± 1.9	498 ± 57	5.3 ± 3.3	

It utilizes a mean stress sensitivity M as a linear function of R_m, when estimating the fatigue strength under oscillating axial load ($R = 0$).

$$f_0 = \frac{2 \cdot f_{-1}}{1+M} \text{ with } M = 3.5 \cdot 10^{-4} R_m - 0.1. \quad (2)$$

According to Murakami,[12] a differentiation into three distinct defect locations is necessary, that is, (i) surface defects, (ii) defects in contact with the surface and (iii) internal defects. The defect location, covered by the parameter C_1 in Equation 3, alongside the √area parameter in µm, describing the square root of the projected area of an inclusion, perpendicular to the maximum principal stress and the hardness of the material HV in kgf/mm^2 are critical in predicting the fatigue limit under alternating load f_{-1} in MPa. Considering the effect of mean stresses via the stress ratio R on the materials fatigue limit, Murakami[12] suggests an exponential correlation as per Equation 3, with the exponent α showing a weak dependency on the materials hardness.

$$f = \frac{C_1 \cdot (HV + 120)}{(\sqrt{area})^{1/6}} \cdot \left(\frac{1-R}{2}\right)^{\alpha} \text{ with } \alpha = 0.226 + HV \cdot 10^{-4}. \quad (3)$$

Murakami[12] observed an 8% or 10% lower fatigue limit for specimens, where fatigue failure initiated from inclusions directly at the surface or in touch with the surface, compared with those, where failure had occurred from internal defects. Reflecting these results, the C_1 parameter varies from 1.43, 1.41 and 1.56 for the described cases.[11,12]

As the present study focuses on subsurface fatigue and the bulk material properties, surface effects as those described by Murakami and those related to the surface roughness, slip localisation and geometrical notches need to be avoided to correctly predict the true material properties of case and core in carburised parts. Hence, the surface integrity as a result of the ultrasonic shot-peening process is addressed in this section.

3.1 | Specimen dimension and treatment parameters

The geometry of the HCF specimens was chosen to match the highly stressed area of the VHCF specimens, keeping the size effect constant for both test conditions. The general dimensions of the specimens are given in Figure 1. Without prior knowledge of the cyclic behaviour of the steels or the maximum inclusions size, Murakami's √area model[11,12] as per Equation 3 was used to determine the shot-peening parameters, assuming inclusions of up to 100 µm in diameter at or in touch with the surface, targeting 400 MPa of compressive residual stress for the first 100 µm of material. In order to

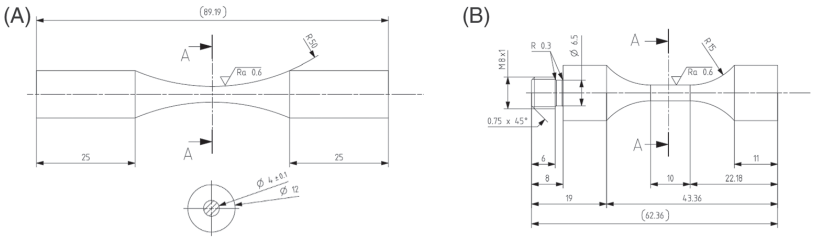

FIGURE 1 Fatigue specimen dimensions for (A) high cycle fatigue and (B) very high cycle fatigue

avoid excessive tensile stresses in the fatigue specimens, the treated layer was designed to be as thin as possible intending the material beyond 150 μm being essentially untreated. As materials of different hardness and differently shaped specimens were tested, the treatment parameters had to be varied (see Table 3). The principle of ultrasonic shot-peening is an electrical–mechanical conversion of a 20-kHz sine wave at a piezo-electrical emitter that randomly excites the shot-peening media inside a hermetic treatment chamber, ensuring uniform treatment of the rotating part. As high-quality media is used (balls from ball bearings), a superior surface finish is usually achieved. Large media mass proved ideal in producing relatively shallow residual stresses, requiring low media velocities to limit the magnitude of the introduced stresses on the surface.

3.2 | Hardness and surface roughness

The microhardness measurements (see Figure 2A) were carried out in accordance to ISO6507-1[21] in (i) 0.3 mm steps across the cross-section of the specimens starting at 0.1 mm (LECO M-400-G3 hardness tester) and (ii) 0.05 mm steps across the treated outer layer. No increase in hardness was detected as a result of the shot-peening treatment, possibly owning to the high dislocation density from the quenching and low-temperature tempering at 170°C. Cecchin et al.[22] reported that for highly annealed or unquenched materials, shot-peening resulted in a dislocation pile-up and subsequent hardness increase towards the surface, whereas materials tempered at 150°C or 300°C featured a decrease in dislocation density and reduction in hardness as a result of the rebounding of the elastically deformed core and a secondary yielding of the surface layer. Measurement of the full width at half maximum diffraction peaks (FWHM), performed alongside the residual stress measurements, support this interpretation as the obtained FWHM measurements at the surface were generally lower than those beyond 50 μm, indicating either a grain coarsening or dislocation annihilation.

Owning to the martensitic/bainitic microstructure with partially deformed dendrites as shown in Figure 2B, large variations in the local microhardness were documented throughout the fatigue specimens, especially for the harder steel 34CrNiMo6 2D (cf. Table 2). Also, the forging direction, transverse to the orientation of the specimen is apparent. Similarly, large hardness variations are typically found in marine bevel gears in the transition zone between the hard case and soft core.

Surface roughness measurements were carried out on a MAHR Perthometer M2 prior and post shot-peening in accordance to the ISO 4288/ASME B46.1[23] over 5.6 mm in longitudinal direction. Whereas the machined specimens retained surface marks left by the tool, the yielding caused by the shot-peening medium left randomly distributed peaks and valleys. Owning to the low quantity and high quality of the media (ball bearings with high sphericity and low surface roughness) used during

TABLE 3 Ultrasonic shot-peening process parameters for all steel variants and specimen types

Material	Specimen	Amplitude (μm p/p)	Media Ø (mm)	Material media	Media mass (g)	Rotation (1/min)	Coverage (%)
18CrNiMo7-6 2D, 3D and 18NiCrNiMo14-6 3D	HCF	20	1.5 mm	100Cr6	4.8	5	125
	VHCF	20	1.5 mm	100Cr6	4.2	5	125
34CrNiMo6 2D	HCF	20	2 mm	304L	3.3	5	125
	VHCF	20	2 mm	304L	2.8	5	125

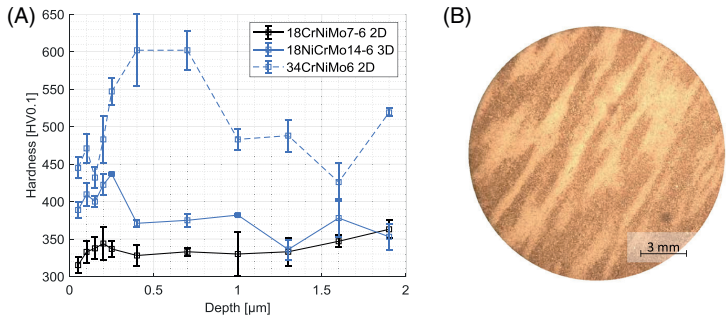

FIGURE 2 (A) Microhardness measurements on steels 18CrNiMo7-6 2D, 18NiCrMo14-6 3D, 34CrNiMo6 2D and (B) directional microsegregation structure on 34CrNiMo6 2D VHCF specimen (etched cross-section)

ultrasonic shot-peening, only an incremental increase in surface roughness was detected (see Table 4 for averaged R_a and R_z results).

4 | RESULTS

The following section covers the evolution of the residual stresses, the uniaxial fatigue results for all materials and test conditions, the derived SN curves according to DIN 50100[16] and MLM,[17] the fractrographic analysis of all VHCF specimens and the iteration of the shear fatigue strength. It forms the basis for the subsequent model derivation and fatigue prediction across the entirety of the treated layer.

4.1 | Evolution of residual stresses

The residual stresses were measured on all materials during the shot-peening recipe formulation and on three 34CrNiMo6 2D VHCF specimens after $8.0{\cdot}10^6$, $3.3{\cdot}10^7$ and $1.2{\cdot}10^8$ cycles at stress amplitudes 400, 375 and 350 MPa in order to assess the dislocation annihilation and degradation of the residual stresses. All measurements were done on a Stresstech X3000 stress analyser using the X-ray diffraction (XRD) method in tangential and longitudinal direction in 30-µm steps. The results of the treated but untested 18CrNiMo7-6 2D, 34CrNiMo6 2D and the tested 34CrNiMo6 2D are illustrated with error bars in Figure 3. As for the untested materials, the intended 400 MPa of compressive stresses for the first 100 µm of the material, alongside a sharp decrease of the compressive stresses towards 150 µm were uniformly achieved.

The initial and final, tangential and longitudinal residual stresses were found to be very comparable across all materials. For those subjected to low stress amplitudes for extended time periods, a reduction in compressive residual stresses was most apparent. The relaxation of the internal strain can be quantified either through an absolute reduction in the compressive stress of approximately 100 MPa or through a reduction in the affected layer thickness of approximately 40 µm. In contrast, large stress amplitudes seemed to mobilise and redistribute dislocations, such that surface compressive residual stresses were decreased, but the affected layer thickness increased. Judging by the moderate reduction in compressive residual stress across the critical surface layer, the shot-peening treatment was deemed successful.

TABLE 4 Longitudinal roughness measurements prior and after ultrasonic shot-peening

Roughness (ASME B46.1)	R_a (µm)	R_z (µm)
Machined	0.38	2.05
Ultrasonic shot-peened	0.39	2.08

4.2 | Uniaxial fatigue

As shown by other researchers,[24,25] the cyclic behaviour of high strength steels under cyclic uniaxial loading can be described in a duplex or multi-stage SN curve. In this study, both slopes of the SN curve were defined through two sets of Basquin parameters[16] (see Equation 4), where N_f describes the number of cycles to failure, C the Basquin constant for $\sigma_a = 1$, k the slope of the decreasing fatigue strength and σ_a the load amplitude during testing.

$$N_f = C \cdot \sigma_a^{-k}. \tag{4}$$

Using the staircase method,[16] the fatigue limit in the long-life regime under fully reversed axial f_{-1} as well as repeated axial loading f_0 and f_{-7} (only 34CrNiMo6 2D) were estimated, considering run-outs alongside failures. An approximation of a continuous SN curve of the $R = -1$ results was achieved with the MLM by Pascual and Meeker.[17] The model parameters ($\beta_{0\mu}$, $\beta_{1\mu}$, β_{0s}, β_{1s}) and the fatigue limit $f_{-1,MLM}$, that define the mean log cycles to failure μ_{log} (σ_a) and the standard deviation of log cycles to failure s_{log} (σ_a), are iterated to maximize the sample likelihood parameter, yielding mean fatigue strength as a function of time or load cycles (see Equation 5).

$$\begin{aligned} &\mu_{\log}(\sigma_a) = \beta_{0\mu} + \beta_{1\mu} \ln(\sigma_a - f_{-1,MLM}), \sigma_a > f_{-1,MLM}, \\ &s_{\log}(\sigma_a) = \exp[\beta_{0s} + \beta_{1s} \ln(\sigma_a)], \sigma_a > f_{-1,MLM}, \\ &f_{-1}(N_f) = \exp\left(\frac{\ln(N_f) - \beta_{0\mu}}{\beta_{1\mu}}\right) + f_{-1,MLM}. \end{aligned} \tag{5}$$

The $R = -1$, 0 SN curves, MLM $R = -1$ curves (for failure probabilities 5, 50 and 95%) and the staircase results for $R = -7$ are given in Figure 4A–D for all tested steels. The defining model parameters are listed in Tables 5 and 6. Even though tests were performed at $R = 0.05$, Table 6 contains the estimated $R = 0$ fatigue parameters, assuming a linear trend between the fatigue results achieved for $R = -1$ and $R = 0.05$.

As two distinct parts of the $R = -1$ SN curve were tested at 30 Hz and 19.5 kHz, an evaluation of the frequency effect on the cyclic behaviour of the steels is

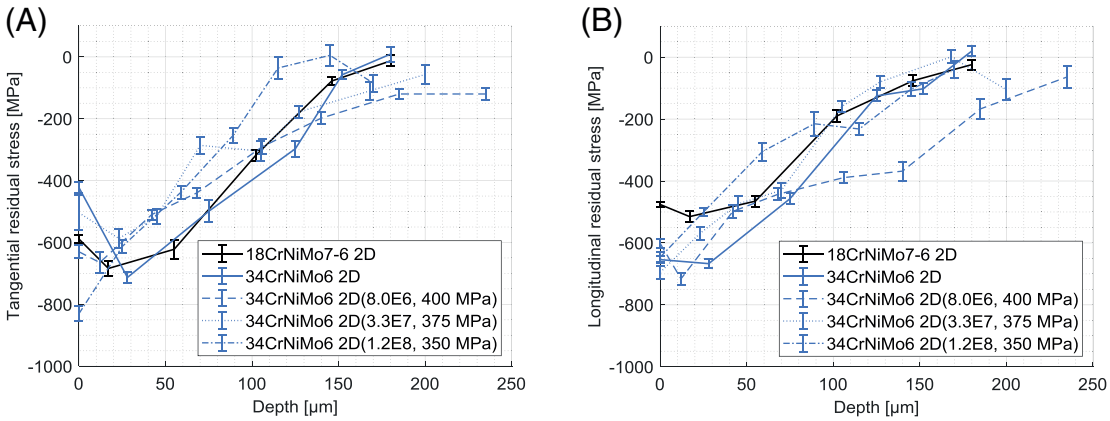

FIGURE 3 Residual stress plots for untested 18CrNiMo7-6 2D, 34CrNiMo6 2D and tested 34CrNiMo6 2D VHCF specimens with fractures after $8.0 \cdot 10^6$, $3.3 \cdot 10^7$ and $1.2 \cdot 10^8$ cycles and 400, 375 and 350 MPa stress amplitudes in (A) tangential and (B) longitudinal direction

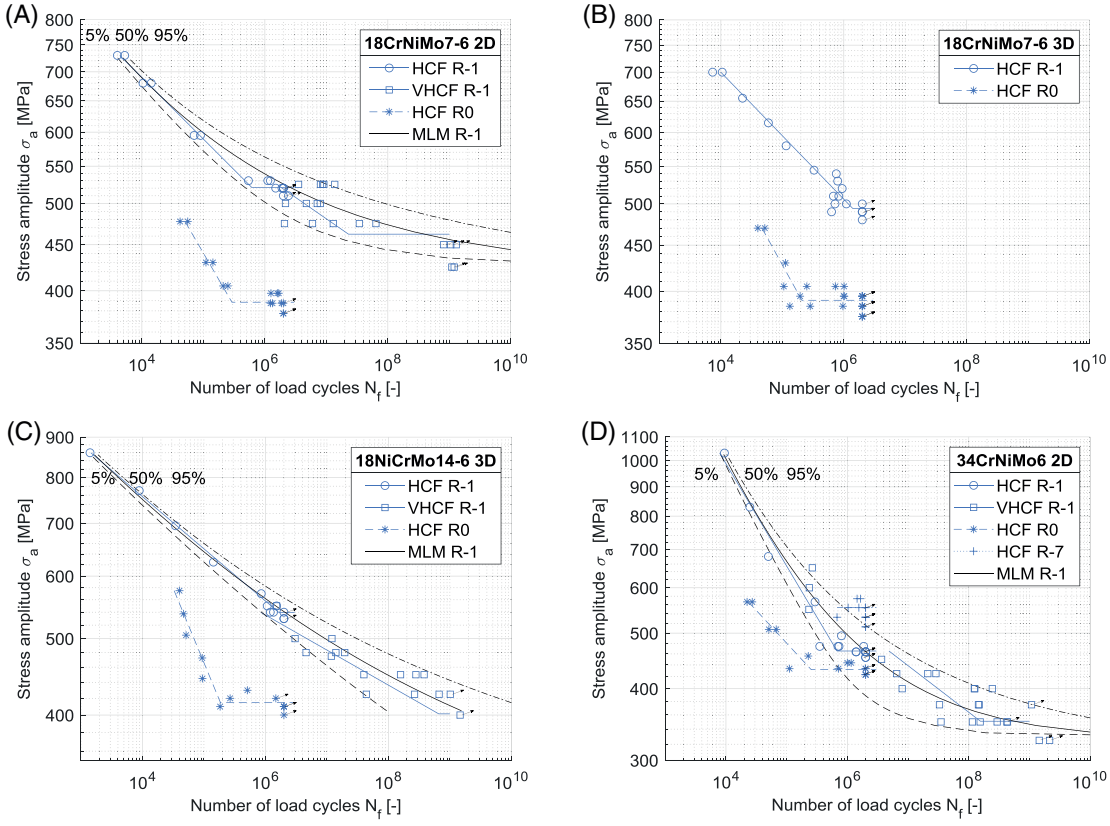

FIGURE 4 SN curves for uniaxial push–pull conditions under $R = -1$, $R = 0$ and $R = -7$, including MLM SN curves. (A) Steel 18CrNiMo7-6 2D, (B) steel 18CrNiMo7-6 3D, (C) steel 18NiCrMo14-6 3D and (D) steel 34CrNiMo6 2D

TABLE 5 Uniaxial fatigue data at $R = -1$ for HCF, VHCF regime and MLM for materials 18CrNiMo7-6 2D, 18CrNiMo7-6 3D, 18NiCrMo14-6 3D and 34CrNiMo6 2D

Fatigue properties	HCF			VHCF			MLM				
R-1	logC	k	f_{-1} (MPa)	logC	k	f_{-1} (MPa)	$\beta_{0\mu}$	$\beta_{1\mu}$	β_{0s}	β_{1s}	$f_{-1,MLM}$ (MPa)
18CrNiMo7-6 2D	45.6	14.7	521 ± 2	63.6	21.1	462	40.5	−5.6	40.1	−6.4	422
18CrNiMo7-6 3D	44.4	14.2	494 ± 9								
18NiCrMo14-6 3D	47.5	15.1	540 ± 4	67.4	22.5	401	64.3	−8.9	24.9	−4.1	282
34CrNiMo6 2D	20.8	5.6	465 ± 2	39.5	12.3	351	31.0	−3.3	19.6	−3.2	325

TABLE 6 Uniaxial fatigue data at $R = 0$ and $R = -7$ for HCF regime and materials 18CrNiMo7-6 2D, 18CrNiMo7-6 3D, 18NiCrMo14-6 3D and 34CrNiMo6 2D

Fatigue properties	HCF, R0			HCF, R-7
R0, R-7	logC	k	$f_0/2$ (MPa)	f_{-7} (MPa)
18CrNiMo7-6 2D	27.5	8.5	380 ± 3	
18CrNiMo7-6 3D	26.3	8.1	380 ± 8	
18NiCrMo14-6 3D	19.2	5.3	404 ± 9	
34CrNiMo6 2D	28.5	8.8	415 ± 3	554 ± 6

limited to $2{\cdot}10^6$ cycles, utilizing the results from the HCF staircase testing and the VHCF Basquin parameters. The fatigue strengths for both methods are 521/528 MPa for steel 18CrNiMo7-6 2D, 540/529 MPa for steel 18NiCrMo14-6 3D and 465/506 MPa for steel 34CrNiMo6 2D. They suggest a minor frequency effect for steels 18CrNiMo7-6 2D and 18NiCrMo14-6 3D and a balance between the thermic and athermic effects of the high strain rate on the crack initiating dislocation motion. Similar to the results by Tsutsumi et al.[26] for low-carbon steels, material 34CrNiMo6 2D exhibits a higher fatigue strength at ultrasonic test frequencies at $2{\cdot}10^6$ cycles, suggesting a retardation of the dislocation motion due to the high strain rate.

4.3 | Fractorgraphic analysis

The fractographic analysis of the HCF specimens was performed on a digital microscope (Hirox RH-2000), revealing exclusively surface-initiated failures in the HCF and a combination of surface and subsurface failures in the LLF regime. Investigating the VHCF specimens on a field emission scanning electron microscope (MIRA 3 XMU) equipped with EBSD and EDS detectors (both EDAX/Ametek), only subsurface initiated failures were observed (see Figure 5) with a majority of the failures starting from elongated clusters or agglomerates of $MgO\text{-}Al_2O_3$ spinel (Figure 5B) even when testing at stress levels that had exclusively resulted in surface failures on HCF specimens. The second internal failure type, detected on three 34CrNiMo6 2D and one 18NiCrMo14-6 3D specimens, was crack initiation from soft grains in the martensitic/bainitic matrix (Figure 5D). Performing EBSD measurements, islands of austenite were identified in the martensitic microstructure of the carbon-rich steel 34CrNiMo6 (Figure 6A). A carbon content of 0.7 wt.% is common for the surface of case carburised gear teeth, featuring between 5% and 25% retained, soft austenite adding ductility to the 700 HV hard surface layer. As the austenite is significantly softer than the surrounding tempered martensite, a crack initiation from large austenite grains seems plausible, especially since the measured defect size was up to 150 µm in diameter or 250 µm according to the Murakami √area parameter and thereby three times larger than the average spinel inclusion. Matrix failures were only observed during VHCF testing at elevated load levels in excess of the documented fatigue limit in the LLF regime. The final internal failure type was crack initiation from voids, detected on a single 34CrNiMo6 2D specimen loaded at 400 MPa and failure after $1.3{\cdot}10^8$ cycles. Figure 5E combines the SE and EDS images of the deformed void alongside the detected $MgO\text{-}Al_2O_3$ spinel, manganese sulphide MnS and calcium sulphide CaS inclusions.

Measurements of the $MgO\text{-}Al_2O_3$ inclusions across all analysed fracture surfaces revealed an almost identical distribution for all materials. Disregarding the detected matrix and void failures, a combined Weibull probability plot of all materials comparing the failure probability function to the logarithmic defect size (√area) was created, revealing the average inclusion size to be 80 µm and a possible maximum of 108.5 µm for a fictitious test volume of 100 specimens (Figure 6B).

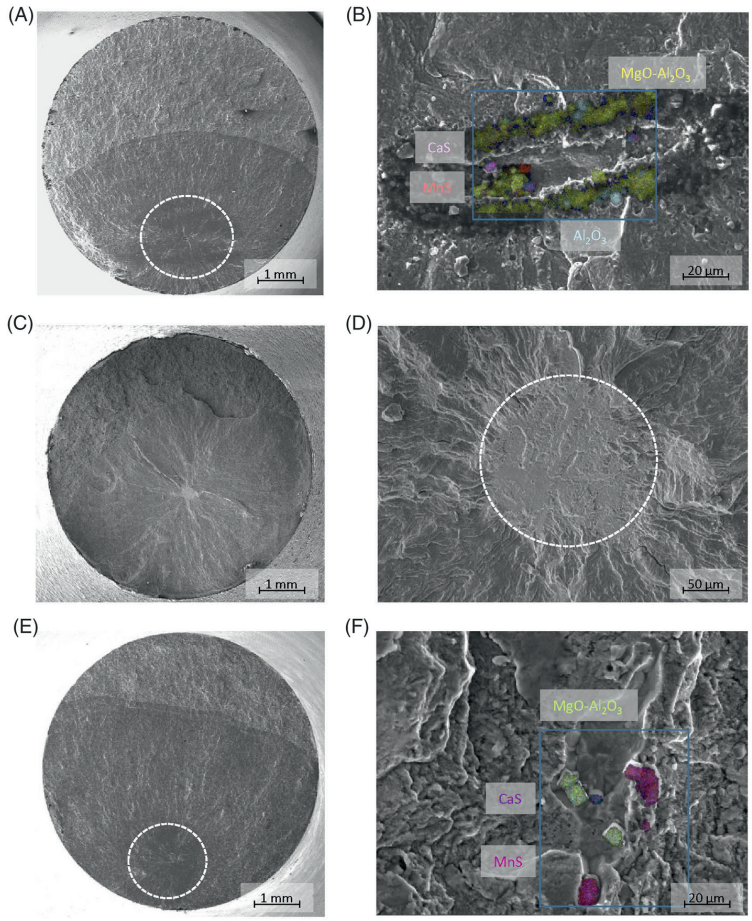

FIGURE 5 Internal failure types with initiation from (i) clustered nonmetallic inclusion type MgO-Al_2O_3 spinel (34CrNiMo6 2D, $N_f = 8{\cdot}10^6$, $\sigma_a = 400$ MPa) (a) complete fracture surface with indicated fisheye ($D_{fisheye} = 1913$ µm), (B) inclusion in the center of the fisheye ($\sqrt{area} = 76$ µm), (ii) matrix failure (34CrNiMo6 2D, $N_f = 2.3{\cdot}10^5$, $\sigma_a = 550$ MPa) (C) complete fracture surface without a clear fisheye, (D) discontinuity in the center of the fracture origin, (iii) initiation from a void (34CrNiMo6 2D, $N_f = 1.3{\cdot}10^8$, $\sigma_a = 400$ MPa) (E) complete fracture surface with indicated fisheye ($D_{fisheye} = 1710$ µm) and (F) partially deformed void and trapped CaS, MnS, MgO-Al_2O_3 inclusions in the center of the fisheye

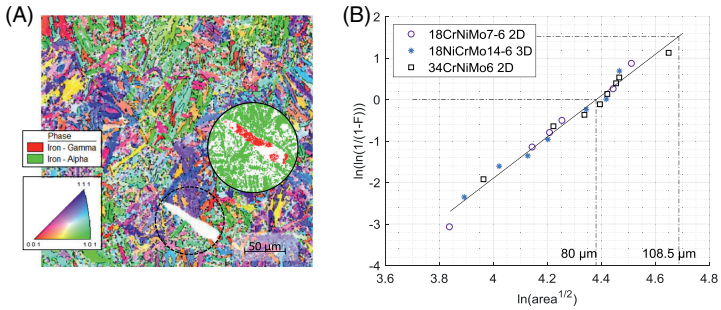

FIGURE 6 (A) Microstructure of steel 34CrNiMo6 2D obtained from EBSD measurements showing the grain size and crystallographic orientation of the martensite. Color coding accord to the inverse pole figure of the surface normal direction. Encircled area showing austenitic region (red color) in the martensitic microstructure (green color). (B) Average and maximum inclusions size for all investigated VHCF fracture surfaces in Weibull probability plot

4.4 | Shear fatigue

As the same shot-peened HCF specimens of steels 18CrNiMo7-6 3D and 34CrNiMo6 2D were tested under torsion (dimensions in Figure 1), the stress state in the surface layer is multiaxial with constant, compressive stresses and alternating shear stresses. In order to correctly assess the shear fatigue strength t_{-1}, the Liu and Zenner (LZ) shear stress intensity, multiaxial fatigue criterion[10] was used in an iterative manner. The LZ criterion was chosen over other integral or critical plane, multiaxial fatigue criteria due to its model accuracy when exposed to a large data base, composed of 407 multiaxial fatigue experiments.[27] Varying the alternating torque ($R = -1$) by 250 N mm, run-outs and failures were documented for steel 34CrNiMo6 2D at an amplitude of 4500 N mm. At that load, the oscillating shear stress on the surface of the hourglass shaped specimens was approximately 375 MPa, a value significantly higher than the shear strength of the material due to the introduced compressive residual stresses.

The LZ criterion integrates the damage parameter over all planes inside a volume element, defined through the Euler angles ϕ and ψ. It weights the effect of the shear mean τ_{sm} and shear amplitude stresses τ_{sa}, the normal mean σ_{nm} and normal amplitude stresses σ_{na} on each plane through the use of the model parameters a, b, c and d (Equation 6 and 7). Four fatigue data points, commonly the fatigue strength for fully reversed axial loading f_{-1}, for repeated axial loading f_0, for fully reversed torsional loading t_{-1} and for repeated torsional loading t_0 are used when deriving the model parameters. Applying the presented fatigue results under axial loading for steel 34CrNiMo6 2D at $2{\cdot}10^6$ cycles and the outlined approximation for t_0 (see Equation 8[28]), the missing fatigue strength under fully reversed torsion t_{-1} can be approximated by solving max (E_{LZ}) = 1 at 4500 N mm for the first 250 µm of the shot-peened specimen in their smallest cross-section, assuming constant material properties.

$$E_{LZ} = \frac{\sqrt{\frac{15}{8\pi}\int_0^{2\pi}\int_0^{\pi}\left(a\tau_{sa}^2\left(1+c\tau_{sm}^2\right)+b\sigma_{na}^2\left(1+d\sigma_{nm}\right)\right)\sin(\psi)\,d\psi\,d\phi}}{f_{-1}}, \tag{6}$$

$$a=\frac{1}{5}\left(3\kappa^2-4\right),\quad b=\frac{1}{5}\left(6-2\kappa^2\right),\quad c=\frac{7}{3at_0^2}\left(\left(\frac{2f_{-1}}{t_0}\right)^2-\kappa^2\right), \tag{7}$$

$$d=\frac{28}{15bf_0}\left(\left(\frac{2f_{-1}}{f_0}\right)^2-1-\frac{acf_0^2}{21}\right),$$

$$\frac{4t_{-1}}{t_0}-\frac{2f_{-1}}{f_0}=1. \tag{8}$$

Figure 7A shows the predicted material utilisation E_{LZ} for the outer layer of a, after $3.4{\cdot}10^6$ cycles, fractured 34CrNiMo6 2D specimen loaded at 4500 N mm. The shear fatigue strength was iterated to 342 MPa. According to Liu et al.,[10] a high failure probability is estimated for the entire treated layer with two maxima, one on the surface and one at a depth of 180 µm. Whereas the shown fracture surface in Figure 7B features a subsurface crack initiation from a MgO-Al_2O_3 inclusion at roughly 200 µm, all other failures initiated from the surface.

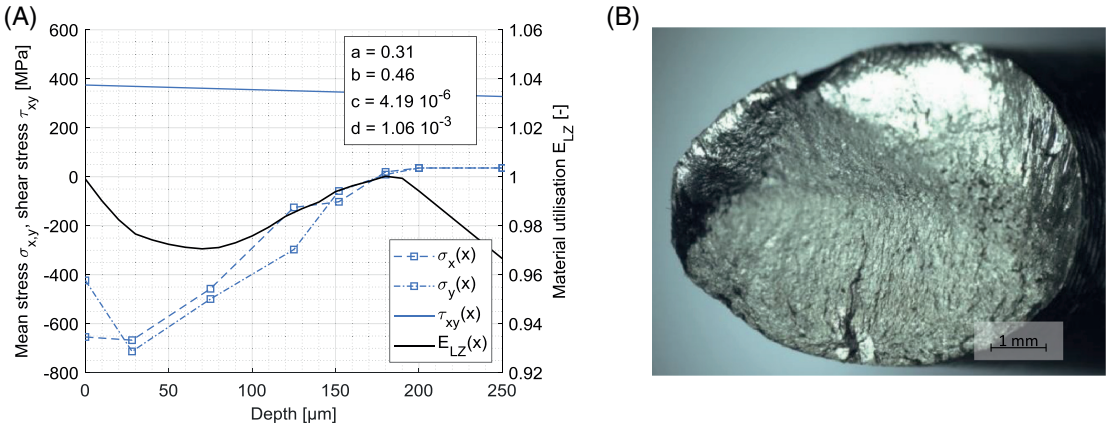

FIGURE 7 Shear fatigue testing—(A) subsurface stress state and material utilisation for a 34CrNiMo6 2D HCF specimen under 4500 N mm and (B) fracture surface of the same specimen after $3.4{\cdot}10^6$ cycles, showing crack initiation from MgO-Al_2O_3 inclusions in 0.2 mm depth

Owning to the stress gradient in the HCF specimen, a significantly smaller volume than during push–pull testing is subjected to large, cyclic stresses and a local stress redistribution has to be considered. Because most failures under torsion initiated from the surface, the geometrical notch factor α_τ, the stress redistribution factor n based on the local stress gradient and the surface roughness factor $K_{F\tau}$ (see Table 4 for R_z of shot-peened specimen) are considered according to the FKM guideline.[13] A statistical size factor K_{size} was derived from the weakest link theory, comparing the numerically obtained, highly stressed volume under axial and torsional loading.[29] The parameters λ and s in Equation 9 describe the standardized normal distribution factor and the standard deviation during push–pull fatigue testing.

$$t_{-1} = t_{-1,LZ} \cdot K_\tau \text{ with } K_\tau = \frac{\alpha_\tau}{n} \cdot K_{size} + \frac{1}{K_{F\tau}} - 1 \text{ and } K_{size} = 1 + \lambda \cdot \frac{s}{f_{-1}}. \quad (9)$$

The derived SN curves, accounting for all outlined influence factors, in combination with the raw test data, composed of the surface shear stresses and cycles to failure, are shown in Figure 8. Table 7 lists all influence factors, the estimated fatigue strength, load and geometry parameters.

5 | MODEL DERIVATION

As shown in Equation 6 for the Liu and Zenner multiaxial fatigue, shear stress intensity criterion,[10] four model constants need to be defined, when weighting the influence of shear and normal stresses on the local material utilisation, requiring four fatigue data points to predict the mentioned model constants. Commonly, the fatigue limit f_{-1} for fully reversed axial loading, f_0 for repeated axial loading, t_{-1} for fully reversed torsional loading and t_0 for repeated torsional loading are used, where t_0 is typically approximated using the mean stress sensitivity M and the fatigue ratio κ or through Equation 8.[28] An estimation of the fatigue parameters for the entire carburised layer, based on the presented fatigue results and literature findings, is outlined in this chapter.

The obtained fatigue results (Table 5 HCF strength at $2{\cdot}10^6$ cycles), alongside the fractographic analysis, suggest that hard steels are far more susceptible to inclusions of the same composition, size and orientation than medium

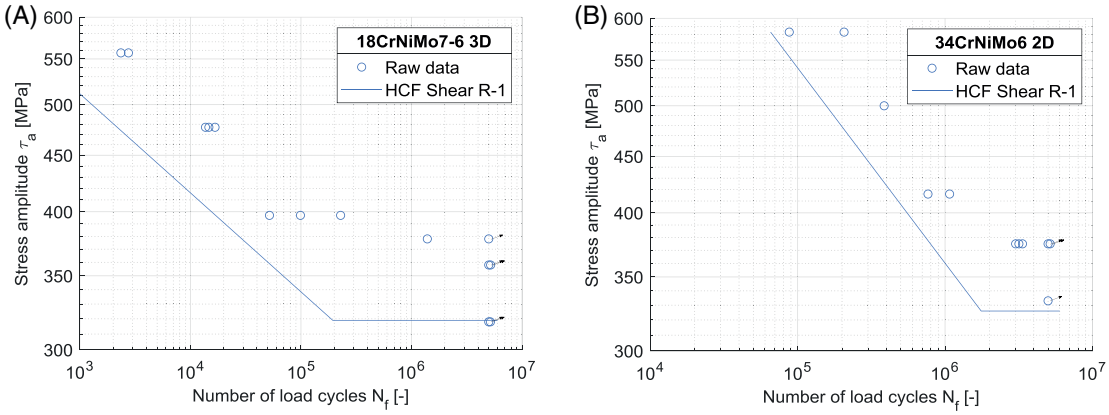

FIGURE 8 Raw data and SN curves for torsional loading at $R = -1$ for (A) 18CrNiMo7-6 3D and (B) 34CrNiMo6 2D

TABLE 7 Fatigue strength under fully reversed torsional loading t_{-1} for 18CrNiMo7-6 3D and 34CrNiMo6 2D HCF specimen

	Geometry and load			Influence factors				HCF, shear R-1			
Material	M (N mm)	Ø (mm)	τ_a (MPa)	α_τ	n	$K_{F\tau}$	K_{size}	$t_{-1,LZ}$ (MPa)	logC	k	t_{-1} (MPa)
18CrNiMo7-6 3D	4750	4.00	378	1.002	1.082	0.974	0.97	345	33.2	11.2	319
34CrNiMo6 2D	4500	3.96	375	1.002	1.055	0.97	0.979	342	20.5	5.7	329

strength steels. Accounting for the criticality of inclusions on the fatigue properties of hard steels, an f_{-1} prediction as a function of hardness according to the lower limit of the Murakami √area model beyond 550 HV is proposed, utilizing the documented average inclusion size of 80 µm. The behaviour of the fatigue strength as a function of time is considered through the MLM and outlined at the end of this chapter. Contrasting the average microhardness for each steel with the obtained fatigue strength at $2{\cdot}10^6$ cycles, nearly constant fatigue properties are reported within the hardness range of 350 to 500 HV. Also considering the inclusions size in the outlined hardness range, a constant fatigue strength, relying on Murakami's lower limit at 550 HV is implemented in Equation 10. As core hardness values below 300 HV are not to be expected on carburised 18CrNiMo7-6 gears, the fatigue strength below 300 HV is of lesser importance but is adequately approximated with Murakami's upper limit. Figure 9 plots the fatigue strength of the tested steels at $2{\cdot}10^6$ cycles against the mean microhardness', the predictions by FKM,[13] Murakami,[12] Velten,[30] Winderlich[31] and implements the fatigue model outlined in Equation 10.

$$f_{-1}(HV)=\begin{cases} f_{-1,\mathrm{up}}(HV)=1.6\,HV & \text{for } HV<300,\\ f_{-1,\mathrm{low}}(HV)=\dfrac{1.56\cdot(HV+120)}{(\sqrt{area})^{\frac{1}{6}}} & \text{for } HV>550,\\ f_{-1,\mathrm{low}}(550\,HV)\approx 505\,MPa & \text{for } 300\le HV\le 550. \end{cases} \tag{10}$$

The fatigue model aligns itself thereby with the findings by Garwood and Nishijima,[32,33] whereby for soft and mild steels, an approximately linear trend between hardness and fatigue limit exists, whereas hard steels are much more susceptible to internal defects.

In order to predict the fatigue limit under fully reversed torsion t_{-1}, the steels 18CrNiMo7-6 3D and 34CrNiMo6 2D were tested up the $5{\cdot}10^6$ cycles and the results compared with literature findings, comprising test results on varying steels.[34–56] Rather than assuming a constant ratio between the axial and torsional fully reversed fatigue strength as for the von Mises criterion or the FKM guideline, a linear trend is derived that lies within the range suggested by Suresh.[57] Figure 9B plots the reported and measured fatigue ratios against the materials' hardness.

A linear regression, equally weighting the literature findings and own fatigue results, was used to predict the fatigue ratio κ and thereby the fatigue limit under reversed torsion t_{-1} across the entire case hardened layer (see Equation 11). Considering the stress gradient, surface roughness and volume effect as outlined in Section 4.4 guaranteed a close correlation between the shear fatigue results and proposed linear trend.

$$\kappa(HV)=-5\cdot10^{-4}\,HV+\sqrt{3}\ \text{ and }\ t_{-1}(HV)=\frac{f_{-1}(HV)}{\kappa(HV)}. \tag{11}$$

Predicting the fatigue limit under repeated axial loading f_0 through the mean stress sensitivity M, Murakami's √area model[12] is compared with the FKM guideline,[13] the fatigue results and literature findings. Whereas the FKM guideline agrees well with M obtained for the medium strength steels 18CrNiMo7-6 2D, 3D and 18NiCrMo14-6 3D, it overestimates the mean stress sensitivity for the hard steel 34CrNiMo6 2D significantly. In contrast, Murakami's suggestions agree far better with the hard steel 34CrNiMo6 2D but underestimate the mean stress

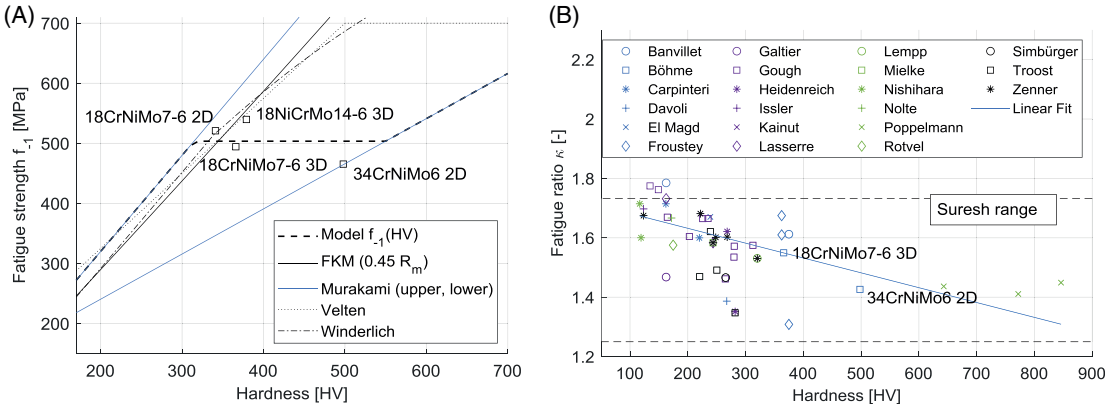

FIGURE 9 The material model for carburised parts as a function of hardness for (A) the fatigue limit under fully reversed axial load f_{-1} at $2{\cdot}10^6$ cycles and (B) the fatigue ratio κ (□ referring to results for $5{\cdot}10^6$ cycles)

sensitivity for the other three tested steels. Seemingly, the internal notch factor α_σ, as the result of the documented $MgO\text{-}Al_2O_3$ inclusions, reduces the fatigue limit f_{-1} and the mean stress sensitivity M. In order to appropriately predict M for hard steels, the concept of exterior/macroscopic notches is applied to internal notches and the FKM guideline. According to Bell and Benham,[58] the allowable stress amplitude for a notched specimen for varying mean stress is determined by a notch factor α_σ. Whereas Bell and Benham[58] predict a decreasing notch factor for increasing mean stresses, a constant notch factor within the $R_{-1}R_0$ range is assumed here, greatly simplifying the proposed model. The mean stress sensitivities obtained in this study and the documented results by other researchers[11,37,38,43,44,46–49,54–56,59,60] suggest that the FKM guideline works well in predicting M for medium strength and soft steels but overestimates M for hard steels that are most probably affected by internal notches. Predicting the notch factor α_σ as a function of the theoretical upper fatigue limit $f_{-1,up}$ and the obtained fatigue limit f_{-1}, a revised mean stress sensitivity as per Equation 12 is suggested.

$$f_0 = \frac{2 \cdot f_{-1}}{1 + M_k} \text{ with } M_k = \frac{M}{\alpha_\sigma} \text{ and } M = 3.5 \cdot 10^{-4} \cdot R_m - 0.1. \tag{12}$$

As soft and mild steels follow almost a linear trend for $f_{-1}(HV$ or $R_m)$ independent of internal defects, the notch factor α_σ approximates to unity, leaving the mean stress sensitivity as predicted by the FKM[13] unchanged. For hard steels, M is reduced by the internal notch factor α_σ, expressed through the ratio between the upper fatigue limit $f_{-1,up}$ and the true fatigue limit f_{-1}.

$$\alpha_\sigma = \frac{f_{-1,up}}{f_{-1}}. \tag{13}$$

Plotting the measured mean stress sensitivities from this study against the material's microhardness in Figure 10A, literature references,[11,37,38,43,44,46–49,54–56,59,60] the model prediction by FKM[13] and Murakami[12] alongside the herein proposed mean stress concept, the limitation of the FKM and Murakami model and the improvement, when predicting the mean stress sensitivity as a function of the outlined notch factor are made evident.

In a case study, all three models are compared against the fatigue results for steel 34CrNiMo6 2D in Figure 10B. Shown are the FKM guideline[13] using M according to Equation 2, the Murakami model[12] as per Equation 3 and (iii) the outlined mean stress model, in Equations 12 and 13.

Table 8 summarizes the data illustrated in Figure 10B and lists the obtained fatigue properties and mean stress sensitivities for 34CrNiMo6 2D, comparing the different fatigue models.

The prediction of the allowable stress amplitude under tensile and furthermore compressive mean stresses, critical for fatigue predictions in gears subjected to Hertzian and residual stresses, is adequately captured by the outlined notch factor concept. The proposed material model covers three and, by extension,[28] four fatigue data points, needed for multiaxial fatigue evaluation of

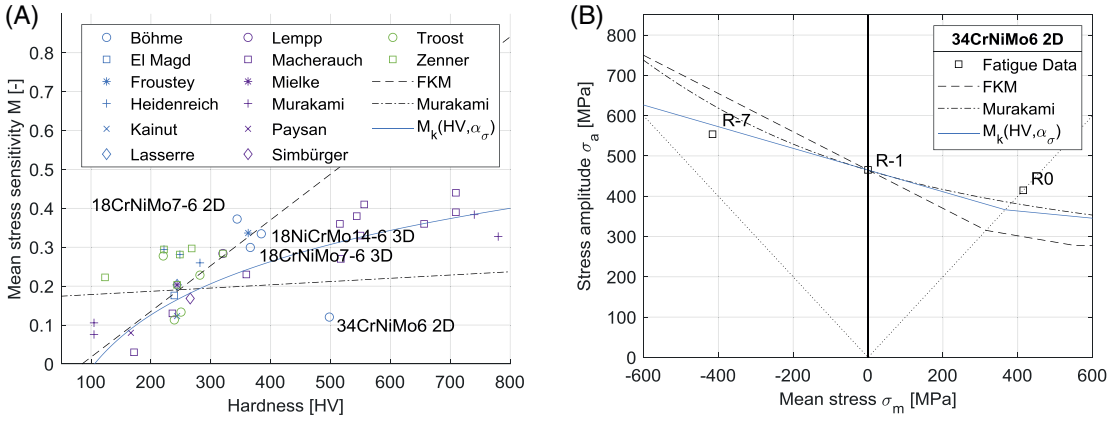

FIGURE 10 Mean stress sensitivity (A) as a function of hardness from test results (◦ referring to results for $2 \cdot 10^6$ cycles) and literature findings, comparing the predicted mean stress sensitivity as per FKM, Murakami and Equation 12 and (B) as a Haigh diagram for the tested steel 34CrNiMo6 2D showing the allowable stress amplitude according to the FKM model, Murakami and proposed mean stress effect

TABLE 8 Fatigue strength and mean stress sensitivity prediction for 34CrNiMo6 2D against obtained fatigue data

Fatigue model	Mean stress sensitivity	Fatigue strength		
For 34CrNiMo6 2D	M (−)	$R = -1$	$R = 0$	$R = -7$
498 HV, R_m = 1643 MPa		(MPa)	(MPa)	(MPa)
Fatigue data	0.12	465	415	554
FKM	0.48	465	315	721
Murakami	0.21	465	384	681
M_k (HV, α_σ)	0.28	465	364	587

case carburised gears or otherwise thermochemically treated steel, focusing on large components as per the production process of the tested steels. The definition of all fatigue data points pivots of the fatigue strength under fully reversed axial loading f_{-1} as t_{-1} is defined through the fatigue ratio κ and f_0 through the mean stress sensitivity M, making an approximation of the cyclic behaviour of the carburized layer as a function of time possible through implementation of the uniaxial push–pull fatigue results for the HCF and VHCF domain. Inspiration for the proposed life factor K_{NT} is taken from the ISO10300 gear standard,[61] defining $K_{NT} = 1$ for the knee in the HCF domain. As subsurface fatigue failures on gears tend to initiate in a range of 400–550 HV, using the MLM based equation for steel 34CrNiMo6 2D is deemed appropriate. The life factor K_{NT}, according to Equation 14

$$f_{-1}(N_f) = f_{-1,HCF} \cdot K_{NT} \text{ with } K_{NT} = \left(\exp\left(\frac{\ln(N_f) - \beta_{0\mu}}{\beta_{1\mu}} \right) + f_{-1,MLM} \right) / f_{-1,HCF}, \quad (14)$$

is proposed using the variables defined in Table 5.

6 | DISCUSSION

The presented fatigue results and modelling concept form the basis for subsequent multiaxial fatigue calculations of carburised marine bevel gears, intended for later publications. A material model is outlined, capturing the change in cyclic behaviour with increasing carbon content throughout the case hardened layer and improving the prediction of the axial and shear fatigue strength and mean stress sensitivity, whilst introducing an MLM-derived life factor. The described sample preparation by means of ultrasonic shot-peening and the analysis of the shear fatigue results define an approach, applicable to other materials and scenarios, where bulk material properties are of interest. Ultimately, the presented equations enable a simplified prediction of the critical material parameters for multiaxial fatigue predictions of carburised or otherwise thermochemically treated steels and rely solely on a measured hardness profile and the estimation of the mean inclusions size.

Summarizing the obtained fatigue properties, the harder steel 34CrNiMo6 2D showed inferior fatigue properties compared with the softer steels 18CrNiMo7-6 2D, 3D and 18NiCrMo14-6 3D when tested under fully reversed axial loading. Part of the decrease in fatigue properties can be attributed to the increase in retained austenite fraction due to an incomplete martensitic transformation and resulting two-phase microstructure. Matrix or intergranular failures from austenite grains were observed on steel 34CrNiMo6 2D during VHCF testing but not on steel 18CrNiMo7-6 2D. As most of the failure causing discontinuities were nonmetallic inclusions, their contribution to the fatigue properties outweigh the effect of the retained austenite. Research into electro-slag-remelted steels suggests a reduction in the fatigue scatter for high over commercial purity steels, when applied to rotating bending tests on carburised specimen.[62] The works by Wyszkowski et al.[63] and Spangenberg[62] into the positive effect of nickel alloyed carburised steels suggest an increase in fatigue strength owning to the higher ductility of the nickel alloyed martensite (carburised specimen under rotating bending). For steels with a low carbon content (18CrNiMo7-6 2D and 18NiCrMo14-6 3D), the same trend was observable in the HCF but not in the VHCF regime, where the nickel alloyed 18NiCrMo14-6 3D showed inferior properties; 3D forging featuring a four times larger forging reduction ratio compared with the tested 2D variant of the steel 18CrNiMo7-6 did not yield the expected improvement in fatigue properties. The average fatigue strength under fully reversed axial loading was approximately 5% lower and the standard deviation four times larger, yielding a 10% lower f_{-1}(P = 10%) fatigue strength. During HCF staircase testing, a majority of the 3D forged specimens failed from inclusions. A mixture of surface and subsurface failures were documented for the 2D forged steel, suggesting a lower purity of the 3D variant, possibly owning to the positioning of the two forgings in the casting. The HCF and VHCF tests prove the bimodal nature of fatigue failures initiating from the surface and subsurface material

layers. The application of the MLM to the entirety of the fatigue results leads to very large standard deviations in the overlapping area of the SN curve. As a minor frequency effect was documented for the tested steels, a prediction of the MLM derived mean fatigue strength as a function of time seems appropriate.

7 | CONCLUSIONS

Based on fatigue experiments covering a wide range of loading conditions followed by microstructural and fracture surface characterisation, we present a material model that enables the prediction of the four cyclic material parameters (f_{-1}, t_{-1}, f_0 and t_0[28]) for carburised steel parts and facilitates the derivation of the governing model parameters for multiaxial fatigue calculations. Key findings are as follows:

i. The four tested steels show an almost identical slope of the SN curves in the HCF and VHCF regime with either nonexistent or minor plateaus, enabling the prediction of a continuous fatigue curve with the maximum likelihood method. The tested hard steel featured the steepest slope in the VHCF regime, yielding a fatigue limit under fully reversed axial loading inferior the milder steels. The documented behaviour of the hard steel was attributed to the effect of internal inclusions and modelled through Murakami's √area model and a novel approach for the mean stress sensitivity.
ii. The performed 3D over 2D forging yielded no noticeable improvement in the cyclic behaviour of the steel. The Ni-alloyed steel 18NiCrMo14-6 3D proved superior in HCF regime and thereby beneficial for high impact applications but worse in the VHCF regime.
iii. A set of equations to predict the fatigue limit under fully reversed axial loading is proposed, relying on the √area model by Murakami and assuming a constant fatigue strength between 300 to 550 HV.
iv. Although the hard steel showed poor cyclic properties under axial loading, the fatigue limit under fully reversed torsion was on par with the other tested steel, indicating a reduced sensitivity towards internal inclusions. The proposed equation for the fatigue ratio and, thereby, shear strength relies on the microhardness throughout the carburised layer.
v. The mean stress sensitivity is critical when estimating the effect of mean compressive stresses on the allowable stress amplitude in the carburised layer. Especially for hard steels, a significant discrepancy was elaborated and overcome by proposing a new mean stress sensitivity model, depending on the internal notch factor.

ACKNOWLEDGEMENTS

The authors would like to thank Sonats, Europe Technologies for supporting this project through the ultrasonic shot-peening, recipe formulation and residual stress measurements, in addition to the members of the JIP project for material suggestions, discussions and heat treatment of the tested steels. The authors H.B., A.W., A. S and S.H. gratefully acknowledge funding of the VHCF part of this work by the German Research Foundation (DFG) through the Collaborative Research Centre CRC 920—Project-ID 169148856, subproject C04.

DATA AVAILABILITY STATEMENT

The data used in this manuscript can be made available on request from the authors.

NOMENCLATURE

√area	square root of the projected area of an inclusion
2D, 3D	forging method stretching or stretching-upsetting-stretching
a, b, c and d	model parameters LZ criterion
A	total elongation
C, k	Basquin constants
E_{LZ}	material utilisation LZ criterion
EBSD	electron backscatter diffraction
EDS	energy dispersive X-ray spectroscopy
$f_{-1,0,-7}$	axial fatigue strength, $R = -1, 0, -7$
F	cumulative distribution of $\sqrt{area}_i$
FB	flank breakage
FWHM	full width at half maximum diffraction peaks
G	grain size
HCF	high cycle fatigue
HV	Vickers hardness
$K_{F\tau}$	surface roughness factor
K_{NT}	life factor
K_{size}	statistical size factor
LLF	long-life fatigue
LZ	Liu and Zenner fatigue criterion
M	mean stress sensitivity (FKM)
MLM	maximum likelihood method
n	stress redistribution factor
N_f	number of cycles to failure
R	stress ratio
R_a, R_z	average, mean roughness
R_m	ultimate tensile strength
R_{p02}	yield strength
s	standard deviation

$s_{\log}(\sigma_a)$	standard deviation of log cycles to failure
SEM	scanning electron microscopy
SN	stress amplitude vs. number of cycles
$t_{-1,0}$	shear fatigue strength, $R = -1, 0$
TFF	tooth flank fracture
TIFF	tooth interior fatigue fracture
VHCF	very high cycle fatigue
wt.%	weight percent
Z	reduction of area
α	mean stress factor (Murakami)
$\alpha_{\sigma,\tau}$	notch factor axial, shear
$\beta_{0\mu}$, $\beta_{1\mu}$,β_{0s}, β_{1s}	MLM parameters
κ	fatigue ratio (f_{-1}/t_{-1})
λ	standardized normal distribution factor
$\mu_{\log}(\sigma_a)$	mean log cycle to failure
σ_a, τ_a	stress amplitude axial, shear
σ_{nm}, σ_{na}	normal mean and amplitude stress
τ_{sm}, τ_{sa},	shear mean and amplitude stress
ϕ, ψ	Euler angles

ORCID

Stephan André Böhme https://orcid.org/0000-0001-9703-583X
Alexei Vinogradov https://orcid.org/0000-0001-9585-2801
Horst Biermann https://orcid.org/0000-0002-6036-0687
Anja Weidner https://orcid.org/0000-0002-6432-902X
Alexander Schmiedel https://orcid.org/0000-0003-0008-5473
Sebastian Henkel https://orcid.org/0000-0003-1686-7728

REFERENCES

1. Boiadjiev I, Witzig J, Tobie T, Stahl K. Tooth flank fracture—basic principles and calculation model for a subsurface initiated fatigue failure mode of case hardened gears. In: *International Gear Conference 2014: 26th–28th August 2014, Lyon*. Oxford: Chandos Publishing; 2014:670-680.
2. ISO. *ISO/TS 6336-4:2019—Calculation of Load Capacity of Spur and Helical Gears—Part 4: Calculation of Tooth Flank Fracture Load Capacity*. Switzerland: ISO copyright office; 2019.
3. Klein M, Seabra J, Höhn BR, Michaelis K, Annast R. Theoretical and experimental investigations about flank breakage in bevel gears. *Indl Lubr Tribol*. 2011;63(1):5-10.
4. MackAldener M. *Tooth Interior Fatigue Fracture & Robustness of Gears*. Department of Machine Design, KTH - Stockholm: Stockholm; 2001.
5. Böhme SA, Merson D, Vinogradov A. On subsurface initiated failures in marine bevel gears. *Eng Fail Anal*. 2020;110:104415. https://doi.org/10.1016/j.engfailanal.2020.104415
6. Findley WN. A theory for the effect of mean stress on fatigue of metals under combined torsion and axial load or bending. *J Eng Ind*. 1959:301-306.
7. Dang Van K. Sur la résistance à la fatigue des métaux. *Sciences et Technique de l'Armement*. 1973(3eme fascicule): 647-722.
8. Oster P. *EHD-Zahnflankenbeanspruchung - Beanspruchung der Zahnflanken unter Bedingungen der Elastohydrodynamik*. FVA Heft 131, TU München; 1982.
9. Hertter T. *Rechnerischer Festigkeitsnachweis der Ermüdungstragfähigkeit vergüteter und einsatzgehärteter Stirnräder*. Munich: Institut für Maschinen- und Fahrzeugtechnik, TU München; 2003.
10. Liu J, Zenner H. Berechnung der Dauerschwingfestigkeit bei mehrachsiger Beanspruchung - Teil 1 und 2. *Materialwissenschaft Und Werkstofftechnik*. 1993;24:240-249. and 296–303.
11. Murakami Y. Material defects as the basis of fatigue design. *Int J Fatigue*. 2012;41(Supplement C):2-10.
12. Murakami Y. *Metal Fatigue: Effects of Small Defects and Nonmetallic Inclusions*. Cambridge, MA: Academic Press; 2019.
13. FKM. *Analytical Strength Assessment of Components*. 6th edition. Frankfurt: VDMA; 2012.
14. Steutzger M. *Größeneinfluß auf die Zahnfußfestigkeit*. Forschungsvorhaben Nr. 162: Forschungsvereinigung Antriebstechnik eV. 1997.
15. Tobie T, Hippenstiel F, Mohrbacher H. Optimizing gear performance by alloy modification of carburizing steels. *Metals*. 2017;7(10):415. https://doi.org/10.3390/met7100415
16. DIN. DIN 50100:2016 - Schwingfestigkeitsversuche - Durchführung und Auswertung von zyklischen Versuchen mit konstanter Lastamplitude für metallische Werkstoffproben und Bauteile. In: 2016.
17. Pascual F, Meeker W. Analysis of fatigue data with run-outs based on a model with non constant standard deviation and a fatigue limit parameter. *J Test Eval*. 1997;25:292-301.
18. Pessard E, Morel F, Verdu C, Flacelière L, Baudry G. Microstructural heterogeneities and fatigue anisotropy of forged steels. *Mater Sci Eng a*. 2011;529:289-299.
19. ISO. *ISO 6336-5:2016—Calculation of Load Capacity of Spur and Helical Gears—Part 5: Strength and Quality of Materials*. Switzerland: ISO copyright office; 2016.
20. Mathesiusova R, Kriz A. The difference in quality of 18CrNiMo7-6 steel and its influences at deformation after carburizing. *Metal*. 2012. 2012; Brno, Czech Republic
21. ISO. *ISO 6507-1:2018—Metallic Materials - Vickers HARDNESS test—Part 1: Test Method*. Switzerland: ISO copyright office; 2018.
22. Cecchin D, Kobza E, Cazzolli M, et al. Influence of tempering conditions on shot-peened tool steel components in-depth residual stress profiles. *Adv Mat Res*. 2014;996:769-774.
23. ASME. ASME B46.1 - Surface Texture. In: *Surface Roughness, Waviness and Lay*. New York: ASME; 2009.
24. Mughrabi H. On 'multi-stage' fatigue life diagrams and the relevant life-controlling mechanisms in ultrahigh-cycle fatigue. *Fatigue Fract Eng Mater Struct*. 2002;25:755-764.
25. Sakai T, Sato Y, Oguma N. Characteristic S-N properties of high-carbon-chromiumbearing steel under loading in long-life fatigue. *Fatigue Fract Eng Mater Struct*. 2002;25:765-773.
26. Tsutsumi N, Murakami Y, Doquet V. Effect of test frequency on fatigue strength of low carbon steel. *Fatigue Fract Eng Mater Struct*. 2009;32(6):473-483.

27. Papuga J. A survey on evaluating the fatigue limit under multiaxial loading. *Int J Fatigue*. 2011;33:153-165.
28. Zenner H, Simbürger A, Liu J. On the fatigue limit of ductile metals under complex multiaxial loading. *Int J Fatigue*. 2000; 22:137-145.
29. Rabb R. *Todennäköisyysteoriaan pohjautuva väsymisanalyysi*. Norderstedt: Books on Demand; 2013.
30. Velten E. *Entwicklung eines Schwingfestigkeitskonzeptes zur Berechnung der Dauerfestigkeit thermochemisch randschichtverfestigter bauteilähnlicher Proben*. Darmstadt: TH Darmstadt; 1984.
31. Winderlich B. Das Konzept der lokalen Dauerfestigkeit und seine Anwendung auf martensitische Randschichten, insbesondere Läserhärtungsschichten. *Mat-Wiss U Werkstofftech*. 1990;21:378-389.
32. Garwood MF, Zurburg HH, Erickson MA. *Correlation of laboratory tests and service performance, interpretation of tests and correlation with service*. Ohio: ASM; 1951:1-77.
33. Nishijima S. Statistical analysis of fatigue test data. *J Soc Mater Sci Japan*. 1980;29:24-29.
34. Banvillet A, Palin-Luc T, Lasserre S. A volumetric energy based high cycle multiaxial fatigue citerion. *Int J Fatigue*. 2003;25(8): 755-769.
35. Carpinteri A, Spagnoli A. Multiaxial high-cycle fatigue criterion for hard metals. *Int J Fatigue*. 1985;23(2):135-145.
36. Davoli P, Bernasconi A, Filippini M, Foletti S, Papadopoulos IV. Independence of the torsional fatigue limit upon a mean shear stress. *Int J Fatigue*. 2003;25:471-480.
37. El Magd E, Mielke S. Dauerfestigkeit bei überlagerter zweiachsiger statischer Beanspruchung. *Konstruktion*. 1977;29 (Heft 7):253-257.
38. Froustey C, Lasserre S. *Fatigue des aciers sous sollicitations combinees - Application a l'acier 30NCD16*. Talence: ENSAM; 1988.
39. Galtier A. *Contribution a l'etude de l'endommagement des aciers sous sollicitations uni ou multiaxiales*. Bordeaux: E.N.S.A.M. CER de Bordeaux; 1993.
40. Gough HJ. Engineering steels under combined cyclic and static stresses. *J Appl Mech*. 1950;17(2):113-125.
41. Gough HJ, Pollard HV. The strength of metals under combined alternating stresses. *Proc Inst Mech Eng*. 1935;131:1-103.
42. Gough HJ, Pollard HV, Clenshaw WJ. *Some Experiments on the Resistance of Metals to Fatigue Under Combined Stresses*. Reports and memoranda 2522. London: London H.M.S.O.; 1951.
43. Heidenreich R. *Schubspannungsintensitätshypothese - Dauerschwingfestigkeit bei mehrachsiger Beanspruchung*. Niederrad: Frankfurt am Main; 1983.
44. Heidenreich R, Zenner H. *Festigkeitshypothese - Berechnung der Dauerfestigkeit für beliebige Beanspruchungskombinationen*. Niederrad: Frankfurt am Main; 1976.
45. Issler L. *Festigkeitsverhalten metallischer Werkstoffe bei mehrachsiger phasenverschobener Beanspruchung mit verschiedenen Spannungszeitverläufen*. Stuttgart: Universität Stuttgart; 1973.
46. Kaniut C. *Zur Betriebsfestigkeit metallischer Werkstoffe bei mehrachsiger Beanspruchung*. Aachen: RWTH Aachen; 1983.
47. Lasserre S, Froustey C. Multiaxial fatigue of steel—testing out of phase and in blocks: validity and applicability of some criteria. *Int J Fatigue*. 1992;14(2):113-120.
48. Lempp W. *Festigkeitsverhalten von Stählen bei mehrachsiger Dauerschwingbeanspruchung durch Normalspannungen mit überlagerten phasengleichen und phasenverschobenen Schubspannungen*. Stuttgart: Technische Universität Stuttgart; 1977.
49. Mielke S. *Festigkeitsverhalten metallischer Werkstoffe unter zweiachsiger schwingender Beanspruchung mit verschiedenen Spannungszeitverläufen*. Aachen: RWTH Aachen; 1980.
50. Nishihara T, Kawamoto M. The strength of metals under combined alternating bending and torsion with phase difference. *Mem College Engng Kyoto Imperial University*. 1945;11:85-112.
51. Nolte F. *Dauerfestigkeitsuntersuchungen an Stahlwellen bei umlaufender Biege- und überlagerter statischer Verdrehbeanspruchung*. Berlin: TU Berlin; 1973.
52. Poeppelmann CM. *Axial and Torsion Fatigue of High Hardness Steels*. Toledo: University of Toledo; 2011.
53. Rotvel F. Biaxial fatigue tests with zero mean stresses using tubular specimens. *Int J Mech Sci*. 1970;12(7):597-613.
54. Simbuerger A. *Festigkeitsverhalten zäher Werkstoffe bei einer mehrachsigen phaseverschobenen Schwingbeanspruchung mit körperfesten und veränderlichen Hauptspannungsrichtungen*. Darmstadt: TH Darmstadt; 1975.
55. Troost A, Akin O, Klubberg F. Dauerfestigkeitsverhalten metallischer Werkstoffe bei zweiachsiger Beanspruchung durch drei phasenverschoben schwingende Lastspannungen. *Konstruktion*. 1987;39:479-488.
56. Zenner H, Heidenreich R, Richter I. Dauerschwingfestigkeit bei nichtsynchroner mehrachsiger Beanspruchung. *Materialwissenschaft Und Werkstofftechnik*. 1985;16(3):101-112.
57. Suresh S. *Fatigue of materials*. New York: Cambridge University Press; 2006.
58. Bell WJ, Benham PP. The effect of mean stress on fatigue strength of plain and notched stainless steel sheets in the range of 10 to 10^6 cycles. Symposium on Fatigue Tests of Aircraft Structures: Low-Cycle, Full-Scale, and Helicopters; 1962.
59. Macherauch E, Wohlfahrt H. *Eigenspannungen und Ermüdung*. Oberursel: Ermüdungsverhalten metallischer Werkstoffe; 1985.
60. Paysan B. *Untersuchungen des Einflusses einiger Kerbformen auf die Tragfähigkeit von Wellen bei umlaufender Biegung und überlagerter statischer Torsion*. Berlin: TU Berlin; 1970.
61. ISO. ISO 10300-2:2014 - Calculation of load capacity of bevel gears. In: *Part 2: Calculation of surface durability (pitting)*. Switzerland: ISO copyright office; 2014.
62. Spangenberg S. *Untersuchungen zur Schwingfestigkeit einsatzgehärteter Stähle*. Düsseldorf: TU Berlin; 2000.
63. Wyszkowski J, Priegnitz H, Ratkiewicz A, Gozdzik E, Ratkiewicz A. Influence of residual austenite on certain properties of case-hardened steel. *Rev Met*. 1971;411:411-422.

How to cite this article: Böhme SA, Vinogradov A, Biermann H, Weidner A, Schmiedel A, Henkel S. Fatigue of carburised CrNiMo steel: Testing and modelling concept. *Fatigue Fract Eng Mater Struct*. 2020;1–17. https://doi.org/10.1111/ffe.13394

A.3 Paper III

Abstract This publication focuses on the numerical stress prediction in case-carburized bevel gears and on their fatigue assessment. Four gear sets are analyzed for the common fatigue failure modes of pitting, tooth root breakage, and subsurface fatigue. The proposed algorithm, enabling the prediction of the dominant failure type and region, relies on the previously published material model for carburized CrNiMo steels. It utilizes a 2D plane strain simplification as only the mean cross-section is analyzed and evaluates the shear mean and amplitude stresses through the maximum rectangular hull method. A novel multiaxial fatigue criterion is presented and validated.

Received: 7 December 2020 | Revised: 12 March 2021 | Accepted: 31 March 2021

DOI: 10.1111/ffe.13475

ORIGINAL ARTICLE

FFEMS Fatigue & Fracture of Engineering Materials & Structures WILEY

A novel predictive model for multiaxial fatigue in carburized bevel gears

Stephan André Böhme[1] | **Alexei Vinogradov**[1] | **Jan Papuga**[2] | **Filippo Berto**[1]

[1]Department of Mechanical and Industrial Engineering, Norwegian University of Science and Technology (NTNU), Trondheim, 7491, Norway

[2]Faculty of Mechanical Engineering, Czech Technical University in Prague, Technická 4, Prague 6, 166 07, Czech Republic

Correspondence
Stephan André Böhme, Department of Mechanical and Industrial Engineering, Norwegian University of Science and Technology (NTNU), Trondheim 7491, Norway.
Email: stephan.a.bohme@ntnu.no

Funding information
ESIF, EU Operational Program Research, Grant/Award Number: CZ.02.1.01/0.0/0.0/16_019/0000826; Norwegian Research Council, Grant/Award Number: 270828

Abstract

This publication focuses on the numerical stress prediction in case-carburized bevel gears and on their fatigue assessment. Four gear sets are analyzed for the common fatigue failure modes of pitting, tooth root breakage, and subsurface fatigue. The proposed algorithm, enabling the prediction of the dominant failure type and region, relies on the previously published material model for carburized CrNiMo steels. It utilizes a 2D plane strain simplification as only the mean cross-section is analyzed and evaluates the shear mean and amplitude stresses through the maximum rectangular hull method. A novel multiaxial fatigue criterion is presented and validated.

KEYWORDS

Dang Van criterion, fatigue in case hardened steel, multiaxial fatigue criterion, numerical modeling, rolling contact fatigue

1 | INTRODUCTION

Typical fatigue failure modes of cylindrical and bevel gears are pitting, tooth root breakage, and subsurface fatigue, with the latter becoming increasingly prevalent on highly loaded, carburized gears. Currently, a transition from surface failure to subsurface initiated fatigue failure is taking place, as pitting or tooth root breakages are successfully avoided by means of macrogeometry and microgeometry optimization, material and lubricant improvements, and/or by post-processing steps such as shot peening or superfinishing. Subsurface fatigue,[1] flank breakage (FB),[2] tooth interior fatigue fracture (TIFF),[3] or tooth flank fracture (TFF)[4] describes a similar subsurface failure mode initiated by stress shear. Such cases are documented on truck gearboxes, power plants, wind turbines, and on marine propulsion equipment, where it has evolved into the most critical failure mode for azimuthing thrusters. Aimed at predicting and preventing subsurface initiated failures of large marine bevel gears, this work continues the efforts of the "improved reliability of thrusters" joint industry project and combines the previously published material model for carburized CrNiMo steel[5] with numerical stress and multiaxial fatigue predictions.

The works by Höhn and Oster,[6] Hertter,[7] Witzig,[8] and Boiadjiev et al.,[9] which have led to the proposals of the ISO/TS 6336-4[4] and ISO/TS 10300-4[10]on TFF in cylindrical and bevel gears, rely on the analytical prediction of the Bernoulli bending and Timoshenko shear stresses in a gear tooth, ignoring the effect of the bending moment on the shear stress distribution[11] and the transverse normal stress in the point of load introduction.[12] Balduzzi et al.[11] and Hofmann[12] outline analytical methods to

estimate these stress components in non-prismatic beams, enabling improved analytical stress prediction in cylindrical or bevel gear teeth. Similarly, Weber[13] proposed an analytical shear and bending stress model relying on the approximation of the gear tooth as a wedge. Due to the multitude of overlaying stress components in a gear tooth and the inherent inaccuracy of any analytical model, a 2D finite element model (FEM) was pursued in this study. As such, only the mean cross-section of a pinion or wheel bevel gear tooth is analyzed, relying on the 2D plane strain assumption for the prediction of the stresses along the tooth flank. The developed FEM relies on linear elastic material behavior and a load distribution derived from loaded tooth contact analysis (LTCA)[14] or by analytical calculations.[15] Focusing on the mean cross-section is deemed appropriate as bevel gears are typically manufactured with a heightwise and lengthwise crowning, leading to a stress concentration in the middle of the tooth. Comparing the subsurface stress states in cylindrical[13] and bevel gears[16] as a result of 2D plane strain and full 3D contact and stress analysis gives further merit to the above proposed simplifications. If sufficient distance to the heel or toe of the gear tooth is kept (>5 mm), the plane strain assumption holds true and leads to conservative results in the material depth critical for subsurface fatigue crack initiation. Focusing on the detrimental orthogonal shear stress amplitude along a path perpendicular to the loaded contact point, the difference between the 2D plane strain and 3D stress state is small (<10%) for all material depths.

Besides the simplified stress prediction, the ISO/TS 6336–4[4] (i) inaccurately predicts the hardness profile for large gears, (ii) omits the tensile residual stresses in the core of the gear tooth, and (iii) does not weight the static residual stresses through a material-dependent model parameter. For large gears, the carburizing process is commonly divided in two stages, a boost phase with a carbon potential of 0.9% to 1.3% in the furnace to realize the intended case hardening depth (CHD) economically and a second phase with a 0.6% to 0.8% carbon potential to achieve the desired surface carbon content.[17] An initial hardness plateau and a steep transition from the hard case to the soft core are the results. Whereas the hardness profile by Lang[18] resembles a single-stage carburizing process, the model by Thomas[19] is able to capture both the single and dual-stage processes through the use of the maximum hardness depth y_{HVmax}.The proposed ISO fatigue criterion[4,8,9] bears resemblance to the Dang Van multiaxial fatigue criterion as it predicts a shear stress amplitude and combines it with the hydrostatic stress component or, in the case of gears, the residual stress component. In contrast to the Dang Van criterion, the static stress component is not weighted through a material-dependent model parameter (see b_{DV} in Equation 13) but kept constant across the gear's cross-section. If the missing tensile residual stresses are added to the ISO/TS6336-4, the local material utilization, defined as the reverse of the safety factor, peaks in the core rather than in the case/core interface.

The aim of this study, alongside the material model presented in Böhme et al.,[5] is to improve upon the above-listed points and to enable a comprehensive assessment of all gear typical fatigue failure modes in one calculation. For an initial assessment, the popular Dang Van critical plane multiaxial fatigue criterion (DV)[20] is studied. Subsequently, its accuracy is assessed by comparing it to a fatigue data set, composed of 23 test results under static, compressive and tensile normal stresses, and oscillating shear stresses.[21–24] It is benchmarked against these multiaxial fatigue criteria: the Sines criterion,[25] the Crossland criterion,[26] the Liu and Zenner criterion,[27] Papuga's integral criterion,[28] and the Hertter criterion.[7] A novel multiaxial fatigue criterion is derived and included in the comparison and applied to several gear sets that failed with varying fatigue failure modes.

2 | MATERIAL AND METHODS

The gears listed in Table 1 form the basis for the herein outlined stress and fatigue models, covering all gear typical fatigue failure modes. Whereas G1 and G2 are large marine bevel gears with a history of subsurface fatigue failures, G0 and F0 are test gears of the FVA411 research project[29] studying pitting failures and tooth root breakages, respectively. The large range of studied gear sizes (170 to 1,120 mm outer pitch diameter d_{e2}) and practical versus test gear loading conditions (1,359 to 1,838 MPa maximum surface pressure p_{H}) ensure the applicability of the developed model to a wide range of gears.

Bearings, rails, and gears are subjected to rolling contact fatigue with Hertzian stresses being by in large responsible for potential component failure. Excluding dynamic effects or changes to the applied load, the stress state on the surface of a bearing or rail characterized through the half-Hertzian contact width b_{H} and the maximum pressure p_{H} remains constant, whereas both parameters change during the meshing of the pinion and wheel, not just along the instantaneous contact line but also along the contact path. The subsurface state of this position- and time-dependent stress state presents itself as a superposition of Hertzian, shear, out-of-phase bending, and frictional shear stresses. In the case of carburized gears, static residual stresses, either compressive in the case or tensile in the core, are imposed on the load-related stresses. Occasionally considered,[7,30] but in this

TABLE 1 Studied gears, ranging from marine bevel gears transmitting up to 3.5 MW to small test gears of 170 mm diameter

		G1		G2		G0		F0	
Description	**Unit**	**Pinion**	**Wheel**	**Pinion**	**Wheel**	**Pinion**	**Wheel**	**Pinion**	**Wheel**
Failure mode	-	TFF		TFF		Pitting		Tooth root breakage	
Pressure angle, α	°	20		20		20		20	
Number of teeth, z	-	14	37	14	37	9	34	18	57
Outer pitch diameter, d_e	mm	348.1	920.1	423.7	1,120	45.01	170.03	53.69	170.02
Tooth width, b	mm	170		200		26		20	
Mean spiral angle, β_m	°	35		35		33		33	
Profile shift, x_{hm1}	-	0.33		0.33		0.45		0.45	
Tooth thickness factor, x_{sm1}	-	0		0		0.05		0.05	
Case hardening depth, CHD	mm	2.6		3.5		1		0.9	
Surface/core hardness	HRC/HV	60/400		60/380		60/450		60/450	
Power, P	kW	2,500		3,500		94.25		178.86	
RPM, n	1/min	660	249.7	531	200.9	4,500	3,454.5	4,880	1,541
Cycles to failure, N_f	-	$3{\cdot}10^8$		$3{\cdot}10^8$		$7.7{\cdot}10^7$		$7{\cdot}10^6$	

Note: G1 and G2 as examples of gears failing from subsurface fatigue, G0 from pitting, and F0 from tooth root breakage.

study neglected, are thermal, elasto-hydrodynamic, and roughness effects. The complexity of the stress state, the gear geometry, and superposition of the individual stress components lend themselves to a numerical rather than analytical evaluation of a gear tooth. At the same time, 3D finite element contact simulations are cumbersome, depending greatly on an accurate geometry representation, the occurring displacements between the pinion and wheel, and the chosen mesh-mating conditions.

Combining those considerations with the fact that a gear tooth is often significantly larger in width (along the tooth flank) than in thickness or height, and as analytical or seminumerical solutions of the stress distribution along the path of contact are readily available,[14,15] a simplified numerical 2D plane strain tooth model is pursued in this study. Keeping the extremely complex nature of multiaxial fatigue analysis in mind, focusing on the 2D mean cross-section of either a pinion or wheel tooth ensures the implementation of a large number of contact instances, a fine mesh, and spherical angles θ and ϕ to analyze a multitude of planes in each node. Section 2.1 outlines the meshing of the gear tooth, the load approximation, the strength, and the residual stress model, alongside the estimation of the local shear stresses on each material plane. In the closing part of this section, an application of the Dang Van critical plane multiaxial fatigue criterion to the stress state and material model is presented. Figure 1 outlines the workflow inside the developed MATLAB based calculation model, and it depicts the sections covered in this part of the article.

2.1 | Meshing of 2D cross-section

The bevel gear's mean cross-section is derived by modeling the virtual cylindrical gear's involute normal cross-section and meshed by intersecting a set of horizontal and vertical curves (grid lines) with the profile of the gear tooth. A corner node is placed on every intersection. The distance between the parallel grid lines is set by the chosen element size e_s. Earlier study[31] suggests that for a pure Hertzian contact, a load introduction over at least eight nodes, is advisable to capture the subsurface stresses accurately. The contact between two meshing bevel gear teeth is simplified to the in Figure 2B visualized Hertzian contact model, where each position along the path of contact is represented as a line contact on a 2D half-plane (cylinder/plane model) and governed by the maximum contact pressure p_H and by the half Hertzian contact width b_H as a result of the external force F and the equivalent radius of curvature ρ_{eq}.

The load instances or contact positions i are defined for each corner node on the load-carrying flank. The above-outlined mesh resolution ($8{\cdot}e_s < 2{\cdot}b_H$) results in a very fine mesh on the surface of the gear tooth and in a large number of elements and of contact positions. Avoiding excessively large matrices during the calculation, every second, fourth, and eight heightwise grid lines beyond the depth of $s_{mn}/16$, $s_{mn}/4$, and $x > 0$ (s_{mn}, mean normal circular tooth width) are removed. Subsequently, a framed Delaunay triangulation is carried out, connecting all nodes to triangular elements. By default,

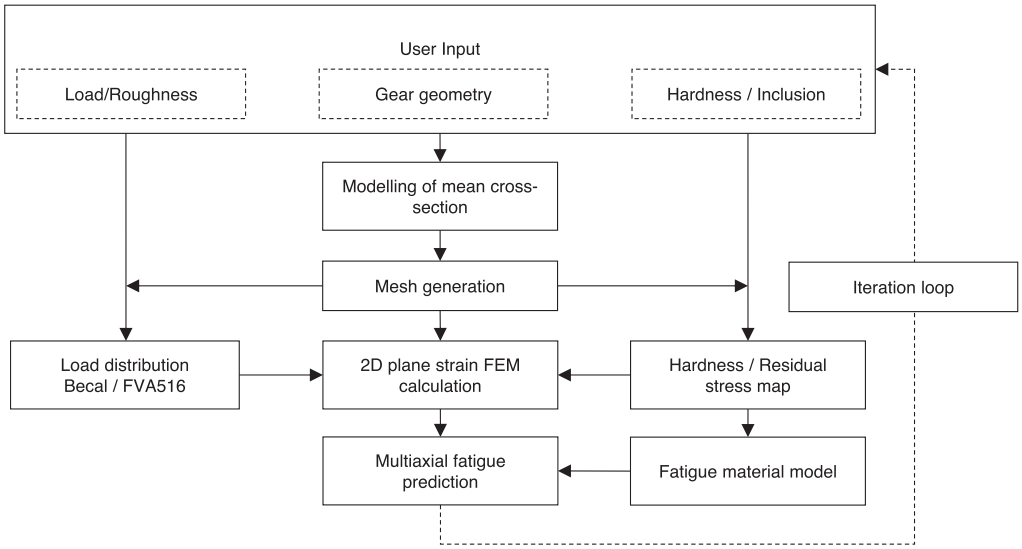

FIGURE 1 Outline of the calculation model and iteration loop, optimizing a given gear design against fatigue

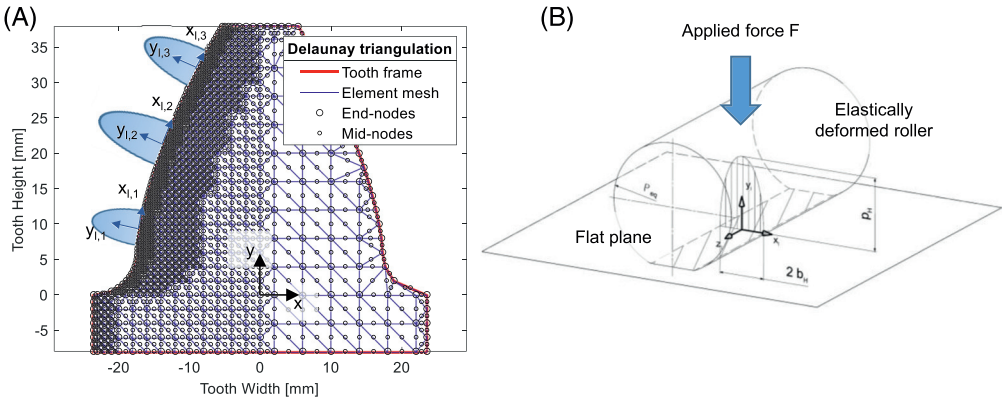

FIGURE 2 (A) Gear mesh of normal cross-section (visualization for 0.5 mm mesh) and (B) Hertzian contact model for each contact position and tooth segment [Colour figure can be viewed at wileyonlinelibrary.com]

calculations are carried out for "T6" triangular elements, adding mid-side nodes between the already defined corner nodes. The mesh is exemplified in Figure 2A for G1 with a 0.5 mm element size to better visualize the frame, the mesh layout, and the locations of the global and local coordinate systems that are contact position specific. Similarly visualized are the assumptions for each contact position, whereby the meshing of curved gear teeth is simplified to a cylinder/plane contact (Figure 2B). The element sizes used for the calculation of the in Table 1 listed gear sets are 0.2, 0.3, 0.05, and 0.04 mm.

2.2 | Analytical surface model

The first step in calculating the subsurface stresses in an arbitrary bevel gear tooth is the prediction of the maximum surface stresses $p_{H,i}$, the equivalent radius of curvature $\rho_{eq,i}$, and friction coefficient μ_i for each contact position i. Considering the transmitted torque, accurate tooth geometry, and occurring relative deflections between pinion and wheel, a LTCA using the FVA program Becal[14] is generally considered the best practice for spiral bevel and hypoid gears. If the detailed tool and

machine data used to simulate the tooth geometry in the LTCA are not available, a simplified analytical approach[15,32] can be pursued. Developed for the prediction of micropitting damage in the mean cross-section of bevel gears, the estimated load distribution in the FVA516[15] yields very comparable results to the LTCA for gears with standard microgeometries and centered contact pattern positions. Figure 3 compares the surface stresses $p_{H,i}$, the equivalent radius of curvature $\rho_{eq,i}$, the local friction coefficient μ_i, and the half Hertzian contact width b_{Hi} predicted for the mean cross-sections of G1 and G2 according to Hombauer[15] and Baumann et al.[14] Clearly visible is an almost linear increase in $\rho_{eq,i}$ along the tooth profile from the pinion root to the tip, a maximum surface stress $p_{H,i}$ around the pitch point (15.5 mm for G1 and 19 mm for G2), and a friction coefficient as a product of the local pressure and sliding velocity.[33] The half-Hertzian contact width $b_{H,i}$, a product of $p_{H,i}$ and $\rho_{eq,i}$, governing the depth of the acting stresses inside the gear tooth, reaches its maximum not around the pitch point but further towards the tooth tip,[34] indicating that if a singular TFF critical contact position is to be studied, not the pitch point but half tooth height should be considered. Based on the conducted evaluation of Hombauer[15] against Baumann et al.,[14] a good approximation of the load distribution is achieved for moderately loaded large bevel gears. For highly loaded test gears (test gears G0 and F0), the load increase towards the tip and root leads to inaccuracies when relying on Hombauer[15] for the prediction of the load distribution, requiring the LTCA for accurate results. Similarly, modified microgeometries or large gear displacements need to be considered through the LTCA.

As pure rolling between pinion and wheel teeth is only present along the pitch line, the product of the linearly increasing sliding velocity and pressure distribution gives rise to friction in the contact, governed through the friction coefficient μ_i as outlined by Hombauer[15] and defined by Klein[32] and Wech.[33] For the constellation "pinion pushes wheel," the friction force is oriented away from the pitch line on the pinion and towards the pitch line on the wheel. This change in direction when passing the pitch line needs to be considered in the numerical stress calculation.

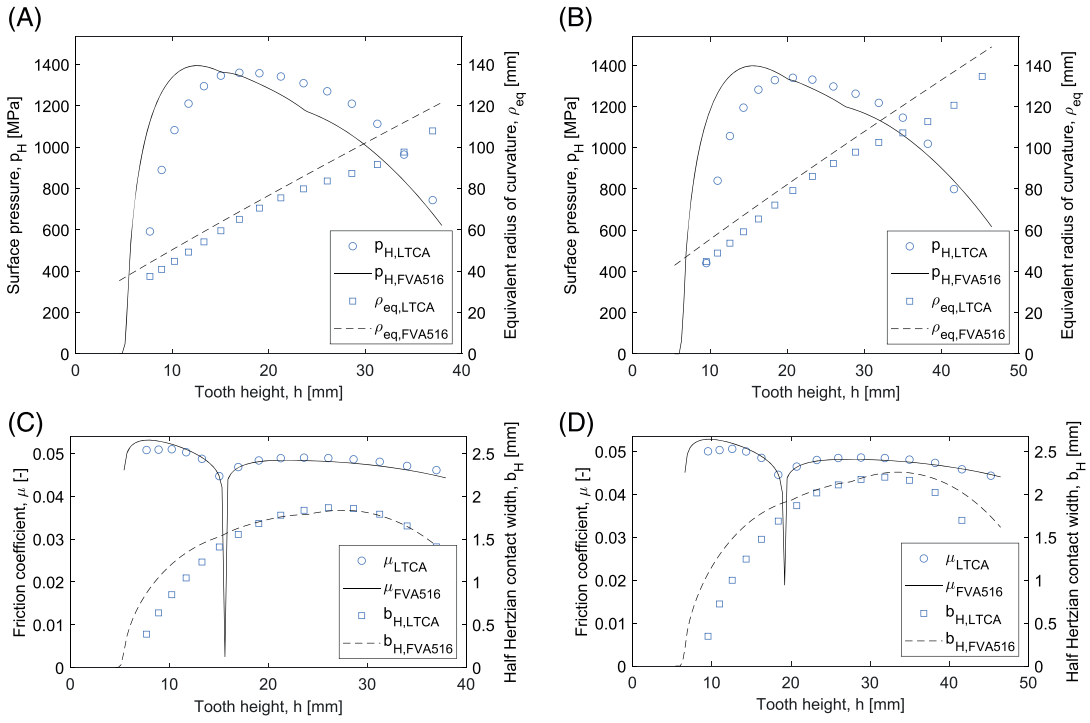

FIGURE 3 Prediction of load and geometry changes along the tooth profile for (A–C) G1 and (B–D) G2 [Colour figure can be viewed at wileyonlinelibrary.com]

2.3 | Hardness and residual stress map

This section describes the process of assigning a hardness value and residual stress matrix to each node n in the 2D mesh of the mean cross-section. Based on numerous hardness measurements on large marine bevel gears,[31,35] and results from the JIP partners, comprised among others of bevel gear suppliers, a better correlation for large gears is achieved with the Thomas[19] than Lang model[18] as the predicted hardness profile intersects the specified CHD (equivalent to the 550 HV depth) and does not overestimate the local hardness when transitioning from the hard case to the soft core.[35] The model by Thomas relies on two second-order polynomials to describe the hardness profile up to and beyond the CHD, using a tangential constraint in the intersection. It considers a hardness peak larger than the specified surface hardness HV_s in a specific depth y_{HVmax}. Here, y_{HVmax} is used not to capture the depth of the hardness peak but the steep transition from the hard case to the soft core of large gears as a result of the two-stage carburizing process outlined in the introduction. Figure 4A visualizes four hardness profiles for module 5 and 20 bevel gears and both models. Whereas Lang predicts two identical hardness profiles plotted against the normalized depth y/CHD, Thomas enables the representation of a steeper case-to-core transition for the large gear. Evident is also the missing intersection of the Lang model through the specified CHD but rather 0.94 CHD. For the small and large gear, y_{HVmax} was set to −0.25 and 0.3 mm, respectively. In the case of large y_{HVmax}, a cap should be applied to the predicted hardness profile using the specified surface hardness to avoid excessive subsurface hardnesses.

Measuring the hardness profile in the tooth height direction, the hardness of both surface and core and the CHD vary as a result of the tooth profile, carbon exposure, and quenching response. Capturing those differences, the implemented hardness model allows the specification of three sets of hardness parameters in the heightwise direction. Microhardness measurements on large[35] and small gears[36] describe a 15–20% lower CHD in the tooth root compared to the pitch or midpoint and an approximately 15% higher CHD in the tooth tip.[35] The surface and core hardnesses follow similar but less pronounced trends, changing approximately 3% and 15%, respectively, from the root to the tip. Surface hardness $HV_{S,i}$, core hardness $HV_{C,i}$, and CHD_i are assigned to each surface node by linear interpolation of the three specified hardness sets and its heightwise position. To allocate a hardness to each subsurface node, the closest surface node is identified, and its distance and hardness parameters ($HV_{S,i}$, $HV_{C,i}$, and CHD_i) are applied to the Thomas model. For the subsequent residual stress predictions, the local tooth width $s_{n,i}$ and the pressure angle α_i are similarly assigned to the surface and subsurface nodes.

Based on neutron diffraction measurements,[37] X-ray and contour method results,[13,38] an iteration of the residual stress model by Lang[18] is presented, assuming unchanged compressive residual stresses up to the specified CHD and a fourth-order polynomial to capture the tensile residual stresses in the core. The proposed model

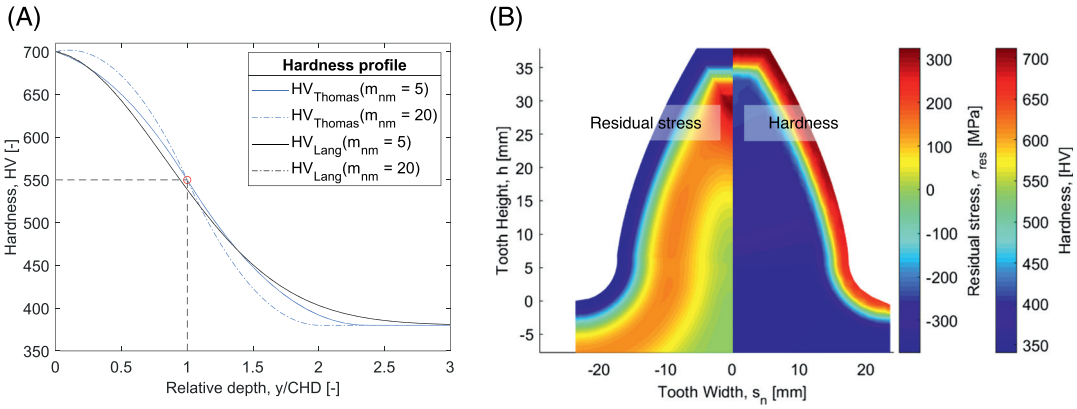

FIGURE 4 Hardness and residual stress prediction (A) visualizing the model differences between Thomas[19] and Lang[18] in the prediction of the hardness profile for small and large gears (m_{mn} = 5, 20) and (B) residual stress and hardness prediction for G1 for interpolated hardness parameters from CHD = [2.1; 2.6; 3.0] mm, HV_s = [59; 60; 60.5] HRC, HV_c = [346; 393; 409] HV in tooth profile positions h = [2; 18; 36] mm [Colour figure can be viewed at wileyonlinelibrary.com]

resembles the equations by Wirth[29] and Weber[13] and predicts peaking tensile residual stress either in the case/core interface or in the core. The constants a, b, and c must be iterated, based on the continuous and tangential constraints in the CHD and the stress equilibrium condition for each path $s_{n\alpha,i}$.

$$\begin{aligned}
&\sigma_{res,n}(y_l) = -5/4\ (HV_i(y_l) - HV_{C,i}) && \text{for } HV_i(y_l) - HV_{C,i} \le 300\,\text{HV}\\
&\sigma_{res,n}(y_l) = 2/7\ (HV_i(y_l) - HV_{C,i}) - 460 && \text{for } HV_i(y_l) - HV_{C,i} > 300\,\text{HV}\\
&\sigma_{res,n}(y_l) = a\ (y_l - s_{n\alpha,i})^4 + b\ (y_l - s_{n\alpha,i})^2 + c && \text{for } y_l \ge CHD_i\\
&\text{with } s_{n\alpha,i} = \frac{s_{n,i}}{2\cos\alpha_i} \text{ and } \int_0^{s_{n\alpha,i}} \sigma_{res,n}(y_l)\,dy_l = 0
\end{aligned} \tag{1}$$

Not considered is the effect of the concave/convex transition of the tooth profile from the root to the tip on the residual stress distribution. Results compiled in the closing report of the FVA369[39] suggest somewhat elevated compressive residual stress levels in the tooth root of carburized but otherwise untreated gears, but a quantification remains difficult due to a lack of tooth root measurements. Unconsidered is also the negative effect of an excessively large CHD (>0.20 m_{mn}) on the tooth root safety[1,34,36] due to a reduction in compressive surface stress, an increase in surface oxidation and/or grain coarsening.

The final step in the prediction of the residual stress map is the conversion of the residual stress in each node from its local to the global coordinate system, using the node-specific pressure angle α_i. Equation 2 outlines a residual stress matrix and its transformation, that assumes zero residual stresses perpendicular to the surface (i.e., σ_x) and equal tangential and longitudinal stresses (i.e., σ_y and σ_z), following the suggestion by Lang and Weber.

$$S_{res,n} = T \cdot \begin{bmatrix} 0 & 0 & 0 \\ 0 & \sigma_{res,n} & 0 \\ 0 & 0 & \sigma_{res,n} \end{bmatrix} \cdot T' \tag{2}$$

$$\text{with } T = \begin{bmatrix} \cos(\alpha_i) & \sin(\alpha_i) & 0 \\ -\sin(\alpha_i) & \cos(\alpha_i) & 0 \\ 0 & 0 & 1 \end{bmatrix}$$

Figure 4B plots the hardnesses and residual stresses for the mean cross-section of a G1 pinion tooth. Clearly visible are the increasing tensile residual stresses in the core of the gear tooth as a result of the narrowing tooth profile and the hardness profile differences from the tooth root to its tip.

2.4 | Material model

Due to its superior load carrying capacity, marine bevel gears are commonly made of carburized 18CrNiMo7-6 steel.[1,40] Capturing the cyclic behavior of CrNiMo steel as a function of its hardness, cleanliness, and of the number of load cycles, the material model outlined in Böhme et al.[5] is implemented. It covers the fatigue limit under fully reversed and repeated axial loading (f_{-1}, f_0) and torsional fully reversed loading t_{-1} (repeated torsional loading t_0 according to Zenner & Simbürger[41]) in the high cycle fatigue (HCF) and very high cycle fatigue (VHCF) regime. Equation 3 outlines the fatigue model, relying in part on Murakami's $\sqrt{area}$ model.[42] The $\sqrt{area}$ parameter describes the square root of the projected area of an inclusion, perpendicular to the maximum principal stress, κ the fatigue ratio, and M_k mean stress sensitivity, considering the effect of internal notches on the fatigue limit under repeated axial loading.

$$\begin{aligned}
&f_{-1} = \begin{cases} 1.6\,HV & \text{for } HV < 300 \\ \dfrac{1.56 \cdot (HV + 120)}{(\sqrt{area})^{\frac{1}{6}}} & \text{for } HV > 550 \\ 505\,MPa & \text{else} \end{cases} \quad \text{and} \quad f_0 = \frac{2 \cdot f_{-1}}{1 + M_k}\\
&t_{-1} = \frac{f_{-1}}{\kappa} \quad \text{with} \quad \kappa = -5\ 10^{-4}\,HV + \sqrt{3} \quad \text{and} \quad \frac{4t_{-1}}{t_0} - \frac{2f_{-1}}{f_0} = 1
\end{aligned} \tag{3}$$

Fatigue parameters (f_{-1}, f_0, t_{-1}, t_0) are assigned to each node inside the modeled mean cross-section according to the local hardness and to the specified mean inclusion size (default $\sqrt{area} = 80\ \mu m$[5]). The size factor[5] derived from the weakest link theory[43] accounts for the significantly larger highly stressed volume in gear teeth than is the one in the tested fatigue specimen. The stress amplitude vs. the number of cycles (SN) curves and failure probabilities documented in Böhme[5] rely on the maximum likelihood method (MLM). Due to the bimodal nature of fatigue failures from surface defects and from subsurface inclusions, alongside the frequency effect of the tested steel 34CrNiMo6, large standard deviations were estimated. Here, not the MLM but pearl string method[44] derived standard deviation in the VHCF regime is used in the definition of the size factor. The estimated relative standard deviation of 4% suggests an effective, highly stressed volume of 22.26 mm^3 in the tested uniaxial fatigue specimen (hourglass shape, radius 50 mm, Ø 4 mm). Studying the size factor for gears with a mean normal module m_{mn} ranging from 2 to 25 mm, a logarithmic trend when plotting the size factor against the effective volume[43] is observable. To simplify the calculation, the definition of the proposed size factor is altered to rely on the mean normal module rather than on the effective volume similar to the DIN3991.[45]

$$K_X = 1.05 - 0.01 \cdot m_{mn} \text{ with } 0.87 \leq K_X \leq 1 \quad (4)$$

While making an approximation of the size factor extremely easy and capturing the general trend, it inherently favors a larger number of teeth on a given diameter and a smaller module. The above-mentioned study suggests that the opposite usually holds true, but since the absolute difference between both predictions is small (less than 2%), the proposed correlation is deemed acceptable.

The lifetime factor K_{NT} as outlined in Böhme[5] according to the MLM,[46] capturing the 50% failure probability is implemented.

$$K_{NT} = \left(\exp\left(\frac{\ln(N_f) - 31.0}{-3.3}\right) + 325\,\text{MPa}\right)/465\,\text{MPa} \quad (5)$$

In gear standards,[1,40,45] the specified fatigue strength is not stated for a 50 but 1% failure probability. Based on the outlined relative standard deviation of 4%, a conversion factor is suggested and approximated to $f_{xK} = 0.91$. For comparison, Elstorpff[47] states the conversion factor of 0.9 for pitting damage on case-carburized gears. Figure 5 illustrates the modeled fatigue properties of G1 for K_{NT} and $K_X = 1$ along with the predicted hardness map, both for the entire cross-section and for a path perpendicular to the tooth profile. In contrast to the increase in hardness from the core to the case, the fatigue properties remain constant until the CHD of 2.6 mm is reached: a result of the observed fatigue properties of the tested 34CrNiMo6 and 18CrNiMo7-6 steels.[5]

2.5 | Numerical subsurface stresses

For the numerical prediction of the subsurface stresses in an arbitrary bevel gear tooth, the stiffness matrix C, according to the plane strain and linear elastic conditions, is defined. Depending on the chosen element type (default T6), the number of nodes per element, the coordinates, and weights of the Gaussian integration points are set, setting the element stiffness. No significant stress or processing time differences were found for 3 or 7 integration points during the Gaussian quadrature algorithm, resulting in accuracy grade 5 with 7 points being chosen as the default setting. Whereas fixed constraints are assigned to all surface nodes in the base of the tooth model, a surface stress $p_{H,i}$, a half Hertzian contact width $b_{H,i}$, and a friction coefficient μ_i are assigned to each left flank, corner node according to their position in the profile direction. Iterating over each contact position, forces in x and y direction according to the Hertzian stress distribution and friction coefficient are assigned to all surface nodes within a $b_{H,i}$ radius around the centered corner node i. Based on the calculated displacements for each contact position, the strains and stresses of all elements are calculated, yielding the nodal stresses as a stress average of its neighboring elements. To quantify the differences between the programmed numerical model and a commercial FEM software (Siemens NX9), the maximum difference of the von Mises equivalent stress in all nodes and over all contact positions was studied. Focusing on the capability of the numerical model to predict accurate subsurface stresses, an exact representation of the outlined model was recreated in NX9. Figure 6 visualized the maximum stress differences

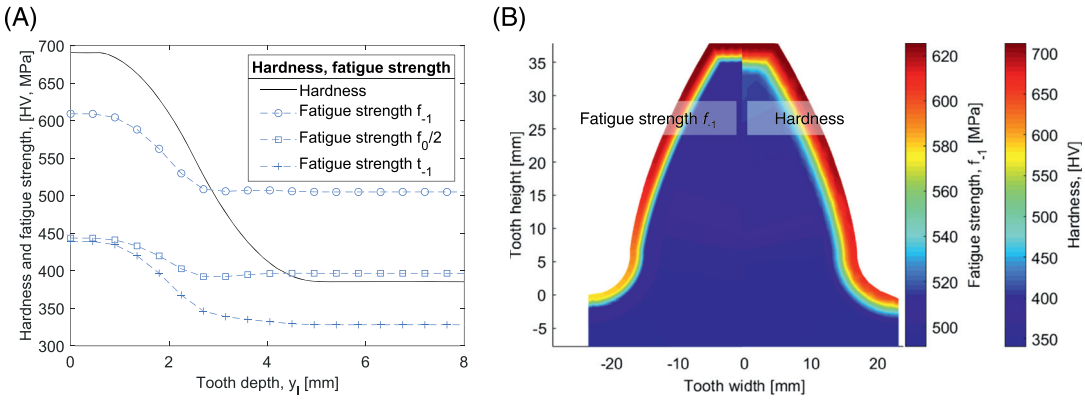

FIGURE 5 Exemplified fatigue strength and hardness correlation for G1 (average strength after $2{\cdot}10^6$ load cycles) for (A) perpendicular to the tooth flank, starting from the pitch point, and (B) the mean cross-section [Colour figure can be viewed at wileyonlinelibrary.com]

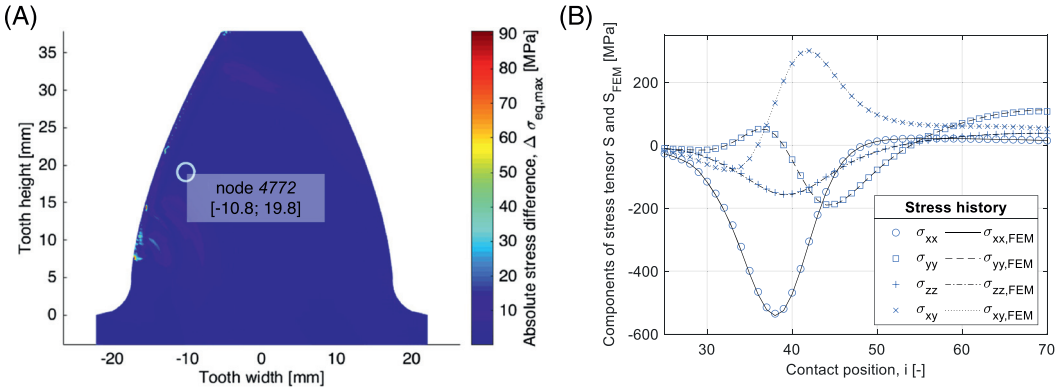

FIGURE 6 Accuracy of the proposed numerical model (A) maximum von Mises equivalent stress difference and (B) all components of stress tensor *S* for node *4772* as a function of time or contact position [Colour figure can be viewed at wileyonlinelibrary.com]

between both models for (a) the von Mises equivalent stress for the entire cross-section and (b) individually for all components of the stress tensor *S* for node *4772* (node with maximum material utilization, coordinates [−10.8; 19.8]). Plotted are the stress differences without the residual stresses and the individual stresses in the global coordinate system.

Except for the pinion dedendum, the predicted stress levels are close to identical, underlining the accuracy of the developed numerical model. As Figure 3 visualizes, the initial contact positions are characterized by low Hertzian stresses and small equivalent radii, resulting in short half-Hertzian contact widths and loading of only a few surface nodes. Considering that subsurface damage typically occurs half-way up the tooth profile, the observable error is deemed noncritical.

With the quality of the numerical stress model established, the number of stress cycles within one load cycle, here defined by a single tooth engagement, needs to be identified. The typical load cycle for node *4772* can be found in Figure 7A with its four active stress components and the von Mises equivalent stress. The paths of individual stress components are clearly out of phase, and a question can be raised, if this load history can be treated as a single load cycle, or if some significant nested cycles are occurring. The analysis according to the Wang and Brown algorithm[48] is depicted in Figure 7B. The method starts with the maximum von Mises stress and analyzes the stress ranges related to the stress tensor in that moment in each time instant. Whenever any half-cycle is interrupted by a trend change (here the point B in the A–C path), it is taken as a new reference point from which the equivalent stress range is calculated. The Wang and Brown algorithm shows that there is one complete cycle A-C-A, into which a small half-cycle B-D is nested. The magnitude of the equivalent stress range of this nested half-cycle is less than one half of the main A-C-A cycle, and thus, the damage related to it should be minimal compared to the total damage. Figure 7A reveals that the stress components in the B-D phase are all outside of the regions where they reach their respective maximums. Based on this analysis, it is obvious that the whole load cycle can be treated as one stress cycle with a negligible impact of such a simplification. Whereas this simplification holds true for the failure mode subsurface fatigue, the pitting damage occurring in the pinion dedendum might have to be treated differently as the magnitude of the B-D half cycle is increased.

2.6 | Shear stress amplitude

The motion of the Hertzian contact area along the tooth flank results in a nonproportional stress field as the principal stress directions and ratios are changing. For failures in the high to very high cycle fatigue regime, stress-based critical plane, or integral multiaxial fatigue criteria are commonly used to assess the local material utilization. They require the prediction of the mean and alternating shear (τ_m and τ_a) and normal stresses (σ_{nm} and σ_{na}) on each node and each material plane. Whereas the critical plane criteria try to identify the worst possible combination of stresses and thereby the plane in which crack initiation is likely to occur, integral methods combine either the stress components or the resulting equivalent stresses on all planes, expressing a total utilization. The traction vector t describes the stress state on a plane Δ, perpendicular to the unit vector $n_{x'}$, defined through

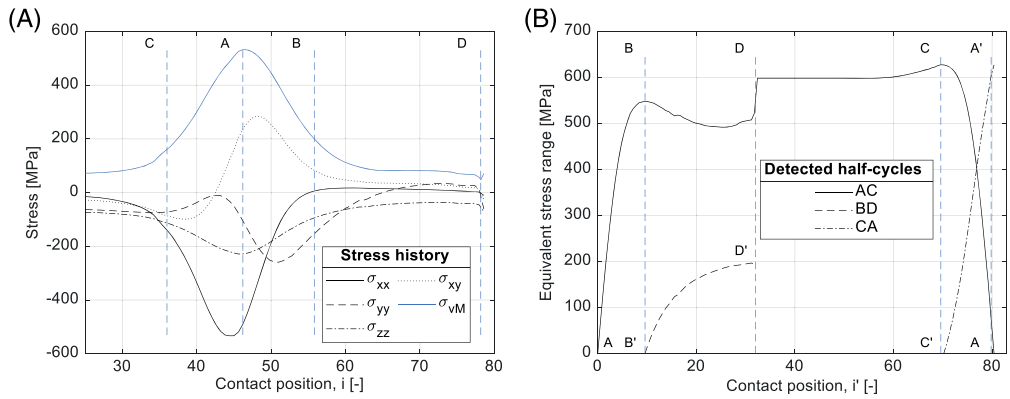

FIGURE 7 (A) Stress cycle and (B) load cycles for node *4772* according to Wang and Brown algorithm [Colour figure can be viewed at wileyonlinelibrary.com]

the spherical angles θ and ϕ. Decomposing t, the normal and shear stresses on Δ can be calculated along the unit vectors $n_{x'}$, $n_{y'}$, $n_{z'}$ (see Equations 6–8 and 8A).

$$n_{x'} = \begin{pmatrix} \sin\varphi\cos\theta \\ \sin\varphi\sin\theta \\ \cos\varphi \end{pmatrix}; n_{y'} = \begin{pmatrix} -\sin\theta \\ \cos\theta \\ 0 \end{pmatrix}; \quad (6)$$

$$n_{x'} = \begin{pmatrix} -\cos\varphi\cos\theta \\ -\cos\varphi\sin\theta \\ \sin\varphi \end{pmatrix},$$

$$t = S \cdot n_{x'} \text{ with } S = \begin{bmatrix} \sigma_{xx} & \tau_{xy} & 0 \\ \tau_{xy} & \sigma_{yy} & 0 \\ 0 & 0 & \sigma_{zz} \end{bmatrix}, \quad (7)$$

$$\begin{aligned} t &= \tau + \sigma_n \cdot n_{x'} = \tau_{x'y'} \cdot n_{y'} + \tau_{x'z'} \cdot n_{z'} + \sigma_n \cdot n_{x'}, \\ \tau_{x'y'} &= t \cdot n_{y'}; \quad \tau_{x'z'} = t \cdot n_{z'}; \quad \sigma_n = t \cdot n_{x'}, \end{aligned} \quad (8)$$

whereas the evaluation of the mean normal stress and of the normal stress amplitude is straightforward, assessing the shear mean and amplitude stresses requires sophisticated methods such as the minimum circumscribing circle (MCC)[20,49] or the maximum rectangular hull (MRH).[50] While the MCC method circumscribes the shear stress path Ψ with the smallest possible circle, capturing the mean shear stress τ_m in its center and the amplitude τ_a in its radius, the MRH method draws a rectangle around the stress path and iterates the maximum stress amplitude in its half diagonal while rotating the rectangular hull to find the highest value. The mean shear stress appears in the center of the rectangle. In Equations 9 and 10, τ^* describes an arbitrary starting position, and a_1 and a_2 correspond to the half of the edge length of the through α rotated rectangle.

$$\begin{aligned} \tau_{m,MCC} &= \min_{\tau^*}\left(\max_t|\tau(t) - \tau^*|\right) \\ \tau_{a,MCC} &= \max_t|\tau(t) - \tau_{m,MCC}|, \end{aligned} \quad (9)$$

$$\begin{aligned} a_{k=1,2} &= \frac{1}{2}\left(\max_t(\tau_k(\alpha,t)) - \min_t(\tau_k(\alpha,t))\right) \\ \tau_{a,MRH} &= \max_\alpha\sqrt{a_1^2(\alpha) + a_2^2(\alpha)}. \end{aligned} \quad (10)$$

Different opinions regarding the accuracy of the MCC and MRH methods exist, suggesting that the MRH method might be beneficial when applied to critical plane criteria and the MCC method when using integral methods.[51] Here, the MRH method is favored as it allows for the significantly faster prediction of τ_m and τ_a.[52] It can easily be vectorized in MATLAB, reducing the three loops over all angles (θ, ϕ) and nodes to a single loop over all nodes. Figure 8B visualizes the predictions of the mean and amplitude shear stress according to the MCC and MRH methods for node *4772*. Whereas both methods predict similar mean shear stresses for the particular node, stress path Ψ and plane Δ, the high degree of non-proportionality results in an approximately 15% higher shear stress amplitude for the MRH method over the MCC method.

For a path through node *4772* and perpendicular to the tooth surface, Figure 9 compares the maximum shear stress amplitude $\tau_{a,MRH}$ with the maximum octahedral shear stress amplitude $\tau_{octa,a}$, with the effective shear stress τ_{eff} (shear stress intensity criterion[24]) and with the

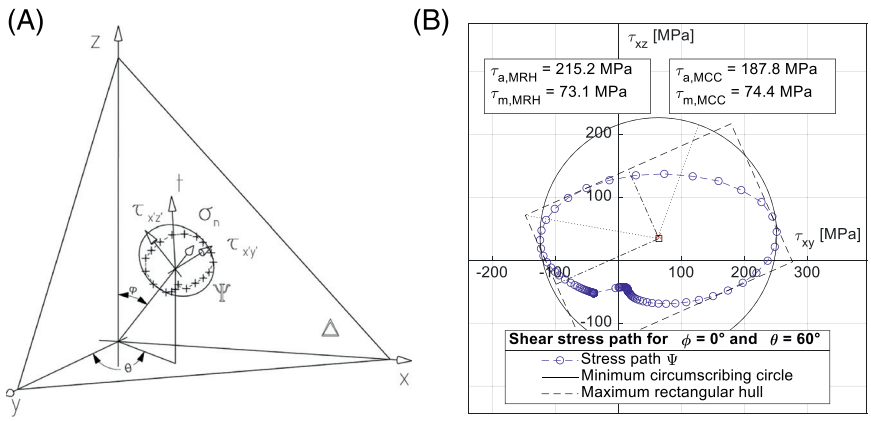

FIGURE 8 (A) Material plane, traction vector and its components; (B) shear stress path, circumscribing circle, and rectangular hull for node *4772* and plane [0°; 60°] [Colour figure can be viewed at wileyonlinelibrary.com]

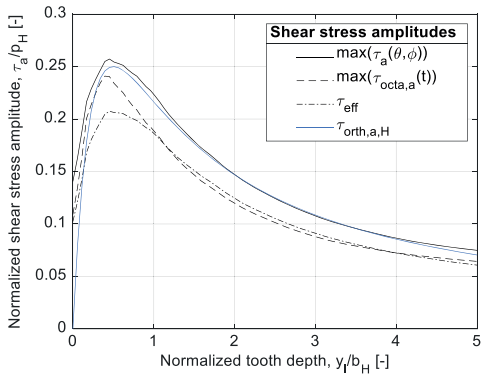

FIGURE 9 Normalized shear stress amplitudes along a path perpendicular to the gear flank, intersecting node *4772* [Colour figure can be viewed at wileyonlinelibrary.com]

analytical prediction of the orthogonal shear stress amplitude $\tau_{orth,a,H}$ based solely on the subsurface stress as a result of the Hertzian stress in the identified surface node. The orthogonal shear stress amplitude is plotted for planes parallel to the surface as early stage subsurface fatigue cracks have been found in similar orientations.

Although the simplified prediction of the critical subsurface shear stresses is not pursued in this publication, it is evident that the orthogonal shear stress amplitude based on the simplified analysis of the Hertzian contact matches the maximum shear stress amplitude according to the MRH method very well. Larger deviations occur in the outer surface layer, where the plane of the maximum shear stress is no longer parallel to the surface and friction effects become relevant.

2.7 | Dang Van criterion

The most commonly applied multiaxial fatigue criterion to components subjected to rolling contact fatigue is the stress-based critical plane Dang Van criterion. It assumes local plasticity in the mesoscale, even if the material is only loaded elastically in the macroscale. Governing the conversion between the meso- and macroscale is a time-invariant residual stress according to Melan's shakedown theorem. Different interpretations of the Dang Van criterion are presented in the literature, using (i) the above-outlined prediction of the shear stress amplitude on a given plane Δ combined with the maximum hydrostatic stress σ_H,[53] (ii) a combination of the instantaneous shear stress amplitude and hydrostatic stress,[20] (iii) the Tresca-like shear stress after identifying and subtracting the residual stress tensor from the deviatoric stress tensor,[30] or (iv) the modifications proposed by Desimone or Kenmeugne,[54,55] limiting the damage locus in the compressive stress regime. Here, the formulation of the Dang Van criterion, using the MRH derived shear stress amplitude and maximum hydrostatic stress, is favored as it predicts better results for non-proportional loading than the instantaneous, original formulation.[53]

$$a_{DV} \cdot \tau_a(\theta,\varphi) + b_{DV} \cdot \max_t(\sigma_H(t)) \leq f_{-1} \qquad (11)$$

The model parameters a_{DV} and b_{DV} are derived from uniaxial and torsional tests (f_{-1}, t_{-1}). The fatigue strength f_{-1} is modified according to the proposed size K_X

and life factor K_{NT} in the calculation of the material utilization D_{DV}.

$$a_{DV} = f_{-1}/t_{-1} = \kappa$$
$$b_{DV} = 3 - 3/2 \cdot \kappa \quad (12)$$

The maximum material utilization per node is estimated by maximizing Equation 13 over all planes defined by the spherical angles θ and ϕ and by maximizing the hydrostatic stress over all contact positions i or time t.

$$D_{DV} = \frac{\max_{\theta,\varphi}(a_{DV} \cdot \tau_a(\theta,\varphi)) + b_{DV} \cdot \max_{t}(\sigma_H(t))}{f_{-1,K}} \text{ with} \quad (13)$$
$$f_{-1,K} = f_{-1} \cdot K_X \cdot K_{NT}$$

Figure 10A visualizes the predicted material utilization for the mean cross-section of a G1 pinion tooth and in Figure 10B for path 1, perpendicular to the tooth surface, determining the maximum utilization at a depth of 3.4 mm and path 2, capturing the maximum utilization at each depth. Since pitting and subsurface fatigue damages do not occur on the same tooth height, path 2 enables the overall comparison of the surface and subsurface fatigue risk of a given gear and loading regime.

Based on the geometry and loads outlined in Table 1, the described numerical stress, and the implemented material model[5] (average strength without conversion factor f_{xK}), a maximum material utilization of 0.88 in the subsurface fatigue typical depth of 3.4 mm is predicted. With pitting damage either initiating directly on the surface or in a shallow depth below the surface,[7,56] the second peak in 0.4 mm depth is treated as a potential surface fatigue damage. The third peak at approximately 8 mm depth is an artifact of the outlined residual stress model, whereby large tensile stresses are estimated for the core of the narrow tooth tip. As a result of the coarsening element size, the material utilization jumps along path 2 around the third peak. Both the low surface and the significantly larger subsurface fatigue probability, along with the predicted plateauing utilization, compare well with service observations on G1. Only a neglectable number of pitting and a large number of subsurface fatigue damages are reported, of which the identified initiation depth varied between 1 and 2 times the CHD and concentrated around 3.1 mm. While the DV criterion proves applicable in predicting the fatigue critical areas of G1, uncertainty remains regarding the predicted material utilization levels, as marine gears in the transmission line of azimuthing thrusters are commonly operating at moderate loads and only occasionally when the vessel is in transit, at nominal loads (nominal refers to the design condition of the gear set as specified in Table 1).

3 | RESULTS AND DISCUSSION

As shown in the previous chapter, the outlined strength and stress models, alongside the Dang Van multiaxial fatigue criterion, are capable of predicting surface and subsurface fatigue failures in bevel gears. Uncertainty regarding the accuracy of the Dang Van criterion warrants the extended multiaxial fatigue analysis presented herein. The predicted utilizations for the presented criteria vary significantly as a result of the large compressive stresses typical for rolling contact fatigue. Overcoming the presented difficulties is a novel integral multiaxial fatigue criterion. As the conducted benchmarking and gear analysis shows, the proposed

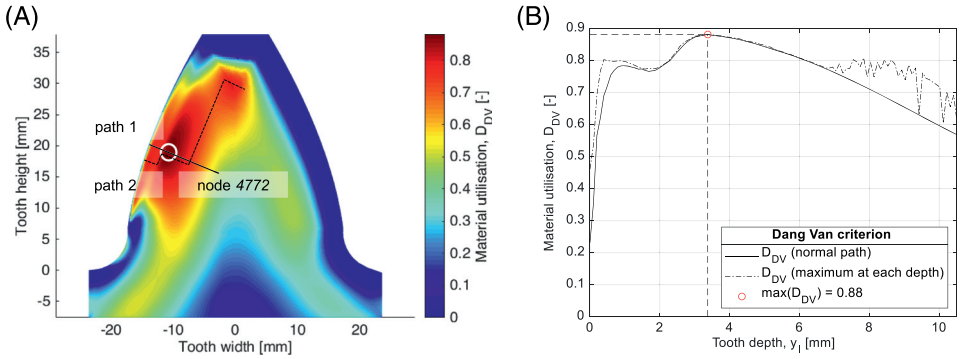

FIGURE 10 Material utilization for G1 according to the Dang Van criterion for (A) the mean cross-section and (B) as paths 1 and 2 intersecting maximum utilization max (D_{DV}) = 0.88 in a depth of 3.4 mm [Colour figure can be viewed at wileyonlinelibrary.com]

criterion is among the best of the available options regarding its accuracy and capacity to predict and differentiate between pitting, tooth root breakage, and subsurface fatigue failures on the studied gear sets.

3.1 | Model development

Two prominent and highly accurate[53] integral multiaxial fatigue criteria are the Liu and Zenner[27] (LZ) and Papuga's integral method (PIN).[28] They integrate the stress parameters obtained on individual evaluated planes over all possible plane orientations to the equivalent stress and compare it to the uniaxial fatigue strength f_{-1}.

$$D_{LZ}=\frac{\sqrt{\frac{15}{8\pi}\int_0^{2\pi}\int_0^{\pi}\left(a_{LZ}\tau_a^2\left(1+c_{LZ}\tau_m^2\right)+b_{LZ}\sigma_{na}^2\left(1+d_{LZ}\sigma_{nm}\right)\right)\sin(\theta)\ d\theta d\varphi}}{f_{-1}}$$
$$a_{LZ}=\frac{1}{5}\left(3\kappa^2-4\right)\text{ and }b_{LZ}=\frac{1}{5}\left(6-2\kappa^2\right)$$
$$c_{LZ}=\frac{28}{3a_{LZ}t_0^2}\left(\left(\frac{f_{-1}}{t_0}\right)^2-\frac{\kappa^2}{4}\right)\text{ and }d_{LZ}=\frac{28}{15b_{LZ}f_0^3}\left(\left(\frac{2f_{-1}}{f_0}\right)^2-\frac{a_{LZ}c_{LZ}f_0^2}{21}-1\right)\tag{14}$$

Both criteria use the mean and alternating shear stresses (τ_m and τ_a) and mean and alternating normal stresses (σ_{nm} and σ_{na}) on each material plane. The four model parameters (a, b, c, and d) are predicted according to the material constants (f_{-1}, f_0, t_{-1}, t_0).

$$D_{PIN}=\frac{\sqrt{\frac{1}{4\pi}\int_0^{2\pi}\int_0^{\pi}\left(a_{PIN}\tau_a\left(\tau_a+c_{PIN}\tau_m\right)+b_{PIN}\left(\sigma_{na}+d_{PIN}\sigma_{nm}\right)\right)\sin(\theta)\ d\theta d\varphi}}{f_{-1}}$$
$$a_{PIN}=\frac{15}{2}\kappa\left(\frac{\pi\kappa-4}{3\pi-4\kappa}\right)\text{ and }b_{PIN}=3f_{-1}\left(1-\kappa\left(\frac{\pi\kappa-4}{3\pi-4\kappa}\right)\right)$$
$$c_{PIN}=10\frac{f_{-1}^2}{a_{PIN}t_0^2}-\frac{20}{3}\frac{b_{PIN}}{\pi a_{PIN}t_0}-1\text{ and }d_{PIN}=6\frac{f_{-1}^2}{b_{PIN}f_0}\left(1-\frac{f_0^2}{3t_0^2}\right)+\frac{4}{3}\frac{f_0}{\pi t_0}-1\tag{15}$$

Figure 11 plots the material utilizations for both criteria against the load history on G1. In the presence of large compressive mean normal stresses and large normal stress amplitudes, the dividend in Equation 14 turns negative under the square root in the LZ criterion. As a result, no utilization is predicted up to a material depth of 4 mm below the loaded gear flank (see Figure 11A). For the same material layer, excessively large utilizations are predicted according to the PIN criterion (see Figure 11B). Given the Hertzian stress state and the outlined material model, $d_{PIN}\sigma_{nm}$ (see Equation 15) fails to adequately reduce the normal and shear stress amplitude.

It is evident that most fatigue criteria were not developed for rolling contact fatigue, leading to inadequate predictions under large compressive mean stresses and normal stress amplitudes. A novel and highly accurate integral multiaxial fatigue criterion (referred to as BO) is proposed to enable a comprehensive fatigue assessment of an arbitrary gear tooth (i.e., assessing the risk for pitting, tooth root breakage, and subsurface fatigue or TFF).

$$D_{BO}=\frac{\sqrt{\frac{15}{8\pi}\int_0^{2\pi}\int_0^{\pi}\left(\left(a_{BO}\tau_a^2+b_{BO}\sigma_{na}^2\right)\left(1+c_{BO}\sigma_{nm}\right)^2+d_{BO}\tau_a\tau_m\right)\sin(\theta)\ d\theta d\varphi}}{f_{-1}}$$
$$a_{BO}=\frac{1}{5}\left(3\kappa^2-4\right)\text{ and }b_{BO}=\frac{1}{5}\left(6-2\kappa^2\right)$$
$$c_{BO}=-\frac{3f_0\left(11-2\kappa^2\right)}{70C}+\sqrt{\left(\frac{3f_0\left(11-2\kappa^2\right)}{70C}\right)^2+\frac{1}{C}\left(\left(\frac{2f_{-1}}{f_0}\right)^2-1-\frac{\kappa^2}{3}\left(\left(\frac{2t_{-1}}{t_0}\right)^2-1\right)\right)}$$
$$d_{BO}=\frac{\kappa^2}{3}\left(\left(\frac{2t_{-1}}{t_0}\right)^2-1-\frac{c^2t_0^2}{35\kappa^2}\left(8-\kappa^2\right)\right)\text{ with }C=\frac{f_0^2}{84}\left(17-4\kappa^2\right)-\frac{f_0^2}{105}\left(8-\kappa^2\right)\tag{16}$$

In contrast to the LZ criterion, the expression $b_{LZ}\sigma_{na}^2\left(1+d_{LZ}\sigma_{nm}\right)$ is replaced with $\left(a_{BO}\tau_a^2+b_{BO}\sigma_{na}^2\right)\left(1+c_{BO}\sigma_{nm}\right)^2$, avoiding the LZ criterion's complex results but achieving a similar trend for tensile mean normal stresses. The same material utilization is furthermore predicted for both criteria for mean-stress-free stress states. The term $d_{BO}\tau_a\tau_m$ was introduced to consider occurring mean shear stresses and to reduce the effect of an increasing mean stress sensitivity on the allowable stress amplitude typical for hard steels. Other expressions for the mean shear stress were also iterated with $d_{BO}\tau_m^2$ yielding the highest result accuracy for the studied fatigue data set (see Table 2). The model parameter d_{BO} was in this case not derived from the fatigue strength under fully reversed torsional loading t_0, but rather the ultimate tensile strength or true fracture strength R_m or σ_f in accordance to the works by Pallarés-Santasmartas.[57]

$$d_{BO}=\left(\frac{f_{-1}}{\sigma_f}\right)^2\text{ and}$$
$$c_{BO}=-\frac{18}{5f_0}\left(\frac{11-2\kappa^2}{17-4\kappa^2}\right)+\sqrt{\left(\frac{18}{5f_0}\left(\frac{11-2\kappa^2}{17-4\kappa^2}\right)\right)^2+\frac{84}{f_0^2\left(17-4\kappa^2\right)}\left(\left(\frac{2f_{-1}}{f_0}\right)^2-d_{BO}-1\right)}\tag{17}$$

While this version of the multiaxial fatigue criterion worked exceptionally well for the comparably soft steels

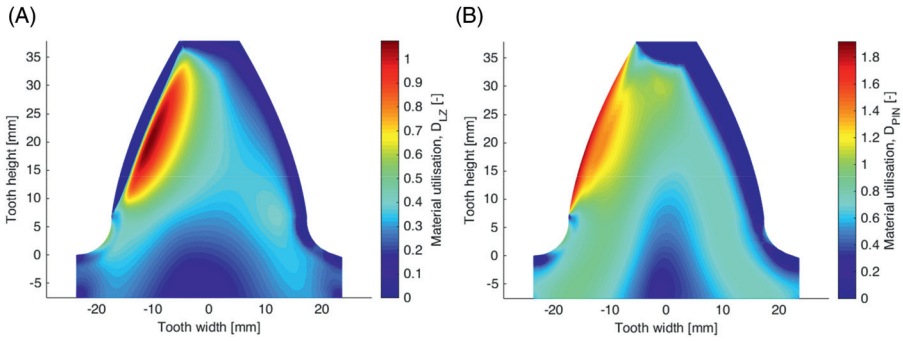

FIGURE 11 Material utilization in G1 according to (A) the Liu and Zenner and (B) PIN criteria [Colour figure can be viewed at wileyonlinelibrary.com]

included in the experimental data set (see Table 2), it ultimately failed to produce the same good results in the surface layer of the studied gear sets.

3.2 | Benchmarking

The DV,[20,53] Sines (SI),[25] Crossland (CR),[26] LZ,[27] PIN,[28] Hertter (HE),[7] and BO criteria were tested against an experimental data set, composed of 23 multiaxial fatigue tests performed on various soft and mild steels.[21–24] Of the results in previous studies,[21–24] only those under compressive or tensile, static, normal stresses, and alternating shear stresses were analyzed. The studied loading conditions resemble thereby the stress state in the material depth critical for subsurface fatigue. While the other criteria are well established, further context is given for the Hertter criterion. Hertter developed his model out of the Liu and Zenner criterion, focusing on the prediction of pitting and tooth root damages in gears. His model considers the mean normal stress σ_{nm} on the strength side rather than the stress side through the mean stress sensitivity M,[58] to avoid the highlighted complex results for the LZ criterion (see Figure 11A). Equation 18 outlines the criterion. The model constants are taken directly from the LZ criterion (see Equation 14).

$$D_{HE} = \sqrt{\frac{15}{8\pi}\int_0^{2\pi}\int_0^{\pi}\frac{\left(a_{LZ}\tau_a^2\left(1+c_{LZ}\tau_m^2\right)+b_{LZ}\sigma_{na}^2\right)}{\left(f_{-1}-M\sigma_{nm}\right)^2}\sin(\theta)\,d\theta d\varphi} \tag{18}$$

Extending the model comparison are variants of the DV criterion where the model parameters are defined either through (f_{-1}, t_{-1}) or (f_{-1}, f_0) and both variants of the BO criterion.

To analyze the accuracy of the individual criteria, the relative error, referred to as the fatigue error index ΔFI, is calculated for each model and test case. The criteria's equivalent stress σ_{eq} is used in the prediction of ΔFI.

$$\Delta FI = \frac{\sigma_{eq} - f_{-1}}{f_{-1}} \tag{19}$$

The closer ΔFI is to 0, the better the experimental results and fatigue predictions align. Positive values express a conservative estimation and negative values a nonconservative prediction. Table 2 lists the maximum and minimum fatigue error index, its range, average, and standard deviation obtained from the 23 experimental data sets. All criteria were evaluated using the MRH method, but as the tests were carried out under proportional loading, the MRH and MCC methods yielded the same results.

Whereas the DV, SI, and CR criteria rely on two model parameters, the LZ, PIN, HE, and BO criteria are integral or shear stress intensity criteria, making use of four model parameters when assessing the overall material utilization. The DV criterion, relying on (f_{-1}, t_{-1}), yields conservative results (aver. ΔFI 8.5%) and considerable scatter, expressed in the derived range (39.5%) and standard deviation (11.4%). Less accuracy is achieved when relying on (f_{-1}, f_0) for the prediction of the model parameters. A significantly larger average fatigue error index is obtained for the SI criterion, indicating an overly conservative evaluation of the data set. The CR criterion achieves the highest result accuracy of the two-parameter criteria, but similar to

TABLE 2 Statistical analysis of the fatigue error index for the DV, SI, CR, LZ, PIN, HE, and BO criteria based on the experimental results[21–24]

ΔFI	DV (f_{-1}, t_{-1})	DV (f_{-1}, f_0)	SI (f_{-1}, f_0)	CR (f_{-1}, t_{-1})	LZ (f_{-1}, f_0, t_{-1}, t_0)	PIN (f_{-1}, f_0, t_{-1}, t_0)	HE (f_{-1}, M, t_{-1}, t_0)	BO (f_{-1}, f_0, t_{-1}, t_0)	BO ($f_{-1}, f_0, t_{-1}, \sigma_f$)
Max [%]	20.9	23.7	41.1	19.7	17.9	17.9	22.3	20.8	21.9
Min [%]	−18.6	−21.7	0.1	−10.7	−14.7	−1.4	−22.2	−7.1	−3.9
Range [%]	39.5	45.3	41.0	30.4	32.6	19.3	44.6	27.9	25.8
Aver. [%]	8.5	8.7	24.9	3.3	1.2	6.1	−0.8	5.1	5.7
SD. [%]	11.4	12.0	12.0	7.6	9.4	4.3	11.7	7.6	6.1

the PIN criterion, it overestimates the material utilization directly on the surface under large Hertzian stresses (see Figure 11B).

Studying the listed integral criteria, all but the HE criterion are on par with the CR criterion. Due to the consideration of the normal mean stresses σ_{nm} through the mean stress sensitivity M rather than a fourth fatigue parameter, the criterion fails to comply with the f_0 case, which worsens the model accuracy (range 44.6% and standard deviation 11.7%). Achieving the same linear dependency on the mean normal stress while avoiding the LZ criterion's complex results is the following modification of the HE criterion.

$$D_{HE,mod} = \sqrt{\frac{15}{8\pi}\int_0^{2\pi}\int_0^{\pi}\left(a_{LZ}\tau_a^2\left(1+c_{LZ}\tau_m^2\right)+b_{LZ}\sigma_{na}^2\right)\sin(\theta)\,d\theta d\varphi} + \frac{\frac{1}{4\pi}\int_0^{2\pi}\int_0^{\pi} d_{HE,mod}\sigma_{nm}\sin(\theta)\,d\theta d\varphi}{f_{-1}} \tag{20}$$

$$d_{HE,mod} = 3\left(\frac{2f_{-1}}{f_0} - \sqrt{1+\frac{1}{21}a_{LZ}c_{LZ}f_0^2}\right)$$

When subjected to the same data set, the ΔFI range and standard deviation drop to 27.3% and to 7.3%, significantly improving predictions of the HE model.

As reported by other researchers,[53] the LZ and PIN are highly accurate for a wide range of stresses and loading conditions but are ultimately not applicable to gears and potentially rolling contact fatigue in general. Table 2 proves the accuracy of the BO criteria with the smallest standard deviation being achieved for the iteration relying on the true fracture strength σ_f. This version of the BO criterion is not pursued further in this publication, as it led to too low material utilizations in the outer material layer critical for pitting.

3.3 | Fatigue predictions

The material utilizations for gears G1, G2, G0, and F0 according to BO are plotted in Figure 12 for their mean cross-sections and in Figure 13 along paths 1 and 2 (solid black line and dotted black line). The depths of 174 and 32 via ultrasonic scanning detected subsurface crack-like indications on G1 and G2 teeth are visualized as three-parameter Weibull distributions in Figure 13A,B (solid blue line) to assess the accuracy of the proposed fatigue model in capturing the critical depth in which failures are likely to initiate. Complementing the model assessment are examples of subsurface fatigue failures in G1 and G2 and pictures taken from the gear testing of G0 and F0[29] in Figure 14.

In contrast to the material utilization predicted for G1 with the DV criterion, the presented model predicts a 34% higher subsurface material utilization (1.18 compared to 0.88). For a potential subsurface fatigue damage, the initiation depth from 2 to 5 mm is estimated, aligning itself well with the reported subsurface crack-like indications during ultrasonic scanning. The high plotted material utilization (average strength, without conversion factor f_{xK}) is indicative of the substantial risk for subsurface fatigue in marine bevel gears even at moderate loads. The predicted surface and tooth root utilizations on G1 and G2 align well with the service experience on both gear sets, whereby few pitting and no tooth root breakages are reported. As Figure 13A,B indicate, an approximately 10% higher material utilization is predicted for G1 over G2, which, compared with the number of failures and crack-like indications detected during ultrasonic scanning on G1 and G2, further underlines the accuracy of the model.Regarding the documented failures on test gears G0 and F0, an accurate prediction of the failure

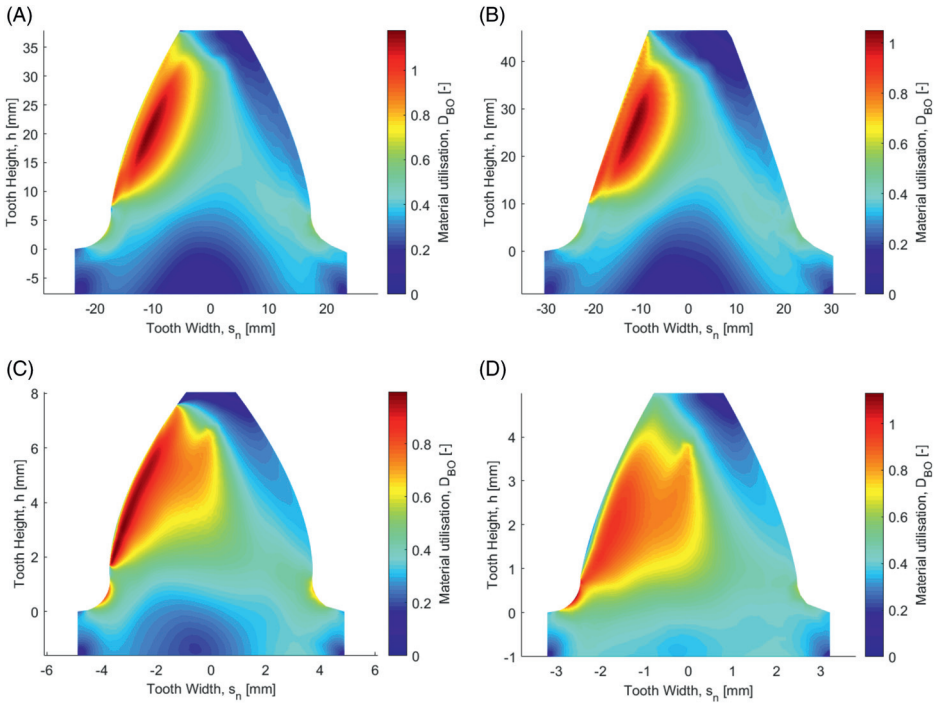

FIGURE 12 Material utilization for mean cross-section of (A) G1, (B) G2, (C) G0, and (D) F0 [Colour figure can be viewed at wileyonlinelibrary.com]

type and its location for G0 towards the surface and across a large portion of the flank and for F0 in the 30° tangent to the tooth root are similarly made. The utilization peak of G0 is predicted near the pitch point, where failures typically initiate before growing across the loaded flank.[29] As reported by Wirth,[29] due to insufficient forging of the first set of test gears, a number of subsurface fatigue damages were reported on G0 wheels. Figure 15 plots the material utilization for a G0 wheel tooth under 300 Nm after $1.6 \cdot 10^7$ load cycles. The observed needle-like segregation structure, with its orientation nearly parallel to the load carrying flank, was simulated through a steeper hardness gradient from case to core. A peak material utilization of 1.01 is predicted at a material depth of 1 mm.

4 | DISCUSSION

An algorithm is presented for the prediction of pitting, tooth root breakage and subsurface fatigue, FB or TFF damages for a given bevel gear design and load regime. The wide range of load conditions and gear sizes covered in this study underline the applicability of the proposed material, stress, and fatigue models to a wide range of gears.

By analyZing the involute tooth profile in the mean cross-section of either pinion or wheel, the actual tooth geometry and 3D stress state are rationalized to ensure a sufficiently fine mesh and material plane resolution. FEM contact analysis is avoided through the implementation of LTCA derived surface stresses, considering the precise gear geometry and load-induced gear displacements. Uncertainty remains regarding the predicted tooth root stresses, and the likelihood of tooth root breakage, as the tooth root was modeled as a continuous radius. As indicated in Figure 13D, a steep stress gradient is present in the tooth root of F0. To improve the predictions, a local stress redistribution for example through the equations by Petersen and Thum,[59] Siebel,[60] and Neuber[61] could be considered.The proposed size factor K_X applies to a well-defined hardness profile and does not cover process and material dependent variations. Caused by heat distortion during carburizing, the material removal on

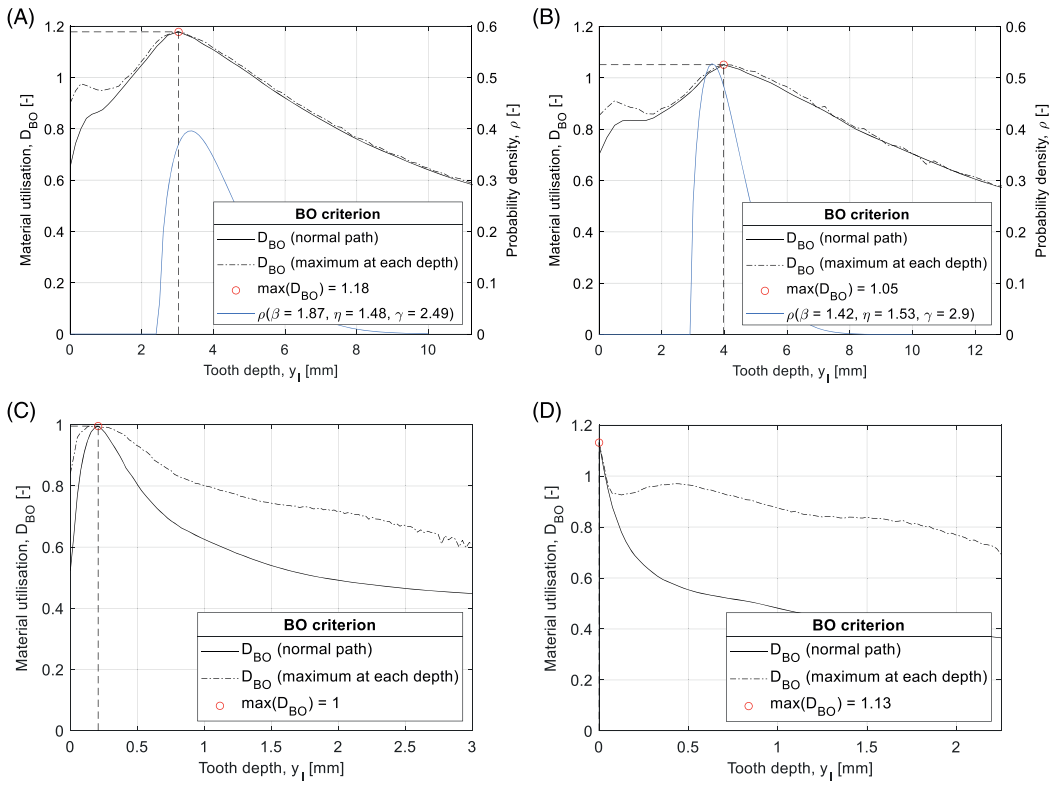

FIGURE 13 Material utilization along paths 1 and 2 for (A) G1 with max (D_{BO}) = 1.18 in 3.0 mm compared to ultrasonic scanning results of 174 crack-like indications, (B) G2 with max (D_{BO}) = 1.05 in 4.1 mm compared to ultrasonic scanning results of 32 crack like indications, (C) G0 with max (D_{BO}) = 1.00 in 0.2 mm, and (D) F0 with max (D_{BO}) = 1.13 in the 30° tooth root tangent [Colour figure can be viewed at wileyonlinelibrary.com]

FIGURE 14 Gear failures due to subsurface fatigue on (A) G1 after approximately $3{\cdot}10^8$ load cycles and (B) G2 after approximately $3{\cdot}10^8$ load cycles, pitting on (C) G0 after $7.7{\cdot}10^7$ load cycles at 200 Nm and 4,500 RPM and tooth root breakage on (D) F0 after $7{\cdot}10^6$ load cycles at 350 Nm at 4880 RPM[29] [Colour figure can be viewed at wileyonlinelibrary.com]

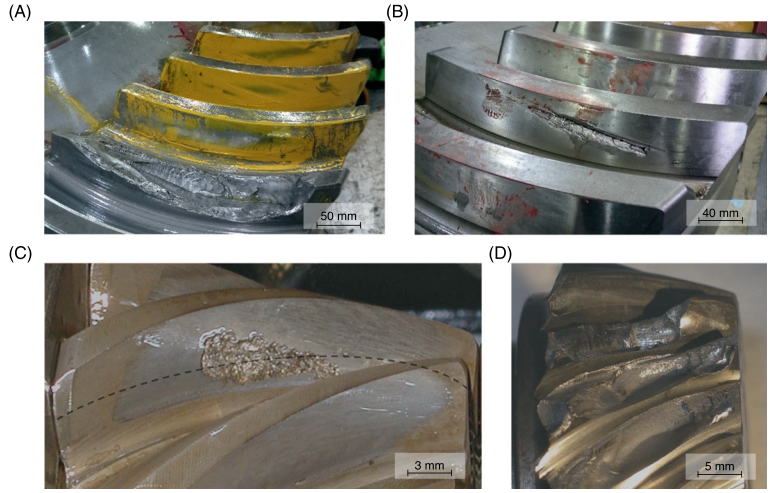

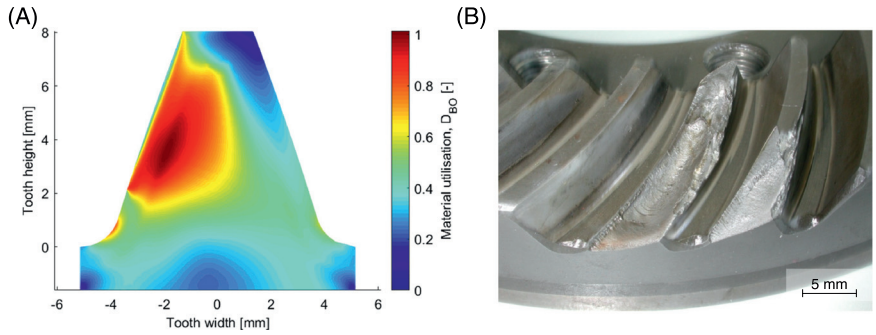

FIGURE 15 (A) Predicted material utilization and (B) gear failures on G0 wheel at 300 Nm and 4,500 RPM after $1.6 \cdot 10^7$ load cycles [Colour figure can be viewed at wileyonlinelibrary.com]

large bevel gears (especially wheels) can vary between 0.5 to multiple millimeters, resulting in varying CHD between the teeth of a single and multiple gear sets. Nor does it consider varying hardenabilities between material batches. It is proposed that these variations are dealt with through adequate safety factor requirements on large gears. More studies are necessary to quantify if the lifetime factor K_{NT}, representative of the material behavior for a carburized CrNiMo steel at around 500 HV, is applicable to the entire gear tooth (i.e., pitting, tooth root breakage, and TFF).As outlined in Section 2.7, the Dang Van criterion is able to identify the material depth in bevel gears typical for surface and subsurface fatigue. Assuming the absence of extreme loads in the service history of the studied gear sets, it underestimates the likelihood of subsurface fatigue failure for large bevel gears. Not a part of the manuscript but of the associated research was the application of the Dang Van criterion to all gears listed in Table 1 and to additional test gears. It predicted a too low subsurface failure probability, favoring surface-initiated failures instead. Furthermore, large failure probabilities were predicted in the core of the gear tooth, where the tensile residual stresses were the largest but load-related stresses were minimal. The proposed multiaxial fatigue criterion improves the prediction of surface and subsurface fatigue predictions of all studied gears and overcomes the inaccuracies of the LZ and PIN criteria. A comparison between bevel gear test results and the predictions made by the proposed multiaxial fatigue criterion are intended for later publications.

5 | CONCLUSIONS

Herein presented material, stress and fatigue models are applicable to a wide range of gear sizes, loading conditions, and fatigue damage types (i.e., subsurface fatigue, pitting, and tooth root breakage). Listed below are the key findings and results of this study.

i. Favoring the Thomas model[19] over the commonly used Lang model[18] enables the accurate prediction of the hardness profile for both large and small gears, considering the auto-tempering response of large gears and the carburizing process with two carbon potentials. By specifying three sets of hardness parameters in the tooth profile direction, the carburizing and quenching results for different sections of the gear tooth are adequately modeled.
ii. Depending on the tooth width in the profile direction, the maximum of the tensile residual stress transitions from the case/core interface in the middle of the gear tooth to the core in its tip. Capturing this transition is the proposed residual stress model. It relies on the well-established Lang model[18] for the prediction of the compressive residual stresses up to the CHD and combines it with a fourth-order polynomial.
iii. To overcome the uncertainties in the subsurface stress prediction of current analytical models, a simplified 2D plane strain numerical model was developed. The contact stresses are predicted either through a "loaded tooth contact analysis"[14] or an analytical approach,[15] avoiding numerical contact analysis. The stress history in each node is assessed through the Maximum Rectangular Hull method, yielding the shear mean and amplitude stress on all material planes.
iv. A novel and highly accurate multiaxial fatigue shear stress intensity criterion was developed to enable the fatigue assessment of an arbitrary gear tooth against

all gear-typical fatigue failure modes (i.e., pitting, tooth root breakage, and subsurface fatigue). Especially, the prediction of the material utilization in the surface near the layer, subjected to large Hertzian stresses, proved to be difficult with already established criteria.

ACKNOWLEDGMENTS

The authors would like to thank Jack Chessa from the UTEP, College of Engineering for sharing its MATLAB-based numerical calculation code on GitHub. Parts of the code were adapted and implemented to improve the fatigue predictions by using numerical rather than analytical stresses. The authors gratefully acknowledge the funding of this research project through the Norwegian Research Council (NFR) – Project ID 270828. Jan Papuga acknowledges support from the ESIF, EU Operational Program Research, Development and Education, from the Center of Advanced Aerospace Technology (CZ.02.1.01/0.0/0.0/16_019/0000826), Faculty of Mechanical Engineering, Czech Technical University in Prague.

DATA AVAILABILITY STATEMENT

The data used in this manuscript can be made available on request from the corresponding author.

ORCID

Stephan André Böhme https://orcid.org/0000-0001-9703-583X
Alexei Vinogradov https://orcid.org/0000-0001-9585-2801
Jan Papuga https://orcid.org/0000-0001-9569-4997
Filippo Berto https://orcid.org/0000-0001-9676-9970

REFERENCES

1. DNV GL. *Class Guideline — DNVGL-CG-0036: Calculation of gear rating for marine transmissions*; 2015.
2. Klein M, Seabra J, Höhn BR, Michaelis K, Annast R. Theoretical and experimental investigations about flank breakage in bevel gears. *Industrial Lubrication and Tribology*. 2011;63(1):5-10.
3. MackAldener M. *Tooth Interior Fatigue Fracture & Robustness of Gears*. Department of Machine Design, KTH - Stockholm: Stockholm; 2001.
4. ISO. ISO/TS 6336-4:2019—calculation of load capacity of spur and helical gears—part 4: calculation of tooth flank fracture load capacity. In. Switzerland: ISO copyright office; 2019.
5. Böhme SA, Vinogradov A, Biermann H, Weidner A, Schmiedel A, Henkel S. Fatigue of carburised CrNiMo steel: testing and modelling concept. *Fatigue & Fracture of Engineering Materials & Structures*. 2020;44(3):788-804.
6. Höhn B-R, Oster P. Der Flankenkontakt—ein elastohydrodynamischer Wälzkontakt. 1995 (VDI-Bericht 1207):93–106.
7. Hertter T. *Rechnerischer Festigkeitsnachweis der Ermüdungstragfähigkeit vergüteter und einsatzgehärteter Stirnräder*. Institut für Maschinen- und Fahrzeugtechnik, TU München; 2003.
8. Witzig J. *Entwicklung eines erweiterten Berechnungsverfahrens zur Ermittlung optimaler Zahnflankentragfähigkeit bis in den Bereich grosser Werkstofftiefe*. Vol Heft 1000. Forschungsvereinigung Antriebstechnik e.V; 2012.
9. Boiadjiev I, Witzig J, Tobie T, Stahl K. Tooth flank fracture—basic principles and calculation model for a subsurface initiated fatigue failure mode of case hardened gears. In: *International Gear Conference 2014: 26th–28th August 2014, Lyon*. Oxford: Chandos Publishing; 2014:670-680.
10. ISO. ISO/TS 10300-4:2019 — Calculation of load capacity of bevel gears — Part 4: Calculation of tooth flank fracture load capacity. In. Switzerland: ISO copyright office; 2019.
11. Balduzzi G, Aminbaghai M, Sacco E, Füssl J, Eberhardsteiner J, Auricchio F. Non-prismatic beams: a simple and effective Timoshenko-like model. *International Journal of Solids and Structures*. 2016;90:236-250.
12. Hofmann TJ. *Beitrag zur verfeinerten Balkentheorie*. Institut für Baustatik der Universität Stuttgart, Universität Stuttgart; 1992.
13. Weber R. *Auslegungskonzept gegen Volumenversagen in einsatzgehärteten Stirnradern*. Institut für Werkstofftechnik, Universität Kassel; 2015.
14. Baumann V, Bär G, Haase A, Hutschreiter B, Hünecke C. *Programm zur Berechnung der Zahnflanken- und Zahnfußbeanspruchung an Kegelrad- und Hypoidgetrieben*. In. Vol Heft 548. Forschungsvereinigung Antriebstechnik e.V: Frankfurt; 1998.
15. Hombauer M. *Bestimmung der Graufleckentragfähigkeit von Kegelrad- und Hypoidverzahnungen*. Vol Heft 1055. Forschungsvereiningung Antriebstechnik e.V.; 2013.
16. Varis K, Rinnevalli J, Vanninen R, Keski-Rahkonen J. *Examination of the Crack Initiation and Propagation in a Spiral Bevel Gear*. Stressfield for Rolls-Royce Marine, 2014.
17. Diemar A. *Simulation des Einsatzhärtens und Abschätzung der Dauerfestigkeit einsatzgehärteter Bauteile*. Erfurt: Fakultät Bauingenieurwesen, Bauhaus-Universität Weimar; 2007.
18. Lang OR. Berechnung und Auslegung induktiv randschichtgehärteter Bauteile. Kloos, K H (Hrsg); Grosch, J (Hrsg): Induktives Randschichthärten Berichtsband, Tagung 23 bis 25 März 1988, München: Arbeitsgemeinschaft Wärmebehandlung und Werkstofftechnik (AWT). 1989:332–348.
19. Thomas J. *Flankentragfähigkeit und Laufverhalten von hartfeinbearbeiteten Kegelrädern*. TU München: Munich; 1998.
20. Van Dang K. Sur la résistance à la fatigue des métaux. *Sciences et Technique de l'Armement*. 1973 (3eme fascicule);647-722.
21. Baier F. *Zeit- und Dauerfestigkeit bei überlagerter statischer und schwingender Zug-Druck- und Torsionbeanspruchung*. Stuttgart: Universität Stuttgart; 1970.
22. Lüpfert H-P, Spies H-J. Fatigue strength of heat-treatable steel under static multiaxial compression stresses. *Adv Eng Mater*. 2004;6(7):544-550.

23. Papuga J, Fojtík F. Multiaxial fatigue strength of common structural steel and the response of some estimation methods. *International Journal of Fatigue.* 2017;104:27-42.
24. Simbürger A. *Festigkeitsverhalten zäher Werkstoffe bei einer mehrachsigen phasenverschobenen Schwingbeanspruchung mit körperfesten und veränderlichen Hauptspannungsrichtungen*, TH Darmstadt; 1975.
25. Sines G. *Behavior of metals under complex static and alternating stresses*. New York: McGraw Hill; 1959.
26. Crossland B. Effect of large hydrostatic pressure on the torsional fatigue strength of an alloy steel. *Proceedings of International Conference on Fatigue of Metals, London*. 1956 (Institution of Mechanical Engineers): 1956, 138–149.
27. Liu J, Zenner H. Berechnung der Dauerschwingfestigkeit bei mehrachsiger Beanspruchung—teil 1 und 2. *Materialwissenschaft und Werkstofftechnik*. 1993;24:240-249.
28. Papuga J, Suchý L, Růžička M. Mean shear stress effect built into the multiaxial fatigue strength estimation method of an integral type. *MATEC Web of Conferences*. 2019;300:1-9, 16010.
29. Wirth C. *Entwicklung eines Berechnungsberfahrens zur Grübchen- und Zahnfußtragfähigkeit von Hypoidrädern*. Vol Heft 887. Forschungsvereinigung Antriebstechnik e.V.; 2009.
30. Cerullo M. Application of Dang Van criterion to rolling contact fatigue in wind turbine roller bearings under elastohydrodynamic lubrication conditions. *Proceedings of the Institution of Mechanical Engineers, Part C: Journal of Mechanical Engineering Science*. 2014;228(12):2079-2089.
31. Böhme SA. *Flankenbruch - Spannungstiefenverlauf in maritimen Kegelradstufen unter Berücksichtigung der Last- und Eigenspannungen [Diploma Thesis]*. Dresden: Institut für Maschinenelemente und Maschinenkontruktion, Technische Universität Dresden; 2012.
32. Klein M. *Bestimmung der Fresstragfähigkeit von Kegelrad- und Hypoidverzahnungen*. Vol Heft 1071. Forschungsvereinigung Antriebstechnik e.V.; 2013.
33. Wech L. *Untersuchungen zum Wirkungsgrad von Kegelrad- und Hypoidgetrieben*. München: TU München; 1987.
34. Wirth C. *Normgerechte Wahl zur Einsatzhärtetiefe der Kegelräder*. Vol Heft 918. Forschungsvereinigung Antriebstechnik e.V.; 2009.
35. Böhme SA, Merson D, Vinogradov A. On subsurface initiated failures in marine bevel gears. *Engineering Failure Analysis*. 2020;110:104415. https://doi.org/10.1016/j.engfailanal.2020.104415
36. Tobie T. *Härtetiefen-Großzahnräder*. Vol Heft 622. Forschungsvereinigung Antriebstechnik e.V.; 2001.
37. Peng RL, Neutron diffraction measurement of residual stress in two carburised gear teeth. Nyköping 2003.
38. Weber R, Rötting J, Scholtes B, Bacher-Höchst M. Load stresses and residual stresses in the tooth interior A2 - Velex, Philippe. In: *International Gear Conference 2014: 26th–28th August 2014, Lyon*. Oxford: Chandos Publishing; 2014:804-813.
39. Stenico A. *Eigenspannungen Zahnfuß*. Vol Heft 745. Forschungsvereinigung Antriebstechnik e.V.; 2004.
40. ISO. ISO 6336-5:2016—calculation of load capacity of spur and helical gears—part 5: strength and quality of materials. In. Switzerland: ISO copyright office; 2016.
41. Zenner H, Simbürger A, Liu J. On the fatigue limit of ductile metals under complex multiaxial loading. *Int J Fatigue*. 2000;22(2):137-145.
42. Murakami Y. *Metal Fatigue: Effects of Small Defects and Nonmetallic Inclusions*. Cambridge: Academic Press; 2019. https://doi.org/10.1016/C2016-0-05272-5
43. Rabb R. *Todennäköisyysteoriaan pohjautuva väsymisanalyysi*. Norderstedt: Books on Demand; 2013.
44. DIN. DIN 50100:2016—Schwingfestigkeitsversuche—Durchführung und Auswertung von zyklischen Versuchen mit konstanter Lastamplitude für metallische Werkstoffproben und Bauteile. In: 2016.
45. DIN. DIN3991-2: Tragfähigkeitsberechnung von Kegelrädern ohne Achsversetzung - Berechnung der Grübchentragfähigkeit. In: 1988.
46. Pascual F, Meeker W. Analysis of fatigue data with run-outs based on a model with non constant standard deviation and a fatigue limit parameter. *Journal of Testing and Evaluation*. 1997;25:292-301.
47. Elstorpff M-G. *Einflüsse auf die Grübchentragfähigkeit einsatzgehärteter Zahnräder bis in das höchste Zeitfestigkeitsgebiet*. München: TU München; 1993.
48. Wang CH, Brown MW. Life prediction techniques for variable amplitude multiaxial fatigue—part 1: theories. *Journal of Engineering Materials and Technology*. 1996;118(3):367-370.
49. Bernasconi A, Papadopoulos IV. Efficiency of algorithms for shear stress amplitude calculation in critical plane class fatigue criteria. *Comput Mater Sci*. 2005;34(4):355-368.
50. Araújo JA, Dantas AP, Castro FC, Mamiya EN, Ferreira JLA. On the characterization of the critical plane with a simple and fast alternative measure of the shear stress amplitude in multiaxial fatigue. *International Journal of Fatigue.* 2011;33(8):1092-1100.
51. Papuga J, Cízová E, Karolczuk A. Validating the methods to process the stress path in multiaxial high-cycle fatigue criteria. *Materials*. 2021;14(1):206.
52. Dantas AP, Araújo JA, Castro FC, Junior TD. The use of genetic algorithms and the maximum rectangular hull for a strong reduction in computational cost for critical plane approaches in multiaxial fatigue. 21st Brazilian Congress of Mechanical Engineering; Natal, Brasil; 2011.
53. Papuga J. A survey on evaluating the fatigue limit under multiaxial loading. *International Journal of Fatigue.* 2011;33(2):153-165.
54. Desimone H, Bernasconi A, Beretta S. On the application of Dang Van criterion to rolling contact fatigue. *Wear*. 2006;260(4–5):567-572.
55. Kenmeugne B, Soh Fotsing BD, Anago GF, Fogue M, Robert J-L, Kenne J-P. On the evolution and comparison of multiaxial fatigue criteria. *International Journal of Engineering and Technology*. 2012;4:37-46.
56. AGMA. Appearance of Gear Teeth - Terminology of Wear and Failure. In: *ANSI/AGMA 1010-E95*. Virginia: American Gear Manufacturers Association; 2007.
57. Pallarés-Santasmartas L, Albizuri J, Avilés A, Saintier N, Merzeau J. Influence of mean shear stress on the torsional fatigue behaviour of 34CrNiMo6 steel. *International Journal of Fatigue*. 2018;113:54-68.

58. FKM. *Analytical Strength Assessment of Components: Made of Steel, Cast Iron and Aluminium Materials in Mechanical Engineering*. 6th ed. Frankfurt: VDMA; 2012.
59. Petersen C, Thum A. Die Vorgänge im zügig und wechselnd beanspruchten Metallgefüge. *Z-Metallkunde*. 1941;33:249-259.
60. Siebel E, Pfender M. Weiterentwicklung der Festigkeitsrechnung bei Wechselbeanspruchung. *Stahl Und Eisen*. 1947;66:318-321.
61. Neuber H. Über die Dauerfestigkeit bei Spannungskonzentration. *Konstruktion 20*. 1968;(7):245-251.

How to cite this article: Böhme SA, Vinogradov A, Papuga J, Berto F. A novel predictive model for multiaxial fatigue in carburized bevel gears. *Fatigue Fract Eng Mater Struct*. 2021;44:2033–2053. https://doi.org/10.1111/ffe.13475

A.4 Paper IV

Abstract A material model for carburized CrNiMo steel and an advanced shear stress intensity, multiaxial fatigue criterion against surface and subsurface fatigue in bevel gears have been developed and presented in earlier publications. This study assesses the accuracy of the proposed methodology by comparing it to load-cotrolled bevel gear tests at varying hardening layer thicknesses. The dominant failure mode was wheel-initiated tooth flank fracture. Fractographic analysis by means of scanning electron microscopy revealed a severely elongated $MgO\text{-}Al_2O_3$ cluster in the only pinion-initiated tooth flank fracture. By correlating the calculated material utilizations and the number of cycles to failure, a reiterated lifetime factor is presented. The refined methodology is shown to be capable to differentiate between and accurately predict pitting and subsurface fatigue under well-defined test conditions.

Engineering Failure Analysis 132 (2022) 105911

Contents lists available at ScienceDirect

Engineering Failure Analysis

journal homepage: www.elsevier.com/locate/engfailanal

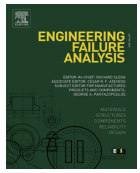

Tooth flank fracture – An applied fatigue study of case hardened bevel gears

Stephan André Böhme [a,*], Gabor Szanti [b], Joni Keski-Rahkonen [c], Tami Komssi [b], José Garcia Santaella [d], Alexei Vinogradov [a]

[a] Norwegian University of Science and Technology (NTNU), Department of Mechanical and Industrial Engineering, Trondheim 7491, Norway
[b] ATA Gears Oy, Tampere FI-33101, Finland
[c] Kongsberg Maritime Finland Oy, Rauma FI-26100, Finland
[d] Tampere University, Faculty of Engineering and Natural Science, Tampere FI-33014, Finland

ARTICLE INFO

Keywords:
Subsurface fatigue
Gear testing
Rolling contact fatigue
Carburized steel

ABSTRACT

A material model for carburized CrNiMo steel and an advanced shear stress intensity, multiaxial fatigue criterion against surface and subsurface fatigue in bevel gears have been developed and presented in earlier publications. This study assesses the accuracy of the proposed methodology by comparing it to load-controlled bevel gear tests at varying hardening layer thicknesses. The dominant failure mode was wheel-initiated tooth flank fracture. Fractographic analysis by means of scanning electron microscopy revealed a severely elongated $MgO\text{-}Al_2O_3$ cluster in the only pinion-initiated tooth flank fracture. By correlating the calculated material utilizations and the number of cycles to failure, a reiterated lifetime factor is presented. The refined methodology is shown to be capable to differentiate between and accurately predict pitting and subsurface fatigue under well-defined test conditions.

* Corresponding author.
E-mail address: stephan.a.bohme@ntnu.no (S.A. Böhme).

https://doi.org/10.1016/j.engfailanal.2021.105911
Received 1 June 2021; Received in revised form 8 November 2021; Accepted 13 November 2021
Available online 18 November 2021

Nomenclature			
varea	Square root of the projected area of an inclusion	NFR	Norwegian research council
a_{BO}, b_{BO}, c_{BO} and d_{BO}	Model parameters BO criterion	p_H	Surface pressure
A	Elongation	P	Power
b	Tooth width	P1	Surface perpendicular path through global $D_{BO,max}$
b_H	Half Hertzian contact width	P2	Path through $D_{BO,max}$ for each depth
BECAL	Bevel Gear Calculation	PIN	Papuga integral multiaxial fatigue criterion
BO	Böhme multiaxial fatigue criterion	R_m	Ultimate tensile strength
CHD	Case hardening depth	R_{p02}	Yield strength
d_e	Outer diameter	R_z	Surface roughness
EBSD	Electron backscatter diffraction	$s_{n,i}$	Chordal tooth thickness for node i
EDS	Energy dispersive X-ray	$s_{n\alpha,i}$	Half tooth thickness for node i
D_{BO}	Material utilization BO criterion	SEM	Scanning electron microscopy
DNV GL	Det Norske Veritas Germanische Lloyd	SN	stress amplitude versus number of load cycles
f_{-1}, f_0	Fatigue limit under fully reversed and repeated axial loading	t_{-1}, t_0	Shear fatigue limit under torsional fully reversed and repeated loading
$f_{-1,K}$	Modified fatigue strength under fully reversed axial loading	T	Oil temperature
f_{xK}	Conversion factor	TFF	Tooth flank fracture
FKM	Forschungskuratorium Maschinenbau	VHCF	Very high cycle fatigue
FZG	Forschungsgesellschaft für Zahnräder und Getriebe	x_{hm}	Profile shift
HV_c	Core hardness	x_{sm}	Tooth thickness factor
HV_i	Hardness in node i	y_{HVmax}	Depth of the hardness peak
HV_s	Surface hardness	y_I	Distance between surface and subsurface nodes
i	Subsurface node	z	Number of teeth
ISF	Isotropic superfinishing	Z	Area reduction
ISO	International Organization for Standardization	Z_{NT}, Y_{NT}	Pitting and tooth root breakage lifetime factors
k_{ap}, k_{fp}	Addendum & dedendum factor	α	Pressure angle
K_{NT}	Lifetime factor	β_m	Mean spiral angle
K_X	Size factor	ϑ, ϕ	spherical angles
LZ	Liu & Zenner multiaxial fatigue criterion	κ	Fatigue ratio
LTCA	Loaded tooth contact analysis	μ	Friction coefficient
m_0	Cutter module	ρ_0	Cutter radius
m_{mn}	Mean normal module	ρ_{eq}	Equivalent radius of curvature
n	Surface node	σ_{nm}, σ_{na}	Normal mean and amplitude stresses
n_1	Pinion RPM	σ_{res}	Residual stress
M_k	Adjusted mean stress sensitivity	τ_m, τ_a	Shear mean and amplitude stresses
MLM	Maximum Likelihood Method		

1. Introduction

Gears, along with the majority of industrial applications, fail predominantly from fatigue. For case hardened cylindrical or bevel gears, typical fatigue failure modes are pitting, tooth root breakage and subsurface fatigue or tooth flank fracture (TFF). Whereas accurate guidelines have been developed for pitting and tooth-root breakage [1,2], ambiguity surrounds TFF as no clear gear rating standard has yet emerged. This research focuses on subsurface fatigue, the dominant failure mode in large marine bevel gears. Earlier

publications [3–5] cover a simplified subsurface fatigue criterion, a material model for carburized CrNiMo steel, a 2D numerical plane strain model and a novel, shear stress intensity, multiaxial fatigue criterion (herein referred to as BO). The BO criterion was developed specifically for fatigue predictions under Hertzian stresses. Based on initial evaluations [5], the proposed methodology is able to differentiate between and accurately predict TFF, pitting and tooth root breakages, extending its applicability from the originally targeted subsurface layer across the entire gear tooth. This article compares the BO criterion against a series of load-controlled bevel gear tests at varying hardening layer thicknesses.

The DNV GL gear rating standard for marine applications [6] features one of the few formalized methods for the prediction of subsurface fatigue. It compares the surface parallel orthogonal shear stress amplitude in the tooth interior with a hardness-derived shear strength. Especially on large gear wheels, where surface hardnesses are typically 1–2 HRC below corresponding pinion values [3], this approach leads to an overestimation of surface rather than subsurface failures. Combining the compressive residual stresses, a result of the case hardening process with the orthogonal shear stress amplitude in the form of a simplified Dang Van criterion leads to an elegant and improved subsurface fatigue prediction [3]. A more accurate fatigue assessment, able to differentiate between pitting failures, tooth root breakages and subsurface fatigue, is possible with the proposed BO shear stress intensity criterion [5]. In a multiaxial fatigue study, comparing the results of different stress-based criteria against test results of steels under static axial, tensile or compressive stresses and oscillating shear stresses, the BO criterion performed on par with the well-established Liu & Zenner (LZ) [7] and Papuga integral method (PIN) [8]. Further merit is given to the BO criterion in a recent study [9] under a wider range of in-phase and out-of-phase loading conditions. Whereas the LZ and PIN criteria work very well under conventional loads [5,9], they under- or overestimate the likelihood of surface failures under Hertzian stresses. Especially the overestimation of surface failure on gears under large Hertzian stresses is a common issue for a range of stress-based, multiaxial fatigue criteria. In contrast, the BO criterion was specifically developed with large Hertzian stresses in mind.

Highly loaded gears are typically case hardened, resulting in considerable static residual stresses and varying material properties throughout the hardened layer. The developed material model for CrNiMo steels [4] attempts to capture those changes. It is based on high and very high cycle fatigue (VHCF) testing of hourglass-shaped specimen under uniaxial and shear stresses. The specimens were extracted among others, from large 18CrNiMo7-6 and 34CrNiMo6 forgings that underwent gear-like production processes. Testing was done under alternating and oscillating loads. The material properties in the soft core and hard case were captured by the different carbon content and hardness of the forgings. Inferior fatigue properties under uniaxial loading were derived for the approximately 150 HV harder 34CrNiMo6 steel beyond $1{\cdot}10^6$ load cycles. Comparable results between both steels were achieved under shear loading. Scanning electron microscopy revealed similar-sized MgO-Al_2O_3 inclusions in the crack initiation sites for both steels and initiation from large austenite grains for some of the 34CrNiMo6 specimen. The results highlight the criticality of non-metallic inclusions on the uniaxial fatigue strength of hard steels, and the changing fatigue ratio κ. As gears are subjected to large compressive mean normal stresses in the case, and tensile stresses in the core (tensile residual stresses), the changing mean stress sensitivity throughout the hardened layer is critical for an accurate fatigue prediction. A novel approach, relying on the apparent notch effect of non-metallic inclusions on the mean stress sensitivity was proposed [4]. It captures a linearly increasing mean stress sensitivity for soft and mild steels as per the FKM Richtlinie [10] and reduces the trend for hard steels, bridging the gap between the FKM and the model predictions by Murakami [11].

The combination of the proposed multiaxial fatigue criterion [5] alongside the stress and strength models have been shown to capture pitting, tooth root breakage and subsurface fatigue failures in both small and large gears. As the actual load history and precise stress distribution were unknown for the examined gear sets, this study pares the BO criterion with load-controlled bevel gear tests at varying hardening layer thicknesses.

2. Experimental

2.1. Material and heat treatment

The test gears were designed and loaded to promote TFF over other fatigue failure modes and to evaluate the effect of the load and the case hardening depth (*CHD*). All pinions were produced from a single melt and a hot rolled 160 mm bar. All wheels were manufactured from a single melt and a 457 mm round forged bar. The materials' chemical compositions, the forging reduction ratios, tensile properties, impact works, degree of purity and heat treatment protocols are listed in Table 1, Table 2 and Table 3. The information given in Table 1 and Table 2 is based on the steel's material certificates and valid for the quenched and tempered condition of the steel prior to case hardening. The tensile properties were determined on 30 mm round bars according to the ISO 6892-1, the impact properties according to the ISO 148-1 and the microinclusions according to the ISO 4967 Method A.

The case hardening process consisted of carburizing, direct quenching in oil and a 5 h tempering at 170 °C. For the B3 gears, a more effective quenching media was used, resulting in slightly elevated surface and core hardness (see Table 3). The large differences in the obtained *CHDs* between the pinions and wheels of batch B1 are due to the increased stock removal on the wheels during hard cutting. The heat treatment of the B1 gears was performed with inadequate clamping, resulting in excessive thermal deflections and thus stock removal on the wheels during hard cutting. HV10 hardness measurements were carried out on multiple pinion and wheel teeth of each gear set after failure. For a minimum of one gear set per heat treatment batch, multiple hardness profiles were obtained along the tooth flank to capture the occurring hardness transition from the tooth root to the tip. Fig. 1 exemplifies the results of the performed hardness measurements on gear set B3-2. Clearly visible are the increasing hardening layer thickness, core and surface hardness from root to tip on the plotted wheel tooth.

The measurements were used to create a model of the hardness distribution of the entire gear tooth [5]. Three sets of hardness

Table 1
Chemical composition and forging reduction ratio of pinion and wheel bars.

Steel melt18CrNiMo7-6	Reduction ratio	Composition (wt.%)										
		C	Mn	P	S	Si	Ni	Cr	Mo	Cu	Al	O
Pinion	6:1	0.17	0.62	0.007	0.002	0.30	1.60	1.65	0.31	0.22	0.031	0.0011
Wheel	5.1:1	0.16	0.53	0.005	0.001	0.26	1.59	1.68	0.29	0.11	0.035	0.0012

Table 2
Tensile properties, impact work and degree of purity of pinion and wheel bars.

Tensile properties [ISO 6892-1]	Yield strength R_{p02} [MPa]	Ultimate strength R_m [MPa]	Elongation A [%]	Area reduction Z [%]	Impact Work [J] [ISO 148-1]	Degree of purity [ISO4967-A]			
						A	B	C	D
Pinion	1144	1436	11.1	49	66/72/73	0.5/0.5	1/0	0/0	1/0.5
Wheel	938	1243	12	56	77/76/68	0/0	1/0.5	0.3/0.3	1/0.5

Table 3
B1-B3 test gear batches with number of produced gears sets, heat treatment parameters and average hardness results.

Heat treatment batches	No. of gear sets	Carburizing durations [h]	$HV_{S1,2}$ [HRC]	$HV_{C1,2}$ [HV]	$CHD_{1,2}$ [mm]
B1	3	36	60/59	430/400	2.5/2.1
B2	1	40	60/59	430/400	2.6/2.4
B3	6	50	61/60	455/425	3.0/2.9

parameters according to the Thomas model [12] (one for the tooth root, one for the pitch line and a third for the tooth tip) were used to describe the hardness transition in tooth profile direction. As shown in Fig. 1, the hardness profiles on the B3-2 pinion tooth were very uniform, whereas the wheel hardness profiles changed significantly from root to tip. Visible is also a steeper hardness transition from case to core on the wheel tooth. The Thomas model allows the description of these differences through the parameter y_{HVmax} as the depth of the hardness peak. Rather than using it for its intended purpose, it is set to control the gradient of the hardness profile. For the two blue lines in Fig. 1A and B (representing the measurements taken on the mid tooth height), y_{HVmax} was set to −0.8 mm for the pinion and 0.48 mm for the wheel. In the gear endurance tests, TFF initiated predominately on the wheels, despite the 9:33 gear ratio and the larger number of load cycles on the tested pinions. With TFF typically initiating in a depth corresponding to 1-2x the *CHD*, the above-outlined hardness differences must be regarded as a contributing factor.

2.2. Gear specimen

Table 4 summarizes the test gears' macro geometry, the measured surface roughnesses and case hardening depths for pinions and wheels. The chosen gear geometry, the use of a high viscosity ISO-VG 220 gear oil and polishing of the gears through isotropic

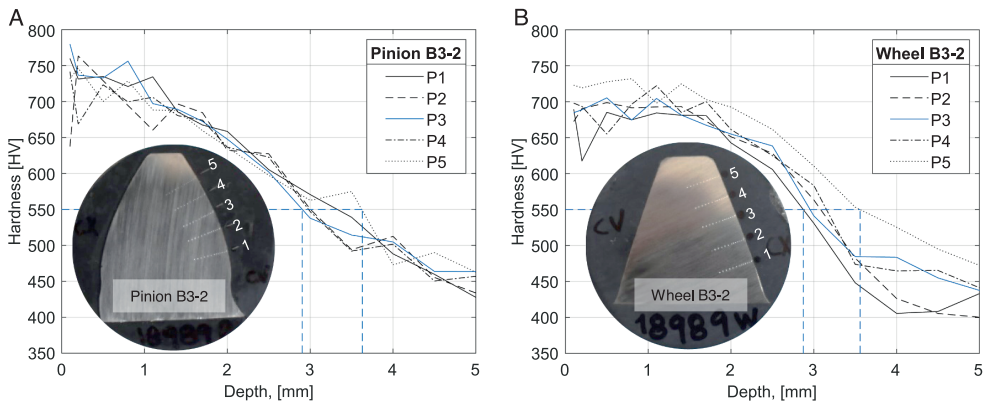

Fig. 1. Hardness measurements and hardness map of (A) pinion gear tooth on B3-2 and (B) wheel gear tooth B3-2.

superfinishing (ISF) were implemented to ensure TFF over pitting, tooth root breakage or scuffing failures even at extreme surface pressures (>2000 MPa).

All test gears featured an identical macro and micro geometry that varied only due to individual machining deviations. In order to capture the resulting surface stresses between meshing pinion and wheel teeth, the actual tooth geometries were obtained by gridded coordinate measurements and used as a point cloud to model the tooth flank. The load dependent gear deflections were estimated through finite element simulations, considering the gear and its environment. To estimate the friction coefficients between the contacting flanks, oil temperature and surface roughness measurements were carried out on each gear set. The average operating temperatures ranged from 33 to 36 °C and the surface roughnesses of the ISF treated teeth from R_z 0.2 to 1.2 µm.

2.3. Test machine and procedure

The tests were carried out on a back-to-back bevel gear test rig. It operates in a mechanical power circuit, meaning that after a static load has been applied, only the internal friction needs to be overcome during operation (see Fig. 2A). The principle is similar to the well-established FZG cylindrical and bevel gear test rigs but uses a hydraulic torque actuator rather than a preloading clutch for the application of load. It pairs two test gears working with two, larger, failure-free transmission gears. Compared to the FZG's bevel and hypoid test rigs, significantly larger gears can be tested with a wheel outer pitch diameter of 450 mm rather than 170 mm, making these test results more transferable to large industrial applications like bevel gears in azimuthing thrusters.

Each axle between the test rig's corners was equipped with a strain gauge and telemetry system to document the transmitted torque, frictional losses and internal dynamics. Between the two test corners, mechanical losses of approximately 50 kW were measured, reducing the surface pressure on the gears tested in corner 2 by roughly 25 MPa. The contact stress analysis showed that the reduction in surface pressure due to frictional losses was in some cases compensated by occurring machining deviations (see Table 5). Unique to gear set B1-1 was a strain gauge and telemetry set-up, by which the bending stresses on 2 wheel teeth could be measured directly during operation (see Fig. 2B).

Endurance testing was done at 1500 RPM and at uniform loads at 750, 875 and 1000 kW. Torque during testing was controlled by the hydraulic actuator based on the torque measurements on the machine axes. Each gear underwent a run-in procedure with a gradual load increase (typically less than 1% of the total test duration). Gears were only replaced after failure or once the run-out limit of $5{\cdot}10^7$ load cycles on the pinion had been achieved. As the set-up required two test gears to be run simultaneously, individual gears were occasionally tested at multiple load levels. An equivalent load was calculated for each gear based on the measured load history using the ISO6336-6 guideline [13]. The specified loads in Table 5 describe, therefore, the friction-corrected, equivalent loads for each gear.

The gears' surface stresses, a result of the applied load, the actual macro- and microgeometry and the load-dependent gear deflections, were modelled through a loaded tooth contact analysis (LTCA with BECAL 5.0 [14]). BECAL is a software developed by the Institute of Machine Elements and Machine Design at the Dresden University of Technology. A spiral bevel gear's tooth geometry cannot be modelled analytically and relies in the case of BECAL on a machining simulation. In order to consider the pitch error and gear deflections alongside the gear's macro- and microgeometry, a no-load contact analysis is initially run, defining the distance between opposing flank points for a discrete number of contact positions. The resulting global ease-off is then used in the loaded tooth contact analysis that predicts the stresses between the meshing gear flanks. As a result of the segmentation of the gear tooth in lengthwise and tooth profile directions, influence coefficients are calculated that capture the interaction between the segments, allowing for a short computing time and high precision.

Resulting stress distributions are plotted in Fig. 3 for the gear flank and mean cross-section of the B1-1, B1-2, B3-1 and B3-2 pinions. As is typical for crowned bevel gears, the highest surface stresses occur in the middle of the tooth, deeming the analysis of the gear's mean cross-section sufficient for the evaluation of surface and subsurface failures.

Fig. 3 highlights the correlation between the applied load, the surface pressure and the contact length, but also the effect of the machining deviations. In Fig. 3A and C, the contact stress distributions for gears B1-1 and B1-2 are shown. These gears were tested together in corners 1 and 2 of the test rig and subjected to an equivalent load of 814 and 859 kW, resulting, despite the 45 kW load difference, in nearly identical contact patterns and stress distributions. Fig. 3B and D plot the contact stress distributions for gears B3-1 and B3-2. Both were tested at approximately 1000 kW, resulting in 100 MPa higher surface pressure and a 4 mm wider contact pattern

Table 4
Macro geometry, measured roughness and hardness on tests gears B1-B3.

Description		Macro Geometry			$R_{z1,2}$	$CHD_{1,2}$
	Unit	Pinion	Wheel	Gear	[µm]	[mm]
Pressure angle, α	°	20		B1-1	0.6/0.4	2.5/2.2
Number of teeth, z	–	9	33	B1-2	1.2/0.6	2.4/2.0
Outer pitch diameter, d_e	mm	122.7	450	B1-3	1.0/0.7	2.5/2.1
Tooth width, b	mm	82		B2-1	0.6/0.4	2.6/2.4
Mean spiral angle, β_m	°	32.8		B3-1	0.4/0.2	2.9/3.0
Profile shift, x_{hm}	–	0.35	−0.35	B3-2	0.4/0.2	3.0/3.0
Tooth thickness factor, x_{sm}	–	0.01	−0.03	B3-3	0.4/0.3	2.9/2.9
Adddendum/Dedendum factor, k_{ap}/k_{fp}	–	1.05/1.3125		B3-4	0.4/0.2	2.8/3.0
Cutter module, m_0	mm	10		B3-5	0.5/0.5	2.9/2.9
Cutter radius, ρ_0	mm	170		B3-6	0.4/0.2	2.9/2.9

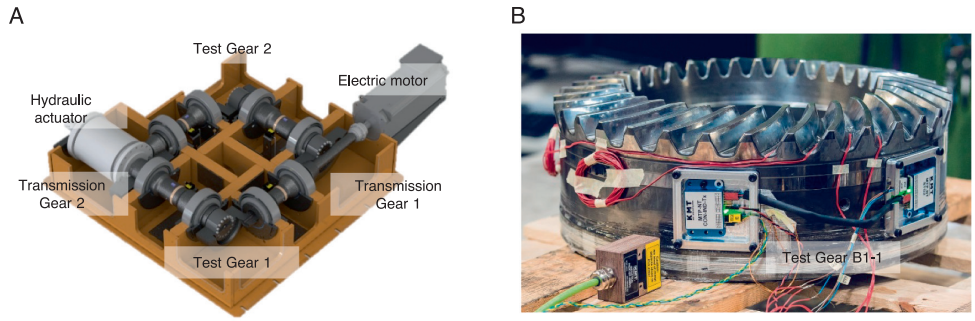

Fig. 2. (A) Schematics of the bevel gear test rig with two test gears and two larger transmission gears and (B) telemetry set-up on test gear B1-1.

Table 5
Load parameters for all test gears, including RPM, equivalent power, maximum surface pressure, average oil temperature and max friction coefficient.

Description		Gears									
	Unit	B1-1	B1-2	B1-3	B2-1	B3-1	B3-2	B3-3	B3-4	B3-5	B3-6
Pinion RPM, n_1	1/min	1500 (for all test gears)									
Power, P	kW	814	859	999	1000	990	1000	800	1050	793	847
Max surface pressure, p_{Hmax}	MPa	1938	1937	2031	2012	2012	2038	1943	2076	1901	1953
Average oil temperature, T	°C	35	33	34	33	36	35	36	35	36	36
Max friction coefficient, μ_{max}	–	0.050	0.053	0.054	0.051	0.048	0.048	0.047	0.048	0.049	0.047

compared to B1-1 and B1-2. Beyond the surface pressure, the equivalent radius of curvature ρ_{eq}, friction coefficient μ and half Hertzian contact width b_H for the mean cross-sections of the 4 gears are also plotted in Fig. 3E to H. Nearly identical ρ_{eq} values are reported for all test gears, underlining the machining accuracy and geometrical comparability of all gears. Subplots G and H in Fig. 3 highlight the subtle differences in the friction coefficient μ as a result of the varying surface roughnesses between the gears. The friction coefficient was predicted according to Hombauer [15], relying on the works by Klein [16] and Wech [17]. With pure rolling only being present in the gear's pitch point, the plotted friction coefficients are minimal at around 9 mm tooth height and increase towards the gear's root and tip. The last parameter included in Fig. 3G and H is the half Hertzian contact width b_H. For a cylinder/plane contact model, it critically affects the depth of the acting shear stresses inside the material.

3. Simulation

The calculation of the material utilization D_{BO}, defined as the inverse of the local safety factor against fatigue, is briefly introduced in this section [5]. All inputs needed for the prediction of D_{BO} are given in the previous sections (i.e. the gear geometry, the load, surface roughness and hardness parameters).

The approach relies on the stress analysis in the gear's mean cross-section and the 2D plane strain simplification. This is deemed appropriate due to the stress concentration in the middle of the tooth for crowned bevel gears (see Fig. 3) and the documented minimal subsurface stress differences between the 2D and 3D analysis [18,19]. As such, a seminumerical approach is pursued, avoiding the need for the finite element contact analysis. In the first step, the mean cross-section of the bevel gear's virtual cylindrical gear is modelled, meshed, and loaded with the LTCA derived stress profile. Herein an improved machining simulation was implemented [5] to capture the tooth root's trochoidal shape. Fig. 4 visualizes the machining simulation and the subsequent mesh generation with a coarse 0.3 mm element size to visualize the mesh layout. For the actual calculations, a finer 0.1 mm element size with 'T6′ triangular elements was used. For these quadratic triangular elements, a full integration over three Gaussian integration points was implemented. All surface nodes below the gear's tooth root diameter had a fixed constraint applied to them, and all surface nodes underneath an instantaneous contact position (defined by its position along the tooth profile, its half Hertzian contact width b_H and surface pressure p_H) were loaded according to their specific Hertzian stress distribution. For the pinion tooth plotted in Fig. 4 and the implemented 0.1 mm mesh resolution, 144 contact positions with non-zero contact stresses were analyzed.

As is shown in Fig. 4B, the element size is doubled after 1/16 and 1/3 of the mean normal circular tooth width s_{mn} as well as in the middle of the gear tooth. This stepped mesh ensures a load introduction of the Hertzian stress profile in each contact position over a large number of nodes and an efficient calculation.

The hardness and residual stress model remained unchanged [5]. Each surface node n is assigned a set of hardness parameters according to the Thomas model [12] and its position in the tooth profile direction. The same is done subsequently for each subsurface node i, based on its closest surface nodes. For the estimation of the residual stresses, the Lang model [20] is used up to the *CHD*, followed by a 4th order polynomial to describe the tensile residual stresses in the core. Lines 1 and 2 in Eq. (1)are according to Lang

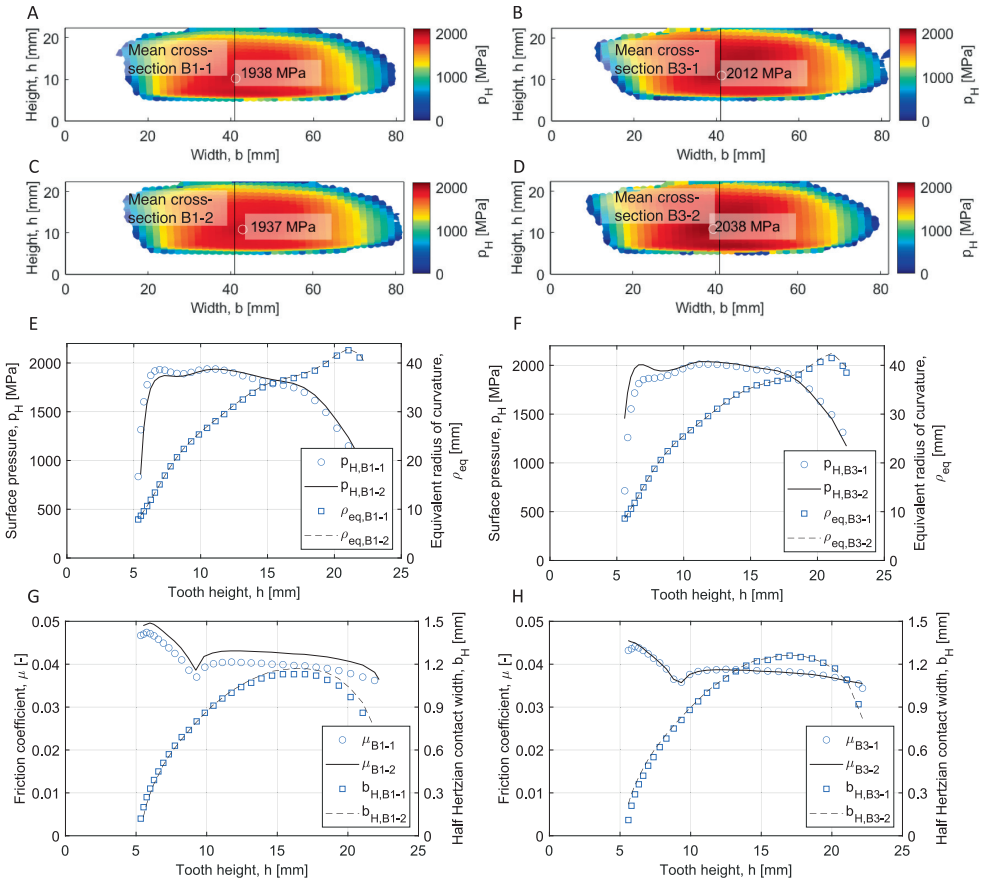

Fig. 3. Prediction of the surface pressure p_H for contact patterns B1-1 in (A), B3-1 in (B), B1-2 in (C) and B3-2 in (D). Comparison of the surface pressure p_H and equivalent radius of curvature ρ_{eq} in the gears' mean cross-section between B1-1 and B1-2 in (E) and B3-1 and B3-2 in (F). Comparison of local friction coefficient μ and half Hertzian contact width b_H in the gears' mean cross-section between B1-1 and B1-2 in (G) and B3-1 and B3-2 in (H).

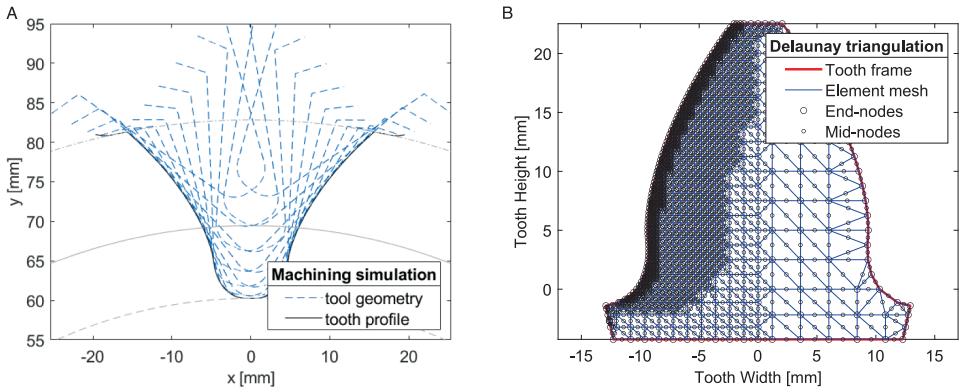

Fig. 4. (A) B1-1 virtual pinion tooth machining simulation and (B) mesh layout.

with lines 3 and 4 describing the polynomial and the equilibrium constraint, used to derive the constants a, b and c along with the tangential constraint in the transition point (CHD).

$$\sigma_{res,i}(y_l) = \begin{cases} -5/4 \cdot \left(HV_i(y_l) - HV_{C,i}\right), HV_i(y_l) - HV_{C,i} \leq 300 \;\; HV \;\; and \;\; y_l < CHD_i \\ 2/7 \cdot \left(HV_i(y_l) - HV_{C,i}\right) - 460, HV_i(y_l) - HV_{C,i} > 300 \;\; HV \;\; and \;\; y_l < CHD_i \\ a \cdot \left(y_l - s_{n\alpha,i}\right)^4 + b \cdot \left(y_l - s_{n\alpha,i}\right)^2 + c, y_l \geq CHD_i \end{cases} \quad (1)$$

$$\text{with} \;\; s_{n\alpha,i} = \frac{s_{n,i}}{2 \cdot \cos\alpha_i} \;\; \text{and} \;\; \int_0^{s_{n\alpha,i}} \sigma_{res,i}(y_l) dy_l = 0$$

The index i in Eq. (1) refers to each subsurface node with its assigned core hardness $HV_{C,i}$ and local hardness $HV_i(y_l)$. The variable y_l describes the perpendicular path from the closest surface node through studied subsurface node i to the middle of the tooth (here described through the half tooth thickness $s_{n\alpha,i}$). Each node's local hardness along with an assumed global inclusions size (set through Murakami's $\sqrt{area}$ parameter ≈80 µm [4]), the fatigue ratio κ and an adjusted mean stress sensitivity M_k, are used to define the local fatigue parameters throughout the gear tooth. They are set according to the material model for CrNiMo steel [4].

$$f_{-1}(HV) = \begin{cases} 1.6 \;\; HV, HV < 300 \\ \dfrac{1.56 \cdot (HV + 120)}{\left(\sqrt{area}\right)^{\frac{1}{6}}}, HV > 550 \end{cases} \quad \text{and} \quad f_0 = \frac{2 \cdot f_{-1}}{1 + M_k} \quad (2)$$

$$505 \;\; MPa, else$$

$$t_{-1} = \frac{f_{-1}}{\kappa} \quad \text{with} \quad \kappa = -5 \cdot 10^{-4} HV + \sqrt{3} \quad \text{and} \quad \frac{4t_{-1}}{t_0} - \frac{2f_{-1}}{f_0} = 1$$

In Eq. (2) f_{-1}, f_0, t_{-1}, t_0 describe the fatigue limit under fully reversed and repeated axial loading and torsional fully reversed and repeated loading (t_0 according to Liu and Zenner [7]) at $2{\cdot}10^6$ load cycles. These fatigue limits are subsequently used to determine the model parameters in the multiaxial fatigue criterion in order to combine the different stress components to an equivalent stress. For the prediction of the local material utilization D_{BO}, the equivalent stress is compared against a modified fatigue strength under fully reversed axial loading $f_{-1,K}$. The modifications include a load cycle dependency, size effect and failure probability conversion. The lifetime factor K_{NT} relied in its first iteration on the high cycle and very high cycle uniaxial fatigue results of the 34CrNiMo6 steel [4]. It is reiterated in this study through the analysis of the gear test results with the Maximum Likelihood Method (MLM) [21] and therefore omitted from Eq. (3). The size factor K_X listed in Eq. (3) describes a simplification of the weakest link theory [22], relying on the comparison of the highly stressed volume in the fatigue specimen and the studied gear sets [4,5]. In its simplified form, it depends on the gear's mean normal module m_{mn} and is identical to the ISO suggested size factor for the tooth root [2]. As such, K_X ignores the differences between the tested pinions and wheels and the effect of the applied load on the highly stressed volume. The calculations in this study rely therefore directly on the weakest link theory and not the outlined equation. For gear standards [1,2,6], the endurance limit is set for a 1 rather than 50% failure probability, requiring a conversion factor f_{xK} to convert the gear test results. For the documented standard deviation of 4% [4], a conversion factor of 0.91 is suggested. The analysis of gear test results and all calculations in this study omit f_{xK}.

$$f_{-1,K} = f_{-1} \cdot f_{xK} K_X K_{NT}$$

$$f_{xK} = 0.91 \;\; \text{and} \;\; K_X = 1.05 - 0.01 \cdot m_{mn} \;\; \text{with} \;\; 0.87 \leq K_X \leq 1 \quad (3)$$

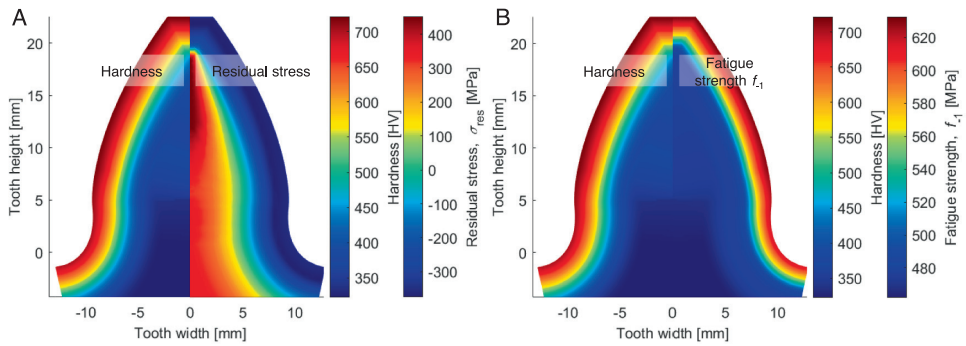

Fig. 5. (A) Hardness and residual stress and (B) uniaxial fatigue strength prediction for a B1-1 pinion tooth for measured hardness parameters CHD = [2.2, 2.5, 3.7] mm, HVs = [703, 718, 720] HV, HVc = [322, 362, 380] HV in tooth profile positions h = [2,8,16] mm.

Fig. 5A plots the hardness against the residual distribution for a B1-1 pinion tooth and the hardness against the fatigue strength f_{-1} in Fig. 5B.

In accordance with the performed hardness measurements (see Fig. 1), an increase in surface and core hardness and *CHD* is visible in Fig. 5A in profile direction. Whereas large marine bevel gears are typically produced with a CHD/m_{mn} ratio from 0.12 to 0.21, the test gears' ratio ranged from 0.21 to 0.32, resulting in a wide layer of compressive residual stress and relatively large tensile stresses in the core, increasing towards the narrow tooth tip. The differences in local hardness and fatigue strength f_{-1} are plotted in Fig. 5B. The in Eq. (2) outlined fatigue model [4] describes a transition from the upper to the lower limit of Murakami's fatigue model [11] within the hardness range 300–550 HV. This transition is visible in Fig. 5B as f_{-1} remains nearly constant in the tooth core and only starts to increase in the case, once the local hardness exceeds 550 HV.

The modelled hardness distribution deviates slightly from the measured core hardnesses. This was done intentionally in order to increase the compressive residual stress levels in the surface. The residual stress model by Lang [20] (see Eq. (1)) predicts diminishing compressive, residual stress levels for gears with high core hardnesses (see Table 3 and Fig. 1). On case hardened gears, the residual stresses are a result of the martensitic transformation, occurring first in the case/core interface, subsequently in the core and finally on the surface. As such, the resulting residual stresses are a function of the local cooling rate and, predominately, the carbon content. It could therefore be argued that the residual stress should be modelled as a function of the carbon profile and not the hardness.

With the static residual stresses and the material properties defined, a numerical stress calculation is carried out for each contact position and the defined 2D plane strain stress state. The resulting time-dependent stress matrices are combined to normal mean and amplitude stresses (σ_{nm} and σ_{na}) and shear mean and amplitude stresses (τ_m and τ_a) on each material plane, defined by the spherical angles θ and ϕ. Whereas the prediction of the normal stresses is straight forward, the maximum rectangular hull method (MRH) was applied to estimate the shear stress components. The predicted stresses are integrated over all material planes to an equivalent stress as per Eq. (4) and compared against the adjusted uniaxial fatigue strength $f_{-1,K}$ (see Eq. (3)). Eq. (4) outlines the stress integration and prediction of the model parameters a_{BO}, b_{BO}, c_{BO} and d_{BO} from the fatigue parameters f_{-1}, f_0, t_{-1}, t_0.

$$D_{BO} = \sqrt{\frac{15}{8\pi}\frac{\int_0^{2\pi}\int_0^{\pi}\left(\left(a_{BO}\tau_a^2 + b_{BO}\sigma_{na}^2\right)\left(1 + c_{BO}\sigma_{nm}\right)^2 + d_{BO}\tau_a\tau_m\right)\sin(\theta)d\theta d\varphi}{f_{-1,K}}}$$

$$a_{BO} = \frac{1}{5}\left(3\kappa^2 - 4\right) \text{and} b_{BO} = \frac{1}{5}\left(6 - 2\kappa^2\right)$$

$$c_{BO} = -\frac{3f_0(11 - 2\kappa^2)}{70C} + \sqrt{\left(\frac{3f_0(11 - 2\kappa^2)}{70C}\right)^2 + \frac{1}{C}\left(\left(\frac{2f_{-1}}{f_0}\right)^2 - 1 - \frac{\kappa^2}{3}\left(\left(\frac{2t_{-1}}{t_0}\right)^2 - 1\right)\right)}$$

$$d_{BO} = \frac{\kappa^2}{3}\left(\left(\frac{2t_{-1}}{t_0}\right)^2 - 1 - \frac{c^2 t_0^2}{35\kappa^2}\left(8 - \kappa^2\right)\right) \quad \text{with} \quad C = \frac{f_0^2}{84}\left(17 - 4\kappa^2\right) - \frac{t_0^2}{105}\left(8 - \kappa^2\right) \tag{4}$$

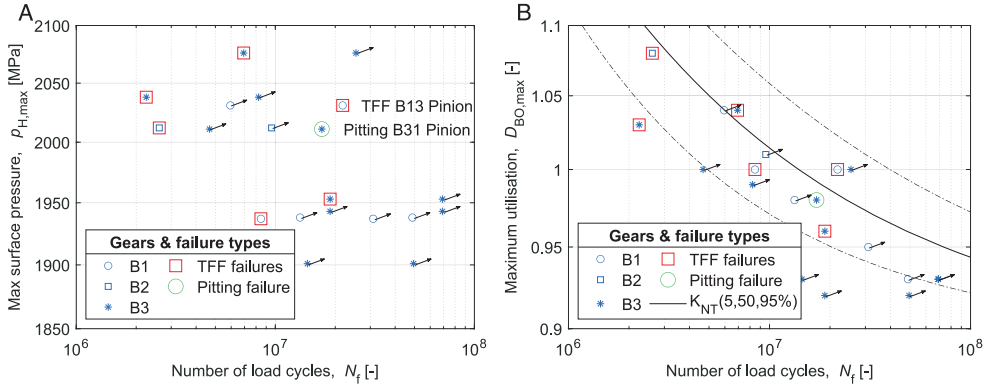

Fig. 6. Gear test results plotted as (A) number of load cycles N_f against maximum surface pressure p_H and (B) number of load cycles N_f against maximum material utilization $D_{BO,max}$.

4. Results & discussion

4.1. Fatigue results

A series of 10 gear sets were endurance tested with their geometry, loads and material properties described in the previous sections of this article. Fig. 6A plots the cycles to failure and run-outs against the corresponding maximum Hertzian contact stress in the mean cross-section. The single pinion-initiated pitting and TFF failures are highlighted. In contrast, Fig. 6B shows the maximum of the material utilization D_{BO} calculated according to Eq. (4) without the lifetime factor K_{NT} and conversion factor f_{xK}.

As a result of the hardness variations between and within the heat treatment batches, plotting the number of cycles N_f against the maximum occurring Hertzian contact stress leads to inconclusive results. Of the 7 observed fatigue failures, 5 TFF failures occurred on the wheels of B1-2, B2-1, B3-2, B3-4 and B3-6, 1 TFF failure on the pinion of B1-3 and 1 pitting damage on the pinion of B3-1. The 9:33 gear ratio on the test gears meant that each pinion tooth was subjected a 3.67x larger number load cycles than corresponding wheel teeth, suggesting that a majority of the fatigue failures should have occurred on pinions rather than wheels.

Plotting N_f against the maximum material utilization $D_{BO,max}$ (see Fig. 6B) leads to far more conclusive results as the available data on the stress and strength differences between the tested pinions and wheels is combined. By omitting K_{NT} and f_{xK} from Eqs. (3) and (4), a quasi-stress amplitude versus number of load cycles curve (SN-curve) is visualized. The a quasi SN-curve was approximated through the use of the maximum likelihood method [21], combining run-outs with TFF and pitting failures. Fig. 7 compares the lifetime factors of the performed gear endurance tests against the VHCF results of the tested 18CrNiMo7-6 and 34CrNiMo6 steels [4] and against those quoted in the ISO standard for pitting and tooth root breakage [2,23].

At fewer cycles, $K_{NT,Gear}$ shows a pronounced load cycle dependency that diminishes in the VHCF regime. It transitions from a lifecycle factor closer to the tested 34CrNiMo6 steel to the 18CrNiMo7-6 steel [4]. The TFF failure on the wheel of B3-2 after $2.25{\cdot}10^6$ load cycles marked in red in Fig. 7A can be seen as an outlier to the predicted SN-curve. It, along with the TFF failures on the B1-3 pinion tooth and B2-1 wheel tooth were investigated further by means of scanning electron microscopy (SEM). Fig. 7B compares $K_{NT,Gear}$ against the pitting and the tooth root breakage related lifetime factors Z_{NT} and Y_{NT} [1,2]. Plotted are the ISO factors without permissible pitting damages and with deteriorating fatigue properties in the VHCF regime. The lifetime factor $K_{NT,Gear}$ is capped conservatively at 1.6 based on the reported yield strength to fatigue ratio of the tested 18CrNiMo7-6 steel. Only a limited number of tests were performed with failures and run-outs occurring between $2{\cdot}10^6$ and $7{\cdot}10^7$ load cycles, resulting in a lifetime factor that is sensitive to small deviations in the calculated material utilizations. By relying on material utilization rather than surface stress, the lifetime factor considers the gear size, the applied load and hardening procedure. As such, other gear test results could be added to complement the presented results.

$$K_{NT,Gear} = \exp\left(\frac{\ln(N_f) - 10.42}{-2.73}\right) + 0.89 \quad \text{with} \quad K_{NT,Gear} \leq 1.6 \tag{5}$$

Utilizing the derived lifetime factor as per Eq. (5), the material utilizations for all test gears were recalculated and plotted for gear sets B1-3, B2-1, B3-1 and B3-4 in Fig. 8 and Fig. 9. Failures are expected for gears with material utilizations close to or larger than 1 and no failures for material utilizations significantly smaller than 1. D_{BO} is plotted in Fig. 8 for the gear's mean cross-section and in Fig. 9 for two paths, one perpendicular to the tooth surface through $D_{BO,max}$ (P1 in Fig. 8 and Fig. 9) and a second one intersecting the maximum utilization for a given material depth (P2 in Fig. 8 and Fig. 9). By doing so, the comparison of surface against subsurface fatigue is enabled as pitting, tooth root breakage and TFF are expected to initiate in different positions along the tooth profile.

Focusing on Fig. 9B and D, the effect of an increasing *CHD* on the predicted depth of the maximum material utilization can be

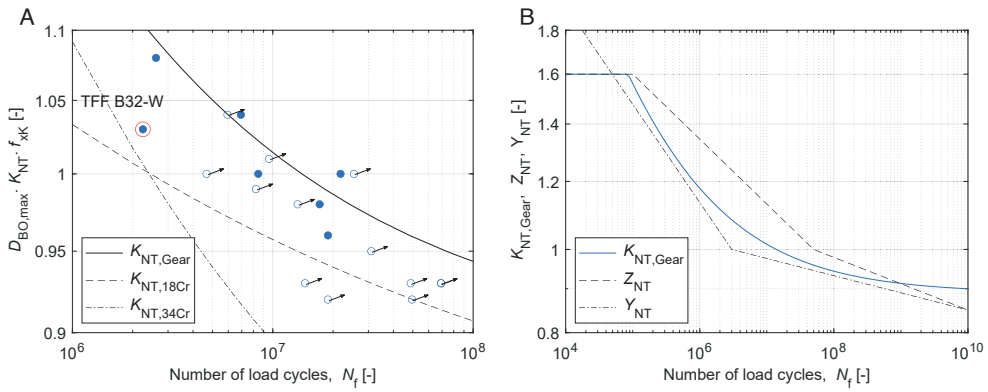

Fig. 7. Comparison between predicted lifetime factor $K_{NT,Gear}$ and (A) reported results for 18CrNiMo7-6 $K_{NT,18Cr}$ and 34CrNiMo6 $K_{NT,34Cr}$ and (B) ISO predictions Z_{NT} and Y_{NT}.

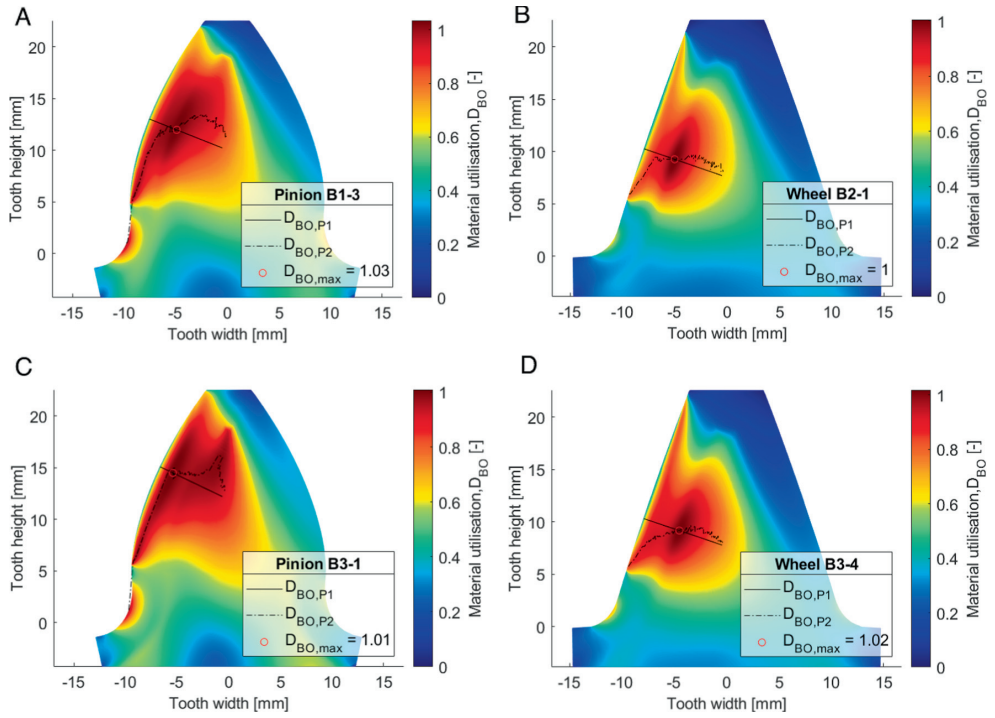

Fig. 8. Material utilizations for mean cross-section of (A) pinion B1-3, (B) wheel B2-1, (C) pinion B3-1 and (D) wheel B3-4.

observed. As listed in Table 4, the case depth of wheel B3-4 was 0.6 mm deeper than for wheel B2-1. Accordingly, the location of the maximum material utilization can be found approximately 0.5 mm deeper on B3-4. Gear set B2-1 with a 2.4 mm *CHD* suffered a TFF damage after $2.61 \cdot 10^6$ load cycles on the wheel, whereas gear set B3-4 with its 3.0 mm *CHD* endured $6.94 \cdot 10^6$ load cycles at a 64 MPa larger surface stress (see Table 5) prior to failure.

Comparing Fig. 9A and B against C and D demonstrates the higher risk for surface fatigue on the tested pinions than wheels. This finding is in good agreement with recent studies on the pitting durability on bevel gear [24], whereby 33.5% Hertzian contact stresses are allowable on driven rather than driving gear flanks. Fig. 9A plots the predicted material utilization for a B1-3 pinion tooth. As shown in the next section, the calculated utilization peak in a depth of 2.7 mm agrees well with the observed TFF initiation 2.4 mm below the surface. A local utilization peak of 1.01 in a depth of 1.3 mm is predicted for the B3-1 pinion and visualized in Fig. 9C. With pitting damages initiating either directly on the surface or in a shallow depth below the surface, the stress and strength model, along with the multiaxial fatigue criterion are deemed appropriate to predict both pitting and TFF damages. The current iteration of the stress model does not consider elasto-hydrodynamic and surface roughness effects on the Hertzian stress distribution. With those effects, a utilization peak closer to the surface is probable. A third peak on B1-3 and B3-1 pinions in the tooth dedendum and a depth of 0.3 mm may indicate a substantial risk for micropitting on these gears. The peak's location on the tooth profile and its absence on the tested wheels corresponds well with the predictions made by Hombauer [15]. With micropitting damages being currently attributed to local oil film thicknesses rather than a fatigue stress analysis, no statement in regard to the applicability of the developed methodology in predicting micropitting damages can be made at this stage. Fig. 10 shows the gear failures on gears B1-3, B2-1, B3-1 and B3-4.

Whereas the pitting damage is clearly visible on B3-1, the TFF damages on B1-3, B2-1 and B3-4 are visible as a crack network, stretching across the loaded pinion and wheel flanks. As reported by other researchers [25–27], once the primary subsurface crack transitions from mode II to mode I, multiple secondary cracks form and grow towards the load-carrying flank. The orientation of the crack network at an angle parallel to the instantaneous contact lines between meshing pinion and wheel teeth is also clearly visible. In addition to the above-mentioned, primary TFF and pitting damages, scuffing marks are also visible on B3-1 on the edges of the pitting damage. This is classified as a secondary damage due to disturbance of the lubrication film in the vicinity of the pit, as well as due to an increase in contact pressure. Furthermore, a minor micropitting damage was observed on the tip of the TFF-affected B1-3 pinion tooth. In order to further examine the TFF damages on the B1-3 pinion and the B2-1 and B3-2 wheels, the damaged teeth were extracted and cut into sections.

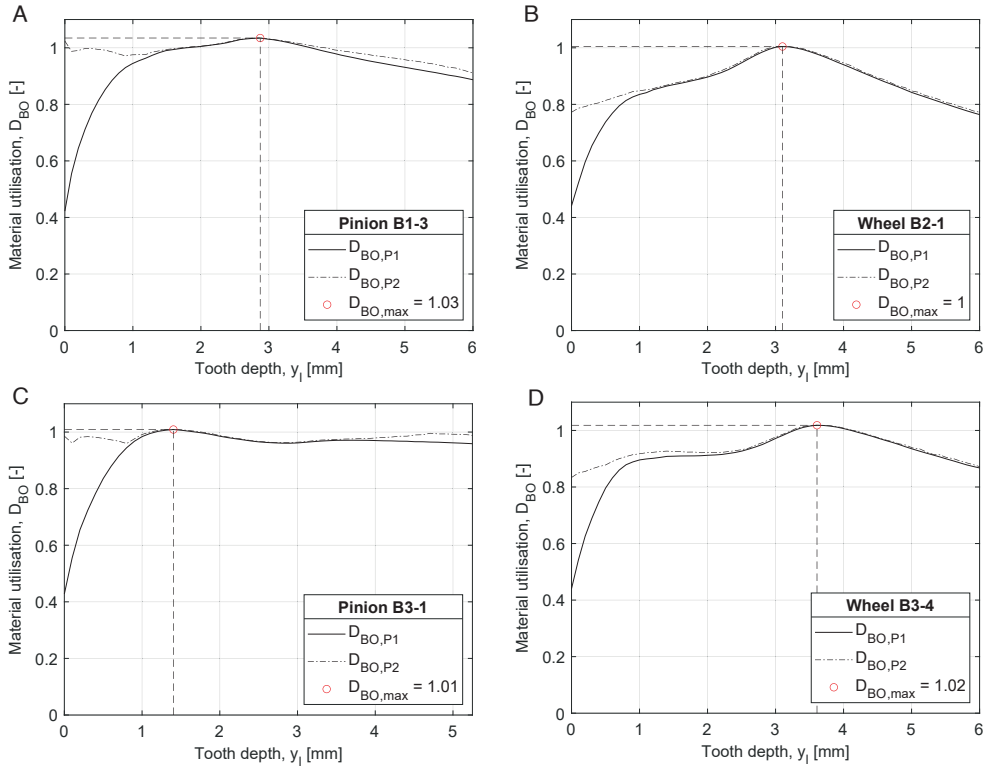

Fig. 9. Material utilization along path 1 & 2 for mean cross-sections of (A) pinion B1-3, (B) wheel B2-1, (C) pinion B3-1 and (D) wheel B3-4.

4.2. Fractographic analysis

The fractographic analysis of the pinion-initiated TFF on B1-3, as well as the wheel-initiated TFF on B2-1 was conducted on a field emission scanning electron microscope (MIRA 3 XMU) equipped with electron backscatter diffraction (EBSD) and energy dispersive X-ray (EDS) detectors. A second wheel-initiated TFF on B3-2 was analyzed on a second field emission scanning electron microscope (TESCAN VEGA 4 LMU), similarly equipped with EBSD and EDS. The wheel analysis did not reveal any insight into the cause of failure or its initiation depth, as excessive plastic deformation of the fracture surfaces removed all fatigue fracture features.

Fig. 11A visualizes the extraction of the analyzed pinion tooth section and the approximate position of the TFF on B1-3 mid flank and mid tooth height. The performed EDS analysis identified a 1.4 mm long MgO-Al_2O_3 spinel in a depth of 2.4 mm in the crack initiation site. The severely elongated spinel was orientated approximately in the pinion's forging direction and in a 45° angle to the load-carrying gear flank. Whereas Fig. 11B visualizes the general orientation of the inclusion on the fracture surface, Fig. 12A and B show the length of the inclusion through SEM and EBSD images.

The comparison between the inclusion size on the B1-3 test gear and the VHCF tested 18CrNiMo7-6 and 34CrNiMo6 steels [4] relies on Murakami's model and its $\sqrt{\text{area}}$ parameter [11]. The $\sqrt{\text{area}}$ parameter describes the square root of the projected area of an inclusion, perpendicular to the maximum principal stress. The maximum principle stress as a result of the Hertzian contact is perpendicular to the load carrying flank, whereas the studied inclusion is tilted in tooth width and profile direction. It is uncertain if the entire length of the identified inclusion should be considered in the calculation of the $\sqrt{\text{area}}$ parameter. The average $\sqrt{\text{area}}$ parameter found on VHCF fracture surfaces of the uniaxial fatigue specimen was 80 µm, compared to the 330 µm for the reported spinel on B1-3. According to Murakami, the large defect size is equivalent to a 20% lower fatigue strength f_{-1} than outlined in Eq. (2). The developed multiaxial fatigue criterion, strength and stress models suggest a large failure probability for B1-3 regardless of the identified inclusion. Either the orientation of the inclusion meant that only its cross-section was critical to the crack initiation or the developed methodology overestimates subsurface failures on pinion teeth. Currently, the same material model is implemented for pinions and wheels, depending only on the measured hardness profiles and not on the different blank sizes, forging methods and ratios.

The wheel-initiated TFF on B3-2 (shown in Fig. 13A) features a heavily deformed fracture surface with faint fatigue features like ratchets or river marks. A closer study of the assumed initiation region 4 mm below the surface did not reveal any significant non-

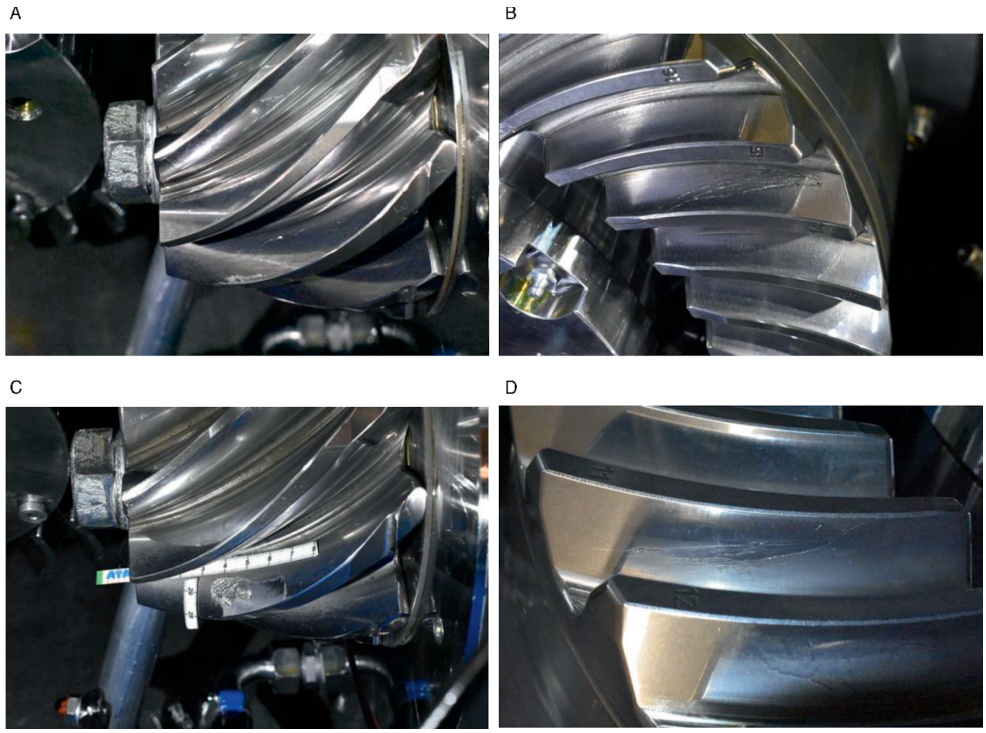

Fig. 10. Gear failures due to subsurface fatigue on (A) pinion B1-3 after $3.1 \cdot 10^7$ load cycles, (B) wheel B2-1 after $2.61 \cdot 10^6$ load cycles and (D) wheel B3-4 after load cycles $6.9 \cdot 10^6$ and pitting on (C) pinion B3-1 after $1.7 \cdot 10^7$ load cycles.

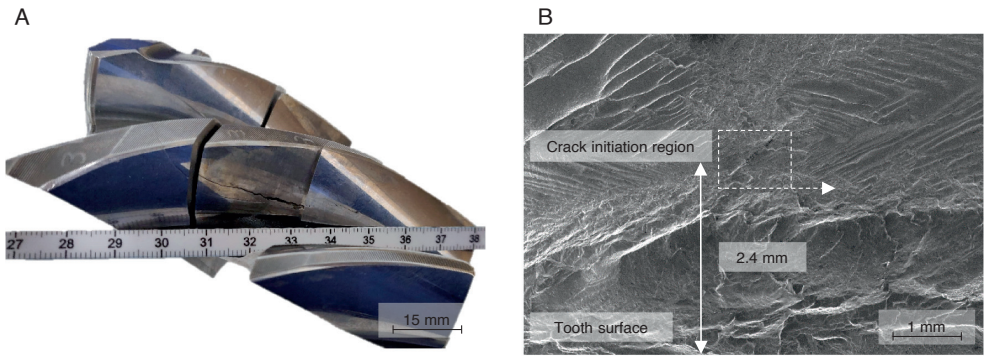

Fig. 11. TFF on pinion B1-3 with crack location and fracture surface extraction in (A) and SEM analysis showing a 1.4 mm long MgO-Al_2O_3 spinel in the crack initiation site.

metallic inclusions but rather a 0.6 mm long ridge, parallel to the tooth surface. With TFF cracks typically initiating parallel to the load-carrying flank under shear in mode II and propagating under bending in mode I, the identified ridge can be considered as a possible initiation site. The observed surface topography bears resemblance to the matrix initiated failures from large, soft austenite grains on the 34CrNiMo6 VHCF specimen [4] (see Fig. 13B). The predicted maximum utilization at 3.7 mm below the surface further supports the identified crack initiation site.

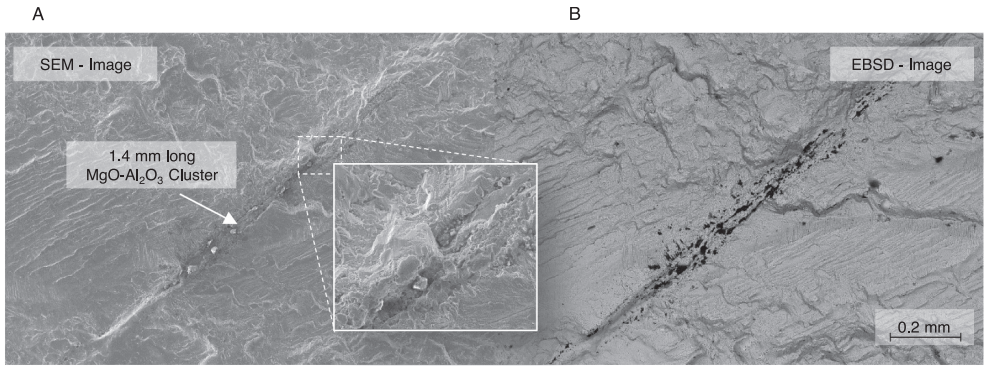

Fig. 12. Study of crack initiating $MgOAl_2O_3$ inclusion on pinion B1-3 through (A) SEM and (B) EBSD.

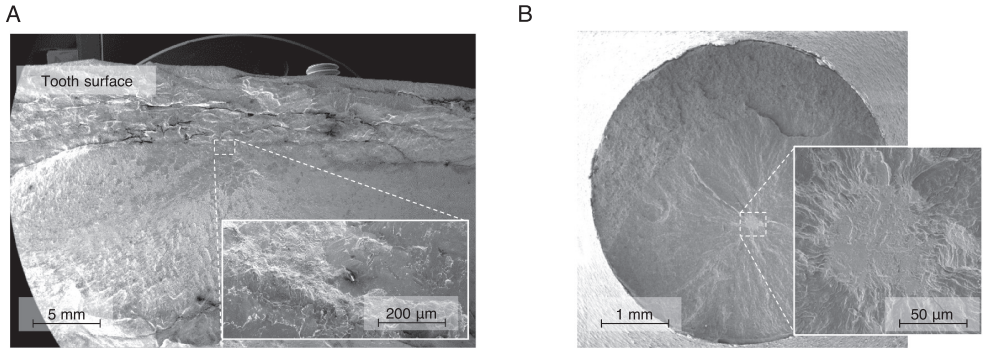

Fig. 13. TFF on wheel B3-2 with (A) fracture surface and a close-up of assumed initiation site compared against (B) crack initiation from large, retained austenite grain [4] in 34CrNiMo6 VHCF uniaxial fatigue specimen.

5. Discussion

As shown through the performed gear endurance tests, the presented methodology, comprised of the strength, stress and fatigue models, can differentiate between and accurately predict pitting and TFF or subsurface fatigue damages. Of the studied gear sets, 6 TFF damages were recorded, of which 5 occurred on the tested wheels. The documentation and accurate modelling of the hardness differences between the studied pinions and wheels were essential in capturing the majority of wheel-initiated TFF damages [12]. The wheels were found to generally have a thinner *CHD* and steeper transition between the hard surface and soft core. As the hardening layer is furthermore used to approximate the initially compressive and subsequently tensile residual stresses, the differences between the tested pinions and wheels are further amplified. Pitting occurred on a single pinion tooth, approximately at half tooth height. The proposed strength and stress models, along with the BO multiaxial fatigue criterion, correctly identify the same location to be critical. In addition, large utilizations are predicted for the pinion dedendum, suggesting a substantial pitting or micropitting risk in this tooth segment. The fatigue model is also able to assess the likelihood of tooth root breakage. The analysis shows an approximately 1.6x higher risk for tooth root breakage on the tested pinions than wheels, compared to the 1.15x predicted by the LTCA and ISO [2,14]. The further analysis and recalculation of gear studies focusing on tooth root breakage [28] is planned for the future to better assess the accuracy of the fatigue model in this respect.

The only pinion-initiated TFF featured a comparably large, elongated non-metallic inclusion in its crack initiation site, suggesting lower fatigue properties than currently implemented in the material model. A large material utilization is predicted regardless in the relevant material depth of 2.7 mm, suggesting that the fatigue model in its current form potentially overestimates subsurface fatigue failures on pinion teeth. Further tests are necessary to quantify the subsurface fatigue differences between pinion and wheel teeth, which could be accounted for through a blank diameter or forging ratio based technological size factor.

A revised load cycle factor K_{NT} is proposed as a result of the performed gear tests. It relies in its approximation on the MLM [21] and considers failures (here pitting and TFF) alongside run-outs. In magnitude and shape, it is shown to be very comparable to the established tooth root and pitting lifetime factors [1,2]. This study tested gears manufactured according to three different heat treatment protocols, making a stress-based prediction of the lifetime factor impossible. By relying on the calculated material

utilization, an approach is presented that incorporates the gear size, the specific heat treatment protocol and the applied load. Consequently, other gear tests could be include and consider in the prediction of the proposed lifetime factor.

The study mentions the previously developed size factor K_X as a function of the gear's mean normal module m_{mn} [5], but utilizes the weakest link theory [22] to consider the volumetric differences between tested pinions and wheels. Due to the larger number of teeth, larger size factors were predicted for the wheels. In this study, the same size factor is applied throughout the gear tooth. However, as tooth root bending stresses act on a much smaller volume than subsurface stresses, the model might overestimate tooth root breakages in its current form.

As shown in the previous studies [5], the estimated material utilizations for different stress-based multiaxial fatigue criteria vary greatly throughout a gear's mean cross-section. Especially in the case of highly loaded gears, a reliable surface and subsurface fatigue prediction becomes difficult with established criteria. The BO criterion, along with the proposed stress and material models, are proven to be capable of differentiating between the major fatigue failure modes on bevel gears, i.e. pitting, tooth root breakage and TFF or subsurface fatigue. Although further stringent studies are necessary to prove the applicability of the developed model to other gear failures than TFF, it opens the door to a fatigue assessment of a gear design in a single calculation. Although this study focused on bevel gears, none of the implemented assumptions exclude an application to cylindrical gears. In fact, the 2D plane strain stress model utilized in this study should yield even more accurate results when applied to cylindrical gears.

The material model implemented in this study was developed for carburized CrNiMo steels and specifically large forgings of 18CrNiMo7-6 [4]. If data on the steel's average inclusion size and hardness profile are available, the presented methodology should be transferable to other case hardening steels (DIN EN 10084) that similarly underwent a heat treatment in a non-vacuum furnace.

6. Conclusion

The herein presented gear test results support the developed material, stress and fatigue models and demonstrate their applicability in predicting typical gear fatigue failure modes. Key findings of this study are:

(i) During testing, the majority of tooth flank fractures initiated on the wheels, despite the gear's 9:33 gear ratio. The larger material removal during final machining and the steeper case to core hardness transition on the studied wheels are believed to be major contributing factors.
(ii) A revised tooth flank fracture lifetime factor is proposed. It is based on the analysis of the calculated material utilization and incorporates thereby the studied gear size, produced hardness profile and occurring surface stresses. The consideration of other endurance tests of different gear sizes, geometries and hardness profiles is thereby enabled to improve upon the proposed lifetime factor.
(iii) A refined hardness, residual stress and material model is presented that accurately captures the subtle differences between the tested pinions and wheels. It improves upon the fatigue assessment and predicts the majority of wheel-initiated tooth flank fractures reliably.
(iv) This study, alongside the previous publications on subsurface fatigue, outline a methodology capable of predicting tooth flank fracture in bevel gears and possibly all typical gear fatigue failure modes in a single calculation framework.

Declaration of Competing Interest

The authors declare that they have no known competing financial interests or personal relationships that could have appeared to influence the work reported in this paper.

Acknowledgement

The authors would like to thank Kongsberg Maritime Finland OY for supporting this research through the "High Torque Gears" project, the financing of the gear tests and for the possibility to analyze and publish the findings. Sincere gratitude is extended to ATA Gears Oy for the co-financing of the gear tests and the pre- and post-analysis of the gear specimens. In addition, the authors gratefully acknowledge the funding of this research project through the Norwegian Research Council (NFR) – Project ID 270828.

Data availability statement

The data used in this manuscript can be made available on request from the corresponding author.

References

[1] ISO 10300-2:2014 - Calculation of load capacity of bevel gears – Part 2: Calculation of load capacity of bevel gears, 2014.
[2] ISO 10300-3:2014 – Calculation of load capacity of bevel gears – Part 3: Calculation of tooth root strength, 2014.
[3] S.A. Böhme, D. Merson, A. Vinogradov, On subsurface initiated failures in marine bevel gears, Eng. Fail. Anal. 110 (2020), 104415.
[4] S.A. Böhme, A. Vinogradov, H. Biermann, A. Weidner, A. Schmiedel, S. Henkel, Fatigue of carburised CrNiMo steel: Testing and modelling concept, Fatigue Fract. Eng. Mater. Struct. 44 (3) (2021) 788–804.
[5] S.A. Böhme, A. Vinogradov, J. Papuga, F. Berto, A novel predictive model for multiaxial fatigue in carburized bevel gears, Fatigue Fract. Eng. Mater. Struct. (2021).

[6] DNVGL-CG-0036: Calculation of gear rating for marine transmissions, 2015.
[7] J. Liu, H. Zenner, Berechnung der Dauerschwingfestigkeit bei mehrachsiger Beanspruchung – Teil 1 und 2, Materialwissenschaft und Werkstofftechnik vol. 24, pp. 240-249 and 296-303, 1993.
[8] J. Papuga, L. Suchý, M. Růžička, Mean shear stress effect built into the multiaxial fatigue strength estimation method of an integral type, MATEC Web of Conferences, vol. 300, p. 16010, 2019.
[9] E. Cízová, "Parametry historie napetového tenzoru a jejich dopad na únavovou životnost," Master, Fakulta strojní Ústav mechaniky, biomechaniky a mechatroniky, Ceské vysoké ucení technické v Praze, 2021.
[10] FKM, Rechnerischer Festigkeitsnachweis für Maschinenbauteile. VDMA, 2012.
[11] Y. Murakami, Metal Fatigue: Effects of Small Defects and Non-metallic Inclusions, Academic Press, Cambridge, 2019.
[12] J. Thomas, Flankentragfähigkeit und Laufverhalten von hart-feinbearbeiteten Kegelrädern, PhD, TU München, Munich, 1998.
[13] ISO 6336-6:2016 – Calculation of load capacity of spur and helical gears – Part 6: Calculation of service life under variable load, 2016.
[14] V. Baumann, G. Bär, A. Haase, B. Hutschreiter, C. Hünecke, Programm zur Berechnung der Zahnflanken – und Zahnfußbeanspruchung an Kegelrad – und Hypoidgetrieben, vol. Heft 548, ed. Frankfurt: Forschungsvereinigung Antriebstechnik e.V., 1998.
[15] M. Hombauer, Bestimmung der Graufleckentragfähigkeit von Kegelrad- und Hypoidverzahnungen (Forschungsvorhaben Nr. 516). Forschungsvereiningung Antriebstechnik e.V., 2013.
[16] M. Klein, Bestimmung der Fresstragfähigkeit von Kegelrad- und Hypoidverzahnungen (Forschungsvorhaben Nr. 519). Forschungsvereinigung Antriebstechnik e. V., 2013.
[17] L. Wech, Untersuchungen zum Wirkungsgrad von Kegelrad- und Hypoidgetrieben, TU München, 1987.
[18] K. Varis, J. Rinnevalli, R. Vanninen, J. Keski-Rahkonen, Examination of the Crack Initiation and Propagation in a Spiral Bevel Gear, Stressfield for Rolls-Royce Marine, 2014.
[19] R. Weber, Auslegungskonzept gegen Volumenversagen in einsatzgeharteten Stirnradern, PhD, Institut für Werkstofftechnik, Universität Kassel, 2015.
[20] O.R. Lang, Berechnung und Auslegung induktiv randschichtgehärteter Bauteile, in: Kloos, K. H. (Hrsg.); Grosch, J. (Hrsg.): Induktives Randschichthärten. Berichtsband, Tagung 23. bis 25. März 1988, München: Arbeitsgemeinschaft Wärmebehandlung und Werkstofftechnik (AWT), pp. 332–348, 1989.
[21] D.R. Petersen, R.E. Link, F.G. Pascual, W.Q. Meeker, Analysis of fatigue data with run-outs based on a model with non constant standard deviation and a fatigue limit parameter, J. Test. Eval. 25 (3) (1997) 292, https://doi.org/10.1520/JTE11341J.
[22] R. Rabb, Todennäköisyysteoriaan pohjautuva väsymisanalyysi, Books on Demand, Norderstedt, 2013.
[23] ISO 6336-5:2016 – Calculation of load capacity of spur and helical gears – Part 5: Strength and quality of materials, 2016.
[24] T. Reimann, Untersuchungen zur erweiterten Quantifizierung der Tellerradgrübchentragfähigkeit bei Kegelrad- und Hypoidverzahnungen (Forschungsvorhaben Nr. 748 I). Forschungsvereinigung Antriebstechnik e.V., 2020.
[25] I. Boiadjiev, J. Witzig, T. Tobie, K. Stahl, Tooth flank fracture – basic principles and calculation model for a subsurface initiated fatigue failure mode of case hardened gears, in: International Gear Conference 2014: 26th–28th August 2014, Chandos Publishing, Lyon, Oxford, 2014, pp. 670–680.
[26] J. Seabra, M. Klein, B.-R. Höhn, K. Michaelis, R. Annast, Theoretical and experimental investigations about flank breakage in bevel gears, Ind. Lubrication Tribol. 63 (1) (2011) 5–10.
[27] M. MackAldener, Tooth Interior Fatigue Fracture & Robustness of Gears, PhD, Department of Machine Design, KTH – Stockholm, Stockholm, 2001.
[28] C. Wirth, Entwicklung eines Berechnungsberfahrens zur Grübchen- und Zahnfußtragfähigkeit von Hypoidrädern (Forschungsvorhaben Nr. 411). Forschungsvereinigung Antriebstechnik e.V., 2009.

Appendix B

Multiaxial fatigue criteria

Several stress-based, multiaxial fatigue criteria have been published since the 1950s. This appendix gives an overview of the most prevalent invariant, critical-plane, integral and gear-specific fatigue criteria and applies them to the stress state and strength model defined in this thesis. The criteria's applicability to the study of Hertzian contact fatigue in general and TFF or subsurface fatigue in gears is studied. Based on the herein presented results, none of the studied criteria should be deemed inapplicable to rolling contact fatigue as the plotted material utilisations depend greatly on the implemented material model. Especially the mean stress sensitivity for hard steels is a point of contention that impacts the predicted results profoundly.

Studied are the Sines [40], Crossland [38], Dang Van [39], Findley [24], McDiarmid [91], Matake [92], Robert [93], Fogue [93], Liu & Zenner [12], Papuga PCR [94], PCRN [95, 96] and PIN [20]criteria in addition to the gear-specific Annast [14], DNV [2], Hertter [6], Hertter modified [19], Oster [25] and ISO6336-4 or FVA556 I,III [1, 15, 27] criteria. The model definitions, the considered stress components, and their weighting through the model parameters are depicted for each criterion. The predicted material utilisation for the mean pinion cross-section of gear set G1 [10, 19] is plotted and compared with the BO and Hs criteria in the surface perpendicular path P1 starting in the gear's design point MB (see Chapter 4). Variations of the Sines, Crossland and Dang Van criterion according to Kenmeugne [102] to improve upon the criteria's prediction capabilities under compressive mean stresses were also tested. Applied to gear set G1, they did not yield an improvement over their standard definition and were therefore not included in this comparison.

B.1 Sines criterion

The Sines criterion [40] uses the amplitude of the second invariant of the stress tensor deviator $J_{2,a}$ and combines it with the mean hydrostatic stress σ_{hyd}. $\sqrt{3J_{2,a}}$ is equivalent to the von Mises stress σ_{vM} and σ_{hyd} to a third of the

first invariant of the stress tensor I_1. The material parameters used for the calibration of the model parameters are f_{-1}, t_{-1} and f_0, the fatigue limits under fully reversed axial loading, fully reversed torsion and oscillated axial loading.

$$D_{SI} = \frac{a_{SI}\sqrt{J_{2,a}} + b_{SI}\sigma_{hyd,m}}{f_{-1}}$$
$$a_{SI} = \frac{f_{-1}}{t_{-1}} = \kappa \qquad b_{SI} = 6\frac{f_{-1}}{f_0} - \sqrt{3}\frac{f_{-1}}{t_{-1}} \tag{B.1}$$

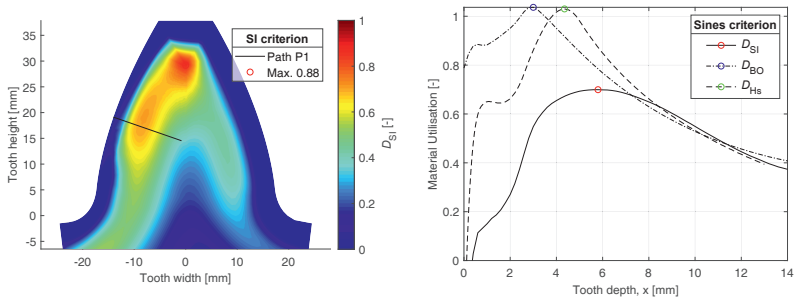

Figure B.1: (a) Material utilisation according to the Sines criterion for the mean pinion cross-section of G1 and (b) compared with the BO and Hs criteria along path P1

B.2 Crossland criterion

Similar to the Sines criterion, the Crossland criterion [38] utilises the same amplitude of the second invariant of the stress tensor deviator $J_{2,a}$ but combines it with the maximum hydrostatic stress σ_{hyd} like the Dang Van criterion [39].

$$D_{CR} = \frac{a_{CR}\sqrt{J_{2,a}} + b_{CR}\sigma_{hyd,max}}{f_{-1}}$$
$$a_{CR} = \frac{f_{-1}}{t_{-1}} \qquad b_{CR} = 3 - \sqrt{3}\frac{f_{-1}}{t_{-1}} \tag{B.2}$$

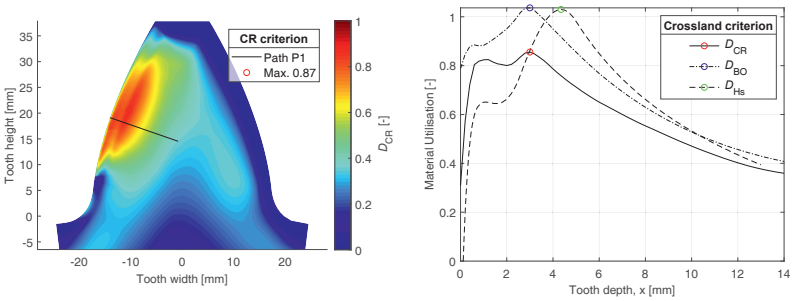

Figure B.2: (a) Material utilisation according to the Crossland criterion for the mean pinion cross-section of G1 and (b) compared to the BO and Hs criteria along path P1

B.3 Dang Van criterion

The Dang Van criterion [39] is referred to as the first mesoscopic criterion that requires the stress study in the least homogeneous agglomerates of grains, typically in the meso- rather than macroscale. It is a widely used criterion for the fatigue analysis of conventional multiaxial fatigue loading and Hertzian contact fatigue. The herein listed definition of the Dang Van criterion relies not on the minimum circumscribing hypersphere but the shear stress amplitude on the examined material plane $\tau_a(\theta, \phi)$ alongside the maximum hydrostatic stress. For non-proportional loading, this version has been shown to be more accurate [96].

$$D_{DV} = \frac{\max\limits_{\theta,\phi}\left(a_{DV}(\tau_a(\theta,\phi)) + b_{DV}\sigma_{hyd,max}\right)}{f_{-1}}$$
$$a_{DV} = \frac{f_{-1}}{t_{-1}} \qquad b_{DV} = 3 - 3/2\frac{f_{-1}}{t_{-1}} \tag{B.3}$$

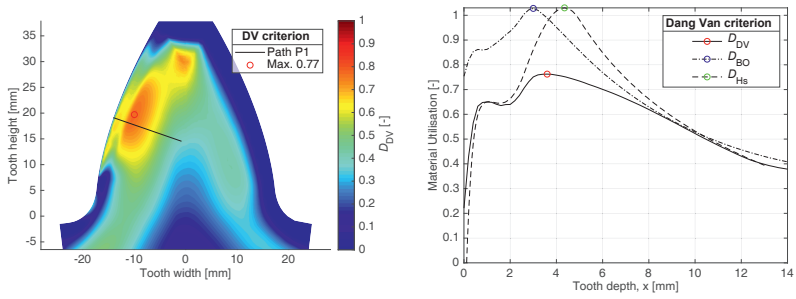

Figure B.3: (a) Material utilisation according to the Dang Van criterion for the mean pinion cross-section of G1 and (b) compared to the BO and Hs criteria along path P1

B.4 Findley criterion

The Findley criterion [24] replaces the Dang Van's maximum hydrostatic stress with the maximum normal stress on the examined material plane $\sigma_{n,max}(\theta,\phi)$. The shear stress amplitude $\tau_a(\theta,\phi)$ and normal stress are weighted through the model parameters a_{FI} and b_{FI}, which are suitably determined from the fatigue parameters f_{-1} and t_{-1}. In the context of subsurface fatigue, the criterion was used by MackAldener on truck, idler gearboxes [23].

$$D_{FI} = \frac{\max\limits_{\theta,\phi}\left(a_{FI}\tau_a(\theta,\phi) + b_{FI}\sigma_{n,max}(\theta,\phi)\right)}{f_{-1}}$$
$$a_{FI} = 2\sqrt{\frac{f_{-1}}{t_{-1}} - 1} \qquad b_{FI} = 2 - \frac{f_{-1}}{t_{-1}} \tag{B.4}$$

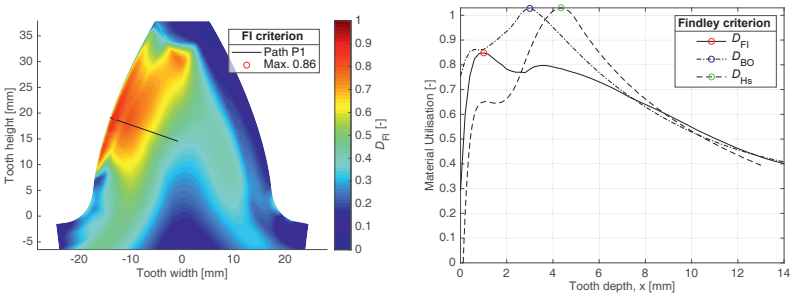

Figure B.4: (a) Material utilisation according to the Findley criterion for the mean pinion cross-section of G1 and (b) compared to the BO and Hs criteria along path P1

B.5 McDiarmid criterion

The McDiarmid criterion utilises $\tau_a(\theta, \phi)$ and $\sigma_{n,max}(\theta, \phi)$ for its equivalent stress prediction. Here, the version that applies to type A cracks or surface parallel cracks is implemented (i.e. $t_{AB} = t_{-1}$) [91]. Other than the Findley criterion, it features empirically determined model parameters based on a large fatigue data set. Its parameter b_{MC} makes use of the material's ultimate tensile strength R_m.

$$D_{MC} = \frac{\max_{\theta,\phi}(a_{MC}\tau_a(\theta,\phi) + b_{MC}\sigma_{n,max}(\theta,\phi))}{f_{-1}}$$
$$a_{MC} = \frac{f_{-1}}{t_{AB}} \quad \text{with} \quad t_{AB} = t_{-1} \qquad b_{MC} = \frac{f_{-1}}{2R_m} \tag{B.5}$$

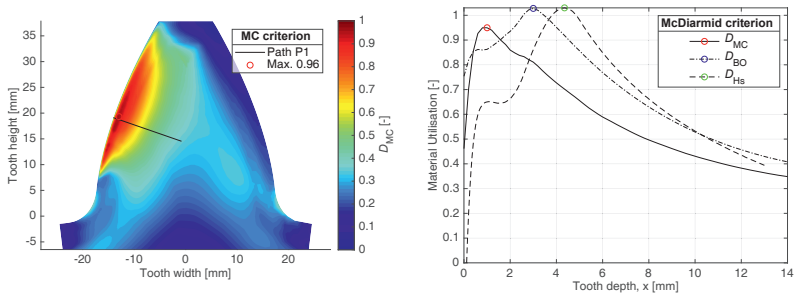

Figure B.5: (a) Material utilisation according to the McDiarmid criterion for the mean pinion cross-section of G1 and (b) compared to the BO and Hs criteria along path P1

B.6 Matake criterion

Another close relative to the Findley criterion is the Matake criterion [92, 103]. It is referred to as a maximum shear stress range criterion. The plane with the highest shear stress amplitude is chosen to predict the largest equivalent stress or material utilisation and not the plane with the largest equivalent stress. The criterion works well for the hard case of the gear tooth that is dominated by the acting shear stresses. For greater material depth where the effect of the maximum normal stress dominates the predicted material utilisation, the resolution with which the Euler angles θ and ϕ are altered results in a large scatter in the predicted utilisation. For the plotted material utilisation in Figure B.6 an element size of 0.2 mm and an angle step size of 5° was chosen.

$$\begin{aligned} \theta_0, \phi_0 &= \arg\max_{\theta,\phi}(\tau_a(\theta,\phi)) \\ D_{MA} &= \frac{a_{MA}\tau_a(\theta_0,\phi_0) + b_{MA}\sigma_{n,max}(\theta_0,\phi_0)}{f_{-1}} \\ a_{MA} &= \frac{f_{-1}}{t_{-1}} \qquad b_{MA} = 2 - \frac{f_{-1}}{t_{-1}} \end{aligned} \tag{B.6}$$

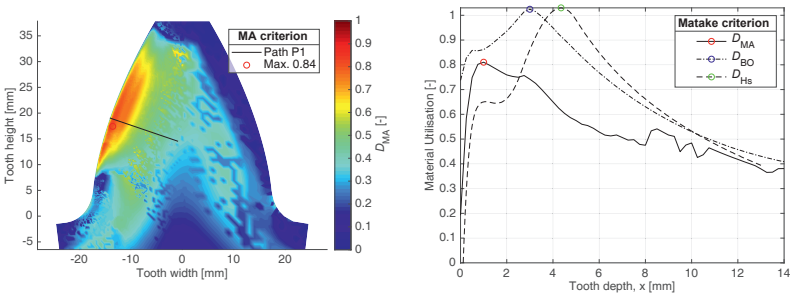

Figure B.6: (a) Material utilisation according to the Matake criterion for the mean pinion cross-section of G1 and (b) compared to the BO and Hs criteria along path P1

B.7 Robert criterion

Another close relative to the Findley criterion is the Robert criterion [93], utilising the shear stress amplitude τ_a in combination with the same model parameters a and b. It expands upon the Findley criterion through the division of the maximum mean normal stress on the examined material plane into the amplitude and mean normal stress on the examined material plane $\sigma_{n,a}$ and $\sigma_{n,m}$.

$$
\begin{aligned}
D_{RO} &= \frac{\max\limits_{\theta,\phi}(a_{RO}\tau_a(\theta,\phi) + b_{RO}\sigma_{n,a}(\theta,\phi) + d_{RO}\sigma_{n,m}(\theta,\phi))}{f_{-1}} \\
a_{RO} &= 2\sqrt{\frac{f_{-1}}{t_{-1}} - 1} \qquad b_{RO} = 2 - \frac{f_{-1}}{t_{-1}} \\
d_{RO} &= \frac{2f_{-1}}{f_0} - \frac{f_0}{2}\left(\frac{1}{t_{-1}} - \frac{1}{f_{-1}}\right) - 2 + \frac{f_{-1}}{t_{-1}}
\end{aligned}
\tag{B.7}
$$

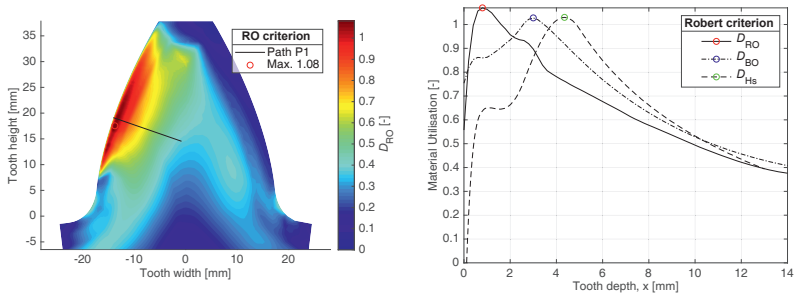

Figure B.7: (a) Material utilisation according to the Robert criterion for the mean pinion cross-section of G1 and (b) compared to the BO and Hs criteria along path P1

B.8 Fogue

The Fogue criterion [93] is the first integral rather than critical plane criterion in the herein provided comparison. Like the BO criterion, it calculates the spatial average of the damage parameter of all material planes. The considered stresses are similar to the Robert criterion, whereas the utilised model parameters differ significantly.

$$
\begin{aligned}
D_{FO} &= \frac{\sqrt{\frac{1}{4\pi}\int_0^{2\pi}\int_0^{\pi}\left(a_{FO}\tau_a + b_{FO}\sigma_{n,a} + d_{FO}\sigma_{n,m}\right)^2 \sin(\phi)\, d\phi d\theta}}{f_{-1}} \\
b_{FO} &= \sqrt{\frac{15 - 3\sqrt{25 - 8(\kappa^2-3)^2}}{2}} \\
a_{FO} &= \sqrt{\frac{12\kappa^2 - 21 + b_{FO}^2}{2}} \\
d_{FO} &= \frac{-(3b_{FO} + 2a_{FO}) + \sqrt{(3b_{FO} + 2a_{FO})^2 + 45\left(4\left(\frac{f_{-1}}{f_0}\right)^2 - 1\right)}}{3}
\end{aligned}
\tag{B.8}
$$

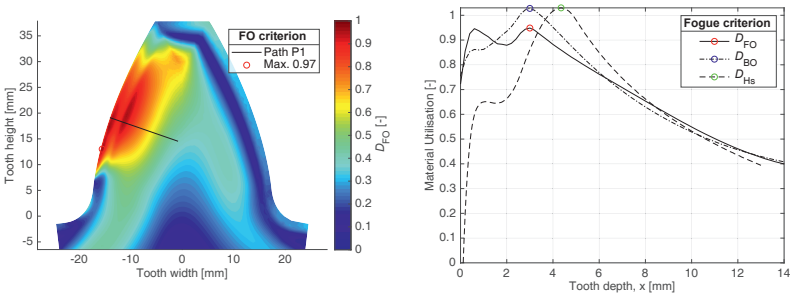

Figure B.8: (a) Material utilisation according to the Fogue criterion for the mean pinion cross-section of G1 and (b) compared to the BO and Hs criteria along path P1

B.9 Liu & Zenner

The application of the Liu & Zenner criterion [12] to Hertzian contact fatigue and fatigue in gears has been discussed in [6, 19]. When studying the allowable shear stress amplitude under varying static, hydrostatic stresses, the Liu & Zenner criterion predicts an exponential growth under compressive hydrostatic stresses. In a gear tooth, rail or bearing, this leads to a negative expression under the square root in the criterion's numerator for the outermost material layer.

$$
\begin{aligned}
D_{LZ} &= \frac{\sqrt{\frac{15}{8\pi}\int_0^{2\pi}\int_0^{\pi}\left(a_{LZ}\tau_a^2\left(1+c_{LZ}\tau_m^2\right)+b_{LZ}\sigma_{n,a}^2\left(1+d_{LZ}\sigma_{n,m}\right)\right)\sin(\phi)\,d\phi d\theta}}{f_{-1}} \\
a_{LZ} &= \frac{1}{5}\left(3\kappa^2-4\right) \qquad b_{LZ} = \frac{1}{5}\left(6-2\kappa^2\right) \\
c_{LZ} &= \frac{28}{3a_{LZ}t_0^2}\left(\left(\frac{f_{-1}}{t_0}\right)^2-\frac{\kappa^2}{4}\right) \\
d_{LZ} &= \frac{28}{15b_{LZ}f_0}\left(\left(\frac{2f_{-1}}{f_0}\right)^2-\frac{a_{LZ}c_{LZ}f_0^2}{21}-1\right)
\end{aligned}
\tag{B.9}
$$

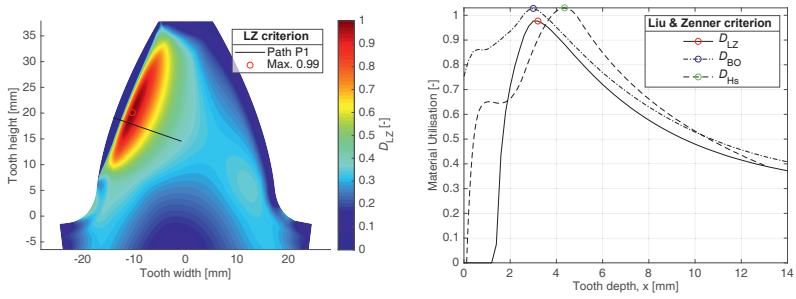

Figure B.9: (a) Material utilisation according to the Liu & Zenner criterion for the mean pinion cross-section of G1 and (b) compared to the BO and Hs criteria along path P1

B.10 Papuga PCR

The PCR criterion, proposed by Papuga in [94], represents his first iteration of a multiaxial fatigue criterion, applicable to both ductile and brittle materials. The model parameters are altered depending on the material's fatigue ratio κ

$$
\begin{aligned}
D_{PCR} &= \frac{\sqrt{a_{PCR}\tau_a^2 + b_{PCR}\left(\sigma_{n,a} + \frac{t_{-1}}{f_0}\sigma_{n,m}\right)}}{f_{-1}} \\
&\text{for} \quad \kappa \geq \sqrt{\frac{4}{3}} \\
a_{PCR} &= \frac{4\kappa^2}{4+\kappa^2} \qquad b_{PCR} = \frac{8f_{-1}\kappa^2\left(4-\kappa^2\right)}{(4+\kappa^2)^2} \\
&\text{for} \quad \kappa < \sqrt{\frac{4}{3}} \\
a_{PCR} &= \frac{\kappa^2}{2} + \frac{\sqrt{\kappa^4-\kappa^2}}{2} \qquad b_{PCR} = f_{-1}
\end{aligned}
\tag{B.10}
$$

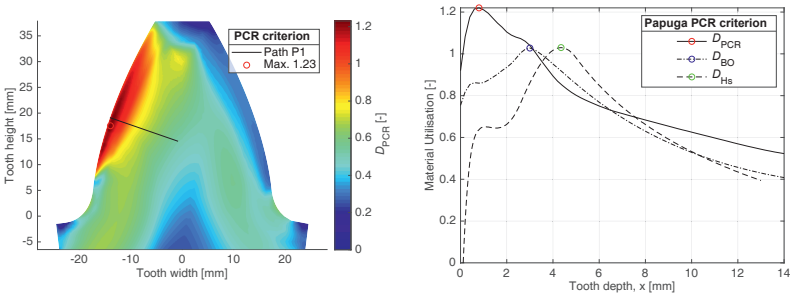

Figure B.10: (a) Material utilisation according to the Papuga PCR criterion for the mean pinion cross-section of G1 and (b) compared to the BO and Hs criteria along path P1

B.11 Papuga PCRN

Papuga's PCRN criterion [95, 96] is an iteration of the PCR criterion, significantly improving upon its result accuracy. Compared to other stress-based multiaxial fatigue criteria, it features one of the best prediction accuracies [104].

$$
\begin{aligned}
D_{PN} &= \frac{\max\limits_{\theta,\phi} \sqrt{a_{PN}\tau_a(\tau_a + c_{PN}\tau_m) + b_{PN}\sqrt{\sigma_{n,a}(\sigma_{n,a} + d_{PN}\sigma_{n,m})}}}{f_{-1}} \\
\kappa_0 &= \frac{f_0}{t_0} \qquad z = \left(\frac{8\kappa_0 f_{-1}}{t_0\,(4+\kappa_0^2)}\right)^2 \\
&\text{for } \kappa \text{ and } \kappa_0 \geq \sqrt{\frac{4}{3}} \\
a_{PN} &= \left(\frac{4\kappa^2}{4+\kappa^2}\right)^2 \qquad b_{PN} = \frac{8 f_{-1}\kappa^2\,(4-\kappa^2)}{(4+\kappa^2)^2} \\
c_{PN} &= \frac{z}{a_{PN}} - 1 \qquad d_{PN} = \frac{z}{b_{PN}^2}\left(4f_{-1}^2 - z\,t_0^2\right) - 1 \\
&\text{for } \kappa \text{ and } \kappa_0 < \sqrt{\frac{4}{3}} \\
a_{PN} &= \frac{\kappa^2}{2} + \frac{\sqrt{\kappa^4 - \kappa^2}}{2} \qquad b_{PN} = f_{-1} \\
c_{PN} &= \frac{2f_{-1}^2}{a_{PN} t_0^2}\left(1 + \sqrt{1 - \frac{1}{\kappa_0^2}}\right) - 1 \qquad d_{PN} = \left(\frac{2f_{-1}^2}{b_{PN} f_0}\right)^2 - 1
\end{aligned}
\tag{B.11}
$$

For Hertzian contact fatigue, the PCRN, similar to the Liu & Zenner crite-

rion, produces negative expressions under square root, specifically in the term $\sqrt{\sigma_{n,a}(\sigma_{n,a} + d_{PN}\sigma_{n,m})}$. The plotted material utilisation in Figure B.11 was produced with a modified version of the criterion according to Equation B.12.

$$D_{PN} = \frac{\max\limits_{\theta,\phi} \sqrt{a_{PN}\tau_a(\tau_a + c_{PN}\tau_m) + b_{PN}\sqrt{\sigma_{n,a}|\sigma_{n,a} + d_{PN}\sigma_{n,m}|}}}{f_{-1}} \tag{B.12}$$

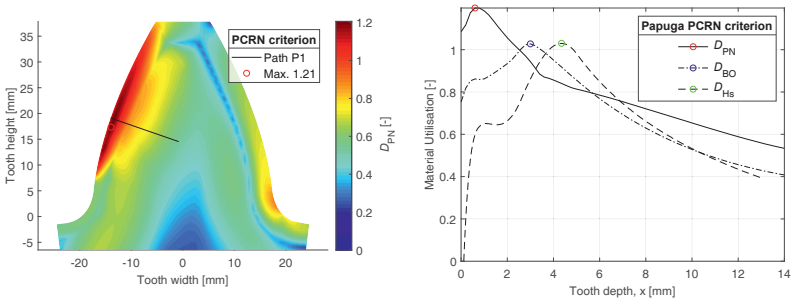

Figure B.11: (a) Material utilisation according to the Papuga PCRN criterion for the mean pinion cross-section of G1 and (b) compared to the BO and Hs criteria along path P1

B.12 Papuga PIN

The PIN criterion by Papuga [20] is an integral criterion compared to the critical plane PCR and PCRN criteria. As documented by other researchers [20, 90], it features an exceptional result accuracy when predicting failure under conventional, non-Hertzian, multiaxial fatigue loading. As outlined in [19], it predicts a too high surface utilisation under Hertzian stresses for the herein implemented material model.

$$\begin{aligned}
D_{PI} &= \frac{\sqrt{\frac{1}{4\pi}\int_0^{2\pi}\int_0^{\pi}\left(a_{PI}\tau_a\left(\tau_a + c_{PI}\tau_m\right) + b_{PI}\left(\sigma_{n,a} + d_{PI}\sigma_{n,m}\right)\right)\sin(\phi)\,d\phi d\theta}}{f_{-1}} \\
a_{PI} &= \frac{15}{2}\,\frac{\kappa(\pi\kappa - 4)}{3\pi - 4\kappa} \qquad b_{PI} = 3f_{-1}\left(1 - \frac{\kappa(\pi\kappa - 4)}{3\pi - 4\kappa}\right) \\
c_{PI} &= 10\frac{f_{-1}^2}{a_{PI}t_0^2} - \frac{20b_{PI}}{3\pi a_{PI}t_0} - 1 \\
d_{PI} &= 6\frac{f_{-1}^2}{b_{PI}f_0}\left(1 - \frac{f_0^2}{3t_0^2}\right) + \frac{4f_0}{3\pi t_0} - 1
\end{aligned} \tag{B.13}$$

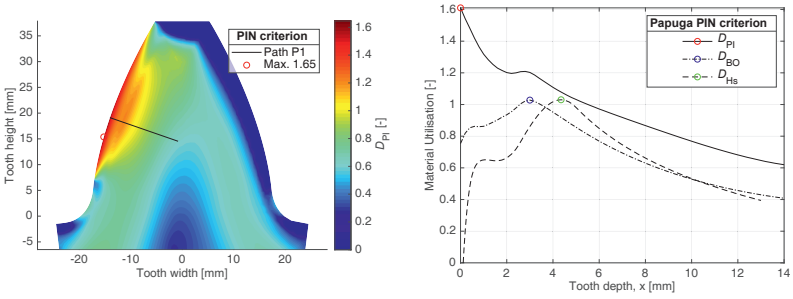

Figure B.12: (a) Material utilisation according to the Papuga PIN criterion for the mean pinion cross-section of G1 and (b) compared to the BO and Hs criteria along path P1

B.13 Annast

The Annast criterion [14] relies on the main principle shear stress τ_{H12} for the prediction of the local material utilisation. From pure Hertzian contact, the maximum shear stress below the point of load introduction can readily be calculated based on the Hertzian contact stress p_H and the half Hertzian contact width b_H. The shear stress is compared to an assumed shear strength of 0.55 HV. As the static residual stresses are not considered in the criterion, Annast suggests applying the criterion to the transition point from case to core, where residual stresses are assumed to be neglectable. For gear set G1, the maximum shear stress should be compared to the shear strength in a depth of approximately 5 mm, where the Annast criterion produces very comparable results to the Hs criterion.

$$\tau_{H12}(x) = \frac{p_H}{Z_K}\left(\frac{x}{b_H} - \frac{\left(\frac{x}{b_H}\right)^2}{\sqrt{1+\left(\frac{x}{b_H}\right)^2}}\right) \tag{B.14}$$

$$D_{AN}(x) = \frac{\tau_{H12}(x)}{0.55\,HV(x)}$$

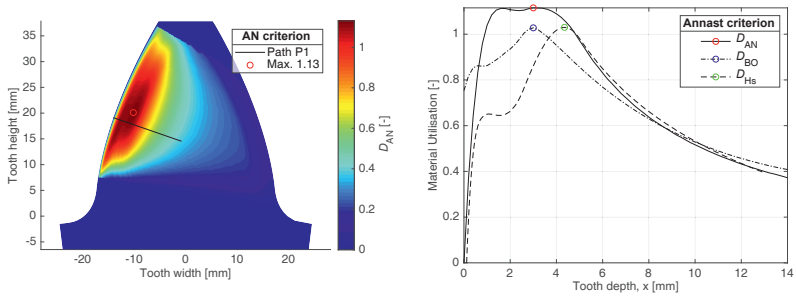

Figure B.13: (a) Material utilisation according to the Annast criterion for the mean pinion cross-section of G1 and (b) compared to the BO and Hs criteria along path P1

B.14 DNV

For a number of load cycles $> 3 \cdot 10^6$, the DNV subsurface fatigue criterion [2] assumes a constant shear fatigue strength, equivalent to 0.625 HV. The acting orthogonal shear stress as a result of the Hertzian contact between the meshing gear teeth is estimated according to Equation B.15. In contrast to the Annast criterion, the Hertzian contact width b_H is increased with a factor of 1.2 and the calculated minimum safety factor as the inverse of the maximum material utilisation D_{DNV}, requiring the iteration of Equation B.15.

$$\begin{aligned} \tau_{xy,a}(x) &= 0.25 \, \frac{\sigma_H}{Z_K} S_{DNV} \cos\left(\frac{\frac{x}{a_H} - 0.5}{\frac{x}{a_H} + 0.5} \frac{\pi}{2} \right) \\ D_{DNV}(x) &= \frac{\tau_{xy,a}(x)}{0.625 \, HV(x)} \\ a_H &= 1.2 \, S_{DNV} \, b_H \quad \text{with} \quad S_{DNV} = \frac{1}{\max(D_{DNV})} \end{aligned} \tag{B.15}$$

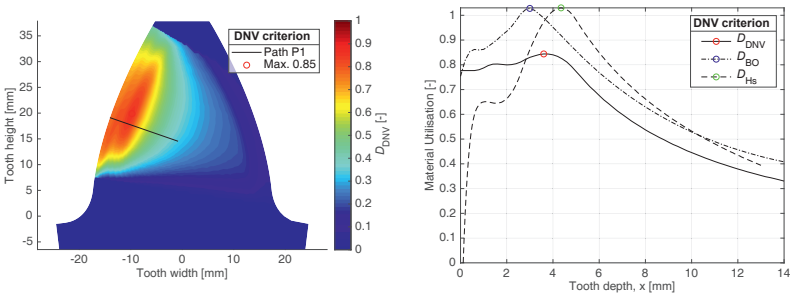

Figure B.14: (a) Material utilisation according to the DNV criterion for the mean pinion cross-section of G1 and (b) compared to the BO and Hs criteria along path P1

B.15 Hertter

Hertter developed his criterion for the prediction of pitting and tooth root breakage in cylindrical gears [6]. He proposed a modification to the Liu & Zenner criterion that removes the mean normal stress $\sigma_{n,m}$ from equivalent stress prediction and adds it to the uniaxial fatigue strength f_{-1} as a product with the mean stress sensitivity M rather than a 4th model parameter. As such, the criterion fails to intersect the f_0 load case and does not achieve the same result accuracy as other herein listed multiaxial fatigue criteria. As Hertter only studied the surface failure modes pitting and tooth root breakage, potential tensile residual stresses in the core were disregarded.

$$
\begin{aligned}
D_{HE} &= \sqrt{\frac{15}{8\pi}\int_0^{2\pi}\int_0^{\pi}\frac{a_{LZ}\tau_a^2\left(1+c_{LZ}\tau_m^2\right)+b_{LZ}\sigma_{n,a}^2}{\left(f_{-1}-M\sigma_{n,m}\right)^2}\,\sin(\phi)\,d\phi d\theta} \\
a_{LZ} &= \frac{1}{5}\left(3\kappa^2-4\right) \qquad b_{LZ} = \frac{1}{5}\left(6-2\kappa^2\right) \\
c_{LZ} &= \frac{28}{3a_{LZ}t_0^2}\left(\left(\frac{f_{-1}}{t_0}\right)^2-\frac{\kappa^2}{4}\right)
\end{aligned}
\tag{B.16}
$$

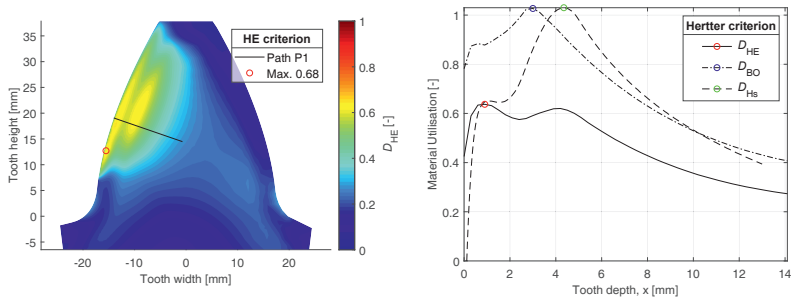

Figure B.15: (a) Material utilisation according to the Hertter criterion for the mean pinion cross-section of G1 and (b) compared to the BO and Hs criteria along path P1

B.16 Hertter - Wirth

Wirth modified the Hertter criterion through the consideration of the slip factor Z_S outlined in the ISO10300-2 and the FVA411 project [9, 21] and the implementation of positive tensile, residual stresses in the core of the gear tooth [105]. Hertter's material model and multiaxial fatigue criterion remained unchanged. Both modifications do not change the subsurface material utilisation in the mean pinion cross-section of G1 significantly and only demote the risk for pitting through the use of the slip factor Z_S. As shown in chapter 4, when bending stresses are considered alongside the Hertzian contact stresses, a higher material utilisation is naturally predicted in the pinion dedendum over the wheel addendum, essentially describing the same effect as Z_S. Wirth's tensile residual stress function has the shape $\sigma_{res,ten}(x) = a\,(x - s_{n\alpha})^4 + c$. The parameter a is adjusted to ensure a transition from compressive to tensile residual stresses in x_c, the depth where the hardness profile transitions to the constant core hardness. The parameter c is iterated to ensure stress equilibrium along $s_{n\alpha}$. By only considering two model constants, a tangential constraint from the compressive to the tensile residual stress curves can not be ensured (see Figure B.17). Also, by transitioning to the tensile residual stresses in x_c, tensile stresses are first predicted in a large material depth, where they have little effect on the material utilisation in the TFF-relevant depth. A significantly steeper transition is achieved if the tangential constraint (between Lang's original compressive residual stress curve [28] and a 4th order polynomial to approximate the tensile residual stress in the core) is placed in the CHD (see Chapter 2). Equation B.17 outlines the material strength or hardness modification by Wirth through the use of Z_S. Figure B.16 plots the resulting material utilisation for G1 under the consideration of Z_S and the modified residual stress profile.

$$\begin{aligned} HV(x) &= HV_0(x)Z_S \quad \text{for} \quad 0 < x < a \\ HV(x) &= HV_0(x) \quad \text{for} \quad x > b \\ \text{Linear interpolation of } Z_S &\quad \text{for} \quad a \leq x \leq b \\ a/b_H = 0.5 &\quad \text{and} \quad b/b_H = 1 \end{aligned} \tag{B.17}$$

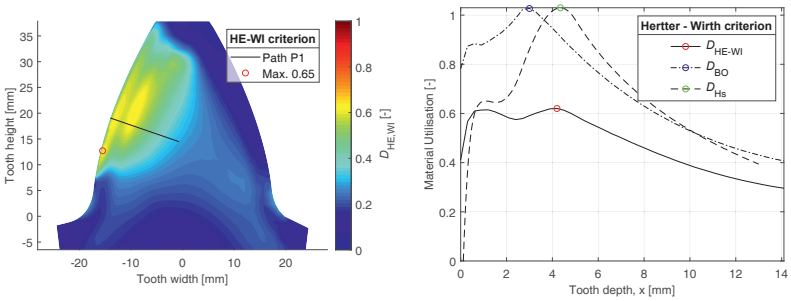

Figure B.16: (a) Material utilisation according to the Hertter-Wirth criterion for the mean pinion cross-section of G1 and (b) compared to the BO and Hs criteria along path P1

The maximum material utilisation in a depth of 4.2 mm is the same for the original Hertter criterion and the Hertter-Wirth criterion. Wirth's residual stress model predicts tensile stresses in a greater material depth than the Hertter criterion predicts the maximum material utilisation (5.1 mm compared to 4.2 mm). The tensile residual stresses have therefore no effect on the maximum material utilisations. Figure B.17 plots the herein proposed residual stress model and the Wirth model. The missing tangential constraint between compressive and tensile residual stress and the later onset of the tensile residual stresses are visualised along path P1.

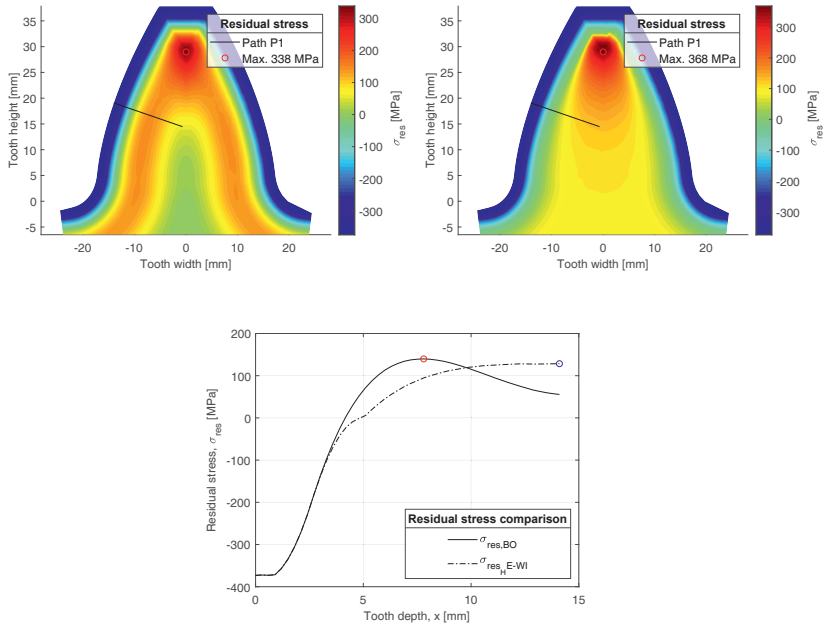

Figure B.17: Residual stresses for the mean pinion cross-section of G1 for (a) the herein outlined residual stress model, (b) Wirth's model and along path P1 in (c) comparing both approaches

B.17 Hertter - Böhme

The modified Hertter criterion was presented in Paper III [19] and extracts, like the original Hertter criterion, the mean normal stress $\sigma_{n,m}$ from Liu & Zenner criterion. Instead of relying on the mean stress sensitivity M for the weighting of $\sigma_{n,m}$, the model parameter $d_{HE,mod}$ is correctly predicted using the uniaxial fatigue strength under alternating load f_0. As a result, the accuracy of the criterion when exposed to conventional multiaxial fatigue loading is significantly improved [19].

$$
\begin{aligned}
D_{HE,mod} &= \frac{\sqrt{\frac{15}{8\pi}\int_0^{2\pi}\int_0^{\pi}\left(a_{LZ}\tau_a^2\left(1+c_{LZ}\tau_m^2\right)+b_{LZ}\sigma_{n,a}^2\right)\sin(\phi)\,d\phi d\theta} + \frac{1}{4\pi}\int_0^{2\pi}\int_0^{\pi}\left(d_{HE,mod}\sigma_{n,m}\right)\sin(\phi)\,d\phi d\theta}{f_{-1}} \\
a_{LZ} &= \frac{1}{5}\left(3\kappa^2-4\right) \qquad b_{LZ} = \frac{1}{5}\left(6-2\kappa^2\right) \\
c_{LZ} &= \frac{28}{3a_{LZ}t_0^2}\left(\left(\frac{f_{-1}}{t_0}\right)^2-\frac{\kappa^2}{4}\right) \\
d_{HE,mod} &= 3\left(\frac{2f_{-1}}{f_0}-\sqrt{1+\frac{1}{21}a_{LZ}c_{LZ}f_0^2}\right)
\end{aligned}
\tag{B.18}
$$

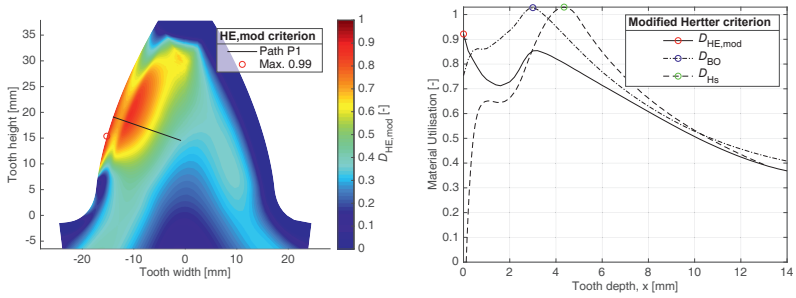

Figure B.18: (a) Material utilisation according to the modified Hertter-Böhme criterion for the mean pinion cross-section of G1 and (b) compared to the BO and Hs criteria along path P1

B.18 Oster

Oster [25] developed his criterion for the prediction of the load-carrying capacity of cylindrical gears under Hertzian and elastohydrodynamic stresses. Based on the shear stress intensity criterion, he proposed the calculation of the spatial average of the maximum of the shear stress amplitude over all planes and the deduction of a similarly calculated, static residual stress. His studies form the basis for the later works by the FZG in Munich on TFF [14, 15] and the ISO6336-4 technical report [1]. The considered stress components are atypical compared to other presented multiaxial fatigue criteria and overestimate the local material utilisation in the absence of compressive residual stresses (i.e. the tooth interior). The maximum shear stress rather than shear stress amplitude is compared to the local fatigue strength.

$$D_{OS}(x) = \frac{\tau_{eff,max}(x) - \Delta\tau_{eff,RS}(x)}{\tau_{zul}(x)} \tag{B.19}$$

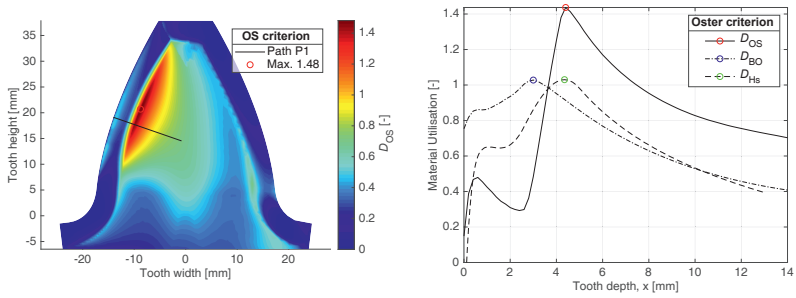

Figure B.19: (a) Material utilisation according to the Oster criterion for the mean pinion cross-section of G1 and (b) compared to the BO and Hs criteria along path P1

B.19 ISO6336-4

The ISO6336-4 Technical report [1] is the culmination of the TFF-focused efforts by the FZG in Munich and the FVA [6, 14, 15, 27]. It is an implementation of the approach suggested in the FVA project 556 I [15]. The shear stress amplitude is calculated as the difference between the maximum effective shear stress $\tau_{eff,L}$ and the mean effective shear stress $\Delta\tau_{eff,L,RS}$. Relying on the Oster criterion [25], the effective residual stress is deducted from the shear stress amplitude and compared to the local shear strength τ_{zul}. As Figure B.20 shows, the predicted material utilisation is very comparable to the Hs criterion. Contrary to the Hs criterion, the individual stress components are not weighted according to model parameters and the stress and correction factor definitions are somewhat ambiguous.

$$D_{ISO}(x) = \frac{\tau_{eff,L}(x) + \Delta\tau_{eff,L,RS}(x) - \tau_{eff,RS}(x)}{\tau_{zul}(x)} + c \tag{B.20}$$

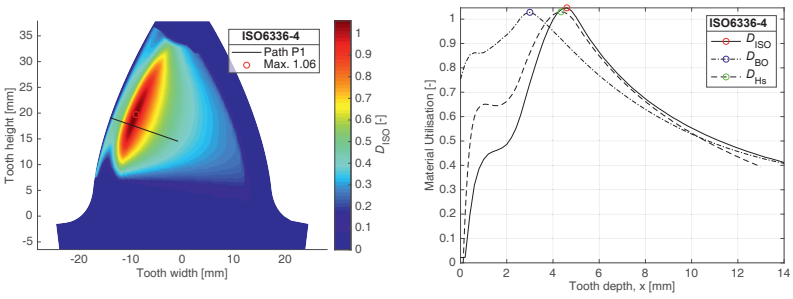

Figure B.20: (a) Material utilisation according to the ISO6336-4 for the mean pinion cross-section of G1 and (b) compared to the BO and Hs criteria along path P1

Appendix C

Size factor

The size factor proposed in [19] relies on the weakest link theory [58] and the numerical comparison of the effective volume V_{eff} of the tested 34CrNiMo6 steel during uniaxial fatigue testing in the VHCF regime [32] and 10 bevel gear sets with a mean normal module range of $m_{mn} = 2.22 - 24.71$ mm. Based on the obtained fatigue test results (i.e. the uniaxial fatigue strength under alternating loading f_{-1} and the pearl string method derived standard deviation in the VHCF regime s), a relative standard deviation $s_r = 4$ % was calculated for the 34CrNiMo6 steel, yielding an effective or reference volume of $V_{eff} = V_{ref} = 22.26$ mm^3. Equation C.1 illustrates the calculation of V_{eff} through the reliability R_i and volume V_i of each element i in the FEM calculation of the hourglass shaped, 34CrNiMo6 specimen. The von Mises equivalent stress σ_{vM} and its maximum over all elements are furthermore required.

$$\begin{aligned} \lambda_i &= \frac{1}{s_r}\left(\frac{\sigma_{vM,i}}{\max\limits_i(\sigma_{vM,i})} - 1\right) \quad \text{with} \quad s_r = \frac{s}{f_{-1}} \\ R_i &= \int_{\lambda_i}^{\infty} \frac{1}{\sqrt{2\pi}} e^{-\frac{x^2}{2}} dx \\ V_{eff} &= \sum_{i=1}^{n} V_i \frac{\log R_i}{\log 0.5} \end{aligned} \tag{C.1}$$

The size factor K_X itself is calculated through the ratio between the established reference volume V_{ref} and a second effective volume V_{eff}, the reliability of a single link P and the standardised normal distribution factor λ.

$$
\begin{aligned}
n_A(V_{eff} > V_{ref}) &= \frac{V_{eff}}{V_{ref}} \\
n_A(V_{eff} \leq V_{ref}) &= \frac{V_{ref}}{V_{eff}} \\
P &= 1 - 0.5^{\frac{1}{n_A}} \\
\int_{-\infty}^{\lambda} \frac{1}{\sqrt{2\pi}} e^{-\frac{x^2}{2}} dx - P = 0 &\xrightarrow{\text{yields}} \lambda \\
K_X(V_{eff} > V_{ref}) &= 1 + \lambda s_r \\
K_X(V_{eff} \leq V_{ref}) &= \frac{1}{1 + \lambda s_r}
\end{aligned}
\tag{C.2}
$$

Table C.1 lists the studied 10 gear sets, their mean normal module m_{mn} their total volume (teeth only, pinion and wheel) V_{tot}, effective volume V_{eff} and size factor according to Equation C.2.

Gears	m_{nm}	V_{tot}	V_{eff}	K_X
G7	24.71	$3.30 \cdot 10^7$	7830	0.877
G6	17.38	$1.75 \cdot 10^7$	5640	0.881
G5	15.88	$1.52 \cdot 10^7$	6555	0.887
G4	14.59	$1.07 \cdot 10^7$	5215	0.890
G3	13.82	$6.35 \cdot 10^6$	852	0.916
G2	20.65	$1.84 \cdot 10^7$	2999	0.889
G1	16.85	$1.04 \cdot 10^7$	4144	0.893
B3-1	9.55	$1.37 \cdot 10^6$	272	0.936
G0	3.57	$6.26 \cdot 10^4$	8	1.031
F0	2.22	$3.48 \cdot 10^4$	16	1.011

Table C.1: Size factor derivation based on 10 studied gear sets with m_{mn}, V_{tot}, V_{eff} and K_X

Figure C.1 plots the calculated size factors against the effective volume in C.1a and against the mean normal module in C.1b.

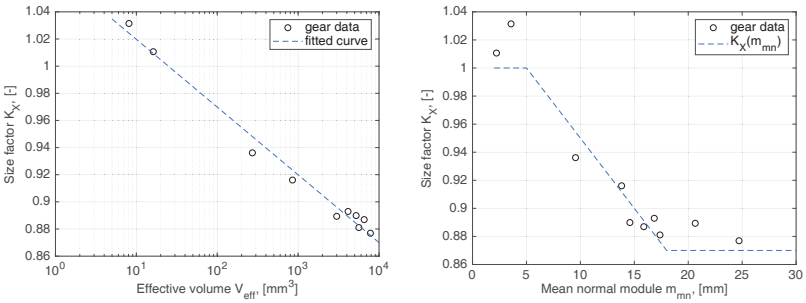

Figure C.1: (a) Maximum hydrostatic stress for the mean pinion cross-section of G1 according to numerical calculation and (b) along path P1 compared with the analytical model

Based on the observable, linear trend of the size factor as a function of the mean normal module m_{mn} an approximation of the size factor according to Equation C.3 is suggested.

$$K_X = 1.05 - 0.01 m_{mn} \quad \text{with} \quad 0.87 \leq K_X \leq 1 \tag{C.3}$$

The suggested correlation for the size factor aligns itself with other gear standards like the DIN3991-2 [5] or ISO10300-3 [80]. Of the studied gear sets, three were test gears with surface pressures in excess of 1800 MPa (G0, F0 [9] and B3-1 [41]) and seven were large, industrial bevel gears with surface pressures below 1400 MPa. As a result, the proposed size factor and module correlation underestimate the effect of high stresses or load on large gears. In addition, it favours a larger number of gear teeth and smaller module on a given diameter, a correlation which did not hold true for the studied gear sets (compare G1 and G4). The error that is introduced through the simplification is small and can therefore be ignored. For a more accurate differentiation between pinion and wheel teeth and the risk for subsurface fatigue, separate size factors should be calculated.

ISBN 978-82-326-6184-8 (printed ver.)
ISBN 978-82-326-6399-6 (electronic ver.)
ISSN 1503-8181 (printed ver.)
ISSN 2703-8084 (online ver.)

NTNU

Norwegian University of
Science and Technology